

T 212
D30
BAN

CENTRAL LIBRARY	
FEZPUR UNIVERSITY	
Accession No.	<u>T 212</u>
Date	<u>06/08/13</u>

**SYNTHESIS, SWIFT HEAVY ION IRRADIATION
AND CHARACTERIZATION OF CONDUCTING
POLYMER BASED NANOSTRUCTURED
MATERIALS FOR BIOMEDICAL AND SENSOR
APPLICATIONS**

**A thesis submitted in partial fulfillment of the
requirements for the degree of
Doctor of Philosophy**

Somik Banerjee

Registration No.042 of 2011



Department of Physics, School of Science and Technology

Tezpur University, Tezpur-784028

Assam, India

February, 2012

Synthesis, swift heavy ion irradiation and characterization of conducting polymer based nanostructured materials for biomedical and sensor applications

Abstract

The path-breaking discovery of high conductivity in polyacetylene in 1977 by A. J. Heeger, A. G. MacDiarmid and H. Shirakawa opened up a whole new field of research, which won them the Noble prize in the year 2000. Since then the field of conducting polymers has undergone tremendous developments and a wide range of commercial applications have evolved. Conducting polymers have found applications in different areas such as microelectronics, sensors, electrodes for batteries and supercapacitors, EMI shielding etc. Conducting polymers are also being considered for a range of biomedical applications including the development of artificial muscles, controlled drug release and the stimulation of nerve regeneration. Recently, one dimensional (1D) nanostructures such as nanofibers, nanowires, nanorods, nanobelts, and nanotubes have attracted considerable attention of the scientific community owing to their unique applications in mesoscopic physics and fabrication of nanoscale devices. 1D nanostructures are ideal systems for investigating the dependence of electrical, thermal and mechanical properties on quantum confinement and dimensionality. 1D conducting polymer nanostructures deserve a special mention mainly because they combine the advantages of organic conductors with low dimensionality. Among the family of π -conjugated polymers, polyaniline is especially attractive and have been investigated by several research groups worldwide mainly because of its unique properties like good environmental stability, solubility and simple acid/base doping/dedoping chemistry, making it a promising material for a wide range of applications. Polyaniline nanostructures have been synthesized by using templates such as surfactants, micelles or seeds. One-dimensional (1D) polyaniline nanostructures including nanorods, nanotubes and nanofibers, have also been studied as these nanostructured materials are expected to perform better wherever there is an interaction between the material and the surrounding environment. 1D Polyaniline nanostructures have been used in different

applications and it has been observed that in most cases the performance is far better than their bulk counter part.

Swift heavy ion (SHI) irradiation of polymers can induce irreversible changes in their macroscopic properties such as chemical, electronic, electrical, morphological, tribological and optical properties due to events such as electronic excitation, ionization, chains scission and cross-links as well as mass losses associated with the ion-polymer interaction. SHI irradiation has also been used to modify polymers for biomedical applications. SHI (energy > 1 MeV/u) irradiation deposits the energy in the material in the near surface region mainly due to the electronic excitation. The extent of damage formation and property modification depends strongly on energy, mass and charge state of the ion, its fluence and target density. The impinging ions do not get implanted in the material due to their large range typically a few tens of μm . Ionization trail produced by SHI causes bond cleavages producing free radicals, which are responsible for most of the chemical transformations in polymers such as chain scission, cross linking, generation of active sites, double and triple bond formation, emission of atoms, molecules and molecular fragments.

The present thesis is a description of a number of experiments in the dynamic research field of conducting polymer based nanostructured materials, in general, and polyaniline based nanostructured materials, in particular. We have synthesized polyaniline nanofibers doped with two different types of dopants viz., HCl and camphorsulfonic acid (CSA) using interfacial polymerization and polyaniline nanofiber reinforced polyvinyl alcohol nanocomposites using *in-situ* rapid-mixing polymerization techniques. The polyaniline based nanostructured materials have been characterized by X-ray diffraction (XRD), transmission electron microscopy (TEM), scanning electron microscopy (SEM), Fourier transform infra red spectroscopy (FTIR), micro-Raman spectroscopy (μRS), ultra-violet visible (UV-Vis) absorption spectroscopy. The conductivity relaxations and charge transport mechanism in these materials have been investigated using dielectric spectroscopy and ac conductivity studies. SHI irradiation of the polyaniline based nanostructured materials have been carried out with 90 MeV oxygen ions (O^{7+}) at different fluences viz., 3×10^{10} , 1×10^{11} , 3×10^{11} and 1×10^{12}

ions/cm² with a view of studying the ion irradiation effects on the physico-chemical properties of the nanostructured materials and to utilize the modifications in some specific application areas.

The thesis contains eight chapters, each of which is again divided into several sections and sub-sections. **Chapter 1** begins with an overview of the exciting and emerging field of conducting polymers with an emphasis on conducting polymer based nanostructured materials. Thereafter the potential applications of conducting polymer nanostructures in the field of biomedical science and sensor technology have been reviewed. The chapter also includes literature related to swift heavy ion irradiation induced modifications of conducting polymers. At the end of the chapter, scope of the thesis along with the statement of the thesis problem and the major objectives of the present work has been spelt out.

The mechanisms of formation of polyaniline by chemical polymerization and polyaniline nanofibers by interfacial and rapid mixing polymerization techniques have been discussed in **Chapter-2**. The theoretical framework developed to account for the charge transport mechanisms and relaxations in conducting polymers and conducting polymer based nanostructured materials have been reviewed in this Chapter. Theories developed for explaining ion-solid interactions have also been discussed in brief.

The materials and methods used for the synthesis and characterization of polyaniline nanofibers and polyaniline nanofibers reinforced PVA nanocomposites have been discussed in **Chapter 3**. Principles of various characterizations techniques like XRD, SEM, TEM, FTIR, UV-Vis spectroscopy, micro-Raman spectroscopy (μ RS), ac conductivity, dielectric spectroscopy and the biochemical assays used for the study of biological activity of the polyaniline based nanostructured materials have been explained. Fabrication of piezoelectric sensors based on the polyaniline based nanostructured materials and the characterization of the sensors for studying different parameters such as sensitivity, response time and linearity have also been discussed.

Chapter-4 describes the synthesis of PANi nanofibers using interfacial polymerization and the analysis of the variations in the physico-chemical

properties of PANi nanofibers upon SHI irradiation by different characterization techniques. TEM results show that the size of PANi nanofibers decrease with the increase in irradiation fluence, which has been attributed to the fragmentation of PANi nanofibers in the core of amorphized tracks caused by SHI irradiation. XRD studies reveal a decrease in the domain length and an increase in the strain upon SHI irradiation. The increase in d -spacing corresponding to the (100) reflection of PANi nanofibers with increasing irradiation fluence has been attributed to the increase in the tilt angle of the chains with respect to the (a , b) basal plane of PANi. Decrease in the integral intensity upon SHI irradiation indicates amorphization of the material. Micro-Raman (μ R) studies confirm amorphization of the PANi nanofibers and also show that the PANi nanofibers get de-doped upon SHI irradiation. μ R spectroscopy also reveals a benzenoid to quinoid transition in the PANi chain upon SHI irradiation. Charge transport and relaxation mechanisms in the pristine and irradiated PANi nanofibers have been analysed and are presented in this chapter.

Chapter-5 deals with the synthesis of polyaniline nanofiber reinforced PVA nanocomposites using rapid mixing polymerization technique and the effects of 90 MeV O^{7+} ion irradiations on the physico-chemical properties of the nanocomposites. The pristine polyaniline nanofiber reinforced PVA nanocomposites as well as the irradiated samples have been thoroughly characterized and the interpretations of the results are incorporated in this chapter. Modifications in the domain length, strain, normalized integral intensity and the overall degree of crystallinity of the PANi nanofiber reinforced nanocomposites upon SHI irradiation have been investigated using X-ray diffraction technique. FTIR analysis reveals significant variations in the chemical structure of the PANi nanofibers upon SHI irradiation. PALS study shows that the positron lifetimes τ_1 and τ_2 decrease sharply from the pristine material to that for irradiated sample with fluence of 3×10^{10} ions/cm² but saturates thereafter. The effect of 90 MeV O^{7+} ion irradiation upon the charge transport and the relaxation mechanisms in the nanocomposite films studied using dielectric spectroscopy and ac conductivity measurements indicate that the conductivity of the PANi nanofiber reinforced PVA nanocomposites enhance upon SHI irradiation.

The applications of polyaniline based nanostructured materials as potential antioxidants have been investigated and the results are presented in **Chapter-6**. It has been observed that polyaniline nanofibers have much better antioxidant activity and biocompatibility as compared to their bulk counterpart. This chapter also focuses on the SHI irradiation induced variations in the antioxidant activity and biocompatibility of the PANi based nanostructured materials. It has been observed that antioxidant activity and the haemolysis prevention efficiency of the PANi based nanostructured materials increases upon SHI irradiation.

Chapter 7 embodies the fabrication methodology of piezoelectric sensors based on PANi nanofiber reinforced PVA nanocomposites for sensing hazardous chemicals viz., free radicals and hydrochloric acid. This chapter focuses on the interpretation of the experimental results acquired while studying the sensing properties of PANi nanofiber reinforced PVA nanocomposite coated quartz crystal resonators for a class of chemical analytes using a quartz crystal microbalance (QCM). Different parameters such as response time, sensitivity and linearity of the sensors have been determined and incorporated in this chapter. The mechanism of sensing of the analytes by the PANi nanofiber reinforced PVA nanocomposites have also been investigated using different characterization techniques.

Chapter-8 summarizes the major conclusions drawn from the work contained in this thesis. The low dimensionality of the PANi based nanostructured materials leads to significant improvement in their physico-chemical properties as compared to those of their bulk counterparts and makes them promising materials for biomedical and sensor applications investigated and discussed in the present thesis. At the end of this chapter, the future scope of research in the field of conducting polymer based nanostructured materials has been briefly mentioned.

Declaration

I hereby declare that the thesis entitled "**Synthesis, swift heavy ion irradiation and characterization of conducting polymer based nanostructured materials for biomedical and sensor applications**", submitted to the School of Science and Technology, Tezpur University in partial fulfillment of the requirements for the award of the Doctor of Philosophy in Physics, is a record of original research work carried out by me. Any text, figures, theories, results or designs that are not of my own devising are appropriately referenced in order to give due credit to the original author(s). All the sources of assistance have been assigned due acknowledgement. I also declare that neither this work as a whole nor a part of it has been submitted to any other university or institute for any degree, diploma, associateship, fellowship or any other similar title or recognition.

Date: 23.02.2012

Place: Tezpur



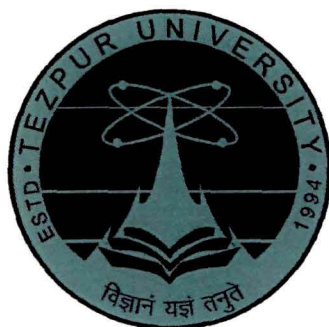
(Somik Banerjee)

Department of Physics

School of Science and Technology

Tezpur University

Tezpur-784028, Assam, India



Tezpur University

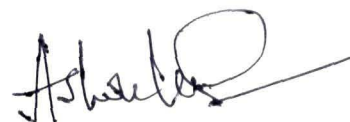
Certificate

This is to certify that the thesis entitled “**Synthesis, swift heavy ion irradiation and characterization of conducting polymer based nanostructured materials for biomedical and sensor applications**”, submitted to the School of Science and Technology, Tezpur University in partial fulfillment of the requirements for the award of the Doctor of Philosophy in Physics, is a record of original research work carried out by Mr. Somik Banerjee under my supervision and guidance.

All help received by him from various sources have been duly acknowledged.

No part of the thesis has been submitted elsewhere for award of any other degree.

Signature of Supervisor:



(Prof. A. Kumar)

Designation: Professor

School: Science and Technology

Department: Physics

Date: 23.02.2012

Place: Tezpur-784028, Assam, India

Dedication

*I dedicate this thesis to my beloved father
Late Kirit Banerjee, who gave me the
dream of success but could not live to see
the dream converting into reality*

&

*My beloved mother
Mrs. Chandra Banerjee without whose
love and support I could not have been
able to fulfill my father's dream.*

Acknowledgements

*This PhD thesis is the culmination of a few years of fervent learning and research experience. Throughout these years, I have received a lot of support from my family, research guide and friends. Indeed, my doctoral thesis is a dream of my late father **Mr. Kirit Banerjee** coming true. Each word written in this page expresses my deep gratitude to all those who played a crucial role during my Ph.D. work and without whom this thesis would not have been possible.*

*It gives me enormous pleasure to express my deep sense of gratitude to my research supervisor **Prof. Ashok Kumar** for his dynamic and meticulous supervision all throughout my research work at Tezpur University. His scientific perceptions, constant encouragement, moral support and courage in allowing me to explore the gigantic scientific landscape have helped me immensely not only to develop myself as a hard-working individual but also to grow passion and imagination to invent and discover. His valuable suggestions and criticism have inspired me to put my best efforts into my work. Needless to say, I shall be highly obliged to him for all my life for being the best mentor any student can ask for. Thank you so much Sir for being there with words of inspiration, wisdom and optimism that always helped me to see the bright side of things.*

I would like to extend my sincere gratitude to Dr. D. K. Avasthi, Senior Scientist, Inter University Accelerator Centre (IUAC), New Delhi for his keen interest, fruitful discussions and suggestions regarding the swift heavy ion irradiation studies of conducting polymer based nanostructured materials. I sincerely acknowledge Dr. Udayan De, Retired Scientist, Variable Electron Cyclotron Centre (VECC), Kolkata and Dr. D. Sanyal from the same Research Institute for their timely help, comments and valuable suggestions for the Positron Annihilation Lifetime Spectroscopy studies on Polyaniline nanofibers reinforced PVA nanocomposites. I also acknowledge Dr. Fouran Singh, Mr. P. K. Kulriya, Mrs. Indra Sulania for the help extended by them during the irradiation experiments conducted at IUAC, New Delhi.

I appreciate having capitalized on this great opportunity given to me at Tezpur University. The facilities at Tezpur University have allowed me to enhance my personal experience and life both academically and personally. I would like to take this

opportunity to thank Prof. Amarjyoti Choudhury, Pro-Vice Chancellor, Tezpur University for enriching me with his inspiring thoughts and ideas. It is my immense pleasure to acknowledge the help extended by Prof. B.K. Konwar, Vice-Chancellor, Nagaland University and Professor, Department of Molecular Biology and Biotechnology, Tezpur University for his encouragement, inspiration and fruitful discussions in carrying out some of the works related to biomedical applications of conducting polymer based nanostructured materials. I would also like to acknowledge Prof. Jayanta Kumar Sarma, Dr. Nidhi Saxena Bhattacharyya, Dr. Nilakshi Das, Dr. Gazi A. Ahmed, Dr. Dambarudhar Mohanta, Dr. Pritam Deb, Dr. Kishore Baruah, Dr. P. K. Karmakar, Dr. Mrinal Das and Dr. Pobitra Nath of the Department of Physics, Prof. S. K. Duloi and Prof. N. Karak from the Department of Chemical sciences for their encouragement, criticism and inspiration to carry out this work. The technical staff of the Department of Physics is also highly acknowledged for the help extended for different experimental works carried out by me.

I would like to thank Mr. Joston P. Nongkynrih of Sophisticated Analytical Instrumentation Facility (SAIF), NEHU, Shillong for helping me with TEM experiments. Special thanks are extended to Mr. Rahul Singhal for helping me with micro-Raman spectroscopy, Mr. Ratan Baruah for helping in SEM measurements and Mr. Prakash Kurmi for XRD measurements. I would also like to acknowledge the Pelletron staff of IUAC who helped me immensely during the irradiation experiments. I would also like to acknowledge the Department of Chemical Sciences and the Department of Molecular Biology and Biotechnology, Tezpur University for co-operation and concerns to characterize some of the samples on various aspects.

I would also like to acknowledge University Grants Commission, New Delhi for offering me Meritorious Fellowship and Department of Science and Technology for financial assistance (vide project no. SR/S2/CMF-28/2008), which helped me carry on with my research work and reach this stage.

I would also like to express my gratitude to the past and present members of the Materials Research Laboratory, Department of Physics, Tezpur University: Dr. Abu Mohd. Pharhad Hussain, Dr. Smritimala Sarmah, Chandrani Nath, Jayanta Hazarika,

Anup Nath, Paragjyoti Chutia, Inanendra Upadhyay, Meghraj Adhikary, Raja Chetia, Dimpul Konwar, Anjalu Ramchiary and Sauravjyoti Hazarika. I would like to specially thank Kunal Borah for being such a wonderful friend and brother. I acknowledge the help I received during various stages of my research work from my lab-mate, Madhuryya Deka with whom I had plenty of useful discussions. A special mention for Subasit Borah, one of my fellow research scholars with whom I had some profitable discussions. Special acknowledgement goes to Dr. Sanjeev Bhattacharyya, Dr. Jyoti Prasad Saikia, Dr. Ankur Gogoi, Dr. Upamanyu Das, Dr. Swati Baruah, Dr. Nabanita Dutta, Debashis Sarmah, Ranjan Dutta Kalita, Prakash Barman, Sikhajyoti Ozah, Bondita Goswami, Madhulekha Gogoi, Jagat Dwipendra Ray, Himjyoti Dutta, Tanuj Mahanta, Nastagis Niyaz Ahmed, Subhasish Baruah and Samrat Tamuli.

I am indebted to my parents, my father Late Kirit Banerjee and my mother Mrs. Chandra Banerjee, who showed me this beautiful world and always stood by me during hardships and ups and down in my life. I sincerely acknowledge the constant support and encouragement I received from my uncles and aunts all throughout my life. I am blessed with a wonderful younger brother in Tanmoy Banerjee (Tutun) and would sincerely acknowledge him for his love and support. I also extend my heartfelt thanks to my dear cousins Sayantee Chakraborty (Buiya didi), Anindita Sengupta (Sona), Shounik Chakraborty (Bubul), Arnab Sen (Sonty) and Saurav Bhattacharyya (Boney) for their love. I would specially like to acknowledge Antara Banerjee for making me believe in myself and standing by my side in difficult times during my Ph.D. tenure. At the end, I thank the Almighty for giving me moral strength and courage to carry out my work.

Somik Banerjee
(Somik Banerjee)

Place: Tezpur,

Date: 23.02.2012

CONTENTS

<i>a. Abstract</i>	<i>i</i>
<i>b. Declaration</i>	<i>vi</i>
<i>c. Certificate</i>	<i>vii</i>
<i>d. Acknowledgements</i>	<i>viii</i>
<i>e. Contents</i>	<i>xii</i>
<i>f. List of tables</i>	<i>xix</i>
<i>g. List of Figures</i>	<i>xxi</i>
<i>h. List of abbreviations</i>	<i>xxxvi</i>
<i>i. List of symbols</i>	<i>xxxix</i>
CHAPTER 1: INTRODUCTION	[1-47]
1.1. Conducting polymers	1
1.1.1. Historical Developments	3
1.1.2. Primary features of conducting polymers	5
1.1.2.1. Doping in conducting polymers	7
1.1.2.2. Metal-Insulator transition in doped conducting polymers	11
1.1.2.3. Band structure and charge carriers in conducting polymers	12
1.1.2.4. Transport processes in conducting polymers	16
1.1.3. Polyaniline: a promising conducting polymer	17
1.2. Conducting polymer based nanostructured materials	21
1.2.1. Conducting polymer nanostructures	23
1.2.2. Conducting polymer nanocomposites	24
1.2.2.1. Inorganic-in-organic (I-O) nanocomposites	25
1.2.2.1.1. Core-shell nanocomposites	26
1.2.2.2. Organic-in-inorganic nanocomposites	28
1.2.2.2.1. Intercalated and exfoliated nanocomposites	29
	<i>xii</i>

1.2.2.3. Organic-in-organic nanocomposites	31
1.3. Swift heavy ion (SHI) irradiation of conducting polymers	32
1.3.1. Nuclear energy loss	32
1.3.2. Electronic energy loss	33
1.3.3. Latent tracks	33
1.4. Conducting polymers for biomedical applications	34
1.5. Sensors based on conducting polymers	35
1.5.1. Chemical sensors	36
1.5.2. Biosensors	36
1.5.3. Sensor configuration and sensing principles	38
1.5.3.1. Piezoelectric sensors	42
1.5.3.1.1. SAW sensors	43
1.5.3.1.2. Quartz crystal microbalance (QCM) sensors	44
1.6. Scope of the thesis and statement of thesis problem	45

CHAPTER 2: THEORETICAL ASPECTS [48-83]

2.1. Chemical polymerization	48
2.1.1. Chemical polymerization of aniline	48
2.1.2. Mechanism of polyaniline nanofibers formation	51
2.2. Electronic conduction mechanism in disordered materials	54
2.2.1. Electronic conduction mechanism in polyaniline and polyaniline blends	60
2.2.2. Charge transport in polyaniline based nanostructured materials	62
2.3. Frequency dependence of conductivity	63
2.4. Models for frequency dependent ac conduction in disordered materials	65
2.4.1. Correlated barrier hopping (CBH) model	68
2.5. Modifications in the models for ac conduction	70

2.6.	Dielectric relaxation in amorphous materials	74
2.6.1.	Presentation of dielectric data	76
2.6.2.	Analysis of dielectric spectra: Model functions	78
2.7.	Theories governing ion-solid interactions	80
2.7.1.	Thermal-spike model	81
2.7.2.	Coulomb explosion model	82
CHAPTER 3: EXPERIMENTAL TECHNIQUES		[84-113]
3.1.	Materials	84
3.2.	Synthesis of polyaniline nanofibers	85
3.3.	Synthesis of polyaniline nanofibers reinforced PVA nanocomposites	87
3.4.	Swift heavy ion (SHI) irradiation	88
3.4.1.	Parameters related to ion beam	91
3.4.1.1.	Fluence	91
3.4.1.2.	Count	92
3.4.1.3.	Beam energy	92
3.5.	Characterization techniques	93
3.5.1.	Electron microscopy	93
3.5.1.1.	Transmission electron microscopy	93
3.5.1.2.	Scanning electron microscopy	94
3.5.2.	Powder X-ray diffraction (XRD)	96
3.5.2.1.	Calculation of d-spacing, domain length (L) and strain (ε)	98
3.5.2.2.	Degree of crystallinity	100
3.5.3.	FTIR spectroscopy	101
3.5.4.	Ultraviolet-Visible (UV-Vis) spectroscopy	103
3.5.4.1.	Calculation of optical band-gap	105
3.5.5.	Micro-Raman (μR) spectroscopy	105
3.5.6.	Current-Voltage I-V characteristics	107
3.5.7.	Dielectric relaxation spectroscopy	108

3.5.7.1.	Permittivity formalism	109
3.5.7.2.	Impedance formalism	109
3.5.7.3.	Modulus formalism	109
3.5.8.	AC conductivity measurements	110
3.5.9.	Positron annihilation lifetime spectroscopy (PALS)	110
3.6.	Antioxidant activity assay	110
3.7.	Haemolysis prevention assay	111
3.8.	Characterization of quartz crystal microbalance (QCM) based chemical sensors	111
3.8.1.	Response time of the sensor	112
3.8.2.	Linearity of the sensor	113
3.8.3.	Sensitivity of the sensor	113

CHAPTER 4: POLYANILINE NANOFIBERS: [114-174]

**SYNTHESIS, SHI IRRADIATION AND
CHARACTERIZATION**

4.1.	Introduction	114
4.2.	Synthesis of polyaniline nanofibers	117
4.3.	Characterization of pristine and SHI irradiated polyaniline nanofibers	118
4.3.1.	Transmission electron microscopy	118
4.3.2.	X-ray diffraction analysis	124
4.3.3.	Vibrational spectroscopy	129
4.3.3.1.	Fourier Transform Infrared (FTIR) spectroscopy	129
4.3.3.2.	Micro-Raman (μ R) spectroscopy	133
4.3.3.3.	SHI induced benzenoid to quinoid transformation in polyaniline nanofibers	140
4.3.4.	UV-Visible absorption spectroscopy	144
4.3.4.1.	Optical band-gap	145
4.3.4.2.	Urbach's tail	150

4.3.4.3. Quantum confinement effect	153
4.3.5. Dielectric relaxation spectroscopy	154
4.3.5.1. Permittivity formalism	155
4.3.5.2. Impedance formalism	160
4.3.5.3. Electric Modulus formalism	163
4.3.6. AC conductivity and charge transport mechanism	168
4.4. Summary	173

CHAPTER 5: POLYANILINE NANOFIBER [175-204]

REINFORCED PVA

NANOCOMPOSITES: SYNTHESIS, SHI

IRRADIATION AND

CHARACTERIZATION

5.1. Introduction	175
5.2. Synthesis of polyaniline nanofiber reinforced PVA nanocomposites	177
5.3. Characterization of pristine and SHI irradiated polyaniline nanofiber reinforced PVA nanocomposites	178
5.3.1. Electron microscopy	178
5.3.2. X-ray diffraction analysis	180
5.3.3. Fourier transform Infrared (FTIR) spectroscopy	183
5.3.4. UV-Visible absorption spectroscopy	187
5.3.5. I-V characteristics	189
5.3.6. Dielectric relaxation spectroscopy	192
5.3.6.1. Permittivity formalism	192
5.3.6.2. Impedance formalism	195
5.3.6.3. Modulus formalism	197
5.3.7. AC conductivity and charge transport mechanism	198
5.3.8. Positron annihilation lifetime spectroscopy (PALS)	200
5.4. Summary	202

CHAPTER 6: ANTIOXIDANT ACTIVITY AND [205-222]
BIOCOMPATIBILITY STUDIES ON
POLYANILINE BASED
NANOSTRUCTURED MATERIALS

6.1.	Introduction	205
6.2.	Antioxidant activity of polyaniline nanofibers	207
6.3.	Swift heavy ion irradiation induced enhancement in the antioxidant activity of polyaniline nanofibers	209
6.4.	Mechanism behind free radical scavenging by polyaniline nanofibers	211
6.5.	Biocompatibility studies on polyaniline nanofibers	214
6.6.	Swift heavy ion irradiation induced enhancement in the biocompatibility of polyaniline nanofibers	217
6.7.	Antioxidant activity and biocompatibility studies on polyaniline nanofibers reinforced PVA nanocomposites	218
6.8.	Summary	221

CHAPTER 7: POLYANILINE NANOFIBER [223-242]
REINFORCED PVA
NANOCOMPOSITE COATED
QUARTZ CRYSTAL MICROBALANCE
SENSORS

7.1.	Introduction	223
7.2.	Fabrication of polyaniline nanofiber reinforced PVA nanocomposite coated QCM sensor	224
7.3.	Polyaniline nanofiber reinforced PVA nanocomposite modified QCM sensors for sensing free radicals	225
7.3.1.	Characterization of the sensor	226
7.3.1.1.	Linearity	227
7.3.1.2.	Sensitivity	228

7.3.1.3. Response time	228
7.3.2. Mechanism of sensing	228
7.4. Polyaniline nanofiber reinforced PVA nanocomposite modified QCM sensors for sensing hydrochloric acid	234
7.4.1. Characterization of the sensor	235
7.4.1.1. Linearity	236
7.4.1.2. Sensitivity	236
7.4.1.3. Response time	237
7.4.2. Mechanism of sensing	237
7.5. Summary	241

CHAPTER 8: CONCLUSIONS & FUTURE [243-249]

PROSPECTS

8.1. Conclusions	243
8.2. Limitations and future prospects	249

REFERENCES [250-288]

LIST OF PUBLICATIONS 289

List of tables

Table	Captions	Page No.
Table 2.1	Salient features of the different models for ac conduction in amorphous materials.	70
Table 3.1	Physical properties of the materials used in synthesis.	85
Table 3.2	SRIM data for O^{7+} ions in different PANi based nanostructured materials.	92
Table 4.1	(hkl) pseudo-orthorhombic indexation, d spacing, domain length (L) and strain of polyaniline (PANi) bulk, CSA doped PANi nanofibers and HCl doped PANi nanofiber.	125
Table 4.2	Position, Intensity and FWHMs of the prominent FTIR peaks of pristine and 90 MeV O^{7+} ion beam irradiated PANi nanofibers doped with HCl and CSA.	132
Table 4.3	Deconvolution of the micro-Raman (μR) peaks for pristine and 90 MeV O^{7+} ion irradiated PANi nanofibers doped with HCl at different fluences.	138
Table 4.4	Deconvolution of the micro-Raman (μR) peaks for pristine and 90 MeV O^{7+} ion irradiated PANi nanofibers doped with CSA at different fluences.	139
Table 4.5	Optical band-gap (E_{opt}/E_{g3}), defect levels (E_{g1} and E_{g2}) and Urbach tail width (eV) of PANi nanofibers.	152
Table 4.6	Best fit parameters for the M'' spectra at 303 K for the pristine and irradiated PANi nanofibers doped with HCl and CSA [Figs. 4.42 (a, b)].	168
Table 4.7	Values of polaron binding energy (W_M), hopping distance (R_ω) and the density of states $N(E_F)$ calculated using the correlated barrier hopping model.	172

Table 5.1	Composition of the PANi nanofiber reinforced PVA nanocomposites.	177
Table 5.2	Variation of domain length (L) and strain (ε).	181
Table 7.1	Comparison of the domain length (L) and the strain (ε) in the PANi nanofiber reinforced PVA nanocomposites before and after exposure to different concentrations of free radicals.	230
Table 7.2	Values of dc conductivity and 's' parameter obtained from the best fits of the experimental data of ac conductivity (for the PANi nanofiber reinforced PVA nanocomposites before and after exposure to different concentrations of the free radical) with the Eq. (4.19).	234
Table 7.3	Comparison of the domain length (L) and the strain (ε) in the PANi nanofiber reinforced PVA nanocomposites before and after exposure to different concentrations of hydrochloric acid in solution.	239

List of figures

Figure	Captions	Page No.
Figure 1.1	Molecular structures of some of the most popular conjugated polymers.	3
Figure 1.2	Schematic diagram showing the molecular structures of the simplest 3D, 2D and 1D form of carbon materials (a) Diamond, (b) Graphite and (c) Polyacetylene.	6
Figure 1.3	Spatial representation of the sp^2 hybridized carbon atom from top and side view.	6
Figure 1.4	Schematic diagram showing the difference between the doping mechanisms in inorganic semiconductors and conjugated polymers.	8
Figure 1.5	Different methods for doping conducting polymers.	9
Figure 1.6	Schematic representation of (a) the formation of HOMO and LUMO in polyacetylene due to the presence of a continuous system of strongly interacting atomic orbitals. (b) Difference between band structure of conventional polymer, undoped and doped conducting polymer and (c) Detailed band structure of trans-Polyacetylene showing the energy band-gap and associated parameters.	13
Figure 1.7	Molecular structures of conducting polymers illustrating the formation of the localized defects (charge carriers) viz., polarons, bipolarons and solitons. A schematic representation of the modifications in the band structure of conducting polymers after the creation of these localized defects upon doping is also illustrated.	15
Figure 1.8	(a) General molecular structure of polyaniline (PAni). Different oxidation states of PAni (b) Leucomeraldine, (c) Emeraldine, (d) Nigraniline and (e) Pernigraniline.	18

Figure 1.9	Schematic representation of the conversion of Emeraldine base (EB) into the Emeraldine salt (ES) form of polyaniline upon proton doping.	19
Figure 1.10	Variation in colour of (a) \$ 1 gold coin, showing the normal bulk color of gold and (b-f) gold nanoparticles of different colors with increasing particle size.	22
Figure 1.11	Schematic diagram to illustrate the synthesis mechanism of inorganic-in-organic conducting polymer nanocomposites and core-shell type nanocomposites based on conducting polymers.	27
Figure 1.12	Molecular structure of (a) Montmorillonite and (b) Kaolinite.	29
Figure 1.13	Schematic diagram of different types of layered organic-inorganic nanocomposites.	30
Figure 1.14	Schematic diagrams of some of the configurations of conducting polymer sensors (a) Inter-digitated chemiresistor, (b) Thin film transistors based on conducting polymers (c) IGFETs, (d) Fiber optic sensors and (e) electrochemical sensors based on conducting polymer electrodes.	40
Figure 1.15	Configuration of a SAW sensor.	43
Figure 1.16	Configuration of a quartz crystal microbalance sensor device.	44
Figure 2.1	Scheme illustrating the various steps (Step I to Step IV) in the Chemical polymerization of polyaniline.	49-50
Figure 2.2	Double heterogeneous nucleation mechanism of PANi nanofiber formation according to Manohar and group.	53
Figure 3.1	Block diagram for the synthesis of polyaniline nanofibers using interfacial polymerization.	86
Figure 3.2	Block diagram for the synthesis of polyaniline nanofiber reinforced PVA nanocomposites.	88

Figure 3.3	A schematic diagram showing the principle of acceleration of ions in a Pelletron.	89
Figure 3.4	Photographs of (a) the high vacuum irradiation chamber in the Materials Science (MS) beam line at IUAC and (b) sample loaded in the ladder used for irradiating the samples.	91
Figure 3.5	(a) Transmission electron microscope (JEOL JEM 100 CXII) at SAIF, NEHU, Shillong and (b) Scanning electron microscope (JEOL JSM 6390 LV) installed at Tezpur University used for acquiring electron micrographs in the present work.	94
Figure 3.6	Rigaku Miniflex X-ray diffractometer installed at the Department of Physics, Tezpur University.	97
Figure 3.7	(a) Typical X-ray diffractogram of a semi-crystalline polymer and (b) XRD patterns showing the superposition of crystalline peaks and an amorphous hump.	101
Figure 3.8	Layout of a simple FTIR spectrometer.	102
Figure 3.9	Photographs of (a) UV-Visible spectrometer (UV-2450) from Perkin Elmer installed at Department of Physics, Tezpur University and (b) The Renishaw in-Via Raman microscope installed at IUAC, New Delhi.	104
Figure 3.10	Photographs of (a) Keithley 2400-C source meter and (b) HIOKI 3532-50 LCR HiTESTER installed at Materials Research Laboratory, Department of Physics, Tezpur University.	108
Figure 3.11	Experimental set-up of the Quartz crystal microbalance (QCM) interfaced with a PC. The inset shows a gold coated quartz crystal oscillator.	112
Figure 4.1	Snapshots of the various stages of PANi nanofiber formation at various times (a) $t = 0$, (b) $t = 5$ min, (c) $t = 10$ min, (d) $t = 15$ min, (e) $t = 20$ min and (f) $t = 30$ min.	117

Figure 4.2	Transmission electron micrographs of PANi nanofibers doped with (a) 1M HCl and (b) 1M CSA.	118
Figure 4.3	Diameter distribution of PANi nanofibers doped with (a) 1M HCl and (b) 1M CSA.	119
Figure 4.4	Transmission electron micrographs of HCl doped polyaniline nanofibers (a) before irradiation; and after irradiation with 90 MeV O ⁷⁺ ions at fluences (b) 3 × 10 ¹⁰ , (c) 3 × 10 ¹¹ and (d) 1 × 10 ¹² ions cm ⁻² .	120
Figure 4.5	Transmission electron micrographs of CSA doped polyaniline nanofibers (a) before irradiation; and after irradiation with 90 MeV O ⁷⁺ ions at fluences (b) 3 × 10 ¹⁰ , (c) 3 × 10 ¹¹ and (d) 1 × 10 ¹² ions cm ⁻² .	121
Figure 4.6	Diameter distribution of HCl doped polyaniline nanofibers (a) before irradiation; and after irradiation with 90 MeV O ⁷⁺ ions at fluences (b) 3 × 10 ¹⁰ , (c) 3 × 10 ¹¹ and (d) 1 × 10 ¹² ions cm ⁻² .	122
Figure 4.7	Distribution of diameters for the CSA doped polyaniline nanofibers (a) before irradiation; and after irradiation with 90 MeV O ⁷⁺ ions at fluence (b) 3 × 10 ¹⁰ , (c) 3 × 10 ¹¹ and (d) 1 × 10 ¹² ions cm ⁻² .	123
Figure 4.8	(a) X-ray diffraction patterns of polyaniline (PANi) bulk, CSA doped PANi nanofibers and HCl doped PANi nanofibers within 2θ ranging from 10° to 60° and (b) Comparison of the (110) reflection peak for polyaniline (PANi) bulk, CSA doped PANi nanofibers and HCl doped PANi nanofibers.	125
Figure 4.9	X-ray diffraction patterns of pristine and irradiated polyaniline nanofibers doped with (a) HCl and (b) CSA.	127
Figure 4.10	X-ray diffraction patterns of the pristine and irradiated PANi nanofibers doped with (a) HCl and (b) CSA showing the most intense (100) peak of PANi.	127

Figure 4.11	Variation of <i>d</i> -spacing, domain length (<i>L</i>), strain (ϵ) and normalized integral intensity (I/I_0) of PANi nanofibers as a function of irradiation fluence.	128
Figure 4.12	FTIR spectra of pristine and irradiated (a) HCl doped and (b) CSA doped PANi nanofibers.	130
Figure 4.13	Lorentzian deconvolution of the FTIR spectra within 1360–1520 cm^{-1} for (a) pristine HCl doped PANi nanofibers and those irradiated at a fluence of (b) 3×10^{10} , (c) 3×10^{11} and (d) 1×10^{12} ions cm^{-2} .	130
Figure 4.14	Lorentzian deconvolution of the FTIR spectra within 1360–1520 cm^{-1} for (a) pristine CSA doped PANi nanofibers and those irradiated at a fluence of (b) 3×10^{10} , (c) 3×10^{11} and (d) 1×10^{12} ions cm^{-2} .	131
Figure 4.15	MicroRaman (μR) spectra of PANi nanofibers doped with (a) CSA and (b) HCl.	133
Figure 4.16	Micro-Raman spectra of pristine and irradiated PANi nanofibers doped with (a) HCl and (b) CSA in the range 1200–1650 cm^{-1} . Inset shows the micro-Raman spectra of the pristine and irradiated PANi nanofibers doped with (a) HCl and (b) CSA at lower wavelength (300–700 cm^{-1}).	135
Figure 4.17	Lorentzian deconvolution of micro-Raman spectra of HCl doped polyaniline nanofibers (a) before irradiation; and after irradiation with 90 MeV O^{7+} ions at fluences (b) 3×10^{10} , (c) 3×10^{11} and (d) 1×10^{12} ions cm^{-2} .	136
Figure 4.18	Lorentzian deconvolution of micro-Raman spectra of CSA doped polyaniline nanofibers (a) before irradiation; and after irradiation with 90 MeV O^{7+} ions at fluences (b) 3×10^{10} , (c) 3×10^{11} and (d) 1×10^{12} ions cm^{-2} .	137
Figure 4.19	Comparison of the deconvoluted sub peaks representing the C=C stretching vibration of the benzenoid and quinoid rings of pristine and 90 MeV O^{7+} ion irradiated PANi nanofibers doped with (a) HCl and (b) CSA.	140

Figure 4.20	A comparison of the decomposed sub-peaks corresponding to the symmetrical C=C stretching modes of the pristine PANi nanofiber and that irradiated with a fluence of 1×10^{12} ions/cm ² for (a) HCl doped PANi nanofibers and (b) CSA doped PANi nanofibers.	141
Figure 4.21	Comparison of the N-H stretching band at 1670 cm ⁻¹ for the pristine and 90 MeV O ⁷⁺ ion irradiated PANi nanofibers doped with (a) HCl and (b) CSA.	142
Figure 4.22	UV-Visible spectra of pristine and irradiated PANi nanofibers doped with (a) HCl and (b) CSA.	145
Figure 4.23	Plots of $d [\ln (\alpha h\nu)]/d (h\nu)$ vs. $h\nu$ for the pristine HCl and CSA doped PANi nanofibers.	146
Figure 4.24	(a) Linear fit of $\ln (\alpha h\nu)$ vs. $\ln (h\nu-E)$ where $E = E_{g1}$ and (b) Linear fit of $\ln (\alpha h\nu)$ vs. $\ln (h\nu-E)$ where $E = E_{g2}$ and (c) Linear fit of $\ln (\alpha h\nu)$ vs. $\ln (h\nu-E)$ where $E = E_{g3}$ for both the HCl and CSA doped PANi nanofibers.	147
Figure 4.25	$(\alpha h\nu)^2$ vs $h\nu$ plots for the pristine PANi nanofibers doped with HCl and CSA.	148
Figure 4.26	$(\alpha h\nu)^2$ vs. $h\nu$ plots for the irradiated PANi nanofibers (a) doped with HCl and (b) doped with CSA.	149
Figure 4.27	Plot of $\ln \alpha$ vs. $h\nu$ for the pristine and irradiated PANi nanofibers (a) doped with HCl and (b) doped with CSA. The reciprocal of the slopes of the linear portion of these curves have been used to calculate the Urbach's energy.	151
Figure 4.28	Band-gap versus the inverse of the square of the radius of the pristine and irradiated nanofibers illustrating the quantum confinement effect in PANi nanofibers.	154
Figure 4.29	Frequency dependent variation of the real part (ϵ') of the complex permittivity (ϵ^*) for the PANi nanofiber doped with (a) HCl and (b) CSA within the temperature range of 303–373 K.	155

Figure 4.30	Frequency dependent variation of the imaginary part (ε'') of the complex permittivity (ε^*) for the PAni nanofiber doped with (a) HCl and (b) CSA within the temperature range of 303–373 K.	156
Figure 4.31	The imaginary part ε'' of the dielectric function (ε^*) vs. frequency for the PAni nanofibers doped with (a) HCl and (b) CSA at 373 K. The solid line is the best fit of Eq. (4.13) to the experimental data. The dotted line (.....) shows the contribution of dc conductivity and the dashed line (- - -) line shows the contribution of H-N function to the dielectric losses ε'' .	157
Figure 4.32	Variation of the real part (ε') of the complex permittivity (ε^*) as a function of temperature from the pristine and 90 MeV O^{7+} ion irradiated pAni nanofibers doped with HCl at frequencies of (a) 50 Hz, (b) 1 kHz, (c) 10 kHz and (d) 1 MHz.	159
Figure 4.33	Variation of real part (Z') of complex impedance (Z^*) of PAni nanofibers doped with (a) HCl and (b) CSA.	160
Figure 4.34	Variation of imaginary part (Z'') of complex impedance (Z^*) of PAni nanofibers doped with (a) HCl and (b) CSA.	160
Figure 4.35	The imaginary part Z'' of the complex impedance (Z^*) as a function of frequency for PAni nanofibers doped with (a) HCl and (b) CSA at 303 K. The solid line (—) is the best fit according to Eq. (4.14). The dot lines (.....) and the dashed lines (----) show the contribution of the two conductivity relaxation mechanisms to Z'' .	162
Figure 4.36	Variation of real part (Z') of complex impedance (Z^*) of 90 MeV O^{7+} ion irradiated PAni nanofibers doped with (a) HCl and (b) CSA. Inset shows the real part of complex impedance for the HCl and CSA doped PAni nanofibers at	162

303 K.

- Figure 4.37** Variation of imaginary part (Z'') of complex impedance (Z^*) of 90 MeV O^{7+} ion irradiated PANi nanofibers doped with (a) HCl and (b) CSA. Inset shows the imaginary part of complex impedance for the HCl and CSA doped PANi nanofibers at 303 K. The solid lines are fit of the experimental data to a single Cole-Cole equation. 163
- Figure 4.38** Frequency dependence of the real part M' part of the electric modulus function M^* at different temperatures for PANi nanofibers doped with (a) HCl and (b) CSA. 164
- Figure 4.39** Frequency dependence of the real part M'' part of the electric modulus function M^* at different temperatures for PANi nanofibers doped with (a) HCl and (b) CSA. The solid lines represent the best fits of the experimental data to Eq. (4.16) at different temperatures. 165
- Figure 4.40** Temperature dependence of the most probable relaxation frequency obtained from the modulus formalism for PANi nanofibers doped with (a) HCl and (b) CSA. The solid line represents the best fit according to Eq. (4.18). 166
- Figure 4.41** Scaling behaviour of M'' at various temperatures for PANi nanofibers doped with (a) HCl and (b) CSA. 167
- Figure 4.42** Variation of M'' for the pristine and 90 MeV O^{7+} ion irradiated PANi nanofibers doped with (a) HCl and (b) CSA as a function of frequency. Solid lines are the best fits to the experimental points according to the Eq. (4.16). 168
- Figure 4.43** Variation of ac conductivity $\sigma(\omega)$ as a function of frequency and temperature (303-373 K) for PANi nanofibers doped with (a) HCl and (b) CSA. Solid lines are the best fits to the experimental data according to the Eq. (4.19). 169

Figure 4.44	Frequency dependent ac conductivity of the pristine and irradiated PANi nanofibers doped with (a) HCl and (b) CSA.	170
Figure 4.45	Variation in the frequency exponent “s” as a function of temperature for PANi nanofibers doped with (a) HCl and (b) CSA.	171
Figure 5.1	Transmission electron micrograph of the PANi nanofiber reinforced PVA nanocomposite with 6 wt. % of aniline content (sample G3).	178
Figure 5.2	Scanning electron micrographs of the PANi nanofiber reinforced PVA nanocomposites with (a) 2 wt. % (sample G1), (b) 4 wt. % (sample G2) and (c) 6 wt. % (sample G3) of aniline content.	179
Figure 5.3	Scanning electron micrographs of the PANi nanofiber reinforced PVA nanocomposites with 6 wt.% (sample G3) of aniline content (a) before and after irradiation with 90 MeV O ⁷⁺ ions at fluences of (b) 3×10^{10} , (c) 3×10^{11} and (d) 1×10^{12} ions cm ⁻² .	180
Figure 5.4	X-ray diffraction patterns of polyaniline nanofiber reinforced PVA nanocomposite samples with 2 wt.% (sample G1), 4 wt.% (sample G2) and 6 wt.% (sample G3) of aniline content within 2 θ ranging from (a) 10 ^o to 60 ^o and (b) 18-21 ^o showing the comparison of the (110) reflection peak for polyaniline (PANi) in the PANi nanofiber reinforced PVA nanocomposites.	181
Figure 5.5	(a) X-ray diffraction patterns of the pristine and 90 MeV O ⁷⁺ ions irradiated PANi nanofiber reinforced PVA nanocomposite with 6 wt.% aniline (sample G3) and (b) shows the variation of the normalized integral intensity (I/I_0) of the sample G3 as a function of irradiation fluence.	182
Figure 5.6	FTIR spectra of PANi nanofiber reinforced PVA nanocomposite with different concentration of aniline (a) 2	183

	wt. % (sample G1), (b) 4 wt. % (sample G2) and (c) 6 wt. % (sample G3).	
Figure 5.7	Lorentzian deconvolution of the C=C stretching peaks for the benzenoid and quinoid units of the PANi nanofiber reinforced PVA nanocomposites (a) sample G1, (b) sample G2 and (c) sample G3.	184
Figure 5.8	Comparison of the deconvoluted sub-peaks for the C=C stretching corresponding to the benzenoid (para disubstituted benzene) and quinoid (quinine diimine) structures in the PANi chains.	185
Figure 5.9	FTIR spectra of PANi nanofibers reinforced PVA nanocomposites (a) before and after irradiation with 90 MeV O ⁷⁺ ions at a fluence of (b) 3 × 10 ¹⁰ , (c) 3 × 10 ¹¹ and (d) 1 × 10 ¹² ions/cm ² .	186
Figure 5.10	Comparison of the FTIR peaks for the C=C stretching vibrations of the benzenoid rings at 1400 cm ⁻¹ and the quinoid rings at 1460 cm ⁻¹ for the pristine and irradiated PANi nanofibers reinforced PVA nanocomposites.	187
Figure 5.11	UV-Visible spectra of the PANi nanofiber reinforced PVA nanocomposites with 2 wt. % (sample G1), 4 wt. % (sample G2) and 6 wt. % (sample G3).	188
Figure 5.12	UV-Visible spectra of the PANi nanofiber reinforced PVA nanocomposites (sample G3) before and after SHI irradiation with 90 MeV O ⁷⁺ ions.	189
Figure 5.13	I-V characteristic curves for the pristine polyvinyl alcohol (PVA) and the PANi nanofiber reinforced PVA nanocomposites with 2 wt. % (sample G1), 4 wt. % (sample G2) and 6 wt. % (sample G3) of aniline content.	190
Figure 5.14	I-V characteristic curves for PANi nanofiber reinforced PVA nanocomposites (sample G3) before and after irradiation with 90 MeV O ⁷⁺ ions at fluences of 3 × 10 ¹⁰ , 3 × 10 ¹¹ and 1 × 10 ¹² ions cm ⁻² .	191

Figure 5.15	Variation of (a) the real part (ϵ') and (b) imaginary part (ϵ'') of the complex permittivity (ϵ^*) for the PANi nanofiber reinforced PVA nanocomposites with varying aniline content viz., 2 wt. % (sample G1), 4 wt. % (sample G2) and 6 wt. % (sample G3).	192
Figure 5.16	The imaginary part ϵ'' of the complex dielectric function ϵ^* vs. frequency for the PANi nanofiber reinforced PVA nanocomposites with 6 wt. % of aniline content. The solid line is the best fit of Eq. (4.12) to the experimental data. The dotted line (.....) shows the contribution of the dc conductivity and the dashed line (- - -) shows the contribution of H-N function to the dielectric losses ϵ'' .	193
Figure 5.17	Variation of (a) the real part (ϵ') and (b) imaginary part (ϵ'') of the complex permittivity (ϵ^*) for the sample G3 as a function of frequency at different temperatures.	194
Figure 5.18	Variation of the (a) real part (ϵ') and (b) the imaginary part (ϵ'') of the complex permittivity (ϵ^*) as a function of frequency for the sample G3 at different fluences.	195
Figure 5.19	Cole-Cole (Nyquist) plots of the PANi nanofiber reinforced PVA nanocomposite samples with 2 wt. % (sample G1), 4 wt. % (sample G2) and 6 wt. % (sample G3) of aniline content.	196
Figure 5.20	Cole-Cole (Nyquist) plots of the pristine and 90 MeV O ⁷⁺ ion irradiated PANi nanofiber reinforced PVA nanocomposite (sample G3 with 6 wt. % aniline content).	196
Figure 5.21	Variation of the (a) real part (M') and (b) the imaginary part (M'') of the complex modulus (M^*) for the PANi nanofiber reinforced PVA nanocomposites with varying aniline content.	197

Figure 5.22	Variation of the (a) real part (M') and (b) the imaginary part (M'') of the complex modulus (M^*) for the pristine and irradiated PANi nanofiber reinforced PVA nanocomposites (sample G3).	198
Figure 5.23	Variation of ac conductivity for (a) PANi nanofiber reinforced PVA nanocomposites with varying aniline content and (b) pristine and irradiated PANi nanofiber reinforced PVA nanocomposites.	199
Figure 5.24	Temperature dependent variation of the frequency exponent 's' for (a) PANi nanofibers reinforced PVA nanocomposites with varying aniline content and (b) pristine and irradiated PANi nanofibers reinforced PVA nanocomposites.	200
Figure 5.25	Variation of the positron lifetime components for PANi nanofiber reinforced PVA nanocomposites (a) shortest lifetime component τ_1 and (b) intermediate lifetime component τ_2 . The insets in the Fig. 5.25 (a) and (b) are the respective intensities of the lifetime components.	201
Figure 6.1	UV-Vis spectra of solutions of DPPH in methanol after 15 min incubation in dark with (a) no material (blank), (b) 0.5 mg of PANi bulk, (c) 0.5 mg of CSA doped PANi nanofibers and (d) 0.5 mg of HCl doped PANi nanofibers.	207
Figure 6.2	Variation in the antioxidant activity as a function of weight of (a) S3, (b) S2 and (c) S1. The higher the percentage of DPPH scavenging the better is the antioxidant activity of the material.	208
Figure 6.3	Time-dependent antioxidant activity of 0.3 mg of (a) S3, (b) S2 and (c) S1. The results presented are average values of three repetitions.	209
Figure 6.4	UV-vis spectra of solutions of DPPH in methanol after 15 min incubation in the dark with 0.5 mg of pristine and	210

irradiated (a) HCl doped and (b) CSA doped PANi nanofibers. Spectra labelled 1–5 correspond to solutions of DPPH containing no PANi nanofibers, pristine PANi nanofibers and nanofibers irradiated with fluences of 3×10^{10} , 3×10^{11} and 1×10^{12} ions cm^{-2} , respectively.

- Figure 6.5** Variation of antioxidant activity of the PANi nanofibers (a) doped with HCl and (b) doped with CSA as a function of irradiation fluence. 210
- Figure 6.6** Weight dependent free radical scavenging efficiency of pristine and irradiated PANi nanofibers doped with (a) HCl and (b) CSA. 211
- Figure 6.7** Schematic diagram depicting the most probable mechanism for free radical scavenging by PANi nanofibers 213
- Figure 6.8** Scanning electron micrographs showing (a) morphology of the erythrocytes (RBCs) and the damage caused to the erythrocytes by (b) H_2O_2 and (c) H_2O_2 in the presence of HCl-doped polyaniline nanofibers. 215
- Figure 6.9** DPPH scavenging efficiency of HCl doped polyaniline nanofibers before and after reacting with H_2O_2 . 216
- Figure 6.10** Haemolysis prevention efficiency of HCl doped and CSA doped PANi nanofibers. 217
- Figure 6.11** Haemolysis prevention activity of pristine and irradiated PANi nanofibers doped with CSA and HCl. 218
- Figure 6.12** Time dependent scavenging of the free radical (DPPH) by PANi nanofiber reinforced PVA nanocomposite with 6 wt.% of aniline content (sample G3). 219
- Figure 6.13** Weight dependent free radical scavenging efficiencies (antioxidant activities) of the PANi nanofiber reinforced PVA nanocomposites with 2 wt.% (sample G1), 4 wt.% (sample G2) and 6 wt.% (sample G3) of aniline content. The results presented are average values of 10 repetitions. 220

Figure 6.14	Weight dependent haemolysis prevention efficiency of the PANi nanofiber reinforced PVA nanocomposites with 2 wt.% (sample G1), 4 wt.% (sample G2) and 6 wt.% (sample G3) of aniline content. The results presented are average values of 10 repetitions.	221
Figure 7.1	Response characteristics of the PANi nanofiber reinforced PVA nanocomposite modified QCM sensor after exposure to different concentration of free radicals in solutions.	226
Figure 7.2	Calibration curve for determination of free radicals in solution. The frequency shifts of a PANi nanofiber reinforced PVA nanocomposite modified quartz crystal electrode in direct contact to the free radical solutions have been recorded after 2.5 min of exposure.	227
Figure 7.3	Plot for calculating the response time of the sensor for different concentration of free radicals in solution.	228
Figure 7.4	X-ray diffraction pattern of the PANi nanofiber reinforced PVA nanocomposite before and after exposure to different concentration of free radicals in solution showing the variation of the (100) reflection peak of PANi. Inset shows the X-ray diffraction pattern over the entire 2θ range.	229
Figure 7.5	FTIR spectra of PANi nanofiber reinforced PVA nanocomposites (a) before and after exposure to (b) 500, (c) 600, (d) 700, (e) 800 and (f) 900 ppb.	230
Figure 7.6	Comparison of the intensity of the C=C stretching vibration due to the benzenoid and quinoid structures of the PANi nanofiber reinforced PVA nanocomposites before and after exposure to free radicals in solution.	231
Figure 7.7	Z" spectra of the PANi nanofiber reinforced PVA nanocomposites before and after exposure to different concentrations of free radicals in solution.	232
Figure 7.8	Ac conductivity spectra of the PANi nanofiber reinforced PVA nanocomposite before and after exposure to different	233

	concentration of free radicals in solution.	
Figure 7.9	Response characteristics of the PANi nanofiber reinforced PVA nanocomposite modified QCM sensor after exposure to different concentration of hydrochloric acid in aqueous solutions.	235
Figure 7.10	Calibration curve for determination of hydrochloric acid in solution. The frequency shifts of a PANi nanofiber reinforced PVA nanocomposite modified quartz crystal electrode in direct contact to the solutions have been recorded after 2.5 min of exposure.	236
Figure 7.11	Plot for calculating the response time of the sensor for different concentration of hydrochloric acids in aqueous solution.	237
Figure 7.12	X-ray diffraction patterns of the PANi nanofibers reinforced PVA nanocomposites (a) before and after exposure to (b) 100 ppm, (c) 200 ppm, (d) 300 ppm, (e) 400 ppm and (f) 500 ppm of hydrochloric acid in solution.	238
Figure 7.13	Variation of the normalized integral intensity (I/I_0) as a function of the concentration of analyte.	239
Figure 7.14	FTIR spectra of PANi nanofibers reinforced PVA nanocomposite before and after exposure to 500 ppm of hydrochloric acid.	240

List of abbreviations

Abbreviation	Meanings
1D	One dimensional
2D	Two dimensional
3D	Three dimensional
AC (ac)	Alternating current
APS	Ammonium peroxydisulfate
BSEs	Back scattered electrons
BJTs	Bipolar junction transistor
CBH	Correlated barrier hopping
cm	Centimetre
CCD	Charge coupled detector
CSA	Camphor sulfonic acid
CPs	Conducting polymers
DC (dc)	Direct current
DPPH	1,1-diphenyl-2-picrylhydrazyl
DNA	Deoxyribonucleic acid
EB	Emeraldine base
ES	Emeraldine salt
ES-VRH	Efros-Shklovskii variable range hopping
eV	Electron volt
FD	Frequency domain
FWHM	Full width at half maxima
FTIR	Fourier transform infrared spectroscopy
HOMO	Highest occupied molecular orbital
HN (H-N)	Havriliak-Negami
HCl	Hydrochloric acid
HEDS	High energy dead section
HBTs	Heterojunction Bipolar transistor
Hz	Hertz
ICPs	Intrinsically conducting polymers

I-O	Inorganic in organic
IGFET	Insulated Gate Field effect transistor
IUAC	Inter University Accelerator Centre
JFETS	Junction field effect transistors
kHz	Kilo Hertz
KeV	Kilo electron volt
LUMO	Lowest unoccupied molecular orbital
LEDS	Low energy dead section
LF	Low frequency
M-I	Metal-Insulator
MMT	Montmorillonite
MEM	Memory
MV	Megavolt
MS	Materials Science
NMR	Nuclear Magnetic Resonance
NMP	N-methyl pyrrolidone
OLED	Organic light emitting diodes
OFET	Organic field effect transistor
O-I	Organic in inorganic
O-O	Organic in organic
PADPA	<i>p</i> -aminodiphenylamine
PPy	Polypyrrole
PAni	Polyaniline
PEDOT	Poly (3,4-ethylenedioxythiophene)
PPV	Polyphenylene vinylene
PVA	Polyvinyl alcohol
PMMA	Poly (methyl methacrylate)
PVC	Polyvinyl chloride
PTh	Polythiophene
PALS	Positron annihilation lifetime spectroscopy
QCM	Quartz crystal microbalance
QMT	Quantum mechanical tunneling

RBC	Red blood corpuscles
SPR	Surface plasmon resonance
SiC	Silicon carbide
SAW	Surface acoustic wave
SHI	Swift heavy ion
SSH	Su, Schrieffer, Heeger
SRIM	Stopping ranges of Ions in matter
SEM	Scanning electron microscopy
SEs	Secondary electrons
TFT	Thin film transistor
TD	Time domain
TEM	Transmission electron microscopy
UV-Vis	Ultra violet visible spectroscopy
VRH	Variable range hopping
XRD	X-ray diffraction
μ R	Micro-Raman spectroscopy

List of symbols

Symbols	Meanings
k_B	Boltzmann constant
L	Domain length
ε	Strain
d	Dimensionality
T	Temperature
T_M	Mott temperature
T_{ES}	Efros-Shklovskii temperature
$P(\omega)$	Polarization
$\chi(\omega)$	Dielectric susceptibility
τ	Relaxation time
W_M	Polaron binding energy
R_ω	Hopping distance
s	Frequency exponent
ε^*	Complex permittivity
ε'	Real part of complex permittivity
ε''	Imaginary part of complex permittivity
M^*	Complex electric modulus
M'	Real part of complex modulus
M''	Imaginary part of complex modulus
C	Capacitance
$G(\omega)$	Conductance
$^{\circ}\text{C}$	Degree celcius
\AA	Angstrom
λ	Wavelength of radiation
$\sigma(\omega)$	Frequency dependent conductivity
σ_{dc}	DC conductivity

Chapter 1

INTRODUCTION

This chapter embodies an overview of the exciting and emerging field of conducting polymers with an emphasis on conducting polymer based nanostructured materials. The chapter focuses on the potential applications of conducting polymer nanostructures as intelligent material systems and on the potential application of swift heavy ion irradiation for modification of conducting polymer based nanostructured materials. Biomedical applications of conducting polymer based nanostructured materials are also discussed. The chapter also presents an overview of the science and technology behind conducting polymer based sensors in general and piezoelectric sensors in particular. In the end, the chapter outlines the scope of the thesis and statement of the thesis problem.

1.1 Conducting Polymers

Materials are generally classified as insulators, semiconductors, conductors and superconductors based on their electrical properties. A material with conductivity less than 10^{-7} S/cm is regarded as an insulator. Metals have conductivity larger than 10^3 S/cm whereas the conductivity of a semiconductor varies from 10^{-4} to 10 S/cm depending upon the degree of doping. It was generally believed that plastics (polymers) and electronic conductivity were mutually exclusive and the inability of polymers to carry electricity distinguished them from metals and semiconductors. As such, polymers were traditionally used as inert, insulating and structural materials in packaging, electrical insulations and textiles where their mechanical and electrically insulating properties were paramount. In fact, any electrical conduction in polymers was generally regarded as an undesirable phenomenon. The breakthrough happened in the year 1977 when, somewhat accidentally, Alan J. Heeger, Alan G. MacDiarmid and Hideki Shirakawa, discovered that plastics that are generally referred to as insulators can, under certain circumstances, be made to behave like metals [1]. This path-

breaking discovery of high conductivity in polyacetylene in 1977 resulted in a paradigm shift in thinking and opened up new vistas in chemistry and physics [1-4]. Their work was finally rewarded with the Nobel Prize in Chemistry in 2000 for the discovery and development of electronically conductive polymers [5-7].

After the initial discovery in 1977, the field of electronically conducting polymers has surmounted to such heights that it is far ahead of what could have been envisaged when the field was in its formative years. A variety of other conducting polymers and their derivatives were discovered in the subsequent years after the discovery of conductivity in polyacetylene [8-18]. Investigation of electrical conduction properties of conducting polymers was the prime focus of research in the early years [19-24]. Gradually, research in the field of conjugated polymers surpassed the limits of studying conduction processes in doped conjugated polymers and optical properties, electroluminescence and other physical properties of conjugated polymers were being investigated [25-30]. In recent years, distinct development has also been made in understanding of the structure-property relationships for many of the conducting polymers [31-37]. This fascinating progress rate has been stimulated by the field's fundamental synthetic novelty, importance to interdisciplinary research and to the emerging technological applications of these materials in different areas such as molecular electronics [38], electrodes for redox supercapacitors [39, 40], electrochromic displays [41, 42], chemical sensors [43], actuators [44-46], electromagnetic shielding [47-49] and non-linear optics [50].

Intrinsically conducting polymers (ICPs) are completely different from other conducting polymers in which a conducting material such as metal or carbon powder is dispersed in a non-conductive polymer [51]. These polymers often referred to as conjugated polymers belong to a totally different class of polymeric materials with alternate single-double or single-triple bonds in their main chain and are capable of conducting electricity when doped. ICPs, similar to other organic polymers, usually are described by σ (sigma) bonds and π (pi) bonds. While the σ electrons are fixed and immobile due to the formation of covalent bonds between the carbon atoms, the remaining π -electrons can be easily delocalized upon doping. Fig. 1.1 shows the molecular structures of some of the

popular intrinsic conducting polymers that have been synthesized during the last few decades and applied in different application areas. In the next few sections and sub-sections of this chapter, we present a state-of-the-art literature survey of the historical developments in the field of conducting polymers with a special focus on the different characteristic properties of conducting polymers.

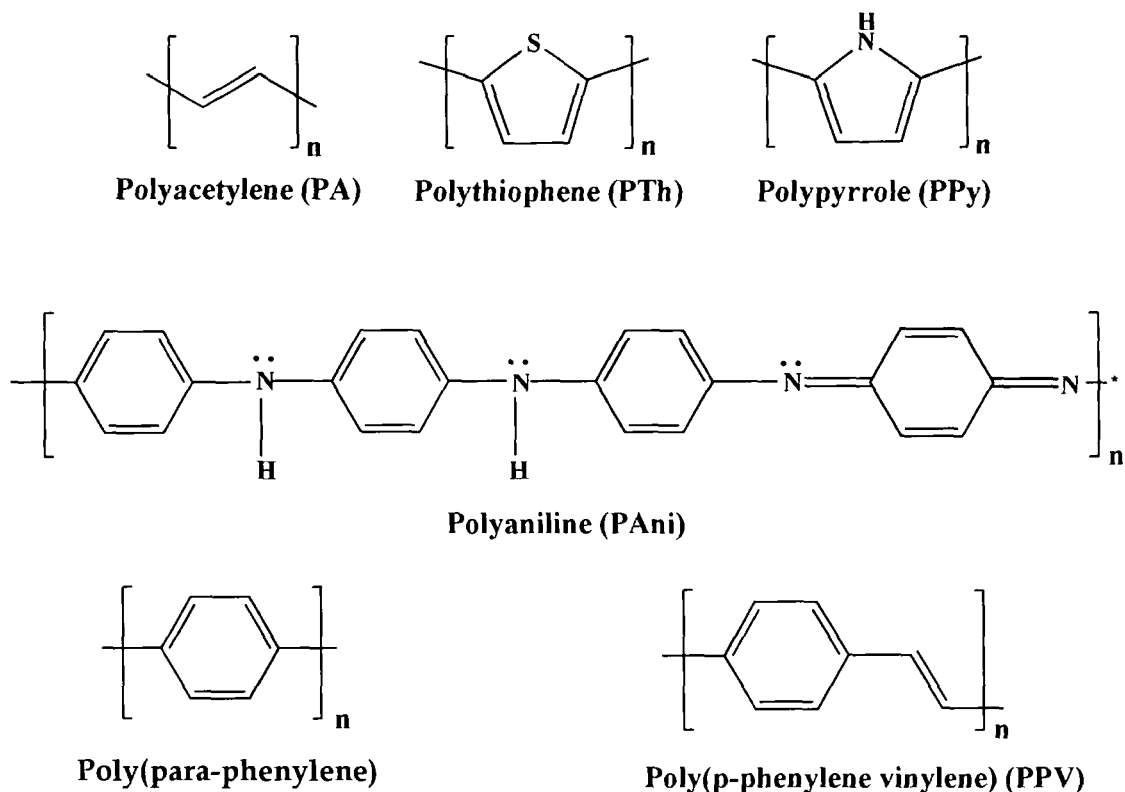


Figure 1.1: Molecular structures of some of the most popular conjugated polymers

1.1.1 Historical developments

Although polymeric materials have been used by mankind since prehistoric times in the form of wood, bone, skin, and fibers, the existence of macromolecules was accepted only after Hermann Staudinger developed the concept of macromolecules during the 1920s, which got him the Nobel Prize in Chemistry in 1953 “for his discoveries in the field of macromolecular chemistry” [52]. This was followed by very important contributions by Wallace Carothers [53] and Noble laureates Karl Ziegler, Giulio Natta and Paul Flory [54] which made the field of macromolecular science popular amongst the scientific community. Because the saturated polymers studied by Staudinger, Flory, Ziegler, and Natta were insulators, they were viewed as uninteresting from the point of view of electronic materials.

The research field of conjugated (conducting) polymers came into focus with the preparation of polyacetylene by Shirakawa and coworkers along with the subsequent discovery of enhancement in its conductivity after "doping" by the group led by MacDiarmid and Heeger [1-4]. The history of conducting polymers, however, dates back to the nineteenth century. Some of the most important representatives in the family of π -conjugated polymers in non-conducting as well as conducting forms viz., polyaniline (PAni) and polypyrrole (PPy), were already being prepared chemically or electrochemically in the nineteenth century, decades before the existence of macromolecules was even accepted and as such they were not called polymers.

Gas industries in the first half of the nineteenth century prepared aniline from the coal tar residues which later played a pivotal role in the development of organic chemistry and the chemical industry [55]. Soon aniline dyes replaced dyes from natural sources and then coal tar dyes found use in medicine for staining tissues [56]. After the discovery of selective toxicity of these compounds by P. Erlich, the chemical production of medicines was initiated and led to the establishment of the pharmaceutical industry [57]. It was in 1862, when Dr. Henry Letheby observed that a bluish-green precipitate was formed at the anode during electrolysis of aniline, which became colourless when it was reduced and regained its blue color when oxidized again [58]. Subsequently, Runge [59] in 1834 and Fritzsche [60] in 1840 isolated aniline and observed the appearance of a blue colour during the oxidation of aniline in acidic media. Letheby's experiments were repeated and his findings were verified by Goppelsroeder [61], Szarvasy [62] and others. A linear octameric structure was proposed and generally accepted for aniline in the first decade of the twentieth century. The existence of polyaniline (PAni) in four oxidation states was also recognized [63]. A reaction scheme for the electro-oxidation of aniline at a carbon electrode was suggested by Yasui in 1935 [64]. It was almost a century after Letheby's observations that Mohilner and co-workers reinvestigated the mechanism of the electro-oxidation of aniline in aqueous sulphuric acid solution at a platinum electrode and characterized polyaniline (PAni) [65]. The first real breakthrough came in 1967, when Buvet and his group established that polyanilines are redox active electronic conductors and

PAni pellets can be used as electrodes for conductivity measurements [66-67]. However, this discovery did not give rise to great excitement during that time. Diaz and Logan initiated research into polymer film electrodes based on polyaniline in 1980, which is still continuing [68]. However, it was the investigations by MacDiarmid *et al.* in the mid 1980s [9-13, 69], and, in particular, the discovery of electrical conductivity for its emeraldine salt form that led to an explosion of interest in this fascinating polymer.

Polypyrrole (PPy), on the other hand, was known as “Pyrrole black” and was formed due to the oxidation of pyrrole in air. PPy is an inherently conducting polymer with interesting electrical properties first discovered and reported in the early 1960s [70]. It was followed by the preparation of coherent and free standing polypyrrole films by electrochemical polymerization by Diaz and his co-workers [71, 72]. Thus, it is evident that although the research in the field of conducting polymers seems to have aroused interest of researchers and public alike in the 1970s, these polymers were already known but not as conducting polymers that we know today. Thus, these materials have a long history and, perhaps without any overstatement, a dazzling future.

1.1.2 Primary features of conducting polymers

The ground state of a carbon atom has six electrons arranged as $1s^2 2s^2 2p^2$, which gives four electrons in the outer electronic orbital. In the presence of other atoms (H, O etc.) these levels may hybridize either into sp , sp^2 or sp^3 orbitals, each possessing their unique spatial character. Fig. 1.2 shows the schematic structure of the simplest three-dimensional (3D), two-dimensional (2D) and the one-dimensional (1D) form of carbon materials. In case of diamond, the carbon atoms are sp^3 hybridized whereas in case of graphite and polyacetylene the carbon atoms exhibit sp^2 hybridization. Out of these three forms of carbon materials, only the 2D and 1D form are conducting. Diamond, which contains only σ bonds, is an insulator and its high symmetry gives it isotropic properties. Graphite and acetylene, on the other hand, both have mobile π electrons. Graphite is known to be a conductor while doped polyacetylene shows highly anisotropic metallic conductivity [1].

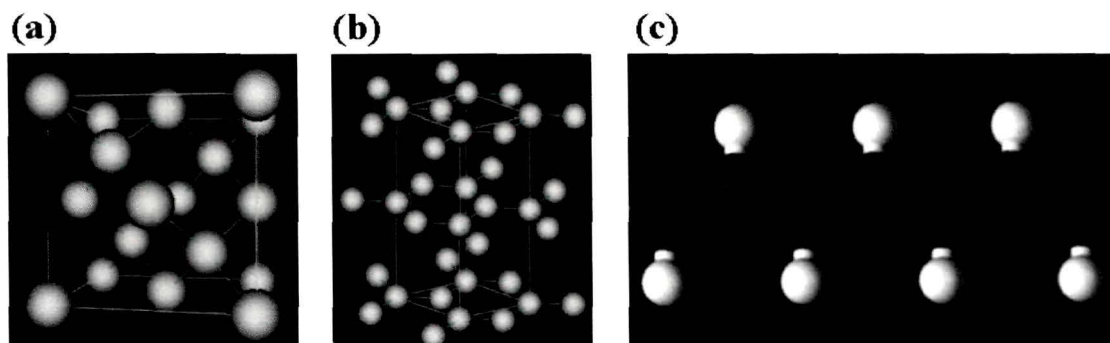


Figure 1.2: Schematic diagram showing the molecular structures of the simplest 3D, 2D and 1D form of carbon materials (a) Diamond, (b) Graphite and (c) Polyacetylene

All the hybridized orbitals in carbon materials are strongly localized, however in case of sp^2 we are left with one unhybridized p_z orbital. This p_z orbital is oriented perpendicular to the three sp^2 orbitals that are coplanar with angles of 120° between one another (Fig. 1.3). In case of an identically hybridized neighbour C atom with similar orientation, these p_z orbitals will overlap and form a molecular π bond. The σ bond between the two C atoms (created by two hybridized sp^2 orbitals) together with the π bond results in a double bond. The stacking of neighbouring sp^2 hybridized C atoms, all with their p_z orbitals parallel, results in an alternating single bond, double bond structure as can be seen from Fig. 1.2 (c).

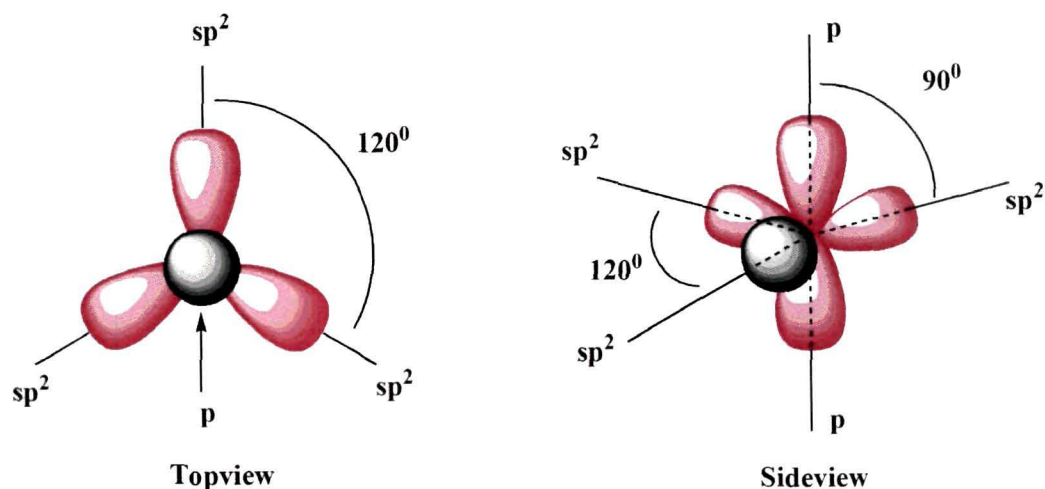


Figure 1.3: Spatial representation of the sp^2 hybridized carbon atom from top and side view.

Conducting polymers are different from other polymers primarily because of this framework of alternate single-double carbon-carbon (carbon-nitrogen) bonds in the polymer backbone chain. In this alternating sequence (conjugation

structure), the positions of the double and single bonds may be exchanged with small or no energy difference [73]. All the conducting polymers have a backbone of σ -bonds between carbon atoms that are sp^2 hybridized leading to one unpaired electron (the π electron) per carbon atom. This allows the overlapping of the remaining out-of-plane p_z orbitals to form a π -band, which leads to electron delocalization along the backbone of the polymer. This electronic delocalization allows charge carriers to move along the backbone of the polymer chain although the mobility is low. The electronic structure in conducting polymers is determined by the number and kind of atoms within the repeat units i.e., the symmetry of the chains. The characteristics of the π -band, therefore, play an important role for determining the semi-conducting or in some cases metallic properties of conjugated polymers. In their pristine form, most of the conducting polymers are insulating except for polyacetylene [*trans*-(CH)_x] that exhibits semi-conducting behavior in the pure form. However, enhancement in the conductivity of conjugated polymers by many orders of magnitude can be achieved through simple chemical or electrochemical oxidation or in some cases reduction by a number of simple anionic or cationic species called dopants [74]. Doped conjugated polymers when in appropriate oxidized or reduced states are semiconductors and in some cases exhibit metallic behavior due to their unique π -conjugation.

1.1.2.1 Doping in conducting polymers

Doping in conjugated organic polymers is something that is responsible for the great scientific and technological importance achieved by these materials since their discovery in 1977. The concept of doping is the unique and central theme that unites all the conducting polymers and differentiates them from all other types of polymers [2, 3, 74]. During the doping process, an organic polymer, either an insulating or semi-conducting polymer could be converted into electronic polymers exhibiting metallic conductivity ($1 - 10^5$ S/cm). Although the term "doping" might look familiar but the concept of "doping" in conducting polymers is much different than that in case of inorganic semiconductors. Fig. 1.4 shows a schematic diagram to explicit the difference between the doping mechanisms in inorganic semiconductors and conjugated polymers. In semiconductor physics,

doping describes a process where dopant species present in small quantities occupy positions within the lattice of the host material, resulting in a large-scale change in the conductivity of the doped material compared to the undoped one. The “doping” process in conjugated polymers is, however, essentially a charge transfer reaction, resulting in the partial oxidation (or less frequently reduction) of the polymer. Unlike inorganic semi-conductors, doping in conjugated polymers is reversible in a way that upon de-doping the original polymer can be retained with almost no degradation of the polymer backbone. Another very important difference between the doping in conjugated polymers and that in inorganic semiconductors is that doping in conjugated polymers is interstitial whereas in inorganic semiconductors the doping is substitutional.

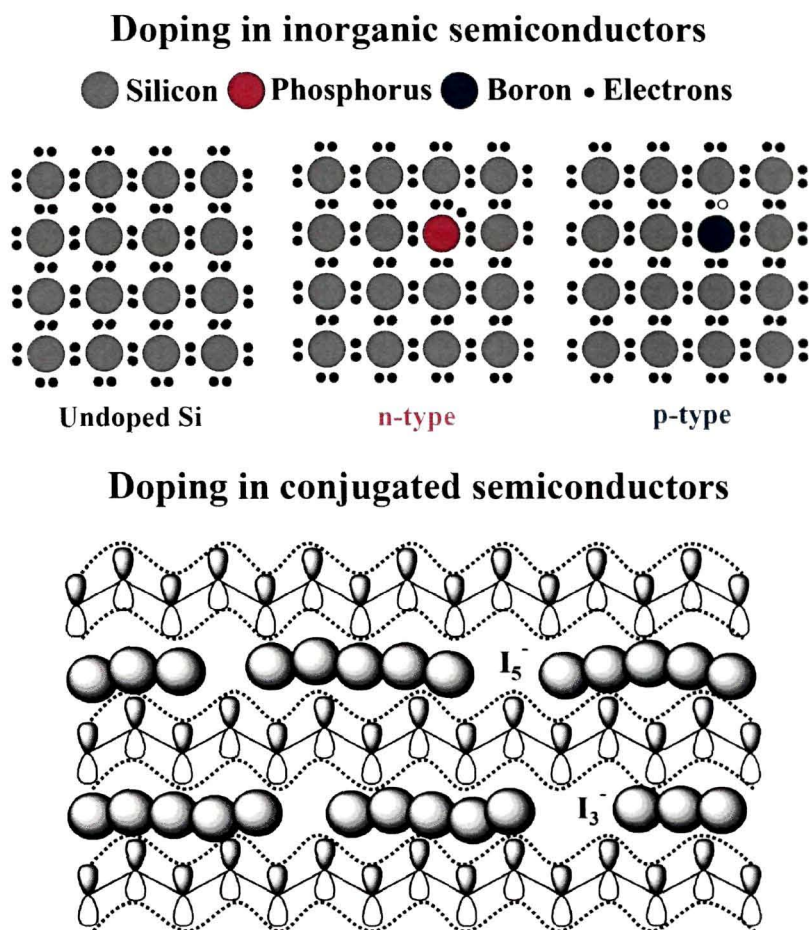


Figure 1.4: Schematic diagram showing the difference between the doping mechanisms in inorganic semiconductors and conjugated polymers

One can easily obtain a conductivity anywhere between that of the undoped (insulating or semiconducting) and that of the fully doped (highly conducting) form of the polymer by simply adjusting the doping level. During

doping and de-doping processes a stabilized doped state of the conducting polymer may be obtained using dopant counterions by chemical or electrochemical processes [75]. Conducting polymers can be *p* or *n* doped chemically and electrochemically to obtain a metallic state [2, 3, 76, 77]. Doping of conjugated polymers can also be carried out by methods that introduce no dopant ions such as field induced charging [78]. In the doped state, the backbone of a conducting polymer consists of highly delocalized π electrons. Fig. 1.5 presents a chart showing the different methods that have been adopted for doping conducting polymers.

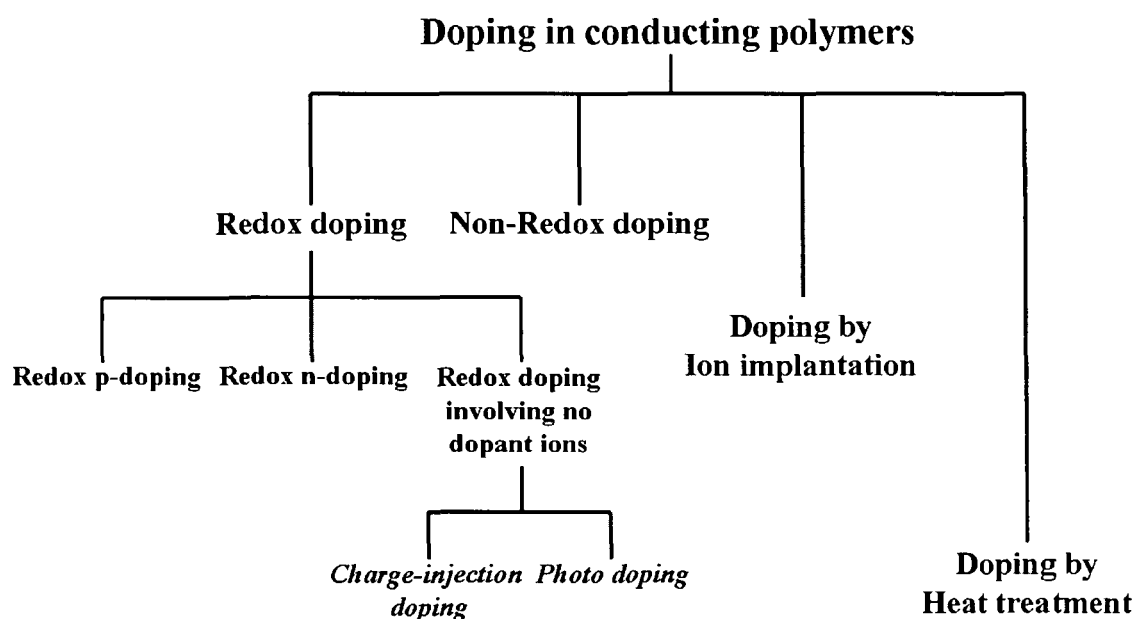


Figure 1.5: Different methods for doping conducting polymers

Doping of conjugated polymers either by oxidation or by reduction in which the number of electrons in the polymeric backbone gets changed is generally referred to as redox doping [74-77, 79]. The charge neutrality of the conducting polymer is maintained by the incorporation of the counterions [80]. Redox doping can be further subdivided into three main classes: *p*-doping, *n*-doping and doping involving no dopant ions viz., photo-doping and charge injection doping [77, 81, 82]. Both chemical and electrochemical redox doping techniques can be employed to dope conjugated polymers either by removal of electrons from the polymer back-bone chain (*p*-doping) or by the addition of electrons (*n*-doping) to the chain. In chemical doping the polymer is exposed to an oxidizing agent such as iodine vapours or a reducing agents viz., alkali metal

vapours, whereas in electrochemical doping process a polymer coated working electrode is suspended in an electrolyte solution in which the polymer is insoluble, along with separate counter and reference electrodes. On the application of a potential difference between the electrodes, charges cross into the polymer in the form of electron addition (*n*-doping) or removal (*p*-doping) and the appropriate counter ion from the electrolyte enters into the polymer film in order to maintain charge neutrality.

Photo-doping is a process where conducting polymers can be doped without the insertion of cations or anions simply by irradiating the polymer with photons of energy higher than the band gap of the conducting polymer. This leads to the promotion of electrons to higher energy levels in the band gap [83]. However, due to rapid recombination of electrons and holes, photo-doping does not sustain after the irradiation of the polymer is stopped. Charge injection doping is another type of redox doping that can also be used to dope an undoped conducting polymer [78, 84, 85]. In this method, thin film of conducting polymer is deposited over a metallic sheet separated by a high dielectric strength insulator. This metal/insulator/semiconductor structure is used to carry out charge injection in the polymer film. The charges are injected into the conducting polymer without involvement of any dopant ion. When an appropriate potential difference is applied across the structure a surface charge layer is formed in the polymer. The accumulation of charge layer for conducting polymer has been extensively studied and experimental signatures of solitons and mid gap absorption have been observed in injected charge layer in polyacetylene in the absence of dopant ion.

The non-redox doping of conducting polymer is a process of doping conducting polymers in which the number of electrons associated with the polymer chain is kept constant. In fact it is the energy level in the conducting polymer that gets rearranged in the non-redox doping process [86]. The best example of non-redox doping is the conversion of emeraldine base form of polyaniline to protonated emeraldine base (polysemiquinone radical cation) when treated with protic acids [69]. It has been observed that the conductivity of

polyaniline is increased by approximately 10 orders of magnitude by non-redox doping.

Ion implantation and heat treatment methods have also been used to dope conducting polymers. Ion bombardment of polyaniline by 100 KeV Ar⁺ ion and 24 KeV I⁺ at a fluence of 10⁶ ions/cm² has been reported [87] and it has been observed that upon I⁺ ion implantation the films become environmentally stable showing enhanced conductivity by 12 orders of magnitude. Heat treatment induced doping has been observed for ladder type of conducting polymers [88]. It has been observed that for ladder type of polymers conductivity increases from 10⁻⁸ to 10⁻⁴ S/cm upon heat treatment, which has been attributed to the improved ordering of the polymer structure and thermally excited charge carriers. However, this technique has rarely been used for doping conducting polymers.

1.1.2.2 Metal-Insulator transition in doped conducting polymers

Metal-Insulator (M-I) transition is one of the most interesting physical aspects of conducting polymers. When the mean free path becomes less than the inter-atomic spacing due to increase in disorder in a metallic system, coherent metallic transport is not possible [89]. When the disorder is sufficiently large the metal exhibits a transition from the metallic to insulating behavior. As a result of this transition which is also known as the Anderson transition all the states in a conductor become localized and it converts into a "Fermi glass" [90] with a continuous density of localized states occupied according to Fermi statistics. Although there is no energy gap in a Fermi glass but due to the spatially localized energy states a Fermi glass behaves as an insulator [90, 91]. It has been found that electrical conductivity of a material near the critical regime of Anderson transition obeys power law temperature dependence [92].

This type of M-I transition has been observed for different conducting polymers viz., polyacetylene, polyaniline, polypyrrole, poly(p-phenylene vinylene) etc. and is particularly interesting because the critical behaviour has been observed over a relatively wide temperature range [93, 94]. In conducting polymers, the critical regime is easily tunable by varying the extent of disorder by means of doping or by applying external pressure and/or magnetic fields [93]. In the metallic regime, the zero temperature conductivity remains finite, and σ (T)

remains constant as T approaches zero [93]. In the critical region, the conductivity follows a power law, whereas in the insulator regime transport occurs through variable range hopping (VRH) among localized states. Although disorder is generally recognized to play an important role in the physics of “metallic” polymers, the effective length scale of the disorder and the nature of the M-I transition are yet central unresolved issues [94-97]. In particular, it has been a matter of in-depth discussion that whether disorder is present over a wide range of length scales or whether the properties are dominated by more macroscopic inhomogeneities. In the former case, the metallic state and the M-I transition can be described by conventional localization physics (e.g. the Anderson transition), while in the latter case, the M-I transition would be better described in terms of percolation between metallic islands [97].

1.1.2.3 Band structure and charge carriers in conducting polymers

A continuous system of strongly interacting atomic orbitals leads to the formation of band-like electronic states. The atomic orbitals of each atom in an inorganic semiconductor or in a metal overlap with each other in the solid state giving rise to a number of continuous energy bands. The electrons provided by each orbital are delocalized throughout the entire array of atoms. The extent of delocalization and the bandwidth are determined by the strength of interaction between the overlapping orbitals. In case of conjugated polymers, the band structure originates from the interaction of the p orbitals of the repeating units throughout the chain. A set of bonding and anti-bonding molecular orbitals is formed by the combination of two or more adjacent p orbitals, in which the electron pairs are shared by more than two atoms resulting in a delocalized π -band. The bonding π -orbital is referred to as the highest occupied molecular orbital (HOMO) and the anti-bonding π -orbital is referred to as the lowest unoccupied molecular orbital (LUMO) [98]. The HOMO and LUMO can be thought to be analogous to the valence and conduction band in case of solid state materials. Fig. 1.6 (a) is a schematic depiction of the formation of HOMO and LUMO in case of *trans*-polyacetylene. The detailed band structure of polyacetylene and the difference in the band structures of conventional polymers

as compared with conducting polymers has been schematically depicted in the Fig. 1.6 (b, c).

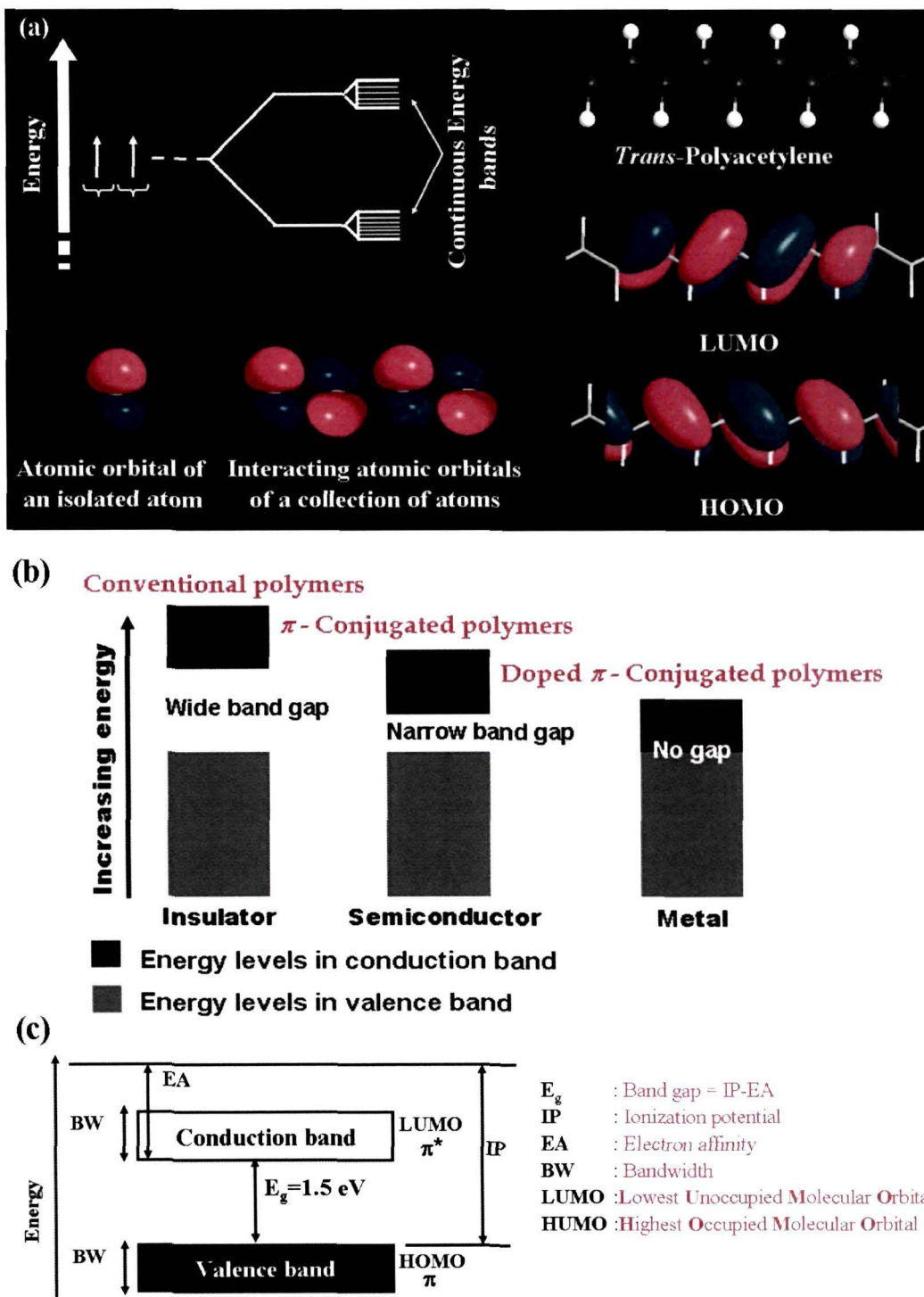


Figure 1.6: (a) Schematic representation of (a) the formation of HOMO and LUMO in polyacetylene due to the presence of a continuous system of strongly interacting atomic orbitals. (b) Difference between band structure of conventional polymer, undoped and doped conducting polymer and (c) Detailed band structure of trans-Polyacetylene showing the energy band-gap and associated parameters.

LIBRARY T.M
T212

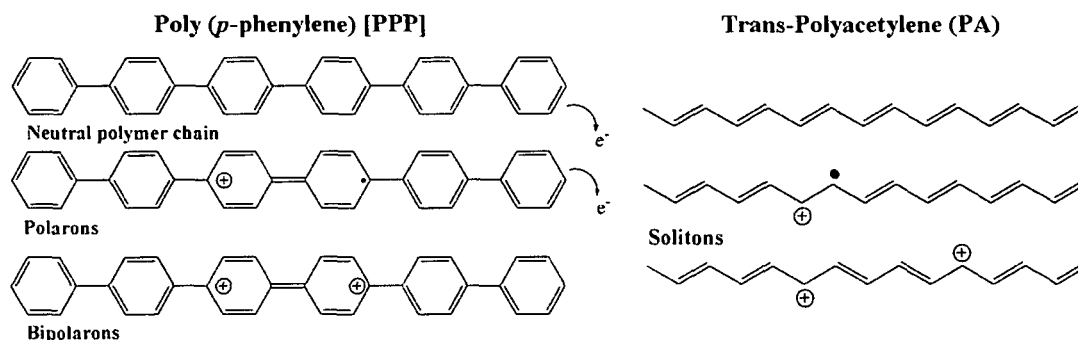
Unless doped, most of the conjugated polymer systems behave as insulators. Although this property of conducting polymers is very similar to that of semiconductors but the underlying physics is quite different. Three-dimensionally bonded materials have rigid structures owing to their four-fold (or six-fold, etc.) coordination of each atom to its neighbors through covalent bonds [98]. Due to the rigidity of the lattice, charge carriers added to the system are accommodated in the conduction and the valence bands without negligible rearrangement of the bonding. In such systems, therefore, the conventional concept of electrons and holes as the dominant excitations has been followed. Bonding in conjugated polymers, on the other hand, has reduced dimensionality since the intra-chain interactions are much stronger than the inter-chain interactions between adjacent chains. These polymers therefore have two-fold coordination and are hence susceptible to structural distortion [99]. As a result, the dominant electronic excitations are inherently coupled to chain distortions, and the equilibrium geometry is determined by the occupancy of the electronic levels via electron-phonon coupling [100].

When a conjugated polymer is doped, the accommodation of an added charge becomes much easier if the charge is localized over a smaller section of the chain. The charge can be localized in the conjugated polymer if the reduction in the ionization energy of the chains due to addition of the charged species can offset the elastic energy gained by the system due to the local rearrangement of the bonding configuration in the vicinity of the charge. The nature of charged defects formed on the polymer backbone during doping depends on the structure of the polymer chain. Different types of charged defects have been observed for conducting polymers with degenerate ground state structures such as polyacetylene and for those with non-degenerate ground state structures such as polyaniline or poly (p-phenylene) [101, 102]. Figure 1.7 shows a schematic depiction of the formation of different types of charge carriers in conducting polymers and the corresponding modifications in their band structure.

When an electron is removed from the π -system of a non-degenerate polymer such as poly (p-phenylene) or polyaniline (PAni) via chemical oxidation, an unpaired electron with spin $\frac{1}{2}$ (a free radical) and a spinless positive charge

(cation) are created as is evident from the Fig. 1.7. The radical and cation are coupled to each other via a local bond rearrangement, creating a polaron which appears in the band structure as localized electronic states symmetrically located within the gap with the lower energy states being occupied by a single unpaired electron [101-103].

Creation of Polarons and bipolarons in poly (*p*-phenylene) and solitons in *trans*-polyacetylene



Electronic band structure of conducting polymers (CP) without and with defect states

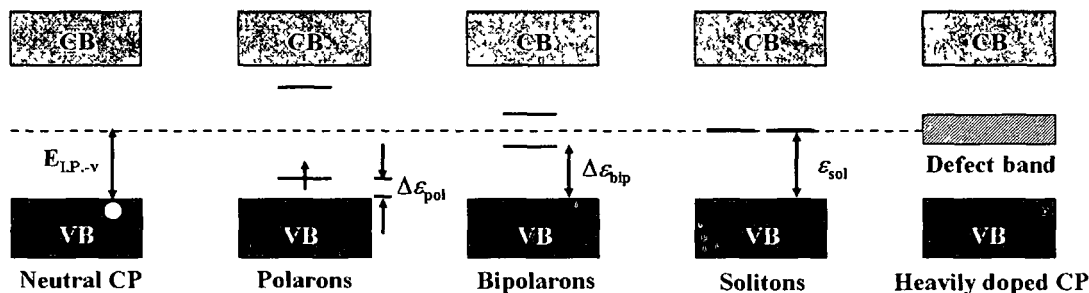


Figure 1.7: Molecular structures of conducting polymers illustrating the formation of the localized defects (charge carriers) viz., polarons, bipolarons and solitons. A schematic representation of the modifications in the band structure of conducting polymers after the creation of these localized defects upon doping is also illustrated.

Further oxidation creates dication in the polymer [Fig. 1.7]. An electron can be removed from either the polaron or the remaining neutral portion of the polymer chain. In the former case, the free radical nature of the polaron is lost and a dication is created comprised of two positive charges coupled through the lattice distortion, creating a new spinless defect known as the bipolaron [104, 105]. Removal of an additional electron from a neutral portion of the chain would create two polarons. Because the formation of a bipolaron produces a larger decrease in ionization energy compared to the formation of two polarons, the former process is energetically favourable. These new empty bipolaron states are

also located symmetrically within the band gap. Further doping creates additional localized bipolaron states, which eventually overlap to form continuous bipolaron bands at high enough doping levels. The case of polyaniline is somewhat different as they have polarons as the major charge carriers. The reason for the non-existence of bipolarons in polyaniline has been elaborated in the section 1.1.3.

In case of conjugated polymers with degenerate ground state structures, the situation is somewhat different. Although, the initial oxidation of *trans*-polyacetylene also creates polarons, but further oxidation leads to the formation of a different type of charged defects in polyacetylene. Since the ground state of *trans*-polyacetylene is twofold degenerate, the bonding configurations on either side of the charged defects only differ by a reversed orientation of the conjugated system and are energetically equivalent resonance forms as can be seen from the Fig. 1.7. It in turn creates isolated, non-interacting charged defects that form domain walls separating two phases of opposite orientation but identical energy. Such defects are called solitons, which results in the creation of new localized electronic states that appear in the middle of the energy gap. As doping increases, these states can overlap to form soliton bands [83].

1.1.2.4 Transport processes in conducting polymers

The revelation of the nature of charge transfer and charge transport processes in conducting polymers is the most interesting theoretical problem of this field. It is also of great practical importance, because in most of their applications fast charge propagation through the conducting polymer is desired. In conducting polymers the polymer backbone is extensively conjugated, which makes charge delocalization possible considerably. Various models have likewise been developed to explain the mechanism of charge transport in conducting polymers. Out of the two approaches that are generally employed, one is the delocalized band model in which, the charges and unpaired electrons are assumed to be delocalized over a large number of monomer units [10, 106]. The other one is the chemical model where it is assumed that the charge is localized in the polymer chain [107], or at most only some monomer units.

The macroscopic charge transport in a conducting polymer matrix represents a superposition of the local transport mechanism. The intrinsic

conductivity, which refers to the conduction process along a conjugated chain, can be described in terms of band theory, which is well-established for solid materials. The neutral (reduced, undoped) polymer has a full valence and empty conduction band separated by a band gap. This intra-chain conduction provides very high intrinsic conductivity [108, 109].

It is now well accepted that non-intrinsic (interstrand and interfiber) transport processes in conducting polymers occur by the movement of charge carriers from the localized defect states viz., polarons, bipolarons or solitons [83, 101-105]. As a result, the theories explaining non-intrinsic charge transport mechanisms in conducting polymer are dominated by thermally activated hopping (or tunneling processes) in which the charge carriers hop across (or tunnel through) barriers created by the presence of isolated states or domains [110-114]. These include models such as intersoliton hopping [110], interchain hopping of bipolarons [111], variable range hopping in three, two and one dimensions [112, 113] and charging energy limited tunneling between conducting domains [114]. These theoretical models that have been developed for explaining transport phenomena in conducting polymers will be discussed in details in Chapter 2.

1.1.3 Polyaniline: a promising conducting polymer

Although the original work depicting the synthesis of polyaniline (PAni) from anodic oxidation of aniline was “Aniline black” published by Letheby [58] in 1862 but unfortunately the electrical properties were not measured at that time. It was MacDiarmid *et al.* in 1986 who found that aniline monomer in an acid aqueous solution can be chemically oxidized by ammonium peroxydisulfate (APS) to obtain green powder of PAni with a conductivity of ~ 3 S/cm [69]. Since its rediscovery as a conducting polymer, PAni has generally been synthesized by both chemical and electrochemical methods [75]. Recently, PAni has also been synthesized using a novel mechano-chemical route [115]. PAni has been a highly investigated conducting polymer because of easy synthesis, low-cost, high environmental stability, complex molecular structure and special doping mechanism by oxidation as well as protonation.

Polyaniline (PAni) has a complex molecular structure dominated by its oxidation states. The allowed oxidation states of PAni have been investigated

[116]. The general molecular structure shown in the Fig. 1.8 (a) for the base form of PANi was for the first time proposed by MacDiarmid *et al.* [117] and later confirmed by ^{13}C -NMR [118]. The base forms of polyaniline (PANi) can exist in four different oxidation states depending upon the values of y [Fig. 1.8 (a)]. Leucoemeraldine, the completely reduced form of polyaniline, has a structure corresponding to $y=1$ in the general structure as can be visualized from the Fig. 1.8 (b). The completely oxidized form of PANi base can be obtained by substituting $y=0$ in the general structure and is known as Pernigraniline [119]. The half-oxidized or so for that matter half reduced form of PANi is called "Emeraldine base" ($y = 0.5$). PANi may also exist in another oxidation state known as Nigraniline for which the value of y is taken as 0.75.

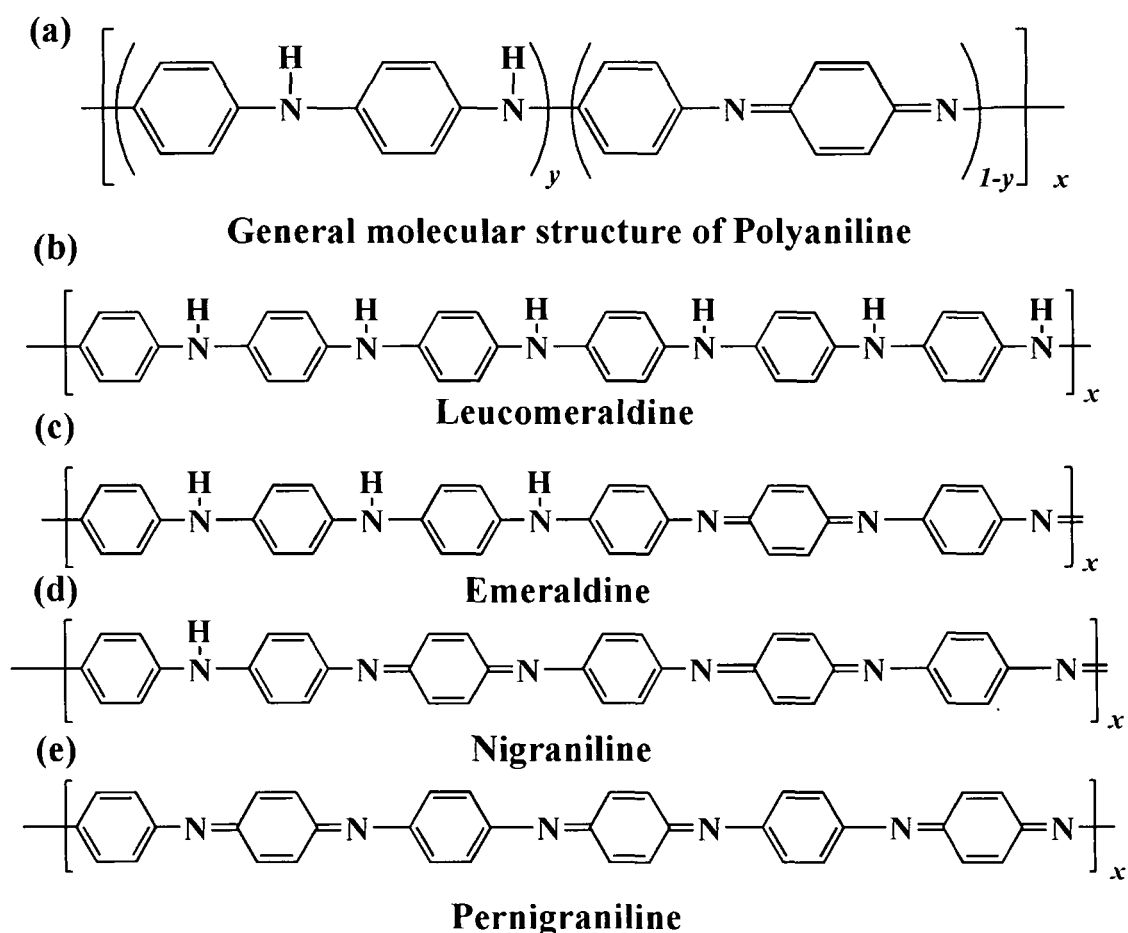


Figure 1.8: (a) General molecular structure of polyaniline (PANi). The different oxidation states of PANi (b) Leucoemeraldine, (c) Emeraldine, (d) Nigraniline and (e) Pernigraniline are depicted in the figure.

Polyaniline (PAni) is unique among the family of π -conjugated polymers because of several characteristic features that it possesses. Firstly, Polyaniline (PAni) is a generalized "A-B" type polymer in which both the carbon rings and nitrogen atoms are within the conjugation path. Thus, in PAni the heteroatoms also contribute appreciably to the formation of π band [120]. The emeraldine form of the polymer is to a large extent different from other π conjugated polymers that have been studied so far because of its charge-conjugation asymmetry [121]. Secondly, PAni is the first example of conducting polymers doped by protons, which was later called "proton doping". Proton doping in emeraldine does not involve a change of the number of electrons associated with the polymer backbone as shown in Fig. 1.9 [69, 122]. The emeraldine base (EB) form of PAni is an insulator constituted by an equal number of reduced $[-(\text{C}_6\text{H}_4)\text{-NH}-(\text{C}_6\text{H}_4)\text{-NH-}]$ and oxidized $[-(\text{C}_6\text{H}_4)\text{-N}=(\text{C}_6\text{H}_4)\text{=N-}]$ units having conductivity of the order 10^{-10} Scm^{-1} but can be transformed into the conducting emeraldine salt (ES) form [σ (295 K) ~ 5 Scm^{-1}], if protons are added to the $-\text{N}=\text{}$ sites. Thus, the proton doping process is significantly different from redox doping that involves the partial addition (reduction) or removal (oxidation) of electrons to or from the polymer backbone [123].

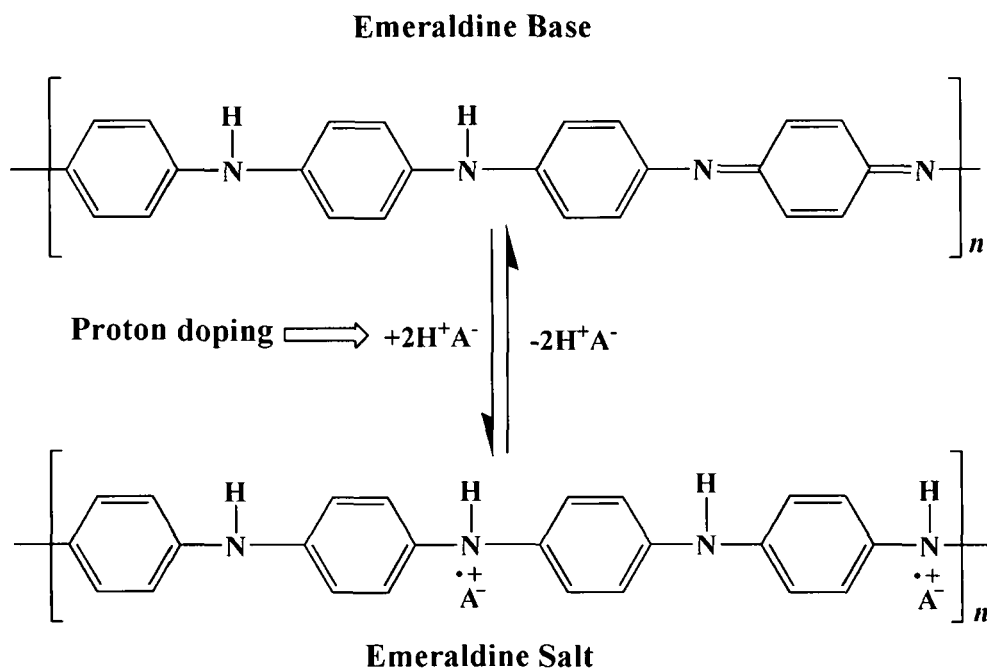


Figure 1.9: Schematic representation of the conversion of Emeraldine base (EB) into the Emeraldine salt (ES) form of polyaniline upon proton doping.

Initially, it was proposed that proton doping only takes place on the imine segment of the emeraldine base to generate a bipolaron [69, 117]. However, this was not supported by theoretical calculations which ruled out the presence of a bipolaron lattice (spinless) in the emeraldine salt form [121]. Furthermore, a strong ESR signal observed from the proton doped emeraldine base also indicated that instead of spinless bipolarons, polarons were the major charge carriers in emeraldine salt [124]. This controversy was solved later by Epstein *et al.* [124, 125] who suggested that spinless bipolarons can convert into two spinning polarons. The bipolaron lattice in the emeraldine is destabilized by local lattice distortion and coulombic interactions [126]. MacDiarmid *et al.* [122] proposed that polarons in emeraldine salt are of semiquinone form. It suggests that the complete protonation of the imine nitrogen atom in the emeraldine base by proton doping results in the formation of a delocalized poly-semiquinone radical cation [69, 122]. The mechanism of proton doping in polyaniline has been investigated in details using *in situ* UV-Visible, fluorescence and ESR spectroscopy by Wan *et al.* [127-129], which confirmed that proton doping took place on the imine segment of poly-emeraldine chain. Thus, the molecular structure of the protonated emeraldine base i.e., emeraldine salt is determined by both oxidation and protonation states.

It has also been observed that the crystalline structure of emeraldine can be distinguished between two classes viz., Class I and Class II, which differs in their ordering and compactness [130]. Class I emeraldine that is obtained by direct preparation (synthesis/precipitation of a salt form) exhibits ES-I crystal structure and the insulating base form is essentially amorphous EB-I. Polyaniline belonging to class II possess ES-II structure in the conducting HCl salt form and EB-II structure in the insulating base form. The emeraldine salt ES-I, is the most compact structure, while the less compact ES-II is obtained by converting crystalline EB-II into a salt form (i.e., by insertion of Cl⁻ anions into a pre-existing crystalline structure). In ES-I the neighbouring columns of chlorine ions are in phase i.e., Cl⁻ ions are at the same level), while in ES-II they are out of phase in the "a" direction i.e., they are shifted by "c/2" [130].

The emeraldine base (EB) form of polyaniline (PAni) is soluble in NMP and is generally used to fabricate free-standing films of the emeraldine base. However, the solution processibility of the doped form (ES form) is very poor since it is insoluble in organic as well as aqueous solution. Many methods such as sulfonation or incorporation of *N*-alkyl-sulfonic acid pendant groups [131, 132], dopant-induced [80], self-doping polymer [133], micro-emulsion polymerization [134], and controlled relative molecular mass [135], have, therefore, been reported for improvement of solubility and processability of PAni.

Polyaniline (PAni) is not only unique in its molecular structure and doping mechanisms but also has unique optical, electrical and magnetic properties, which have been effectively used in several applications areas. Highly conducting form (ES) of PAni is controlled by two completely different processes: protonic acid doping and oxidative doping, while other conductive polymers are affected by their oxidation state alone, resulting in it holding a special position in the field of conducting polymers. PAni has been found to exhibit nonlinear optical properties because of the relatively weak π -binding and the special proton doping process [136]. Magnetic properties of PAni are also interesting in that the magnetic susceptibility changes from a Curie-like to a Pauli-like behaviour as the temperature increases [137]. Moreover, the magnetic properties of PAni are affected by doping structure and degree of protonation, chain structure as well as synthesis conditions [124]. Strong thermo-chromic effect and improved mechanical properties have also been reported for diesters of 4-sulfophthalic acid doped PAni. The development of PAni fiber production techniques have been used to create commercial fibers (PANION) that can be used in solid-state electrochemical devices [138]. PAni has also found applications in diverse areas such as sensors, OLEDs, OFETs, electrodes for supercapacitors, EMI shielding applications etc [48, 139-142].

1.2 Conducting polymer based nanostructured materials

Nanoscience and nanotechnology has emerged as an inimitable and powerful interdisciplinary research area, which has generated several futuristic ideas that are slowly finding important applications in the present day world.

Nanostructured materials (having one of their dimensions less than 100 nm) may be two dimensional (2D) such as quantum well or nanosheets like that of graphene [143], one-dimensional (1D) such as nanofibers or nanowires or nanotubes for that example and zero dimensional (0D) structures such as quantum dots. Nanostructured materials have attracted tremendous interest amongst the scientific community primarily because of their peculiar and fascinating properties, as well as their unique applications. As compared to the bulk counterpart, nanostructured materials exhibit enhanced properties mainly because of their large surface area that becomes extremely important in applications such as catalysis or sensing in which the interaction of the material with the environment is the major criteria determining the efficiency of the device. Another important reason as to why the physico-chemical properties of nanostructured materials are often entirely different from the bulk counterpart is due to the variation in the energy band-gap which leads to a variation in their optical and electrical conduction properties. Fig. 1.10 illustrates the variation in colour of gold with the variation in particle size. Fig. 1.10 (a) shows a gold one-dollar coin depicting the original colour of gold in bulk form whereas the Figs. 1.7 (b-f) show the variation in gold particles with increasing particle size [Fig. 1.7 (b-f)].

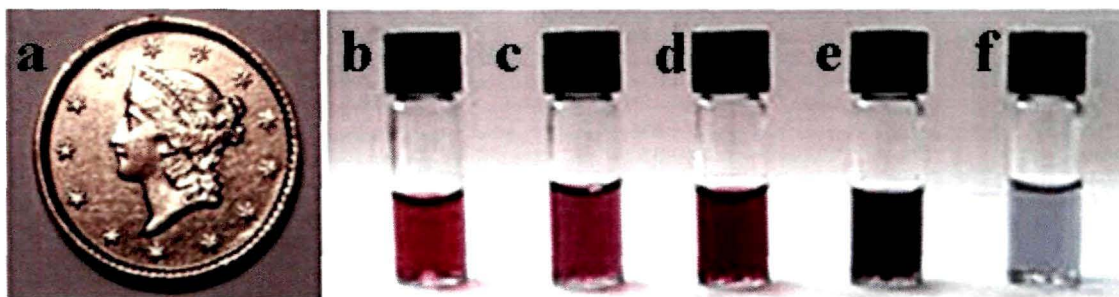


Figure 1.10: Variation in colour of (a) \$ 1 gold coin, showing the normal bulk color of gold and (b-f) gold nanoparticles of different colours with increasing particle size (Courtesy: <http://www.bluesci.org>).

Among different types of nanostructured materials, conducting polymer based nanostructured materials deserve a special mention as they combine the advantage of organic conductors with that of low dimensional materials. These nanostructured materials have some unique properties such as π -conjugated polymeric chains, metal/semiconductor like conductivity, reversible physical

properties by novel doping/de-doping processes. The prospect of these materials being used as molecular wires and nanodevices has made these materials extremely important in nanosciences and nanotechnology. However, the field of conducting polymer based nanostructured materials is still in its infancy and there are several concerns that need to be resolved for realizing the true potential of these nanostructured materials. The first major criteria is the development of simple and efficient methods for the synthesis of conducting polymer based nanostructured materials and the influence of size on the physical properties must be properly investigated. Some sophisticated characterization techniques have to be used or even developed in certain special cases for detailed analysis of the molecular structure and physico-chemical properties of the conducting polymer nanostructures in order to bring out their difference with the bulk and the mechanism underlying their formation. This can help in tailoring the properties of these nanomaterials for specific applications. Tremendous amount of development is also required in the fabrication technology to improve the application of these materials as efficient nanodevices and for future commercial applications.

Conducting polymer based nanostructured materials may be broadly classified into two categories:

- (i) Conducting polymer nanostructures such as nanofibers, nanoparticles, nanowires, nanotubes of pure conducting polymers and
- (ii) Conducting polymer nanocomposites, which are mixtures of metal / metal oxide / ceramic nanoparticles with conducting polymer at nanoscale or nanoscale mixture of conducting polymer nanostructures with another polymer.

The following sub-sections present a brief overview of these two categories of conducting polymer based nanostructured materials in order to give a better insight into the science and technology of these materials.

1.2.1 Conducting polymer nanostructures

Nanostructures viz., nanofibers, nanotubes, nanoparticles, nanowires etc. of pure conducting polymers have created immense excitement in the scientific community because of their potential in different application. The last two

decades have witnessed tremendous development in the field of conducting polymer nanostructures. There are three main strategies that are generally used for obtaining conducting polymer nanostructures: (a) Templateless synthesis, (b) Template-assisted synthesis and (c) Molecular template-assisted synthesis [144].

Conducting polymer nanostructures have been synthesized using different techniques viz., micellar and reverse micellar polymerization, interfacial polymerization, rapid mixing polymerization, seeding polymerization, microemulsion polymerization, electro-spinning and polymerization in the presence of soft and hard templates [145-154]. These materials have also found applications in diverse areas such as chemical and biosensors, memory devices (PAni-MEM), flash welding etc. [155-159].

1.2.2 Conducting polymer nanocomposites

Composite materials are naturally occurring or engineered materials made from two or more constituent materials with significantly different physical or chemical properties as compared to their individual components which remain separate and distinct at the macroscopic or microscopic scale. A common example is "Concrete", a composite construction material composed of cement (commonly Portland cement) and other materials such as fly ash, slag cement, limestone, granite, fine aggregate such as sand, water and chemical admixtures. Concrete is used more than any other man-made material in the world [160]. However, in the microscopic world, due to the reduced particle size of the components the interface interactions play a pivotal role in composite mixtures and this is especially important for a new class of recently developed materials named, the nanocomposites.

Nanocomposites can be defined as multiphase solid materials having unique physical properties and wide application potential with at least one of the phases constrained by some means to grow more than 100 nm in either one, two or three dimensions that are obtained from molecular level mixing of two or more nanosized objects using an appropriate technique [161]. Depending upon the macroscopic physical structures nanocomposite materials can be classified into three broad categories: (a) Fibrous (b) Laminar and (c) Particulate nanocomposites [162, 163].

The first generation of nanocomposites were the nanocomposite plastics which were homogeneous dispersions of small sized inorganic particles throughout a polymer matrix. These nanocomposites were prepared in the 1970's employing sol-gel technique, however, the inorganic phase in these nanocomposites were in some cases not attached chemically to the organic phase. Nanocomposite plastics found tremendous applications in surface coating technology. The second generation of nanocomposite materials emerged in the 1980's when fine particles, minerals and clay fillers were used as a secondary phase in plastics. During 1990's and beyond, the third generation of nanocomposite materials emerged where polymeric materials were reinforced with nanofibers such as carbon nanotubes, SiC whiskers, colloidal silica, nano-clay particles etc [164].

Nanocomposites of intrinsically conducting polymers (ICPs) are materials that utilize conjugated polymers and at least one secondary component that can be inorganic or organic materials or biologically active species [165]. One can derive exciting novel properties from nanocomposites by successfully combining the characteristics of its parent constituents into a single material. Generally, in polymer nanocomposites the polymeric component is utilized to provide mechanical strength and processibility to the resulting nanocomposite material. However, in case of nanocomposites of intrinsically conducting polymers the secondary components viz., inorganic, biological or organic active species are generally used to enhance the processibility and mechanical strength whereas the functionalities of intrinsic conducting polymers are used for different applications [165]. The properties of the secondary components are also utilized in some applications. In a nutshell, conducting polymer nanocomposites are truly hybrid materials which have excellent physicochemical properties resulting from the synergistic effect of the individual properties of two or more components. Conducting polymer nanocomposites can be broadly classified into three classes depending upon the nature of association between the individual components. These are Inorganic-in-Organic (I-O) nanocomposites, Organic-in-Inorganic (O-I) nanocomposites and Organic-in-Organic (O-O) nanocomposites, which are discussed in the following sub-sections.

1.2.2.1 Inorganic-in-organic (I-O) nanocomposites

Inorganic-in-organic nanocomposites refer to materials in which inorganic nanoparticles are embedded in organic matrix. Thus, in these hybrid materials the organic phase plays the role of a host to an inorganic guest. These nanocomposites not only correlate the world of nanoparticles with that of the macromolecules, but often help in surmounting the processing problems associated with intrinsic conducting polymers (ICPs). Several techniques have been adopted to encapsulate inorganic nanoparticles into the host-conducting polymer matrix, which predominantly includes chemical and electrochemical techniques [166]. The encapsulation is generally done *ex-situ* where the inorganic nanoparticles are prepared separately and then added to the conducting polymer matrix in different compositions during the polymerization reaction [164-166]. However, *in-situ* techniques have also been used to synthesize inorganic-in-organic nanocomposites in which the inorganic nanoparticle is synthesized and encapsulated in the conducting polymer matrix simultaneously during polymerization in the same reaction vessel [164-166]. Different conducting polymers viz., polyaniline (PAni), polypyrrole (PPy), polyphenylene vinylene (PPV), poly (3, 4-ethylenedioxythiophene) (PEDOT) have been extensively used as hosts for inorganic metal, metal oxide and ceramic nanoparticles to synthesize inorganic-in-organic conducting polymer nanocomposites [167-171]. Different types of inorganic particles have been encapsulated in conducting polymers by chemical or electrochemical incorporation techniques depending upon the necessity of the application areas where the nanocomposites are intended to be applied. These include metals such as gold (Au) and silver (Ag), metal oxides such as SiO₂, SnO₂, CeO₂, CuO, Fe₂O₃, Fe₃O₄, MnO₂, BaSO₄, Al₂O₃, ZrO₂, n-TiO₂, V₂O₅, WO₃ etc. [172-190]. The methods adopted for preparation of the nanocomposites govern the physico-chemical properties such as its colloidal stability, optical, catalytic, electrochemical, magnetic susceptibility, etc., exhibited by these materials. These properties always add new dimensions to the characteristic of the resulting nanocomposite and in most cases are much better when compared to that of the individual components.

1.2.2.1.1 Core-shell nanocomposites

Among the inorganic-in-organic nanocomposites, those having core-shell structures have attracted tremendous scientific interest and have become more popular leading to some interesting aspects of nanocomposite synthesis. During the past decades, various synthetic methods have been developed for the preparation of core-shell conducting polymer nanocomposites with different metal and metal oxide nanoparticles encapsulated in the core of conducting polymers. Depending upon the composition of these nanocomposites several functionalities have also been observed which are quite different from the pure materials.

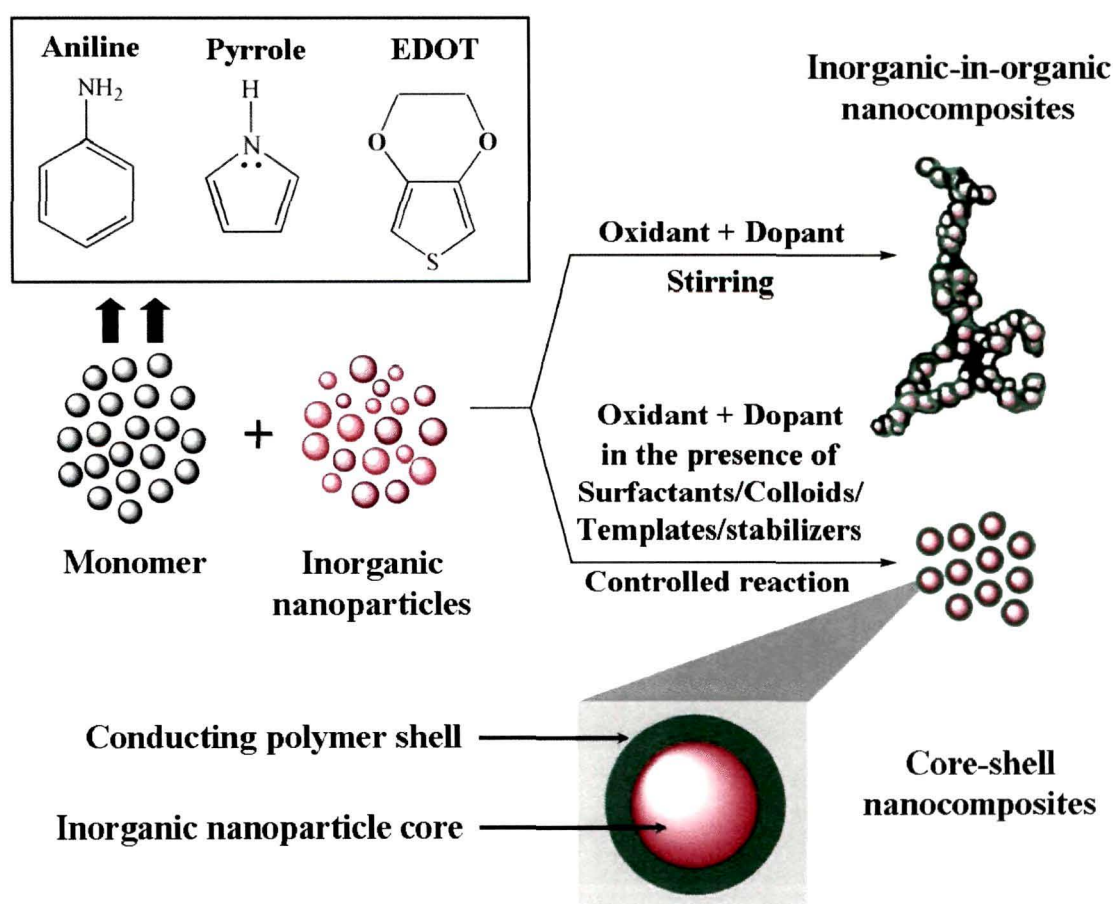


Figure 1.11: Schematic diagram to illustrate the synthesis mechanism of inorganic-in-organic conducting polymer nanocomposites and core-shell type nanocomposites based on conducting polymers.

Core-shell nanocomposites of polyaniline (PAni) and polypyrrole (PPy) were synthesized in stable colloidal forms with silica (SiO_2) particles as the core

[191-193]. Colloidal PPy-gold(Au) core-shell nanocomposites have also been synthesized by a template-guided polymerization technique [194]. Fig. 1.11 shows a schematic diagram to illustrate the formation of both general and core-shell inorganic-in organic nanocomposites based on conducting polymers from the constituents. Deng *et al.* reported the synthesis of ferromagnetic and conducting Fe₃O₄-crosslinked polyaniline nanoparticles in core-shell morphology in the presence of magnetic fluid in aqueous solution [195]. Hematite/silica/polypyrrole (Fe₂O₃/SiO₂/PPy) ellipsoidal sandwich composite spheres as well as SiO₂/PPy ellipsoidal hollow capsules with movable hematite cores were successfully fabricated by hematite (α -Fe₂O₃) olivary particles [196]. A facile and versatile solution route was developed to prepare semiconductor metal oxide nanobelt-conducting organic polymer core-shell nanocomposites by Xu *et al.* [197]. Polypyrrole-coated silver nanocomposite particles have been synthesized by one-step aqueous chemical oxidative dispersion polymerization of pyrrole using silver nitrate as an oxidant [198]. Electromagnetic functionalized core-shell nanocomposites of polypyrrole (PPy) were prepared by a self-assembly process [199]. Yang *et al.* prepared novel sunflower-like organic-inorganic composites comprising of spherical silica and smaller conductive polypyrrole particles through an *in situ* self-assembly polymerization process by choosing chitosan as a modifying agent of silica surface [200]. Polypyrrole (PPy)-coated Ag composites were synthesized through interfacial polymerization technique in the presence of polyvinylpyrrolidone (PVP) by Feng *et al.* [201]. Monodispersed and uniform core/shell nanocomposites including CuO/PAni, Fe₂O₃/PAni, In₂O₃/PAni and Fe₂O₃/SiO₂/PAni were successfully prepared using a double-surfactant-layer-assisted polymerization method [202]. The preparation of CeO₂/polyaniline (CeO₂/PAni) core-shell nanocomposites via chemical oxidation of aniline using CeO₂ as an oxidant was reported by Chuang and Yang [203]. Synthesis of metallic copper nanoparticles coated with polypyrrole was very recently reported by Kobayashi *et al.* [204]. The importance of these types of nanocomposites is evident from the amount of work that has been done in recent years regarding the investigation of the synthesis procedures and related properties of the core-shell nanocomposites.

1.2.2.2 Organic-in-inorganic (O-I) nanocomposites

Another type of nanocomposite materials is the organic-inorganic nanocomposites in which the organic polymer is confined into the inorganic layers for a broad range of applications. A large variety of layered inorganic materials possessing well defined and ordered intralamellar space are available. These materials act as hosts and can be easily accessed by foreign species such as polymers yielding interesting lamellar nanocomposite materials. Lamellar nanocomposites can be divided into two distinct classes, intercalated and exfoliated. These two classes of organic in inorganic nanocomposites are discussed in the following sub-sections. Figs. 1.12 (a, b) show the molecular structures of two layered silicates (clays) viz., montmorillonite and kaolinite, respectively that are often used as inorganic hosts for organic polymers.

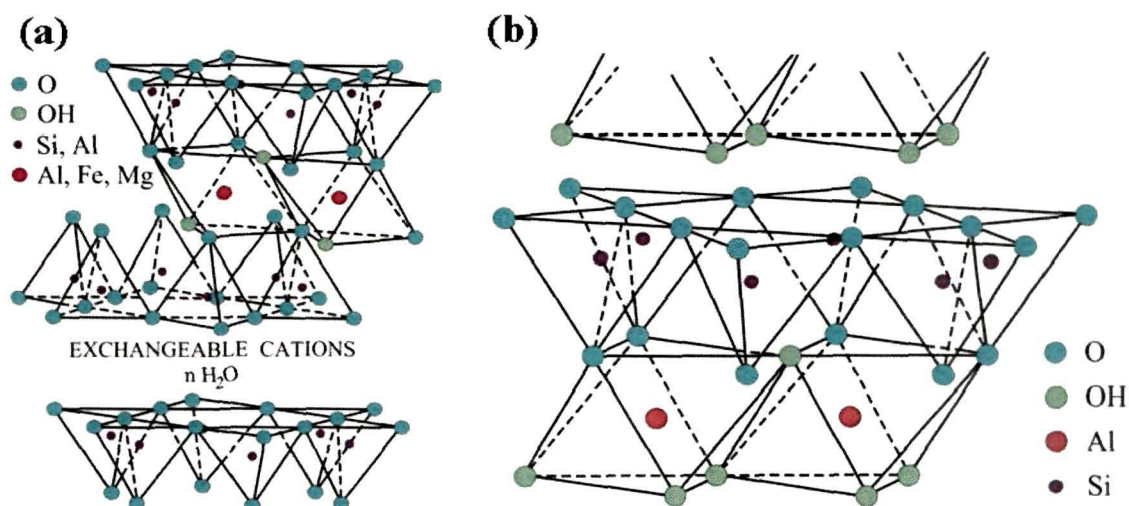


Figure 1.12: Molecular structure of (a) Montmorillonite and (b) Kaolinite (Courtesy: <http://pubs.usgs.gov/of/2001/of01-041/html/docs/clays/smc.htm>)

1.2.2.2.1 Intercalated and exfoliated nanocomposites

Layered silicates have crystal structures with two dimensional spacings in the nanometer range as seen from Fig. 1.12. Clay-Polymer nanocomposites have recently attracted a great deal of attention as they offer enhanced mechanical and thermal properties as compared to conventional materials. These nanocomposites can be subdivided into primarily two groups: intercalated and exfoliated nanocomposites

Polymers intercalated into low-dimensional host lattices form an attractive class of organic-in-inorganic nanocomposites since intercalation can combine

properties of both the guest polymer and the inorganic host in a single material [205]. In the case of intercalation, the organic component is inserted between the layers of clay such that the inter-layer spacing is expanded, but the layers still bear a well-defined spatial relationship to each other. These compounds also serve as model systems for understanding the effect of confinement of the guest on properties in relation to those in bulk [206, 207]. In recent years, there has been extensive study of the factors such as exchange capacity of the clay, the polarity of the reaction medium and the chemical nature of the interlayer cations (e.g. onium ions). Fig. 1.13 shows a schematic diagram of the different types of clay-polymer nanocomposites.

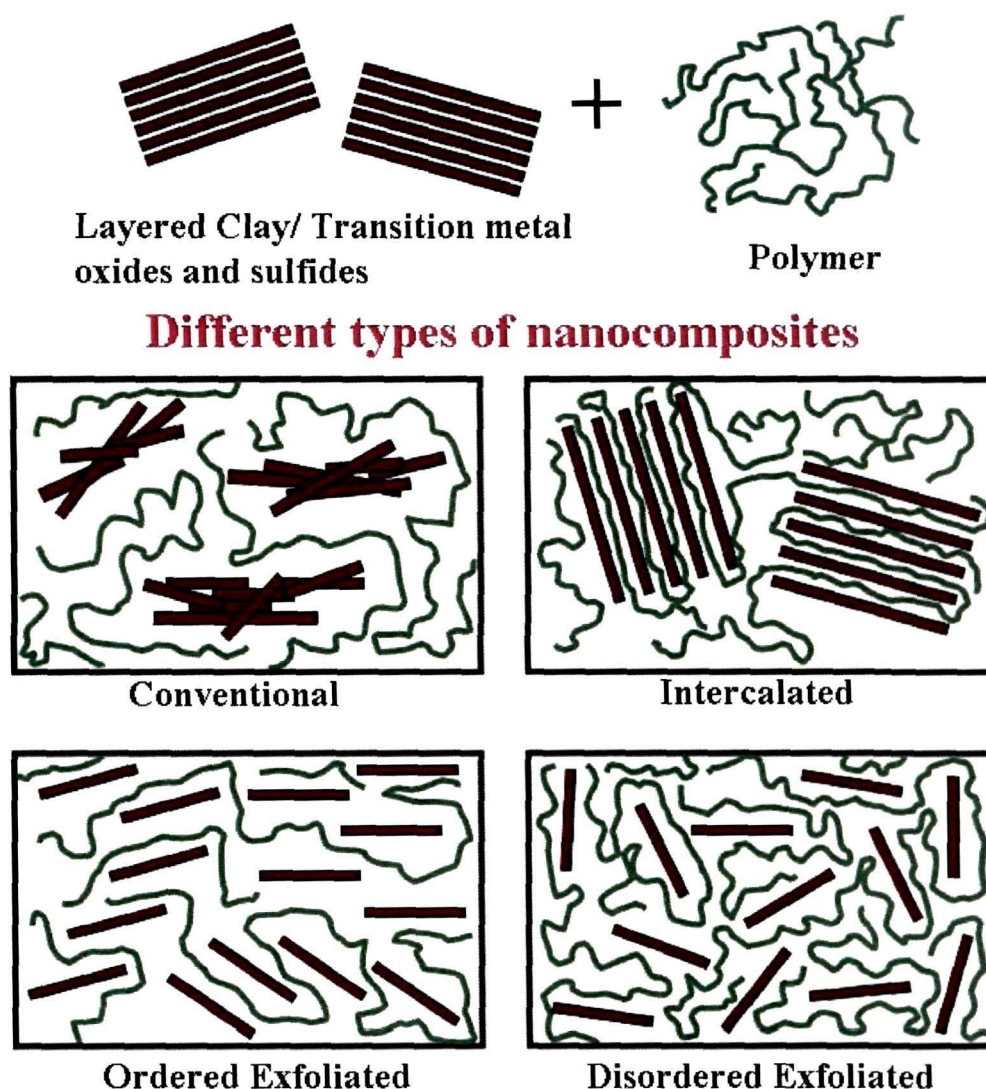


Figure 1.13: Schematic diagram of different types of layered organic-inorganic nanocomposites

In exfoliated nanocomposites, the polymer chains alternate with the inorganic layers in a fixed compositional ratio and have a well defined number of polymer layers in the intra-lamellar space. In an exfoliated structure, the layers of clay completely separate out and the individual layers are distributed throughout the organic matrix. The number of polymer chains between the layers is almost continuously variable and the layers stand $>100 \text{ \AA}$ apart and these nanocomposites are interesting for their superior mechanical properties. Okada *et al.* prepared new molecular scale nanocomposites from saturated polymers (Nylon-6 and other plastic) exfoliated in clay layers [208]. These products show extraordinary mechanical strength compared to that expected by simple mixing of the individual components. Because of these enhanced properties, they find extensive applications in automobile, and furnishing industries. Exfoliated nanocomposites can again be divided into ordered and disordered exfoliated nanocomposites; the major difference being that the former can be detected by X-ray diffraction and the latter is X-ray amorphous.

Despite their relatively large molecular weights, electroactive polymers can play the role of intercalated guest molecules inserted within the van der Waals gaps of layered inorganic phases resulting in a special class of intercalative nanocomposites that are expected to have novel multifunctional properties useful for opto-electronic and electrochemical devices. Both polymer electrolytes and electronically conducting polymers have been used as the organic guests in clay based organic-in-inorganic hybrid nanocomposites. Recently, many related investigations have reported the use of polymer/clay nanocomposites in solid-state electrolytes, where the intercalated or exfoliated state of MMT plays an important role in ion conduction in these electrolytes [209, 210]. Several conducting and non-conducting organic polymers have successfully been inserted into highly oxidizing hosts via intercalation by the groups of Kanatzidis, Nazar, Buttry, and Gomez-Romero *et al.* [211-214]. Conducting polymers viz., Poly (3, 4-ethylene dioxythiophene) has also been intercalated in different layered compounds such as V_2O_5 , VS_2 and MoO_3 [164, 215-217] and has been applied as electrodes for Lithium batteries.

1.2.2.3 Organic in Organic (O-O) nanocomposites

Organic-in-organic (O-O) nanocomposites form another class of nanocomposite materials in which an organic polymer having functionality acts as a guest material for another polymeric host with superior mechanical properties. Generally, insulating polymers having superior mechanical strength and processibility such as poly (methyl methacrylate) [PMMA], polyvinyl alcohol (PVA) etc. are used as host materials [218, 219]. Conducting polymer nanofibers and nanotubes in both conducting and non-conducting forms have been extensively used as guest materials in these types of nanocomposites. Insulating polyaniline (PAni) nanofiber reinforced gel polymer electrolytes have been found to show better ionic conductivity than the pristine polymer electrolyte [220]. Carbon nanotube and nanofiber reinforced polymer composites have been extensively studied and the resulting nanocomposite has been found to have much better mechanical strength and stability with the added advantage of being conducting [221-225]. This class of nanocomposites can be extremely helpful for minimizing the processibility related problems associated with conducting polymers and hence can have potential applications in device fabrication.

1.3 Swift heavy ion (SHI) irradiation of conducting polymers

Ion beams have become an integral part of numerous surface processing schemes and in the modification of surface layers of solids [226, 227]. Swift heavy ion (SHI) irradiation causes exotic effects in different classes of materials which otherwise cannot be generated by any other means. Swift heavy ion irradiation has already been used as an efficient tool for enhancing the physico-chemical properties of conducting polymers such as conductivity, electrochemical stability, sensing properties etc. [228, 229]. The primary phenomena associated with the interaction of ion beam and polymers are cross-linking, chain scission and emission of atoms, molecules and molecular fragments [230, 231].

An important parameter used to characterize the energy transfer from ion to the target is the energy loss dE/dx (eV/Å), defined as the energy deposition per unit length along the ion track. The value of dE/dx varies with varying ion

energies. When an energetic ion interacts with a polymer, depending upon its energy, it can lose its energy in two main processes viz., by interacting with the target nuclei (Nuclear Energy Loss) and by interacting with target electrons (Electronic Energy Loss), which are discussed in the following sub-sections.

1.3.1 Nuclear energy loss

Nuclear energy loss (S_n) arises from collisions between the energetic ion and the target nuclei, which causes atomic displacements and phonons [232]. When the colliding particle imparts energy greater than certain displacement threshold energy (E_d) to a target atom it can displace. E_d is the energy that a recoil atom requires to overcome the binding forces and to move a distance more than the atomic spacing away from its original site. Since the nuclear collision occurs between two atoms with electrons around their nuclei, the interaction of an ion with a target nucleus is treated as the scattering of two screened particles. The incident ion primarily undergoes nuclear energy loss (S_n) at low energies ($\sim 1\text{KeV/nucleon}$) [233]. The nuclear energy becomes important when an ion slows down to approximately the Bohr radius (orbital electron velocity, 2.2×10^6 m/s). Therefore, the maximum nuclear energy loss occurs near the end of the ion track for high energy ions. Nuclear energy loss is derived with the consideration of momentum transfer from the incident ion to the target atom and the inter-atomic potential between them.

1.3.2 Electronic energy loss

Electronic energy loss (S_e) arises from the electromagnetic interaction between the positively charged ion and the target electrons. Electronic energy loss can be explained by primarily two mechanisms: one mechanism is called glancing collision (inelastic scattering, distant resonant collisions with small momentum transfer) and the other is known as knock-on collision (elastic scattering, close collisions with large momentum transfer) [232]. Both glancing and knock-on collisions transfer energy in two ways: electronic excitation and ionization. At high energies (≥ 100 KeV/nucleon) the incident ion primarily undergoes electronic energy loss $(dE/dx)_e$, and if the films are sufficiently thin compared to

the stopping range of the ion, the electronic energy loss is reasonably uniform throughout the film thickness [233].

1.3.3 Latent tracks

On their way through matter, energetic ions lose energy and induce a continuous trail of excited and ionized target atoms. Due to their highly charged state, associated with a high energy transfer, heavy ions are especially suited to create cylindrical zones of irreversible chemical and structural changes. These zones have a diameter of only a few nanometers and are known as latent tracks. Formation of tracks in polymers can be explained on the assumption that particles lose energy during its passage through the matter in two ways: (i) along the trajectory, the energy yield being large, all chemical bonds are broken and (ii) in the neighboring of the trajectory, only the bonds between the monomer units are broken [232, 233].

1.4 Conducting polymers for biomedical applications

Research on conducting polymers for biomedical applications intensified greatly with the discovery that these materials are compatible with many biological molecules such as those used in biosensors in the 1980s. By the mid-1990s conducting polymers were also shown to modulate cellular activities, including cell adhesion, migration, DNA synthesis and protein secretion via electrical stimulation [234-237]. Recently, conducting polymers are also being considered for a range of biomedical applications, including the development of artificial muscles [238], controlled drug release [239] and the stimulation of nerve regeneration [240]. Low cytotoxicity and good biocompatibility of these materials are also evident from the growth of cells on conducting polymers and from the low degree of inflammation seen in test animals over a period of several weeks [241]. Electrochemical actuators using conducting polymers have been developed by several investigators [238, 242-244]. Actuation properties of conducting polymers have been used to release drugs from reservoirs covered by thin PPy bi-layer flaps upon application of a small potential to the PPy [245]. Actuator devices based on conducting polymers have great potential as actuators for many biomedical applications, such as steerable catheters for minimally invasive

surgery [246], micropumps and valves for labs-on-a-chip [247, 248], blood vessel connectors and microvalves for urinary incontinence [249]. With respect to drug delivery applications, electrical stimulation of CPs has been used to release a number of therapeutic proteins and drugs such as NGF [249], dexamethasone [250, 251] and heparin [252]. Treatment of the inflammatory response of neural prosthetic devices in the central and peripheral nervous systems requires precise and controlled local release of anti-inflammatory drugs at desired points in time [251], which can be obtained using specially designed conducting polymers nanostructures. Martin and his group demonstrated that individual drugs and bioactive molecules can be released from polypyrrole and PEDOT nanotubes at desired points in time by using electrical stimulation [251]. Conducting polymers such as polypyrrole and polyaniline have been extensively investigated for tissue engineering applications [249, 253]. Conducting polymers augmented with biological moieties have also been considered to offer advantages for neural probe applications [249, 254, 255]. There have also been some investigations regarding the antioxidant activity of conducting polymers especially polyaniline (PAni) and polypyrrole (PPy) [256, 257].

1.5 Sensors based on conducting polymers

Sensors are very important devices in industry for quantity control and online control of different processes. In order to measure parameters such as temperature, pressure, vacuum, flow etc. physical sensors were used. However, in some special cases such as the detection of evolution of hazardous gases during industrial processes which are very harmful for the environment, chemical sensors are required. Chemical sensors based on metal-oxides have, therefore, been synthesized for detection of various toxic gases produced during industrial processes that destruct the environment [258]. However, the metal-oxide sensors suffer from a major drawback in spite of being selective. Sensors based on metal-oxides generally operate at very high temperature, which is not desired for detecting hazardous chemicals evolving from industrial processes [259]. In order to overcome this problem the active layer of sensors have been replaced by conducting polymers viz., polypyrrole (PPy), polyaniline (PAni), polythiophene (PTh) and their derivatives since early 1980s [260]. Conducting polymers are

redox active materials and when doped these materials exhibit changes in their colour, volume, mass, conductivity, ion permeability and mechanical strength [126]. Detecting the variations in any one of these physical properties indirectly allows the detection of the analyte responsible for provoking the physical change in the conducting polymer. As compared to the commercially available metal-oxide sensors, conducting polymer based sensors have many improved characteristics such as high sensitivities and short response times at room temperature. Another advantage of sensors based on conducting polymers is that they can easily be synthesized by chemical or electrochemical processes, and their molecular chain structure can be modified conveniently by copolymerization or structural derivations [259]. Conducting polymers also have good mechanical properties, which permit simplistic manufacture of sensors [259]. As a result, enormous interest has grown amid the scientific community intended for sensors fabricated from conducting polymers. In the following sub-sections we discuss briefly about chemical and biosensors based on conducting polymers. A description of the different types of configurations and sensing principles used for conducting polymer based sensors has also been presented.

1.5.1 Chemical sensors

Chemical sensors based on conducting polymers have attracted tremendous interest in the scientific community primarily because of the fact that they can be easily fabricated and can operate at room temperature. Chemical sensors based on conducting polymers have been used to detect several types of chemicals either in gaseous form or even in liquid form at room temperatures [261-268]. Several synthesis techniques have also been adopted for fabricating conducting polymer based chemical sensors that include spin-coating, dip-coating, drop-coating, solution casting and Langmuir-Blodgett techniques [259]. Although the chemical sensors based on conducting polymers exhibit very high sensitivity and fast response time they suffer from very poor selectivity [269]. The selectivity of chemical sensors can be, however, improved by several methods. One such method is the use of ion selective membranes as a layer over the conducting polymer sensors [270]. The ion selective membrane allows only a specific analyte to interact with the conducting polymer and produce detectable

change in its physico-chemical properties. Another alternative is using conducting polymer based biosensors in which a reactant specific biomolecule is immobilized in the polymer matrix. Details of biosensors based on conducting polymers have been discussed in the next section.

1.5.2 *Biosensors*

The first biosensing device was created by integrating an enzyme into an electrode [271]; since then, there has been a lot of progress in monitoring and diagnosing biologically important metabolites such as glucose, hormones, neurotransmitters, antibodies and antigens for clinical purposes. Biosensors represent a new trend budding in the clinical diagnostic technology. A biosensor is a device that comprises of a biological sensing element either intimately connected to or integrated within a transducer [249, 272]. The sensing element interacts with the analyte of interest producing a chemical signal that is transmitted to the transducer, which ultimately transforms the input into an electrical signal. Enzymes, tissues, bacteria, yeast, antibodies/antigens, liposomes, organelle etc. are some of the biocomponents that have been used as biochemical transducers [234, 272, 273]. These recognition biomolecules incorporated within a biosensor possess tremendous specificity towards a particular analyte but have some severe problems regarding their stability. These biomolecules are extremely vulnerable to extreme conditions such as temperature, pH and ionic strength and generally have short lifetime in solution [274]. This led to the development of the concept of immobilization of these biomolecules in a suitable matrix; however, immobilization of biomolecules against the environmental conditions results in decreased enzyme activity [275, 276]. The activity of immobilized molecules not only depends upon the surface area, porosity and hydrophilic character of immobilizing matrix but also upon the reaction conditions and methodology chosen for immobilization [272].

Conducting polymers have been extensively used as transducers that integrate the signals produced by biological sensing elements such as enzymes. Biosensors based on conducting polymers viz., polypyrrole (PPy), polyaniline (PAni), polythiophene (PTh) have been extensively used for the estimation of metabolites such as glucose, urea, cholesterol etc. in blood that is of immense

importance in clinical diagnostics [234, 235, 277-284]. Depending on how the chemical signal is sensed and transmitted, biosensors can be divided into several categories: amperometric (measures current), potentiometric (measures potential), conductometric (measures change in conductivity), optical (measures light absorbance or emission), calorimetric (measures change in enthalpy), and piezoelectric (measures mechanical stress).

Conducting polymers offer many important features that make them potential candidates as electrodes for miniaturized biosensors. Firstly, electro-deposition of conducting polymer films can be utilized to localize a biologically active molecule of any geometry and size in the conducting polymer electrodes which is appropriate for the fabrication of multi-analyte micro-amperometric biosensors [285]. Secondly, the chemical structures of conducting polymers are flexible and the electronic and mechanical properties can be modified according to the requirements. In fact, the polymer itself can be modified to bind protein molecules [286]. Another advantage offered by conducting polymers is that electrochemical synthesis allows direct deposition of the polymer on the electrode surface, while simultaneously trapping the protein molecules [287]. Thus, the spatial distribution of the immobilized enzymes, the film thickness for the conducting polymer based electrodes can be modified and the enzyme activity can be modulated by changing the state of the polymer.

However, the most crucial problem associated with the manufacture of conducting polymer based biosensors is the stable immobilization of enzymes without compromising their activity [272]. As such several physical and chemical techniques have been adopted for the immobilization of enzymes in conducting polymer matrices. As compared to some of the conventional procedures used to immobilize enzymes viz., physical adsorption, entrapment, cross-linking and covalent binding in gels and membranes, electrochemical techniques have been preferred for immobilizing enzymes in conducting polymer matrices [272].

1.5.3 Sensor configuration and sensing principles

Sensors based upon conducting polymers may have different configurations and sensing principles. In this section we will briefly discuss about the most common types of configurations that are widely employed for

conducting polymer based sensors with a special emphasis on piezoelectric sensors based on conducting polymers, which forms a major part of the work carried out in the present thesis.

Conducting polymer based sensors have been used in different configurations but the principle of sensing an analyte by conducting polymers depends primarily upon the fact that these polymers are redox active and can exhibit significant variations in their physico-chemical properties during doping and de-doping processes. The main sensing principles of these types of sensors can be summarized as follows [259]:

- a) Redox reactions with the analytes.
- b) Partial charge transfer reaction with the analytes.
- c) Catalytic oxidation is also sometimes the mechanism if a catalyst is incorporated in the conducting polymer matrix.
- d) Acid/base reactions.
- e) Absorption of the analyte in the conducting polymer matrix can change the properties of the material and make the analyte detectable.
- f) Swelling of the conducting polymer upon physical interaction with the analytes can also change the properties of the polymer film and thereby changes the resistivity, mass etc. of the film.

Figs. 1.14 (a-e) depict the schematic configurations of different types of conducting polymer based sensors. The most common type of conducting polymer based sensors is the Chemiresistor, which are resistors with their electrical resistance sensitive to the chemical environment [288-290]. In chemiresistors contact is made between one or several pair of inter-digitated electrodes [291, 292] and the conducting polymer film used to sense the analyte. The change in the resistivity of the conducting polymer film upon exposure to different types of chemical or biochemical analytes is detected and the signal obtained is used to detect the analyte.

Organic thin-film transistors and diodes have also been applied in sensing field [293, 294]. In general, a thin-film transistors (TFTs) based upon conducting polymers consist of a active layer of the polymer in contact with two electrodes ("source" and "drain"), and a third electrode ("gate") which is separated with the

active layer by an insulating film. The analyte can be sensed by detecting the variations in the source-drain current of the device. Diodes fabricated using conducting polymers are also often used in sensing applications [295]. Exposing the conducting polymer diodes to chemical species capable of changing the doping level of the conducting polymer leads to remarkable variations in its effective barrier height, current density and rectification ratio. Thus in comparison with chemiresistors, transistors and diodes provide more parameters for measurements and hence are much more efficient as sensors.

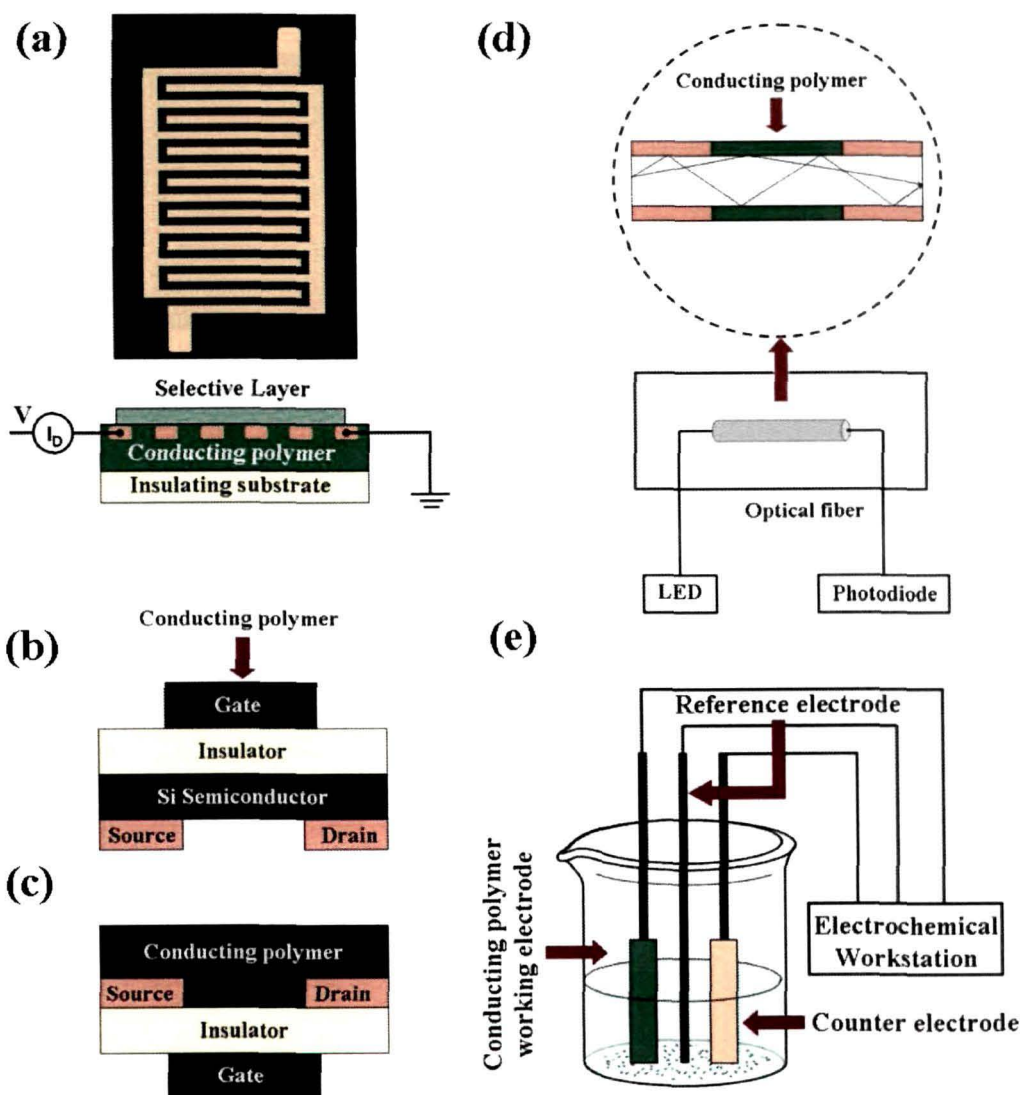


Figure 1.14: Schematic diagrams of some of the configurations of conducting polymer sensors (a) Inter-digitated chemiresistor, (b) Thin film transistors based on conducting polymers (c) IGFETs, (d) Fiber optic sensors and (e) electrochemical sensors based on conducting polymer electrodes.

Electronic configuration of conducting polymers can change upon doping by different chemical agents and can be easily detected by UV-Vis and NIR spectroscopy [296]. New absorption bands corresponding to the formation of polarons and bipolarons can be observed in the absorption spectra; whereas some existing bands might disappear during dedoping. Based upon this principle, optical sensors with conducting polymers as active layers have also been developed for sensing different chemical and biomolecules [297-299]. In some cases fiber optic cables have also been used for detection of analytes at long distances [300-302]. Surface-plasmon resonance (SPR) is another optical technology that has been sometimes applied for detection of chemicals in gaseous forms [303, 304]. In case of a SPR sensor, the minimum in the reflectance curve shifts upon exposure to the analyte, which indicates the existence of the analytes. Although the sensitivity of these types of sensors is high but the detecting procedures are complicated.

Electrochemical sensors using conducting polymer working electrodes have also been used for detection of chemical and biochemical analytes. Electrochemical sensors are devices that extract information about sample from measurement of some electrical parameter. It is easy to categorize them according to the measured electrical parameter, because the three are linked together by the Ohm's Law. In "potentiometric sensors", the potential difference is measured. If the parameter of interest is current, then "amperometric sensors" are used and if we measure resistance or conductance we talk about "conductometric sensors". For sensing gases using these type of sensors the general configuration is somewhat modified and a divided electrochemical cell is used with conducting polymer/metal/Nafion as the working electrode [305-307]. The supporting electrolyte usually is an inorganic acid to provide H⁺ ions for ionic conductance in Nafion film.

However, in the present thesis, we have employed piezoelectric sensors modified by conducting polymers to sense different analytes. The basic scientific principles of these types of sensors have been elaborated in the following section with a state of the art literature survey on the development of piezoelectric

sensors in general and conducting polymer modified piezoelectric sensors in particular.

1.5.3.1 Piezoelectric sensors

Piezoelectricity is a phenomenon exhibited by crystals which don't have a centre of symmetry. It is a phenomenon in which electric polarization (i.e. charge) is induced in the material upon the application of a stress. Conversely, it is the development of an induced strain that is directly proportional to an applied electric field. Different types of materials have been found to show the piezoelectric effect which includes crystals such as quartz and Rochelle salt, and ceramics such as barium titanate (BaTiO_3), PZT etc [308]. However, we will restrict our discussion to piezoelectric crystal sensors only as these types of sensors have been used in the present work.

A piezoelectric quartz crystal resonator is a precisely cut slab from a natural or synthetic crystal of quartz. Piezoelectric crystal sensors are passive solid-state electronic devices, which can respond to changes in temperature, pressure, and most importantly, to changes in physical properties at the interface between the device surface and a foreign fluid or solid. Such changes in physical properties include variations in interfacial mass density, elasticity, viscosity and layer thickness. The incorporation of various chemically sensitive layers has enabled the transition from the microbalance to the mass sensors and resulted in explosive growth in piezoelectric sensors in recent years. This type of sensor operates by observation of the propagation of an acoustic wave through the piezoelectric crystal. The variations in the acoustic wave propagation can be correlated to the amount of analyte captured at the surface that can be used to sense the analyte. The frequency and resonant resistance of the piezoelectric crystal under the influence of the analyte are measured [308]. However, these parameters are influenced by a large number of parameters as mentioned above. A selective sensor is obtained when a sensor surface is coated with selectively interacting thin film. Piezoelectric crystal sensors are generally available in two configurations: surface acoustic wave (SAW) and quartz crystal microbalance (QCMB) sensors.

1.5.3.1.1 SAW sensors

The standard design for a SAW sensor is shown schematically in Fig. 1.15 [308]. This configuration is usually repeated on the same piece of quartz. Hence, one side can be the reference and the other the sensing element. The second side is often coated with a polymer, or similar material, showing selectivity toward the analyte under investigation. The electrodes take the form of IDTs etched on the surface of the quartz by photolithography technique, out of which one is the transmitter IDT which transmits the surface acoustic wave (SAW) and the other is the receiver IDT that receives the signal. Since this device deals with the variation in surface acoustic waves the name SAW sensors have been given.

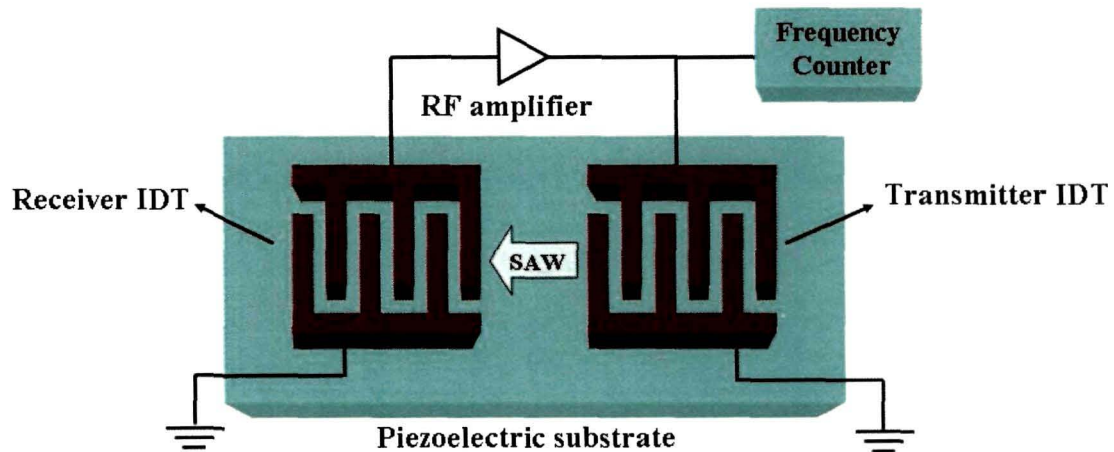


Figure 1.15: Configuration of a SAW sensor

An input radio frequency (RF) voltage is applied across the transmitter IDTs, which induce deformations in the piezoelectric substrate. These deformations give rise to a Rayleigh surface wave confined within one acoustic wavelength of the surface. The wave traverses the gap between the two arrays of IDTs and when it reaches the receiver IDTs, the mechanical energy of the wave is converted back into an output RF voltage. The input and output is connected via an RF amplifier and when the gain in the loop is greater than unity, the circuit oscillates. When a mass arising from a coating or gas is adsorbed on the surface, there is a shift in the SAW device resonant frequency. This phenomenon allows the SAW device to be used as a gas sensor as the frequency shift is proportional to the mass shift. Conducting polymers both in bulk and nanostructured forms have

been used as active layers of SAW sensors for sensing different analytes, which confers these types of sensors with sensitivity towards a specific analyte [309-311].

1.5.3.1.2 Quartz crystal microbalance sensors

A quartz crystal microbalance (QCM) consisting of a thin quartz disk with electrodes plated on it and one of its surface coated with a conducting polymer can be seen in Fig. 1.16 [259]. Internal mechanical stress is produced in a piezoelectric material upon the application of an external electrical potential. The oscillating electric potential applied to the QCM induces an acoustic wave that propagates through the crystal and meets minimum impedance when the thickness of the device is a multiple of a half wavelength of the acoustic wave. A QCM is a shear mode device in which the acoustic wave propagates in a direction perpendicular to the crystal surface [312].

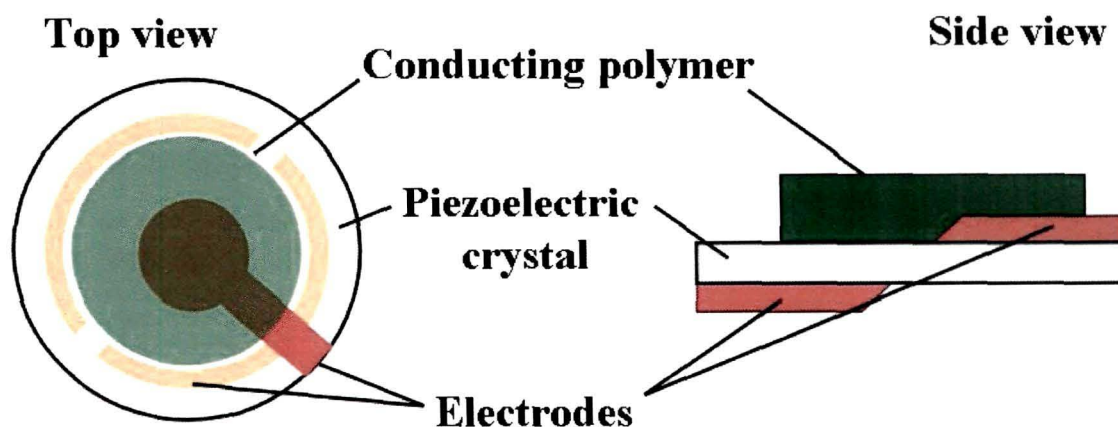


Figure 1.16: Configuration of a quartz crystal microbalance sensor device

Deposition of a thin film on the crystal surface decreases the frequency in proportion to the mass of the film. If the surface of the quartz crystal electrode is coated by a material capable of interacting with the environment of interest, a sensor sensitive to this component can be constructed. The performance characteristics of the QCM sensor such as selectivity, response time and reversibility depend on the chemical nature and physical properties of the coating material. The sensitivity of these types of sensors is very high and they can detect very low concentrations of analyte accurately, since a small change in mass of the quartz crystal brings about remarkable change in its frequency and resonant resistance. These types of sensors, once calibrated, can also be used not only to detect a particular analyte but also to detect the amount of analyte in terms of

mass change of the quartz crystal oscillator, since this type of device can also act like a microbalance. Quartz crystals, coated with different coatings including conducting polymers viz., polypyrrole (PPy), polyaniline (PAni) and their composites, have been used for determination of various compounds [313-322].

1.6 Scope of the thesis and statement of the thesis problem

Conducting polymers are recently being considered for different biomedical applications such as artificial muscles, drug delivery, stimulation of nerve regeneration, tissue engineering etc. Conducting polymers have been found to be potential antioxidants. They have also attracted applications as competent sensing material for various organic vapours, hazardous gases, humidity and warfare stimulants due to their applicability at room temperature. Conducting polymer based nanostructured materials offer the advantages of low dimensionality and enhanced surface to volume ratio that makes them promising materials in biomedical applications and also as sensors. Polymers are highly radiation sensitive materials and irradiation can cause useful modifications in the polymer which cannot be achieved by other means. Irradiation can lead to several interesting physico-chemical modifications in conducting polymer nanostructures leading to the enhancement in their performance.

Considering the above mentioned critical review, the present work aspires to achieve a deeper insight into the synthesis and physicochemical properties of conducting polymer based nanostructured materials. Although swift heavy ion (SHI) irradiation has been used as a tool to tune the properties of conducting polymers, the effects of SHI irradiation upon conducting polymer based nanostructured materials have not been properly elucidated. One of the prime focuses of the present work is the detailed investigation of the effects of SHI irradiation upon the structural, morphological, conformational, optical and charge transport properties of the conducting polymer based nanostructured materials. The present work also emphasizes on the application potential of these nanostructured materials in the field of biomedical science as biocompatible

antioxidants and in the field of chemical sensors as sensitive active layers for quartz crystal microbalance sensors.

In order to fulfill the aforesaid objectives the following systems have been chosen for investigation in the present work:

- Polyaniline (PAni) nanofibers synthesized using interfacial polymerization technique have been chosen because of ease in synthesis, processibility, environmental stability and the unique and exciting properties that polyaniline (PAni) offers as a conducting polymer.
- Another system investigated in the present work viz., PAni nanofiber reinforced PVA nanocomposites have been synthesized by *in-situ* rapid mixing polymerization technique that has been developed with a view to apply these materials in sensing applications.

The above mentioned material systems have been irradiated with 90 MeV O^{7+} ions using the 15 UD Pelletron accelerator installed at Inter University Accelerator Centre (IUAC), New Delhi. The materials have been irradiated at normal beam incidence and at different fluences viz., 3×10^{10} , 3×10^{11} and 1×10^{12} ions/cm² with a view to investigate the fluence dependent variations in the physico-chemical properties of the above mentioned materials.

Both the pristine and SHI irradiated materials have been investigated using sophisticated analytical tools. Electron microscopy has been used to study the morphology and structural details of the nanostructured materials. X-ray diffraction studies have been carried out to investigate the degree of crystallinity, domain length and strain in the nanostructured materials. The conformational variations in the materials have been studied using vibrational spectroscopy employing Micro-Raman (μR) and Fourier Transform Infrared (FT-IR) spectroscopy. UV-Visible spectroscopy has been used to study the optical properties of the pristine and irradiated samples. Dielectric spectroscopy and ac conductivity studies have been carried out with a view to study the relaxation processes and charge transport mechanisms of the samples.

The antioxidant activity and biocompatibility of polyaniline (PAni) nanofibers have been investigated using specific biochemical assays. Swift heavy ion irradiation effects on the antioxidant activity and biocompatibility of these

materials have also been studied. Quartz crystal microbalance coated with PANi nanofiber reinforced PVA nanocomposites have been fabricated for sensing analytes viz., free radicals and hydrochloric acid in solution. Different parameters associated with these sensors viz., sensitivity, response time and linearity have also been studied in the present work.

Chapter 2

THEORETICAL ASPECTS

This chapter deals with the mechanisms of formation of polyaniline by chemical oxidative polymerization and polyaniline nanofibers by interfacial and rapid mixing polymerization techniques. The chapter also presents an overview of the framework developed to account for the electronic conduction in conducting polymers. This is followed by the latest developments regarding the charge transport mechanisms in conducting polymer based nanostructured materials. Dielectric relaxation in amorphous materials and theoretical models developed for understanding ion-solid interactions have also been discussed briefly in this chapter.

2.1 Chemical polymerization

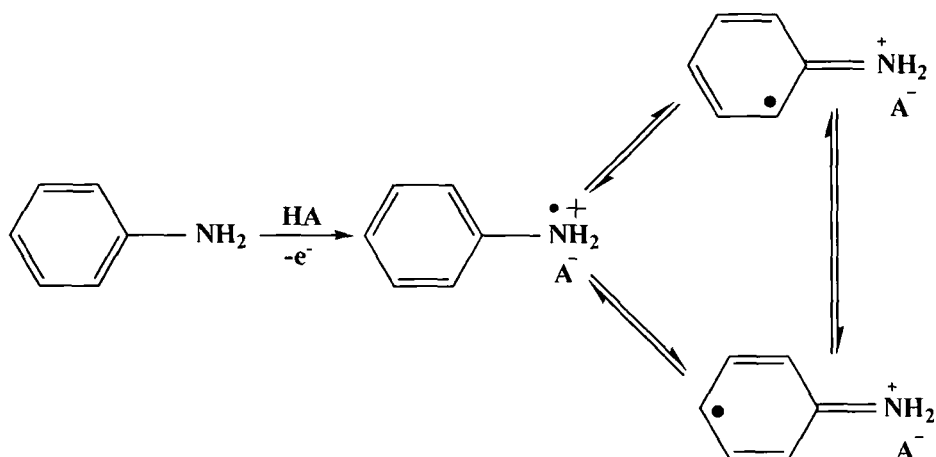
Chemical polymerization has been the most widely used technique for the synthesis of polyaniline in bulk quantities. In the chemical polymerization technique, ammonium persulfate, $(\text{NH}_4)_2\text{S}_2\text{O}_8$, is generally used as the oxidant because of its high oxidizing power. This leads to the incorporation of HSO_4^- / SO_4^{2-} as the dopant anions (A^-) in the product. However, other oxidizing agents like FeCl_3 etc. have also been employed as the chemical oxidant.

2.1.1 Chemical polymerization of polyaniline

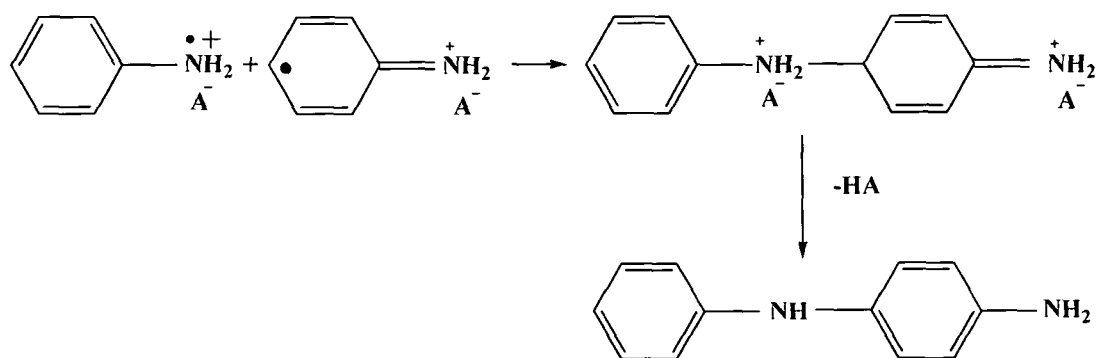
Chemical polymerization of aniline is usually performed in acidic conditions ($\text{pH} < 3$). Aniline is normally insoluble in water but in acidic medium aniline is converted into anilinium ions that are easily soluble in water. The progression of polymerization reaction in the acidic medium also ensures that undesired branched products are not formed in the final product [323]. An oxidant to monomer ratio of less than 1:2 is generally employed primarily because of the fact that $\text{S}_2\text{O}_8^{2-}$ anion is a two-electron oxidizer (acceptor) and as such during polymerization each aniline monomer loses two electrons.

Fig. 2.1 shows a schematic diagram describing the mechanism of formation of polyaniline (PAni) by the chemical polymerization of aniline in the presence of ammonium peroxydisulphate $[(\text{NH}_4)_2\text{S}_2\text{O}_8]$ as the oxidant [126]. The chemical polymerization of aniline upon oxidation by $(\text{NH}_4)_2\text{S}_2\text{O}_8$ proceeds by the formation of *N*- and *para*-radical cations of aniline as can be seen from the step I in Fig. 2.1. This step in which radical cations are formed is the rate determining step. In the second step, the *N*- and *para*-radical cations of aniline couple with each other. Subsequently, re-aromatization of the dication of *p*-aminodiphenylamine (PADPA) takes place. It is then further oxidized to the di-radical di-cation. Coupling predominantly occurs in the "head to tail" configuration i.e., from *N* to *para*. However, some coupling between ortho and *para* positions are also observed, which are responsible for conjugation defects [126].

Step I: Formation of aniline radical cations by oxidation



Step II: Radical Coupling



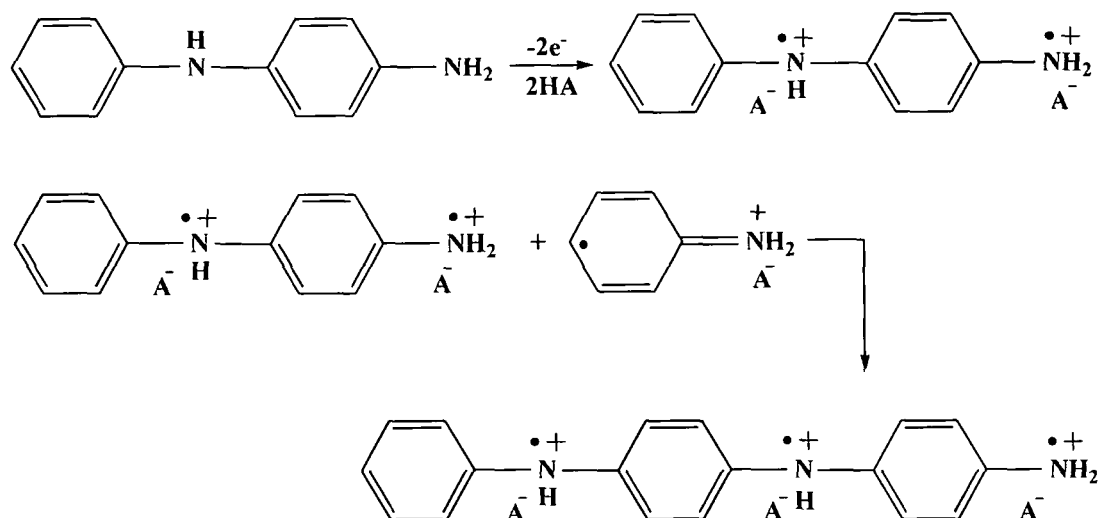
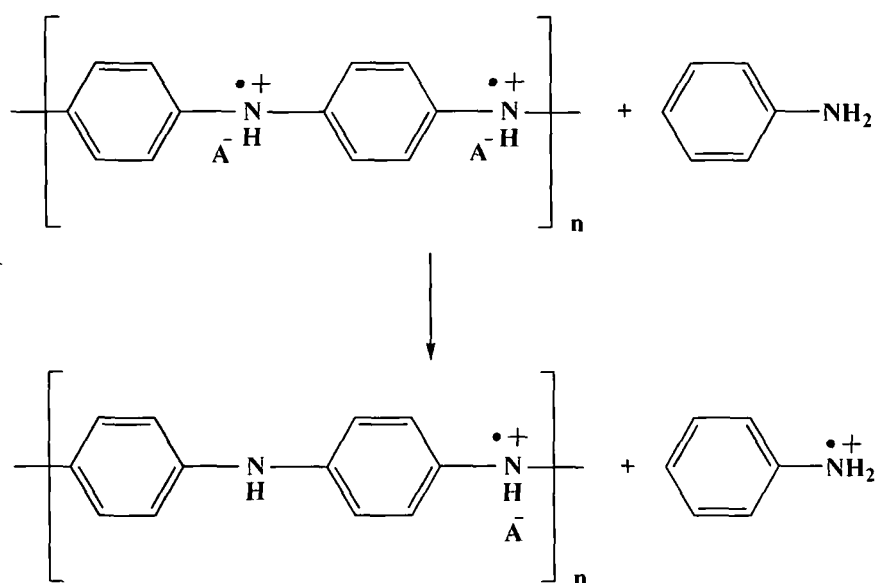
Step III: Chain propagation**Step IV: Reduction of Pernigraniline salt to Emeraldine salt**

Figure 2.1: Scheme illustrating the various steps (Step I to Step IV) in the Chemical polymerization of polyaniline

Chemical polymerization varies significantly from electropolymerization mainly in the subsequent steps (steps III and IV): chain propagation and product formation steps (Fig. 2.1). It has been confirmed from spectroscopic studies, that the initial polymer product is the fully oxidized pernigraniline salt form of polyaniline [126]. When all oxidant molecules in the reaction are used up, the remaining aniline in solution reduces the pernigraniline to the green emeraldine

salt (Step IV). A systematic change in the colour of the solution can be clearly observed during the chemical polymerization of aniline, which reflects the described steps. During the second step, due to the formation of *p*-aminodiphenylamine, a pink coloured solution is observed which changes into deep blue due to the formation of protonated pernigraniline in the third step. In the final step green emeraldine salt precipitates out that also marks the completion of the polymerization reaction.

2.1.2 Mechanism of polyaniline nanofiber formation

Chemical oxidative polymerization of aniline in an acidic medium in the presence of ammonium peroxydisulfate as an oxidant yields particulates of PANi of irregular shapes. In recent years, the one-dimensional nanofiber form of polyaniline (PANi) has attracted tremendous interest from the scientific community because of being a highly processible low dimensional organic semiconductor. Likewise, several synthesis techniques have been adopted by scientists around the world to develop a method for the direct conversion of aniline into polyaniline (PANi) nanofibers [155, 324-328]. It is, however, interesting to note that although the basic phenomenology of these synthesis techniques are quite different in their origin, PANi nanofibers obtained by each of these techniques have a striking similarity in their morphology in spite of having different diameters. This is an indication of the fact that there is a common underlying mechanism behind the formation of PANi nanofibers that may depend upon several factors governing the synthesis procedure.

In the urge for finding the mechanism of PANi nanofiber formation, several important factors for the direct conversion of aniline into PANi nanofibers have been identified. One of the most important factors which determine PANi nanofiber formation from aniline is the induction time [329]. The induction time for chemical oxidative polymerization of aniline using ammonium peroxydisulfate as oxidant in an acidic medium varies from a few minutes to hours depending upon concentration, temperature etc. The products formed are granular polyaniline powders having very little nanoscale morphology. However, it is possible to transform the structure from granules to nanofibers by altering the synthetic conditions during the induction period [329]. It has been observed that

by allowing the reaction to proceed at the interface of an aqueous/organic biphasic system or by adding a small amount of nanofibers (seeds) of known composition during the polymerization yields PANi nanofibers [324, 325]. PANi nanofibers have also been obtained by addition of oligomers of aniline or even by diluting the reaction mixture by a factor of 20 [326-328]. Another important factor is the secondary overgrowth of polyaniline in the nanofiber scaffolds. Kaner and his group observed that at the initial stages of the chemical oxidative polymerization of aniline, nanofibers are formed; however, the final product yields irregularly shaped particulates due to secondary growth [329]. Accordingly, they suggested that it is by controlling the secondary overgrowth that PANi nanofibers can be obtained and thereby presented the idea of interfacial and rapid mixing polymerization techniques for the synthesis of PANi nanofibers [330]. It has also been suggested that the presence of a surface such as walls of the reaction vessel, magnetic stirrer beads can also play an important role in the formation of PANi nanofibers [331, 332]. Although, all of these factors are very important for the synthesis of PANi nanofibers but they don't really give the idea of a common underlying mechanism for PANi nanofiber formation.

The first step in this direction was taken by Manohar *et al.* [332] who proposed a possible mechanism that can be applied for explaining the direct formation of PANi nanofibers from aniline regardless of the technique employed for synthesis and termed it a double heterogeneous nucleation process. Fig. 2.2 depicts that PANi nanofiber formation proceeds by a double heterogeneous nucleation process suggested by Manohar *et al.* [332]. According to this mechanism the formation of aniline dimer on surfaces plays a key role in the formation of PANi nanofiber and that nanofibers are formed by a double heterogeneous nucleation process. If the surface conditions prefer the formation of tetramer nanofibers, i.e., favour high concentration of aniline dimer, directional polymer growth leading to the formation of PANi nanofibers occurs. As shown in Fig. 2.2, a fully oxidized form of aniline dimer can couple with a fully reduced form to yield aniline tetramer. The outer surface of an aniline dimer aggregate (or added insoluble aniline dimer) is oxidized first since it is in contact with the oxidant in solution. Then redox coupling takes place with reduced (unreacted)

dimer present in the interior of the aggregate, and the resulting heat of the reaction brings out fresh unreacted aniline dimer for further reaction with oxidant in solution. Once formed, however, these nanofibers would seed fresh polymer growth on their surface, resulting in bulk nanofibers.

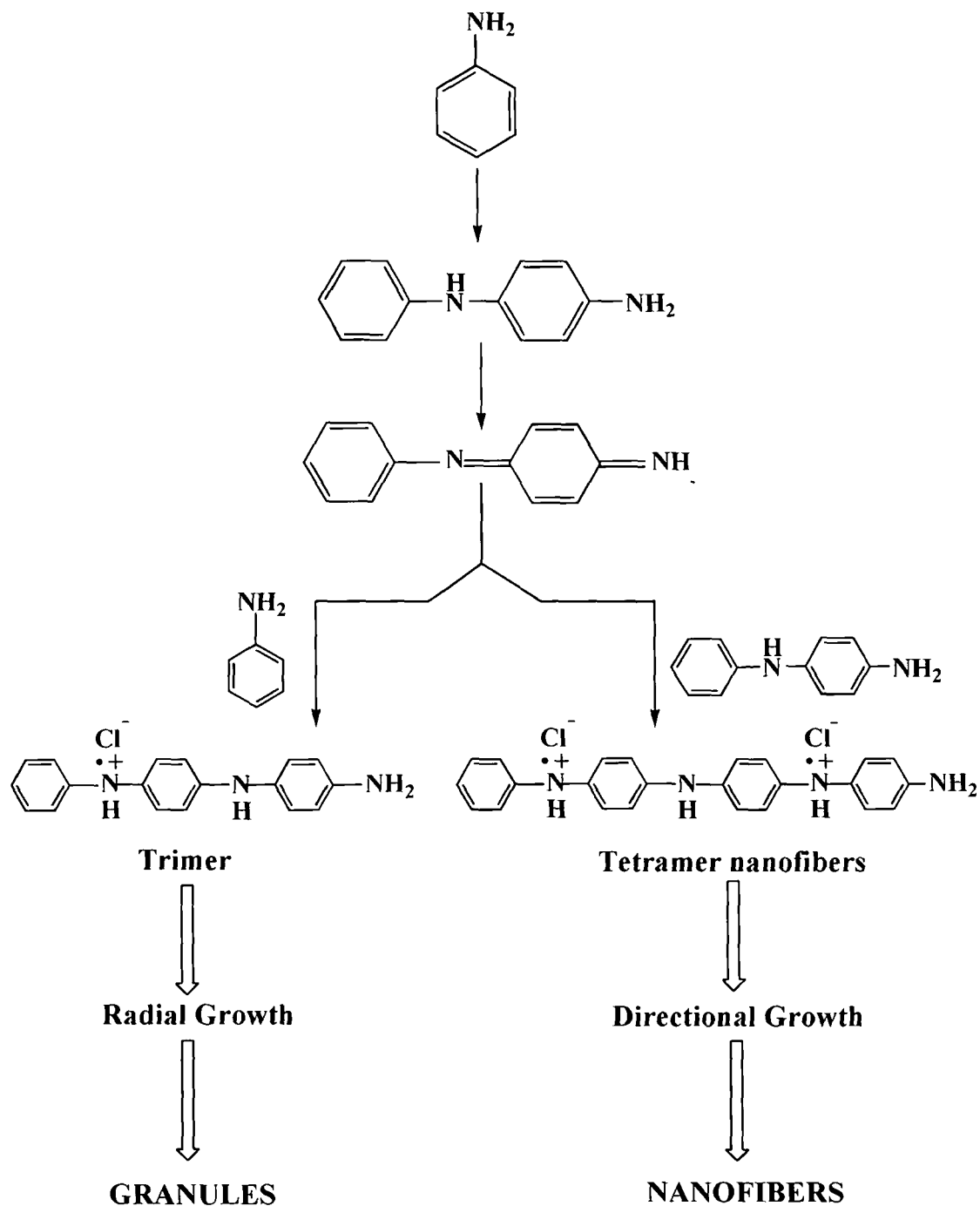


Figure 2.2: Double heterogeneous nucleation mechanism of PANi nanofiber formation according to Manohar and group (Ref [332]).

Granules, on the other hand, are formed by the trimer pathway shown in Fig. 2.2 when aniline dimer reacts non-directionally with aniline monomer in the

solution. This occurs when the surface concentration of aniline dimer is low or if there is no surface available for aniline dimer deposition. The first nucleation takes place on existing surfaces yielding nascent nanofibers and a second on the surface of these nascent nanofibers in which the morphology is rapidly transcribed across multiple length scales to the bulk precipitate of PANi nanofibers.

2.2 Electronic conduction mechanism in disordered materials

Electronic conduction mechanism in disordered material systems such as conducting polymers has been a topic of wide research interests among the scientific community. As pointed out in section 1.1.2.3 of Chapter 1, the two-fold coordination in conjugated polymers make these materials susceptible to structural distortion and in the doped state the most dominant excitations viz., solitons, polarons and bipolarons are inherently coupled to the chain distortions [98, 99]. As a result, the theories explaining non-intrinsic charge transport mechanisms in conducting polymer are dominated by thermally activated hopping (or tunneling processes) in which the charge carriers viz., solitons, polarons or bipolarons hop across (or tunnel through) barriers created by the presence of isolated states or domains [83, 101-105, 110-114]. In this section, the primary features of some of the theoretical models developed and followed to explain the charge transport mechanism in conducting polymers have been highlighted.

Polyacetylene was the first material to have been recognized as conducting polymer and as such transport properties of polyacetylene was investigated by many research groups [333-337]. In case of a single polyacetylene, the elementary excitations are solitons rather than electron-hole pairs as in 3D metals [338]. It was a soliton model proposed for polyacetylene by Su, Schrieffer and Heeger (SSH) that is by far the most successful theoretical model for polyacetylene $(CH)_x$ [333]. According to this model, undoped polyacetylene is a semiconductor due to a commensurate Peierls distortion which doubles the unit cell (dimerization) and opens a band gap at the Fermi level. The soliton is the boundary between the two

different senses of dimerization. Each soliton is associated with a localized mid-gap electronic state. One possible conduction mechanism involves the thermal liberation of bound charges solitons followed by free charged soliton conduction. Such a mechanism leads to a simply activated conductivity [Eq. 2.1] similar to those found in doped semiconductors at low impurity concentrations.

$$\sigma = \sigma_0 \exp\left(-\frac{E_b}{k_B T}\right) \quad (2.1)$$

However, the SSH model is purely one-dimensional. In order to generalize this model in three dimensions Kivelson proposed the intersoliton model [110, 339]. He suggested that motion of a simple soliton discontinuity along a polymer chain does not lead to charge transport, but an inter-chain soliton hopping mechanism contributes to the conduction with conductivity varying as a high power of temperature [339].

Various hopping and tunneling models have also been suggested to account for the non-intrinsic transport mechanisms in conducting polymers. The variable range hopping model proposed by Mott has been found to be the most appropriate to describe charge transport in conducting polymers [112]. The term variable range hopping signifies the fact that the average hopping distance in case of conducting polymers is temperature dependent. The overall conductivity according to the variable range hopping model can be written as:

$$\sigma(T) = \sigma_0 \exp\left[-\left(\frac{T_0}{T}\right)^\gamma\right] \quad (2.2)$$

where γ depends on the dimensionality, d , of the hopping process:

$$\gamma = \frac{1}{1+d} \quad (2.3)$$

For hopping in three dimensions ($d=3$), the exponent has the value of $\gamma = 1/4$. For two dimensional (2D) hopping ($d=2$), $\gamma = 1/3$ and for one-dimensional (1D) hopping ($d=1$), $\gamma = 1/2$.

However, in the variable range hopping model proposed by Mott, the electron-electron interactions were not considered. Efros and Shlovskii pointed out that the Coulomb interaction between localized electrons creates a soft gap known as the "Coulomb gap" in the density of states near the vicinity of the Fermi

level [340]. This assumption leads to a situation where the conductivity is found to be proportional to $T^{-1/2}$ regardless of the dimensionality of the hopping process.

$$\sigma \propto \exp\left[-\left(\frac{T_{ES}}{T}\right)^{1/2}\right] \quad (2.4)$$

In all the three dimensions the term T_{ES} is given by the Eq. 2.5,

$$T_{ES} = \frac{\beta e^2}{\kappa k_B \xi} \quad (2.5)$$

where κ is a macroscopic dielectric constant, β is a numerical constant of the order of unity (for 3D, $\beta = 2.8$) and ξ is the localization length.

If $k_B \gg \Delta$, where $\Delta = (e^3 g_0^{1/2})/\kappa^{3/2}$ is the Coulomb gap (g_0 being the unperturbed density of states), the Coulomb effect becomes negligible and a cross-over from the Efros-Shklovskii (ES) to the Mott VRH hopping is observed. In case of 3D systems the ES-Mott cross-over temperature can be written as:

$$T_{cross} = \frac{16T_{ES}^2}{T_M} = \frac{5.9e^4 g_0 \xi}{\kappa^2 k_B} \quad (2.6)$$

where T_M is the Mott temperature.

The model of variable range hopping has also been modified to account for the dependency of conductivity on the conjugation length and chain structure of polymers. This model of anisotropic variable-range hopping [24, 341] assumes that the wave-function of the hopping site is not spherically symmetric but rather ellipsoidal. The short axis of the ellipsoid is in the order of magnitude of the distance between neighbouring chains and the long axis is proportional to the conjugation length. In the presence of conjugated strands the localization length is apparently given by

$$\alpha^{-1} = m l_{conj} + \alpha_0^{-1} \quad (2.7)$$

where α_0^{-1} is the localization length in the absence of conjugation strands and m represents the number strands, along which the charge carriers 'get a free ride'. Evidently, $m = \alpha_0^{-1}/l_{barrier}$ is large enough and as such the second term in Eq. 2.7 can be neglected and the localisation length in the chain direction becomes

proportional to the conjugation length. In Mott's VRH, the parameter T_0 from Eq. 2.2 is related to the localization length *via*

$$T_0 \propto \alpha^3 / n(E_F) \quad (2.8)$$

where $n(E_F)$ is the density of (localized) states near the Fermi level which participate in the hopping process. For anisotropic variable-range hopping Eq. 2.8 changes to

$$T_0 \propto \alpha_{\perp}^2 \alpha_{\parallel} / n(E_F) \quad (2.9)$$

and with $\alpha_{\parallel} \propto l_{conj}^{-1}$ from Eq. 2.7, Eq. 2.9 becomes

$$T_0 \propto \alpha_{\perp}^2 l_{conj}^{-1} / n(E_F) \quad (2.10)$$

Inserting the value of T_0 from Eq. 2.10 in Eq. 2.2, we get

$$\sigma = \sigma_0 \exp \left[- \left(\frac{T l_{conj}^{-1} n(E_F)}{\alpha_{\perp}^2} \right)^{-\gamma} \right] \quad (2.11)$$

And for $\gamma = 1/2$ (dominance of hops in chain direction), we obtain;

$$\ln \sigma \propto -(l_{conj})^{-1/2} \quad (2.12)$$

More recently, it has been emphasized by Epstein and co-workers [342, 343] that quasi-1D hopping plays a key role in conducting polymers where polymer chains traverse disordered regions to connect 'crystalline islands'. Charge carriers diffuse along such electrically isolated disordered chains as part of the conduction path, but would readily localize owing to the 1D nature of the chains. In such a case, quasi-1D variable-range hopping along the disordered chains with $\gamma = 1/2$ dominates the overall resistance of the polymer. In another hopping model Li and co-workers proposed that conductivity results from anisotropic three dimensional hopping in the network of metallic rods [344].

B. Souillard and his co-workers [345] presented a new mechanism which induces a thermally activated hopping conductivity law where the parameter γ equal to $3/7$ without Coulomb interactions. Considering Anderson strong localization, they obtained the hopping conductivity for a system, where the electrons at the Fermi level exhibit superlocalization and predicted the conductivity relation as follows

$$\sigma(T) \approx \exp \left[- \left(\frac{T_0}{T} \right)^{\frac{\xi}{D+\xi}} \right] \quad (2.13)$$

where ξ denotes the super-localization exponent and D the fractal dimensionality. This variable-range hopping law is very different from the famous Mott's law in 3D with $\gamma = 1/4$. In contrast it yields a result not very far from the exponent $1/2$ predicted by Efros and Shklovskii [340] in the case of Coulomb interactions. No Coulomb interaction is considered in this model so that this hopping law holds for system with very weak electron-electron interactions.

Like the hopping models, several models have also been developed which consider tunneling to be the major charge transport mechanism in conducting polymers. At low temperatures, conductivity in conducting polymers cannot be associated with hopping mechanisms since at low temperatures there are no phonons to assist the hopping process. As such in highly doped samples tunneling between conducting particles is assumed instead of (or in addition to) phonon-assisted tunneling. Tunneling between large particles differs from tunneling between individual grains in a way that for large particles there is a substantial reservoir of accessible states at the Fermi level. Therefore, this process is independent of the temperature and only determined by the geometrical parameters of the barriers between the particles. If the particles get smaller and smaller, a carrier, which has hopped from one particle to another, will create a potential difference between the two particles. At finite temperatures spontaneous hops will occur by thermal fluctuations and all particles will be at slightly different and thermally fluctuating potentials. The detailed analysis shows that the net tunneling current consists of a temperature-independent part and a temperature-dependent part [343]. This concept has been successfully applied by Philipp *et al.* to highly doped polyacetylene [346]. Due to the fact that this concept of tunneling has been limited only to the fibres of the polymer, Pocharsi [347] has tried to modify the inter-fibrillar contacts and hence the tunneling barriers, but apparently without any noticeable effect on the conductivity. Therefore, it is more reasonable to assume that temperature-independent tunneling occurs between

other domains within the samples (amorphous and crystalline or doped and undoped regions).

According to calculations by Sheng and Klafter [348] and Sheng [114], if conduction is by electronic tunneling through non-conducting material separating mesoscopic metallic 'islands' rather than between localized states, the expression for the tunneling conductivity approximately is of the form as given in Eq. 2.14:

$$\sigma = \sigma_0 \exp\left[-\left(\frac{T_0}{T}\right)^{1/2}\right] \quad (2.14)$$

which is of the same form as for 1D variable range hopping. Such a picture should be appropriate for a granular metal in which small metallic grains are surrounded by non-conducting shells. This model takes into account the charging of conducting regions (metallic islands) or the random thermal motion of charge carriers on both side of the tunnel junction. These calculations apply when the conductivity is limited by the electrostatic charging energy when an electron is transferred from one island to the next; the inhibition of tunneling when the thermal energy $k_B T$ is less than the charging energy is referred to as a 'Coulomb blockade' [340]. If, however, the metallic regions are large enough that the electrostatic charging energy is much smaller than $k_B T$ for accessible temperatures, tunneling can occur between metallic states of the same energy on different sides of the barrier without thermal excitation, provided that the wave-functions overlap.

If the size of the metallic islands is of the order of $1\mu\text{m}$, a fluctuation induced tunneling of charge carriers occurs between highly conducting islands. In such a situation, the random thermal motion of the charge carriers within the conducting islands induces a randomly alternating voltage across the gap between the neighboring islands and the temperature dependent conductivity can be given as follows

$$\sigma = \sigma_0 \exp\left[-\frac{T_1}{T + T_0}\right] \quad (2.15)$$

with $T_1 (> 100\text{ K})$ being an additional fitting parameter dependent upon the properties of the potential barriers (insulating islands) between highly conducting

islands. The potential barriers are also sometimes referred to as the interfibrillar spaces rather than the insulating islands. The charge transport results from the tunneling induced by thermal fluctuations, which according to Sheng, can greatly increase the tunneling current as temperature increases [114, 348]. The Sheng model fits well to highly doped or heterogeneous systems such as conducting polymer-polyvinyl chloride composites.

However, the agreement of a vast amount of conducting polymer data with the hopping laws (Eq. 2.2) over a wide temperature range suggests that once localized states are formed in the gap by whatever mechanism, conduction takes place predominantly by the usual variable range hopping processes for lightly or moderately doped samples [335, 349]. In heavily doped samples, the overlap of wave-functions means that a metallic picture is likely to be more appropriate, at least in the ordered regions.

For conducting polymers other than polyacetylene, different solitonic states have different energies, so solitonic conduction mechanisms are not expected. However, states appear in the band gap owing to the formation of polarons, which are basically electrons localized in an electric potential well formed by lattice deformations. Polarons have both charge and spin. Their motion can contribute to charge transport. Polarons of opposite spin often pair up to form bipolarons with zero spin, which can lead to charge transport without spin transport [101-105]. Inspired by the work of Sheng [114] on granular metals, Zuppiroli *et al.* proposed correlated hopping between polaronic clusters as a mechanism of conduction in disordered conducting polymers [113].

2.2.1 Electronic conduction mechanism in polyaniline and polyaniline blends

Polyaniline (PAni) is quite different from polyacetylene or for that matter with any of the conducting polymers in several aspects that have already been discussed in section 1.1.3 of Chapter 1. The highest conductivity that has been achieved for PAni till date is about 250 Scm^{-1} [350, 351]. The crystallinity of highly conducting polyaniline is also much less as compared to polyacetylene, with crystallinity on the order of 50% and domain lengths on the order of 5 nm

(parallel to the stretching direction) and 3 nm (transverse) [352]. Dielectric response studies in PANi revealed the presence of three-dimensional mesoscopic metallic regions [353]. Granular metallicity of PANi samples have been confirmed using scanning tunneling microscopy [354].

Although the conductivity of polyaniline is much lower as compared to polyacetylene and it has a structure that is much more complex as compared to polyacetylene, the overall pattern of temperature dependent conductivity exhibited by both these materials are quite similar. For low conducting PANi samples, the conductivities tend to follow the Eq. (2.2) with $\gamma = 1/2$ [350, 355-357]. However, it has been observed that samples with room temperature conductivity of approximately 20 Scm^{-1} still shows a crossover to metallic temperature dependence near 250 K with the entire conductivity well described by the following equation Eq. (2.19), which is the expression derived for conduction in heterogeneous polymers [358]:

$$\sigma(T)^{-1} = \rho(T) = f_1 \rho_m \exp\left(\frac{-T_m}{T}\right) + f_2 \rho_0 \exp\left[\left(\frac{T_0}{T}\right)^{1/2}\right] \quad (2.16)$$

It is difficult to separate the quasi 1D variable range hopping from the 3D hopping with electron-electron interaction [340], tunneling between macroscopic metallic islands [114] or the correlated hopping between polaronic clusters [113] since they are similar mechanisms yielding the same equation. But for low-conductivity HCl-doped polyaniline with no tendency towards metallic behaviour, an electric field dependence of the conductivity was obtained that can be explained by the quasi-1D hopping mechanism [355]. This supports the picture of metallic crystalline regions linked by disordered regions in which conduction is by quasi-1D hopping [342].

Polyaniline blends, which are basically dispersions of conducting PANi in non-conducting plastics, exhibit almost an identical behaviour in the variation of their conductivity as a function of temperature, except for the fact that the conductivity always tends to zero at zero temperature [358]. A crossover to metallic temperature dependence for conductivity is seen even in the blends but the metallic behaviour is weaker and the crossover temperature is somewhat higher. The similarity for the heterogeneous polyaniline dispersions lends support

to the use of the heterogeneous model for the pure polymers as well. For the dispersions, however, tunneling between mesoscopic metallic islands would be expected to be an important mechanism contributing to the $\exp\{-(T_0/T)^{1/2}\}$ conductivity behaviour.

One intriguing feature of the blends with polyaniline protonated using an organic acid is that blends with polymethyl(methacrylate) (PMMA) are more conducting than the unblended polyaniline, which has been attributed to the reduction of barriers surrounding polyaniline particles during the blending process [358]. In a similar fashion, the effect of aging-induced disorder on transport in polyaniline have been reported to be consistent with the heterogeneous model, the effect of aging being to broaden the barrier regions around conducting grains [357].

2.2.2 *Charge transport in polyaniline based nanostructured materials*

The dependence of electrical conductivity on the diameter of the conducting polymer nanotubes/wires (prepared by the template method) at room temperature has been widely reported [359-361]. It has been found that the room-temperature conductivities of single nanotubes/wires of conducting polyaniline can increase from 0.1-1 S/cm to about 10^3 S/cm with the decrease of their outer diameters from 1500 to 35 nm. The phenomenon has been ascribed to the enhancement in the alignment of the polymer chains.

Since the electrical properties of conducting polymers are strongly influenced by the effect of disorder and temperature, three different regimes (namely, insulating, critical and metallic regimes close to the metal-insulator transition) have been sorted out based on the extent of disorder and conductivity dependence on temperature [362]. Long *et al.* reported temperature dependent resistivity of a single polyaniline nanotube with average outer and inner diameters of 120 nm and 80 nm, which falls in the insulating regime of metal-insulator transition [363, 364]. The tube's room-temperature conductivity has been found to be 47 S/cm. It has been observed that the resistivity follows three-dimensional (3D) Mott-VRH above 66 K, and follows ES-VRH model below 66 K.

From the view point of electrons, the polymer tube/wire with an outer diameter of 120 nm is still three dimensional because the localization length of carriers ($L_C < 20$ nm) is much smaller than the wall thickness or the diameter of the sub-microtube. However, the crossover temperature ($T_{\text{cross}} \sim 66$ K) and the characteristic ES temperature ($T_{\text{ES}} \sim 316-780$ K) of a single polyaniline nanotube/wire are much higher than those of a polyaniline pellet or a polypyrrole film ($T_{\text{cross}} < 15$ K and $T_{\text{ES}} \sim 29-56$ K), which can be possibly due to enhanced strong Coulomb interaction in polymer nanotubes/wires at low temperatures.

2.3 Frequency dependence of conductivity

The electrical conductivity in disordered materials can usually be divided into a frequency independent dc part and a frequency dependent ac conductivity, which increases almost linearly with temperature. The behaviour of ac conductivity in disordered materials whether they are electronic or ionic conductors have been found to show exactly the same behaviour. Hence, a universal power law has been formulated by Joncher [365] in order to explain the frequency dependent conductivity in disordered materials. In case of conducting polymers as well ac conductivity has been found to vary as a power of frequency. It has been observed that above a certain threshold frequency the ac contribution dominates and below it the conductivity is almost frequency independent. The origin of this frequency dependent conductivity lies in the production of a time dependent polarization $P(t)$ when a harmonically oscillating electric field is applied to the material. The dependence of this polarization is related to that of the field variation as given below:

$$P(\omega) = \varepsilon_0 \chi(\omega) E(\omega) \quad (2.17)$$

where ε_0 is the permittivity of free space. The dielectric susceptibility $\chi(\omega)$ in general can be expressed as a complex quantity;

$$\chi(\omega) = \chi_1(\omega) - i\chi_2(\omega) \quad (2.18)$$

The real and imaginary parts of the complex susceptibility are related by Kramers-Kronig (Hilbert) transformation

$$\chi_1(\omega) = \frac{2}{\pi} \int_0^{\infty} \frac{x\chi_2(x)dx}{x^2 - \omega^2} \quad (2.19a)$$

$$\chi_2(\omega) = -\frac{2\omega}{\pi} \int_0^{\infty} \frac{\chi_1(x)dx}{x^2 - \omega^2} \quad (2.19b)$$

The components of dielectric susceptibility are related to those of complex permittivity $\varepsilon(\omega) = \varepsilon_1(\omega) - i\varepsilon_2(\omega)$, according to the Eqs. (2.20a) and (2.20b)

$$\varepsilon_1(\omega) = 1 + \chi_1(\omega) \quad (2.20a)$$

$$\varepsilon_2(\omega) = \chi_2(\omega) \quad (2.20b)$$

The real part of ac conductivity $\sigma_1(\omega)$ can be expressed in terms of the dielectric loss $\varepsilon_2(\omega)$ by

$$\sigma_1(\omega) = \varepsilon_0 \omega \varepsilon_2(\omega) \quad (2.21a)$$

The imaginary part of ac conductivity is given by

$$\sigma_2(\omega) = \varepsilon_0 \omega \varepsilon_1(\omega) \quad (2.21b)$$

and the loss tangent is defined as

$$\tan \delta = \frac{\varepsilon_2}{\varepsilon_1} \quad (2.22)$$

Considering the Debye model, the relaxation of the polarization P characterized by a single and fixed relaxation time constant τ on removal of the electric field is shown in Eq. (2.23)

$$\frac{dP}{dt} = -\frac{P}{\tau} \quad (2.23)$$

The Eq. (2.23) has a solution of the form

$$P(t) = P_0 \exp\left(-\frac{t}{\tau}\right) \quad (2.24)$$

For a continuous distribution of $n(\tau)$, the real part of the ac conductivity can be written as

$$\sigma_1(\omega) = \int_0^{\infty} \alpha n(\tau) \frac{\omega^2 \tau}{1 + \omega^2 \tau^2} d\tau \quad (2.25)$$

where α is the polarizability of a pair of sites assumed to be independent of τ .

Approximately linear frequency dependence observed in amorphous semiconductors and other disordered systems can be obtained from Eq. (2.25) for $n(\tau) \propto 1/\tau$ whence

$$\sigma_1(\omega) \propto \int \frac{\omega d(\omega\tau)}{1 + \omega^2\tau^2} \propto \omega \quad (2.26)$$

The form of $n(\tau)$ required implies that the relaxation time τ itself must be an exponential function of a random variable ξ :

$$\tau = \tau_0 \exp(\xi); \quad \xi = W/kT \quad (2.27)$$

where τ_0 is a constant characteristic relaxation time, and where ξ has a flat distribution, $n(\xi) = \text{constant}$ (i.e. $n(\tau) = n(\xi)d\xi/d\tau \propto \tau^{-1}$). In practice, n and α each may be a function of τ , giving rise to slightly sub-linear frequency dependence [366].

2.4 Models for frequency dependent ac conduction in disordered materials

Several theoretical models have been developed for explaining the universal frequency dependent behavior of conductivity in disordered materials. The basis of many theories of ac conduction in amorphous semiconductors can be related to two macroscopic relaxation mechanisms: (a) classical hopping of a carrier over the potential barrier separating two energetically favorable sites, i.e. in a double-well potential and (b) phonon-assisted quantum-mechanical tunneling through the barrier separating two equilibrium positions. In this section we will briefly discuss the salient features of these models with a special emphasis on the correlated barrier hopping model that has been found to be the most appropriate theory to account for the ac conduction in conducting polymers [366].

In all the models it has been assumed that the pair approximation holds good i.e. the motion of carriers leading to relaxation is contained within a pair of sites and the dielectric response of a carrier moving between a pair of sites (or of a dipole) is accurately Debye-like with relaxation time varying exponentially as function of a random variable, which may be the barrier height, inter-site separation or a combination of both. As can be seen from Eqs. (2.25) and (2.27), three quantities are very important for the calculation of ac conductivity in

disordered materials, these are the polarizability α , the distribution function for relaxation times $n(\tau)$, and the relaxation time expressed in terms of a relaxation variable ξ .

The equation for polarizability within the pair approximation was first evaluated by Pollak and Geballe [367] in which the polarizability for two sites separated in space by R and in energy by Δ was calculated using the rate equations for electron transfer and is given by the Eq. (2.28):

$$\alpha = \frac{e^2 R^2}{12kT} \frac{1}{\cosh^2(\Delta/2kT)} \frac{1}{1+i\omega\tau} \quad (2.28)$$

The effective relaxation time τ that appears in Eq. (2.28) is given by:

$$\tau = \frac{1}{2} \tau_0 [\cosh(\Delta/2kT)]^{-1} \quad (2.29)$$

For multiphonon processes i.e. when the energies involved in the transition, the transition rate may be written as:

$$\omega_y = \frac{1}{\tau_0} \exp\left(\frac{\Delta_y + \Delta_\mu}{2kT}\right) \quad (2.30)$$

where $\Delta_{12} > \Delta = 0$ i.e., the energy of site 2 is higher than that of site 1. For lower energy processes, i.e. single-phonon transitions [368], the transition rate is better described by Eq. (2.31):

$$\omega_y = \frac{\Delta_y}{B[\exp(\Delta_y/kT) - 1]} \quad (2.31)$$

where, the term B contains details of the interactions involved. Eq. (2.31) gives rise to exactly the same form for the polarizability as given in Eq. (2.28), but the form for the effective relaxation time is different, and is given as:

$$\tau = \frac{1}{B\Delta_{12}} \tanh\left(\frac{\Delta_{12}}{2kT}\right) \quad (2.32)$$

Among the different tunneling models, the electron tunneling, small and large polaron tunneling and atomic tunneling models have been employed in different cases for disordered materials to explain the frequency dependent conductivity. The idea of "Electron tunneling" was for the first time presented by Pollak and Geballe for explaining the impurity conduction process in doped crystalline silicon [367]. This concept has been subsequently adopted by Austin

and Mott in case of amorphous semiconductors [369]. If electronic relaxation is responsible for dielectric loss, quantum mechanical tunneling (QMT) is the most obvious charge transfer mechanism. In case of the "*Small polaron tunneling*" model it was assumed that the addition of a charge carrier to a site causes a large degree of local lattice distortion such that the total energy (electronic + distortion) of the system is lowered by an amount equal to the polaron energy leading to the formation of a small polaron [370]. Relaxation due to these small polarons can also be held responsible for the observed frequency dependent conductivity in disordered materials. This model predicts that the tunneling distance decreases more rapidly with increasing frequency than is the case for straight forward QMT i.e electron tunneling. The primary difference between the "*Small polaron model*" and "*Large polaron model*" is that in the latter it has been assumed that there is an appreciable overlap of the polaron distortion clouds [371]. Large polarons, i.e. those for which the spatial extent of the polaron is large compared with the interatomic spacing, and which are of the dielectric or Fröhlich type are characteristic of ionic lattices. In such a scenario, the overlap of the potential wells of neighbouring sites for such polarons because of the long-range nature of the dominant Coulomb interaction results in the reduction of the polaron hopping energy [369]. Another mechanism that might be responsible for dielectric relaxation in amorphous semiconductors is the atomic motion. This led to the development of the "*Atomic tunneling model*" [372]. It has been suggested that the ac conductivity may have a common origin, namely in the two-level systems believed to be present in at least some glasses [373, 374]. However, two-level systems (TLS) resulting from tunneling states do not appear to be present in every amorphous semiconductor, and so even in principle it is unlikely that the ac conductivity behaviour of all amorphous semiconductors can be explained by a single universal (atomic) mechanism. Nevertheless, for wide-gap materials and/or those with a low density of gap states, atomic, rather than electronic relaxation, may be dominant [371].

The term 'hopping' is reserved for those transfer processes that involve (classical) thermal activation over the barrier separating two sites, rather than quantum-mechanical tunneling through the barrier. Thus such a process is

primarily a high temperature phenomenon. In such cases, the relaxation time is given by Eq. (2.27) viz., $\tau \propto \exp(W/kT)$ and no explicit dependence on inter-site separation is generally included. The first application of a pure hopping model to dielectric relaxation in amorphous semiconductors was made by Pollak and Pike [375], who assumed that atoms, fully or partially ionized, hopped over the barrier, of height W , separating two sites, having an energy difference, Δ . The relaxation variable in "Atomic hopping model" is obviously W , which in the simplest case is independent of the inter-site separation R ; furthermore, the dipole moment p and the change in p involved in an atomic transition are not known a priori, and so p may be set equal to a constant value p_0 , independent of W and R [371]. A strictly linear dependence of the ac conductivity on both frequency and temperature (at low temperatures) is predicted by this model. The linear frequency dependence (i.e. $s = 1$) arises because there is no dependence of the hopping distance R_ω (or the dipole moment) on frequency ω . However, it is the correlated barrier hopping model that has been found to be more appropriate for conducting polymers [376-378]. In the next subsection, we present a discussion about the "Correlated barrier hopping model" and also mark out the basic differences among the correlated barrier model and other hopping and tunneling models that have been developed in order to account for the frequency dependent behavior of ac conductivity.

2.4.1 Correlated barrier hopping (CBH) model

The salient feature of the "Correlated barrier hopping model" is that unlike the simple hopping model the relaxation variable W is dependent on the inter-site separation R , and as such the hopping distance is frequency dependent. The overlapping of the Coulomb wells for neighboring sites at a separation R lowers the effective barrier from W_M (the value at infinite inter-site separation) to a value W according to the Eq. (2.33):

$$W = W_M - \frac{e^2}{\pi\epsilon\epsilon_0 R} \quad (2.33)$$

Although this model was for the first time used by Pike [375], the term 'correlated barrier hopping' (CBH) was coined by Elliot [366]. The relaxation time in this case is given by the Eq. (2.34):

$$\tau = \frac{\tau_0 \exp(W/kT)}{\cosh(\Delta/2kT)} \quad (2.34)$$

In the narrow-band limit ($\Delta_0 \ll kT$), and assuming that the centers are distributed randomly in space, the ac conductivity is given as [366, 371, 375]:

$$\sigma_1(\omega) = \frac{1}{24} \pi^3 N^2 \varepsilon \varepsilon_0 \omega R_\omega^6 \quad (2.35)$$

where the hopping distance R_ω at a frequency ω is given by:

$$R_\omega = \frac{e^2}{\pi \varepsilon \varepsilon_0 \left[W_M - kT \ln \left(\frac{1}{\omega \tau_0} \right) \right]} \quad (2.36)$$

The frequency dependence in the CBH model (for both limits) is embodied in the ωR_ω^6 factor and can be expressed in terms of the frequency exponent "s" as [371]:

$$s = 1 - \frac{6kT}{W_M - kT \ln(1/\omega \tau_0)} \quad (2.37)$$

The parameter "s" in the CBH model is predicted to be both frequency and temperature-dependent. For small values of W_M/kT , "s" increases with increasing frequency, unlike all the cases considered so far, although for large values of W_M/kT ($>/100$), "s" is nearer unity and the increase is so small that "s" is effectively frequency independent. Eq. (2.37) also predicts that 's' decreases with increasing temperature, and at low temperatures (i.e. large W_M/kT), 's' decreases approximately linearly from the $T = 0$ value of unity. The difference between the Correlated barrier hopping model with the other models have been elucidated in the Table 2.1, which includes the expressions for the real part of ac conductivity $\sigma_1(\omega)$, the frequency dependence of the hopping distance R_ω , and the expression for the frequency exponent that appears in the universal law for frequency dependent ac conductivity according to Joncher [365].

In case when two electrons hop simultaneously between defects, the equations given are to be modified. The polarizability has to be multiplied by a factor of four, the second term in Eq. (2.33) has to be multiplied by a factor of two, as does Eq. (2.36), and the ac conductivity in the narrow-band limit then becomes:

$$\sigma_1(\omega) = \frac{1}{12} \pi^3 N^2 \epsilon \epsilon_0 \omega R_\omega^6 \quad (2.38)$$

The hopping length is also different for two-electron transport and is given by:

$$R_\omega = \frac{2e^2}{\pi \epsilon \epsilon_0 \left[W_M - kT \ln \left(\frac{1}{\omega \tau_0} \right) \right]} \quad (2.39)$$

However, the functional form for the frequency exponent “ s ” is the same in both cases. The temperature dependence of the “ s ” parameter in the case of CBH [Eq. (2.37)] arises from the correlation between barrier height and inter-site separation. The minimum hopping distance R_{\min} , which is a lower bound (cut-off) to the hopping distance R_ω for this model is given by:

$$R_{\min} = \frac{2e^2}{\pi \epsilon \epsilon_0 W_M} \quad (2.40)$$

2.5 Modifications in the models for ac conduction

The basic models of ac conduction discussed above have also undergone several types of modifications and alterations depending upon the variations encountered in the basic mechanisms. In almost all the models for ac conductivity discussed in the previous sections, a random distribution has been considered for spatial distribution of centers between which dielectric relaxation takes place. It has also been pre-assumed that relaxation occurring by means of classical hopping of atoms over a barrier within an asymmetric double-well potential has a random distribution of barrier heights. Furthermore, the possibility of the involvement of structural inhomogeneities containing the centers responsible for dielectric relaxation has been neglected. However, these factors can greatly affect ac conductivity in amorphous semiconductors. Structural defects such as dangling bonds distributed in the bulk of an amorphous semiconductor can also lead to electronic relaxation either by tunneling or hopping and in such case the spatial distribution of centers are not likely to be random. Two instances for which such non-random spatial distributions can occur are pairing of defects and structural inhomogeneities.

Table 2.1: Salient features of the different models for ac conduction in amorphous materials. Differences between the expressions for the real part of ac conductivity, hopping distance and the frequency exponent "s" are shown in the table

Models	Real part of ac conductivity, $\sigma_1(\omega)$	Hopping distance (R_ω)	Frequency exponent (s)
Electron tunneling	$\frac{Ce^2kT}{\alpha} N^2(E_F)\omega R_\omega^4$	$\frac{1}{2\alpha} \ln\left(\frac{1}{\omega\tau_0}\right)$	$1 - \frac{4}{\ln(1/\omega\tau_0)}$
Small polaron tunneling	$\frac{\pi^4 e^2 kT}{24\alpha} N^2(E_F)\omega R_\omega^4$	$\frac{1}{2\alpha} \left[\ln\left(\frac{1}{\omega\tau_0}\right) - \frac{W_H}{kT} \right]$	$1 - \frac{4}{\ln(1/\omega\tau_0) - W_H/kT}$
Large polaron tunneling	$\frac{\pi^4}{12} e^2 (kT)^2 N^2(E_F) \frac{\omega R_\omega^4}{2\alpha kT + W_{H0} r_0 / R_\omega^2}$	$\frac{1}{4\beta} \left[\ln\left(\frac{1}{\omega\tau_0}\right) - \frac{W_{H0}}{kT} \right] + \left[\left\{ \ln\left(\frac{1}{\omega\tau_0}\right) - \frac{W_{H0}}{kT} \right\}^2 + \frac{8\alpha r_0 W_{H0}}{kT} \right]^{1/2}$	$1 - \frac{1}{R'_\omega} \frac{4 + 6W_{H0} r_0' / kTR_\omega'^2}{(1 + W_{H0} r_0' / kTR_\omega'^2)^2}$
Atomic tunneling	$\frac{\pi}{6} \frac{Np_0^2}{\Delta_0 \lambda_0} \omega \tanh\left(\frac{\Delta_0}{2kT}\right)$	Frequency independent	1
Atomic hopping	$\pi p_0^2 \frac{NkT}{6W_0 \Delta_0} \omega \tanh\left(\frac{\Delta_0}{2kT}\right)$	Frequency independent	1
Correlated barrier hopping	$\frac{1}{12} \pi^3 N^2 \epsilon \epsilon_0 \omega R_\omega^6$	$\frac{2e^2}{\pi \epsilon \epsilon_0 \left[W_M - kT \ln\left(\frac{1}{\omega\tau_0}\right) \right]}$	$1 - \frac{6kT}{W_M - kT \ln(1/\omega\tau_0)}$

Pairing of defects, or more generally clustering of centers, is important for ac conduction if the hopping or tunneling length is comparable to the pair separation or cluster size. Thus this effect can influence all electronic transfer mechanisms, such as QMT or hopping. Likewise the distribution function has been modified and a new expression for ac conductivity has been developed which is given in the Eq. (2.41):

$$\sigma_1(\omega) = \frac{\pi^3}{12} N^2 \epsilon \epsilon_0 \omega R_w^6 \exp \left[\frac{W_M - kT \ln \left(\frac{1}{\omega \tau_0} \right)}{8kT_g} \right] \quad (2.41)$$

The only difference between the Eq. (2.41) with that of the equation for paired defects in the correlated barrier hopping for the case of randomly distributed centers [Eq. (2.38)] is the inclusion of the exponential factor. The frequency exponent “ s ” arising from Eq. (2.41) can be evaluated in the normal way to give [371]

$$s = 1 - \frac{6kT}{W_M - kT \ln \left(\frac{1}{\omega \tau_0} \right)} + \frac{T}{8T_g} \quad (2.42)$$

Another modification in the models for classical hopping of atoms over a barrier within an asymmetric double-well potential has been introduced by Gilroy and Phillips in which a non-random exponential distribution of barrier heights rather than the random distribution $p(W) = 1/W_0$ have been considered as in Eq. (2.43) [379]:

$$p(W) = \frac{1}{W_0} \exp \left(-\frac{W}{W_0} \right) \quad (2.43)$$

where W_0 is related to the glass-transition temperature. The real part of the ac conductivity evaluated using Eq. (2.43) is [379]:

$$\sigma_1(\omega) = \frac{\pi p_0^2 \tau_0^\alpha kT \omega^s}{3 \Delta_0 W_0} \quad (2.44)$$

where Δ_0 is the width of the site-asymmetry distribution, and τ_0 is a characteristic relaxation time. The frequency exponent “ s ” is superlinear and is given by:

$$s = 1 + \alpha \quad (2.45)$$

where $\alpha = kT/W_0$.

Structural inhomogeneities containing the centers responsible for the dielectric relaxation is also another instance of a non-random spatial distribution of centres. These might be internal surfaces within the structure of the amorphous material on which the centers (e.g. dangling bonds) occur, such as voids or molecular clusters. The departure from a continuous random distribution arises in this case from a cut-off in the distribution function, corresponding to the size R_0 of the inhomogeneity (much smaller than the separation between inhomogeneities), beyond which the probability of finding a pair of sites at a distance corresponding to the hopping or tunneling distance becomes negligibly small. This causes a breakdown in the approximations used previously in the evaluation of the integrals involved in the expressions for the ac conductivity and the models have been accordingly modified.

It has been assumed so far that the real and imaginary parts of the ac conductivity can be obtained from the Debye expression for the polarizability of a pair of centers, i.e. involving the term $(1 + i\omega\tau_0)^{-1}$. However, departures from the Debye expression have been observed for many materials [365]. These departures are often accounted for by assuming a distribution of relaxation times $n(\tau)$ to be present. It has been suggested that there is a strong correlation between the degrees of freedom and relaxation is presumed to take place in a series, rather than a parallel fashion [380]. Faster degrees of freedom successively constrain slower ones, thereby naturally generating a wide range of relaxation times. Thus there is no need to invoke a distribution of relaxation times, as required for parallel relaxation mechanisms. One model within the general class of hierarchically constrained models predicts that the temporal decay function should be of the stretched exponential (Kohlrausch) form [380]

$$q(t) = q_0 \exp\left[-\left(\frac{t}{\tau_0}\right)^\beta\right] \quad (2.46)$$

rather than the Debye form $q(t) = q_0 \exp[-(t/\tau_0)]$. Thus, while a microscopic understanding of the processes giving rise to the decay function is still not

available, a much generalized theoretical understanding is beginning to emerge. Intra-site correlation is also important in governing whether a particular electronic defect site is singly or doubly occupied: for the case of amorphous materials, the effective correlation energy is believed to be negative [381], and so the doubly occupied and unoccupied configurations are energetically more stable than is the neutral paramagnetic singly occupied state. The effect of inter-site correlation was first considered by Pollak [382], subsequently by Efros [383] and more recently by Long [371]. The pair approximation is also invoked in the discussion of correlation, since it is assumed that the inter-site Coulombic interaction affects only close neighbors, i.e. pairs of sites; the Coulomb interaction is screened out for further neighbors, and so the occupation of a given site by an electron is assumed not to affect appreciably the occupation of such further neighboring sites. Correlation effects are important at relatively low temperatures, i.e. when $E_{12} \gg kT$, where E_{12} is the inter-site (i.e. intra-pair) correlation energy.

Thus far it has been assumed that the frequency-dependent conductivity can be evaluated within the pair approximation [367], i.e. that the relaxation is confined entirely to pairs of sites, and multiple-site participation is excluded. The pair approximation has been found to be a good approximation at sufficiently high frequencies. However, the pair approximation must break down at low frequencies as $\omega \rightarrow 0$, where a percolation path must be established throughout the sample in the dc limit, if the dc conductivity is due to the same electronic transport mechanism between localized states as is responsible for the ac conductivity. Likewise, two approaches have been adopted to calculate the ac conductivity. The first in which $\sigma_1(\omega)$ is evaluated from the diffusivity of a random-walk process [384, 385] and the second approach in which the problem is formulated in terms of a set of Kirchhoff equations for an RC network equivalent to the hopping/tunneling rates [368].

2.6 Dielectric relaxation in amorphous materials

Dielectric relaxation in solids is one of the most intensely researched topics in physics and yet there is no satisfactory theoretical understanding of the relaxation phenomena. Relaxation consists of the recovery of strain on removal of stress and it implies therefore time dependence, typically under sudden removal

or sudden application of a steady stress. This is the basis of the time-domain (TD) measurement [386]. An equivalent and often preferable method is to subject the material to a harmonically varying stress of an angular frequency ω and this forms the basis of frequency-domain (FD) measurements [365, 387, 388]. Materials are polarized in ac fields by various polarization mechanisms and their permittivity, as a measure of the polarization, shows frequency dependence, namely dielectric relaxation or dielectric dispersion. Dielectric spectroscopy is a technique that measures permittivity and conductivity as a function of frequency in a non-invasive way and can provide insights into the structures and electrical properties of materials at molecular and macroscopic levels.

According to Maxwell's equations, ε^* is time (or frequency) dependent if a time dependent process take place within the sample. Resonance phenomena are due to atomic or molecular vibrations and can be analyzed by optical spectroscopy. Relaxation phenomena, on the other hand, are related to molecular fluctuations of dipoles due to molecules or part of them in a potential landscape. Moreover, drift motion of mobile charge carriers viz., electrons, ions or charged defects also contribute to the dielectric response. Complex dielectric permittivity ε^* is defined as:

$$\varepsilon^*(\omega) = \varepsilon'(\omega) - j\varepsilon''(\omega) \quad (2.47)$$

where $\varepsilon'(\omega)$ and $\varepsilon''(\omega)$ are, respectively, the real and imaginary parts of complex permittivity ε^* . The real part $\varepsilon'(\omega)$ and the imaginary part $\varepsilon''(\omega)$ of complex permittivity though not always, show dielectric relaxation (or dielectric dispersion) in which $\varepsilon'(\omega)$ decreases and $\varepsilon''(\omega)$ increases with increasing frequency. Single dielectric relaxation is characterized by a set of parameters (called relaxation parameters): ε_1 and ε_h are the low- and the high-frequency limits of relative permittivity, respectively, $\Delta\varepsilon = \varepsilon_1 - \varepsilon_h$ the relaxation intensity (or the relaxation magnitude), f_0 the characteristic frequency and $\tau (= 1/2\pi f_0)$ the relaxation time. The complex plane plot (or the Cole-Cole plot) is also used for analysis of dielectric relaxation. In the complex plane plot the imaginary part of the complex permittivity or the loss factor $\varepsilon''(\omega)$ is plotted against the real part of the complex permittivity or the relative permittivity $\varepsilon'(\omega)$, tracing a semicircle if

the dielectric relaxation has a single relaxation time, viz., the Debye type relaxation. The complex plane plots, however, often deviate from a semicircle, which indicates a distribution of relaxation times. The deviation is formulated by various empirical equations which will be discussed in the sub-section 2.6.2.

2.6.1 Presentation of dielectric data

Dielectric information may be presented in a number of equivalent ways and it is important to use the most appropriate form of presentation to match the particular requirement [388]. The following principal dielectric functions may be defined.

(a) The complex permittivity $\varepsilon^*(\omega)$ and susceptibility $\chi^*(\omega)$,

$$\chi^*(\omega) \equiv [\varepsilon^*(\omega) - \varepsilon_\infty] / \varepsilon_0 = \chi'(\omega) - i\chi''(\omega) \quad (2.48)$$

where $\varepsilon_0 = 8.854 \times 10^{-12}$ F.m⁻¹ is the permittivity of free space, ε_∞ is a suitable high-frequency permittivity and the physical emphasis is on parallel processes contributing to the real and imaginary components of the polarization.

(b) The electric modulus, which is the reciprocal of $\varepsilon^*(\omega)$,

$$M^*(\omega) = M'(\omega) + iM''(\omega) = \frac{1}{\varepsilon^*(\omega)} = \frac{\varepsilon'(\omega) + i\varepsilon''(\omega)}{[\varepsilon'(\omega)]^2 + [\varepsilon''(\omega)]^2} \quad (2.49)$$

which emphasizes series processes that may be acting in the material.

(c) The complex capacitance

$$C^*(\omega) = (A/d)\varepsilon^*(\omega) \quad (2.50)$$

which relates to a sample of planar geometry of area A and thickness d , or some other appropriate geometrical factor for other geometries. Susceptance is the quantity corresponding to susceptibility

$$X^*(\omega) = C^*(\omega) - C_\infty \quad (2.51)$$

Their use is recommended wherever the geometry of the sample is not well defined. They both emphasize parallel processes acting in the sample.

(d) The admittance of the sample representing the equivalent parallel conductance $G(\omega)$ and capacitance $C(\omega)$

$$Y^*(\omega) = I/V = i\omega C^*(\omega) \equiv G(\omega) + i\omega C(\omega) \quad (2.52)$$

The frequency dependence of these elements arises from the fact that they represent an equivalent circuit of a system that is not necessarily a parallel combination of frequency-independent elements.

(e) The impedance of the sample which is the reciprocal of admittance

$$Z^*(\omega) = V/I = 1/Y^*(\omega) \quad (2.53)$$

which emphasizes series processes.

These different formalisms are often used to study different relaxation processes occurring in solids. Electrical relaxation phenomena are usually analysed in terms of the dielectric permittivity by the relaxation of the electric displacement vector, D , under the constraint of constant electric field, E . However, in dielectrics containing mobile charges, it seems convenient to concentrate on the relaxation of the electric field, E , under the constraint of a constant displacement vector, D , which leads to the inverse dielectric permittivity and the definition of electric modulus. An advantage of using the electric modulus to interpret bulk relaxation properties is that variations in the large values of permittivity and conductivity at low frequencies are minimized. In this way the familiar difficulties of electrode nature and contact, space charge injection phenomena and absorbed impurity conduction effects, which appear to obscure relaxation in the permittivity presentation, can be resolved or even ignored.

There are several ways of presenting the data and the most common ones are as follows.

(1) Plots of the real and imaginary components either in logarithmic or in linear coordinates against frequency, usually on a logarithmic presentation in view of the very large range of frequencies involved. The log-log form is particularly useful in representing dielectric functions which are often power-law functions of frequency:

$$\chi^*(\omega) \propto (i\omega)^{n-1} \quad \text{where } 0 < n < 1 \quad (2.54)$$

in the frequency region above any loss peaks, which is referred to as the 'universal' law.

(2) Polar plots of the imaginary component against the real component, typically on a linear presentation, but the logarithmic presentation introduced by the Chelsea Dielectrics Group can be very useful [365]. The

usefulness of polar plots is limited mainly to characterization by shape as Debye, Cole–Cole, Cole–Davidson etc. and also as a means of finding series combinations of elements in Z plots.

2.6.2 Analysis of Dielectric spectra: Model functions

Dielectric relaxation processes are usually analyzed using model functions. Starting from the theoretically well founded Debye model, several models have been suggested to explain the experimentally observed spectra in both the time and frequency domain. The most important of these approaches are discussed below:

The Debye function for the frequency dependence of the complex permittivity $\varepsilon^*(\omega)$ is given by:

$$\varepsilon^*(\omega) = \varepsilon_\infty + \frac{\Delta\varepsilon}{1 + i\omega\tau_D} \quad (2.55)$$

where $\Delta\varepsilon = \varepsilon_s - \varepsilon_\infty$ is the dielectric relaxation strength with $\varepsilon_s = \lim_{\omega\tau \ll 1} \varepsilon'(\omega)$ and $\varepsilon_\infty = \lim_{\omega\tau \gg 1} \varepsilon'(\omega)$. The Debye relaxation time τ_D is related to the position of the maximum loss by $\omega_p = 2\pi\nu_p = 1/\tau_D$. The loss peak is symmetric with a half width ω_D of 1.14 decades [389].

In the complex plane plot, a perfect Debye relaxation, i.e. if the dielectric relaxation has a single relaxation time, is represented by a semicircle. The complex plane plots, however, often deviate from a semicircle, which indicates a distribution of relaxation times. The deviation from the ideal Debye behaviour has been encountered in several experimental results and as such different models have been formulated by various empirical equations proposed by Cole and Cole [390], Davidson and Cole [391], Havriliak and Negami [392].

The influence of the distribution of relaxation times, in the permittivity mode, has been introduced by Cole-Cole [390] to account for the symmetrical distribution of relaxation times. According to the Cole-Cole formulation, the frequency dependence of the complex permittivity is given by:

$$\varepsilon^* = \varepsilon_h + \frac{\Delta\varepsilon}{1 + (j\omega\tau)^{1-\alpha}} \quad (2.56)$$

where the parameter α lies between 0 and 1 and describes the symmetrical distribution of relaxation times. The real and imaginary part of the complex permittivity for the Cole-Cole equation can be written as Eqs. (2.57 a & b):

$$\varepsilon' = \varepsilon_h + \frac{\Delta\varepsilon[1 + (\omega\tau)^{(1-\alpha)} \cos\{\pi(1-\alpha)/2\}]}{1 + 2(\omega\tau)^{(1-\alpha)} \cos\{\pi(1-\alpha)/2\} + (\omega\tau)^{(1-\alpha)}} \quad (2.57a)$$

$$\varepsilon'' = \frac{\Delta\varepsilon(\omega\tau)^{(1-\alpha)} \sin\{\pi(1-\alpha)/2\}}{1 + 2(\omega\tau)^{(1-\alpha)} \cos\{\pi(1-\alpha)/2\} + (\omega\tau)^{(1-\alpha)}} \quad (2.57b)$$

Davidson and Cole [391], aiming to account for an asymmetric distribution of relaxation times resulting from a dielectric dispersion within a system, introduced the parameter β in Debye's dielectric function. According to this model, the complex permittivity can be expressed as:

$$\varepsilon^* = \varepsilon_h + \frac{\Delta\varepsilon}{(1 + j\omega\tau)^\beta} \quad (2.58)$$

where β also lies between 0 and 1 and is responsible for the asymmetrical distribution of relaxation times. The real and imaginary part of complex impedance in this case is given as:

$$\varepsilon' = \varepsilon_h + \Delta\varepsilon \cos(\beta\theta) \cos^\beta \theta \quad (2.59a)$$

$$\varepsilon'' = \Delta\varepsilon \sin(\beta\theta) \cos^\beta \theta \quad (2.59b)$$

where $\theta = \tan^{-1}(\omega\tau)$.

A more general equation for expressing the complex permittivity was developed by Havriliak and Negami [392]. According to this model, the complex permittivity is given by:

$$\varepsilon^* = \varepsilon_h + \frac{\Delta\varepsilon}{[1 + (j\omega\tau)^{1-\alpha}]^\beta} \quad (2.60)$$

where the parameters α and β signify the symmetrical and asymmetrical distribution of relaxation times, respectively and both lie between 0 and 1. The real and imaginary components of the complex permittivity in this case are given by the Eqs. (2.61 a & b):

$$\varepsilon' = \varepsilon_h + r^{-\beta/2} \Delta\varepsilon \cos(\beta\theta) \quad (2.61a)$$

$$\varepsilon'' = r^{-\beta/2} \Delta\varepsilon \sin(\beta\theta) \quad (2.61b)$$

where the terms r and θ can be written as:

$$r = [1 + (\omega\tau)^{(1-\alpha)} \sin(\alpha\pi / 2)]^2 + [(\omega\tau)^{(1-\alpha)} \cos(\alpha\pi / 2)]^2 \quad (2.62)$$

$$\theta = \tan^{-1} \frac{(\omega\tau)^{(1-\alpha)} \cos(\alpha\pi / 2)}{1 + (\omega\tau)^{(1-\alpha)} \sin(\alpha\pi / 2)} \quad (2.63)$$

The general nature of the Havriliak-Negami model can be established from the fact that for $\beta = 1$ and $\alpha = 0$, the Debye Equation [Eq. (2.55)] can be obtained. The Cole-Cole equations [Eq. (2.56)] can be obtained if $\beta = 1$ and $\alpha \neq 0$ are considered. Finally by considering, $\beta \neq 1$ and $\alpha = 0$, we get the Davidson-Cole equation [Eq. (2.58)].

2.7 Theories governing ion-solid interactions

Ion beam processing and analysis of materials are indispensable tools for a wide variety of applications and technologies. The basic requirement for performing any study in this field is the availability of energetic ions, which can be obtained in many ways [393]. Once an energetic ion interacts with matter, it loses its energy in the matter by two different types of mechanisms: the nuclear and electronic energy losses that have been discussed in section 1.3 of Chapter 1. In contrast to the interaction of, e.g. energetic electrons or photons with matter, the salient feature of ion solid interaction is the extremely high localization of the energy transferred to the target material. In this way, solids may receive for a very short time ($\sim 10^{-17}$ to 10^{-15} s) within a very tiny volume ($\sim 10^{-17}$ to 10^{-16} cm³) the same energy density which can be compared to that of an exploding hydrogen bomb, by the impact of just one energetic heavy ion.

Low energy ion beams have been used in electronics for semiconductor doping by ion implantation since the 50th century. Heavy ions, on the other hand have not been commercially used till now, but have been used for studying and tailoring the properties of different materials. The interaction of a swift heavy ion with some solid target materials is marked by the formation of latent tracks. Two phenomenological models have been extensively used for explaining the latent track formation in solids upon interaction with swift heavy ions: (a) Thermal spike model and (b) Coulomb explosion model. These two models will be discussed briefly in the following sub-sections.

2.7.1 Thermal-spike model

It was pointed out by Dessauer that the absorption of radiation is a quantized process obeying statistical laws [394]. As such the localized regions of the absorbing medium are heated to high temperatures that can cause widespread changes in materials. This model referred to as the “thermal spike model” has also been used to explain the track formation mechanism in solids [394]. However, in radiation chemistry and biology, thermal effects were not predominant and as such the thermal spike model was largely ignored [395]. It was Seitz [396] who formulated the modern form of the thermal spike model and showed that it is indeed a very important mechanism when it comes to radiation related studies in any branch of science.

In the thermal spike model a heavy-ion track is considered as a linear energy burst [397] and the temperature distribution resulting from such a burst in an infinite medium is given by

$$T(r, t) = T_0 + \left(\frac{Q}{\pi c d 4 x t} \right) \exp\left(\frac{-r^2}{4 x t} \right) \quad (2.64)$$

where T is the temperature at the time t after the burst at a radial distance r from the axis of the track, Q is the heat released per unit length, T_0 is the temperature of the medium before the burst, c , d , and x are, respectively, the heat capacity, density, and thermal diffusivity of the medium. For calculation purposes Eq. (2.64) can be simplified to:

$$T = T_0 + \left(\frac{Q}{\pi c d 4 x t} \right) \quad r^2 < 4 x t \quad (2.65a)$$

$$T = T_0 \quad r^2 > 4 x t \quad (2.65b)$$

and the spike can be considered to have a duration, t_s , given by:

$$t_s = r^2 / 4 x \quad (2.65c)$$

The thermal spike model also takes into account any alteration in the temperature distribution caused by the passage of charged particles through a medium. Thermal spike model also considers the effect of changes in the local energy density on free radical yield as well as on temperature [398]. Thermal spikes, in addition to affecting reaction rates, also generate large pressures in the

rapidly heated material within the spike. These pressures, caused by the tendency of heated materials to expand, can cause plastic deformation in solids [397] and explosive growth of vapour bubbles in liquids [399]. The importance of the thermal spike model has been evaluated by the development of the model to account for the problem of defining temperature under the non-equilibrium conditions in the spike, together with the availability of new experimental data [394]. However, recent studies have shown that the thermal spike mechanism is less important in the production of tracks by heavy ions in solids than was thought to be the case [400]. Nevertheless, the thermal spike model represents an important mechanism for radiation damage, whether we are dealing with heavy ions or with intense ultrasonic or laser beams since a large fraction of the absorbed energy is converted into heat.

2.7.2 Coulomb explosion model

The Coulomb explosion model was first suggested by Fleischer *et al.*, which suggested that the resulting repulsion between the transiently ionized atoms in the solid, called a "Coulomb explosion," can be the reason for the production of a latent track in an insulator which may be seen by chemical etching [401]. This model predicts that a narrow cylinder of densely filled positive ions is created upon irradiation, which strongly repels one another and are ejected (Coulomb explosion) into interstitial positions surrounding a depleted core region. However, for the coulomb explosion model to be valid, the following criteria were laid down by Fleischer *et al.* [401].

- (1) Tracks may be formed by Coulomb explosion model in materials with low mechanical strength, low dielectric constant and small inter-atomic spacing. Since the electrostatic stress has to be larger than the mechanical strength, which is possible only when

$$n^2 > R \equiv E\epsilon a_0^4 / 10e^2 \quad (2.66)$$

- (2) Tracks must be atomically continuous which require at least one ionization per atom. Thus, $n > 1$ is the second criterion for track formation by Coulomb explosion model.
- (3) The third requirement for track formation is that the availability of electrons for replacing the ejected ones in the material must be low and

must not be able to replace the ejected electrons within a time frame of less than $\sim 10^{-13}$ sec. Thus for a track to be formed by the Coulomb explosion model one must have:

$$n_n < en_a / a_0 \mu_n \pi k T t \quad (2.67)$$

where n_n is the number of free electrons in the system, n_a is the number of ionizations per atomic plane, k is the Boltzmann constant and μ_n is the electron mobility.

- (4) The fourth and the final criterion for the Coulomb explosion model to be appropriate for explaining track formation in solids is low mobility of the holes created by the ejection of electrons along the ionized track. Ideally, the hole mobility μ_p must be less than $a_0^2 e / tkT$ for the material in order to sustain the latent tracks.

However, it has been elucidated by Bringa *et al.*, that Coulomb explosion and thermal spike are basically two events that define the early and late aspects of the ionized tracks produced in some solid targets during the passage of a highly energetic ion through it [402]. No matter whether a Coulomb explosion has really taken place in the solid, a thermal spike will eventually occur since at higher excitation densities the repulsive energy in the track produces a spike [402]. Although these two models have been used extensively to explain track formation in solids, there is still a lot of debate regarding the applicability of these models.

Chapter 3

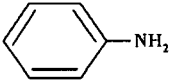
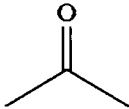
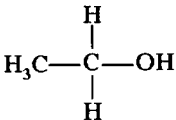
EXPERIMENTAL TECHNIQUES

This chapter primarily deals with the methods and materials used for synthesizing different types of Polyaniline (PAni) based nanostructured materials. This is followed by the discussion of the principles and specifications of different analytical techniques employed for the physico-chemical characterization of the synthesized materials. Various parameters related to Swift Heavy Ion (SHI) irradiation are mentioned in this chapter. The biochemical assays used for investigating the antioxidant activity and biocompatibility of these materials are also briefly described. Thereafter, the methodology adopted for the fabrication of quartz crystal microbalance (QCM) sensors modified by Polyaniline (PAni) based nanostructured materials has been discussed.

3.1. Materials

Monomer aniline (Merck) was used for the synthesis of polyaniline (PAni) based nanostructured materials. Aniline was distilled under reduced pressure and stored in dark prior to use. Hydrochloric acid (HCl) and camphor sulfonic acid (CSA) purchased from Merck were used as dopants. Ammonium peroxydisulfate (APS) also obtained from Merck was used as the oxidant. For the synthesis of Polyaniline (PAni) nanofiber reinforced PVA nanocomposites, Polyvinyl alcohol (PVA) ($M_w = 145000$) purchased from Merck was used. Glycerol (Merck) was used as the plasticizer for the synthesis of PAni nanofiber reinforced PVA nanocomposites. All other chemicals, solvents and reagents used in the synthesis and purification process were of analytical grade and used as received without any further purification. The physical properties of the materials used for the synthesis of different PAni based nanostructured materials in the present work are tabulated in Table 3.1.

Table 3.1: Some physical properties of the materials used in synthesis

Physical properties of the monomer						
Monomer	Molecular structure	Molecular weight	Melting point (°C)	Boiling point (°C)	Density at 25° C (gm/ml)	Oxidation potential (Volt)
Aniline		93.13	-6	184	1.022	0.9
Physical properties of dopants, oxidant and plasticizer used in synthesis						
Dopants/ Oxidant/ Plasticizer		Molecular weight	Melting point (°C)	Boiling point (°C)	Density at 25 °C (gm/ml)	
Hydrochloric acid (HCl)		36.48	N/A	>100	1.20	
Camphor sulfonic acid (C ₁₀ H ₁₆ O ₄ S)		232.3	~200	N/A	N/A	
Physical properties of solvents						
Solvents	Molecular structure	Molecular weight	Melting point (°C)	Boiling point (°C)	Density at 25 °C (gm/ml)	
Acetone		58.08	-94.9	56.53	0.7925	
Methanol	H ₃ C—OH	32.04	-97	64.7	0.7918	
Ammonium persulfate	[NH ₄] ₂ S ₂ O ₈	228.20	120	N/A	1.98	
Ethanol		46.07	-114	78	0.789	
Glycerol	[C ₃ H ₅ (OH) ₃]	92.09	17.8	290	1.261	

3.2. Synthesis of polyaniline nanofibers

Polyaniline (PAni) nanostructures have been synthesized using several techniques such as well-controlled solution synthesis [326, 327], soft-template methods such as micellar [403, 404], microemulsion and reverse microemulsion polymerization [150, 151, 405], hard-template methods [153], template free methods [146], seeding polymerization [325] interfacial polymerization [155, 324] and electro-spinning technology [153]. In the present work, we have used

interfacial polymerization and rapid mixing polymerization techniques for the synthesis of PANi nanofibers and PANi nanofibers reinforced PVA nanocomposites, respectively [155, 324, 329, 330]. Interfacial polymerization has been preferred over other techniques for the synthesis of PANi nanofibers because this technique is very simple and gives a good yield of high quality PANi nanofibers without the use of any template.

Polyaniline (PANi) nanofibers doped with dopant acids viz., hydrochloric acid (HCl) and camphor sulfonic acid (CSA) have been synthesized using the interfacial polymerization technique [155, 324]. The block diagram for the synthesis of PANi nanofibers by interfacial polymerization is shown in Fig. 3.1.

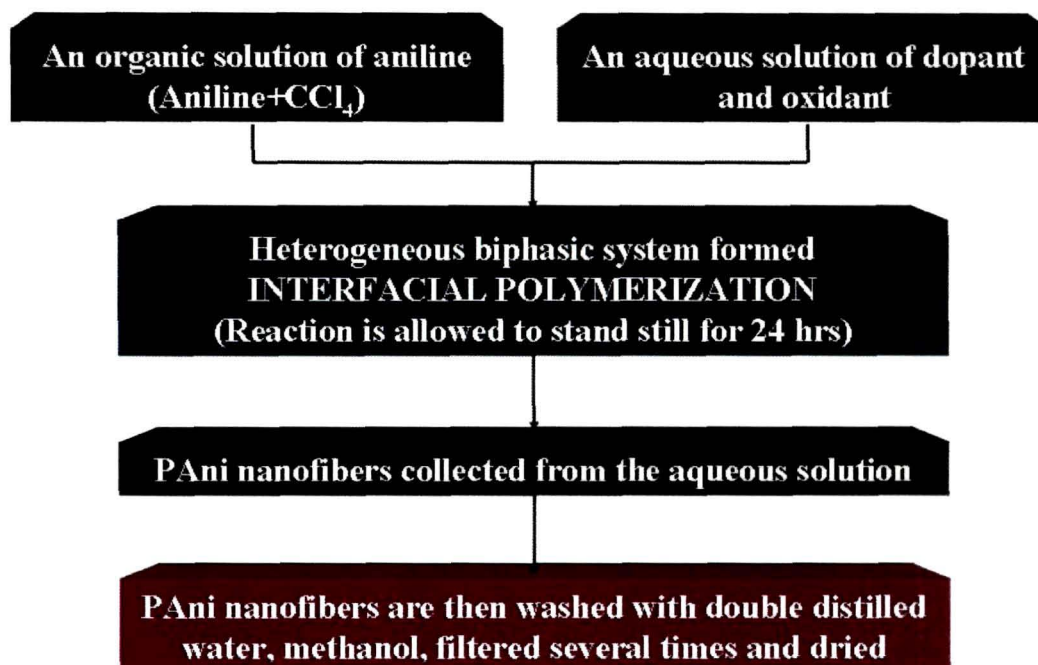


Figure 3.1: Block diagram for the synthesis of polyaniline nanofibers using interfacial polymerization

It is known from the early years of conducting polymer research that polyaniline fibrils of ~ 100 nm in diameter can be synthesized “naturally” during electropolymerization on the surface of the electrodes [144, 166]. Recent works indicate that uniform polyaniline nanofibers can be obtained without the need for any template simply by controlling the electrochemical polymerization kinetics [166]. It has been discovered that the basic morphological unit for chemically synthesized polyaniline also appears to be nanofibers with diameters of tens of nm [330]. The secondary overgrowth of polyaniline on the initially

formed nanofiber scaffolds is responsible for the formation of micron sized particulates of PANi in the final product [329]. Interfacial polymerization is a method by which this secondary overgrowth can be restricted and high quality nanofibers can be obtained.

In interfacial polymerization, a heterogeneous biphasic (organic-aqueous) system is formed by gently pouring an aqueous solution of the dopant and oxidant over an organic solution of the monomer or vice-versa depending on the difference in density between the two phases. However, it is preferred to have the aqueous phase above the organic phase mainly because of the fact that it is easier to collect the PANi nanofibers formed during the reaction. Since the as formed polyaniline product is synthesized in its hydrophilic emeraldine salt form, it diffuses away from the reactive interface into the aqueous layer. This makes more reaction sites available at the interface and suppresses lateral overgrowth. In this way, the nanofibers formed at the interface are collected from the aqueous phase without severe secondary overgrowth.

3.3. Synthesis of polyaniline nanofiber reinforced PVA nanocomposites

Polyaniline nanofiber reinforced PVA nanocomposites have been synthesized using an *in-situ* rapid mixing polymerization. The block diagram depicting the synthesis procedure of PANi nanofiber reinforced PVA nanocomposites films is shown in Fig. 3.2. The process for preparing the PANi nanofiber reinforced polymer nanocomposite films consists of making an aqueous solution of the non-conducting polymer (PVA) and a plasticizer. A definite amount of HCl is added to the solution in order to make its pH less than or equal to 3 (three). The monomer aniline and oxidant are added simultaneously in the molar ratio of 2:1 and the obtained solution is rapidly stirred using a magnetic stirrer. The colour of the clear solution gradually changes to green indicating the formation of PANi nanofibers. The solution is then heated at around 50°-60° C (323-333 K) to make the solution viscous, subsequently it is cast into petri-dish and the solvent is allowed to evaporate slowly giving transparent green films of the PANi nanofiber reinforced PVA nanocomposite.

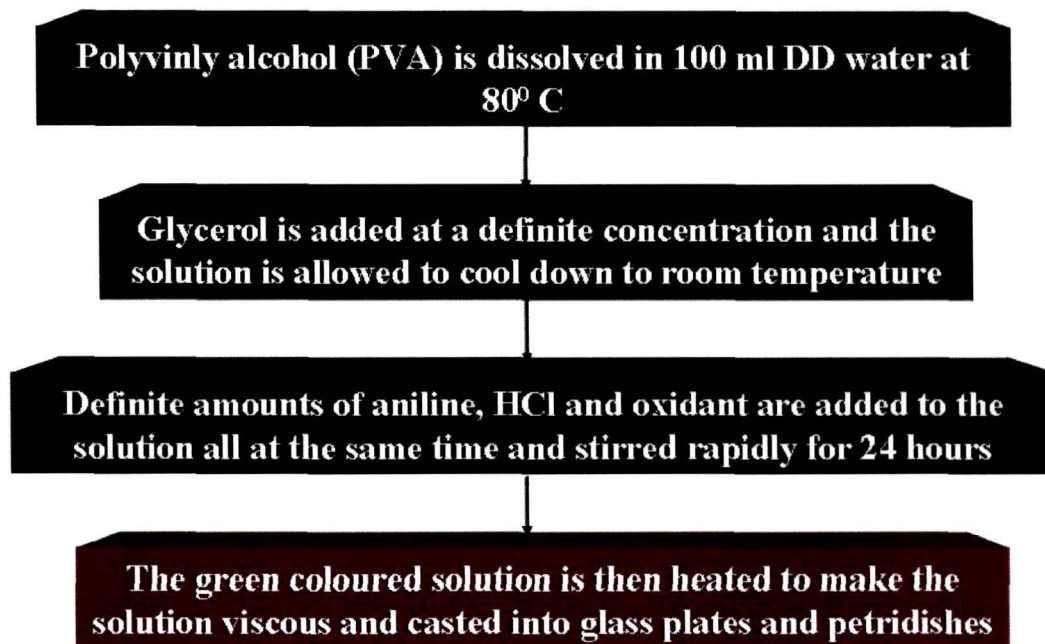


Figure 3.2: Block diagram for the synthesis of polyaniline nanofiber reinforced PVA nanocomposites

3.4. Swift Heavy Ion (SHI) irradiation

Swift heavy ion (SHI) irradiation experiments have been carried out in the Material Science (MS) beam line at Inter University Accelerator Centre (IUAC), New Delhi under ultrahigh vacuum $\sim 10^{-6}$ Torr. The swift heavy ions having high energies (> 1 MeV/u) are provided by the 15 UD Pelletron accelerator at IUAC [406].

The schematic view of the 15 UD Pelletron at IUAC and its different parts are shown in Fig. 3.3. It is basically a tandem electrostatic Van de Graff type accelerator, in vertical configuration, which can go upto a maximum terminal voltage of 16 MV and capable of accelerating any ion from proton to uranium upto an energy of around 200 MeV depending upon the suitable negative ion source and the charge state. The pelletron accelerator consists mainly of two parts: (a) ion source and (b) the accelerating column with many auxiliary parts in between. In the top portion of the tank there are three different ion sources, viz., R.F. source (ALPHATROSS), Source of Negative Ions by Cesium Sputtering (SNICS) and direct extraction negative ion source (Duoplasmatron), which can produce different negative ions to be injected in pelletron tank. These three ion sources working on three different principles can produce almost every type of

negative ions. Duoplasmatron works on the principle of gas discharge, SNICS uses surface ionization and R.F. source utilizes high frequency gas discharge.

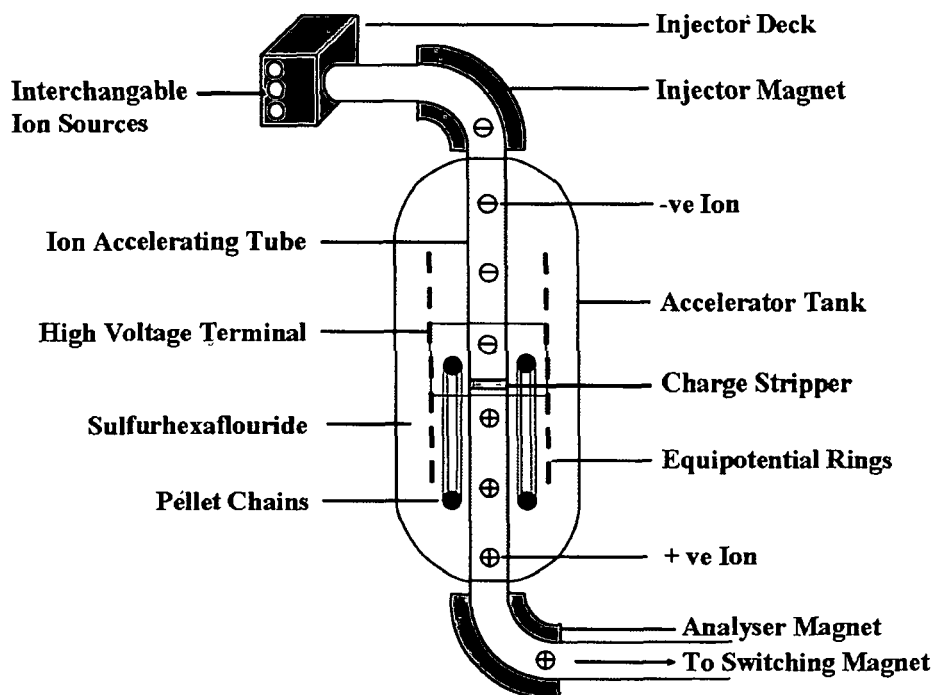


Figure 3.3: Schematic diagram showing the principle of acceleration of ions in a Pelletron (Courtesy: <http://www.iuac.res.in/infrastructure/accelerators/pelletron/index.htm>)

The negative ions emerging from the ion source are first accelerated to 250 keV by the high voltage deck potential and different optical elements focus and inject the same into the vertical accelerating tube. The injector magnet does mass selection by bending the ions by 90° and then injects them into the accelerating tube. The singly ionized negative ions then follow a vertical downward path and get accelerated through the accelerating tube path. It consists of a vertical insulating cylindrical tank of height 26.5 m and diameter 5.5 m, filled with SF₆ (Sulphur hexafluoride) at high pressure (> 200 psi) as an insulating gas. In the top portion of the tank there is an ion source system consisting of a high negative potential deck, SNICS, vacuum system, power supplies and controls of the ion source required to produce and inject the negative ions into accelerating tank. The ion source system is followed by the high voltage accelerating terminal of height 3.18 m and diameter 1.52 m inside the tank. The terminal is connected to the tank vertically through ceramic titanium tubes called accelerating tubes. A potential gradient is maintained through these tubes from high voltage to ground, from top

of the tank to the terminal as well as from the terminal to the bottom of the tank. The insulating column which supports the high potential terminal consists of thirty 1 MV modules, 15 on either side of the terminal. The upper portion of the column is referred to as low energy section and the portion below the terminal as the high energy section. The shorted section with no potential gradient, commonly known as the Dead Section, is provided each in the low and high energy sections for equipment housing. Both are provided with an electron trap and a sputter ion pump. The low energy dead section (LEDS) is also provided with an electrostatic quadrupole lens while the high energy dead section (HEDS) is equipped with a second foil stripper assembly. A shorting rod system is also provided for temporarily shorting selected column modules without entering the pressure vessel. Two insulating shafts run one from each ground end to the terminal and are used to drive four 400 cycle per second (cps) generators, which provide power for the equipments like heater lenses, pumps, foil changer etc., housed in the column, dead sections and terminal. The charging of high voltage terminal to 15 MV is done by using the pelletron charging chains. There are two independent sub systems with one charging chain in each, so that each chain is required to supply 100 μ A current. Negative ions from the ion source are focussed by different optical instruments and then injected by the injector magnet into accelerator with some small energy (>300 KeV) provided by the negative potential deck at the ion source. In the terminal, negative ions are stripped off few electrons by the positive ions which are again accelerated as they proceed towards the bottom of the tank at the ground potential.

The beam energy gained by the ion in the accelerating tube at the end of the tube is determined by,

$$E_{beam} = (q + 1)V_T \quad (3.1)$$

where V_T is the terminal voltage, q is the number of positive charges on the ion after stripping. These high energy ions were analyzed to the required energy with the help of 90° bending magnet known as analyzer magnet and directed to the desired experimental area with the help of switching magnet which can deflect the beam into any one of the seven beam lines in the beam hall for the experiments.

Fig. 3.4 (a, b) shows the Materials Science (MS) beam line and the samples loaded in a ladder. For ion irradiation, the samples of area $1\text{cm} \times 1\text{cm}$ are mounted on a sample holder (ladder) made up of copper. The ladder in the Material Science (MS) chamber is rectangular and 24 samples can be loaded with six samples on each side at a time. After sample loading the ladder is inserted in the MS vacuum chamber. Vacuum inside the irradiation chamber is maintained with the help of a rotary and turbo-molecular pump at $\sim 10^{-6}$ torr during irradiation. All the samples in the present work have been irradiated at normal beam incidence.

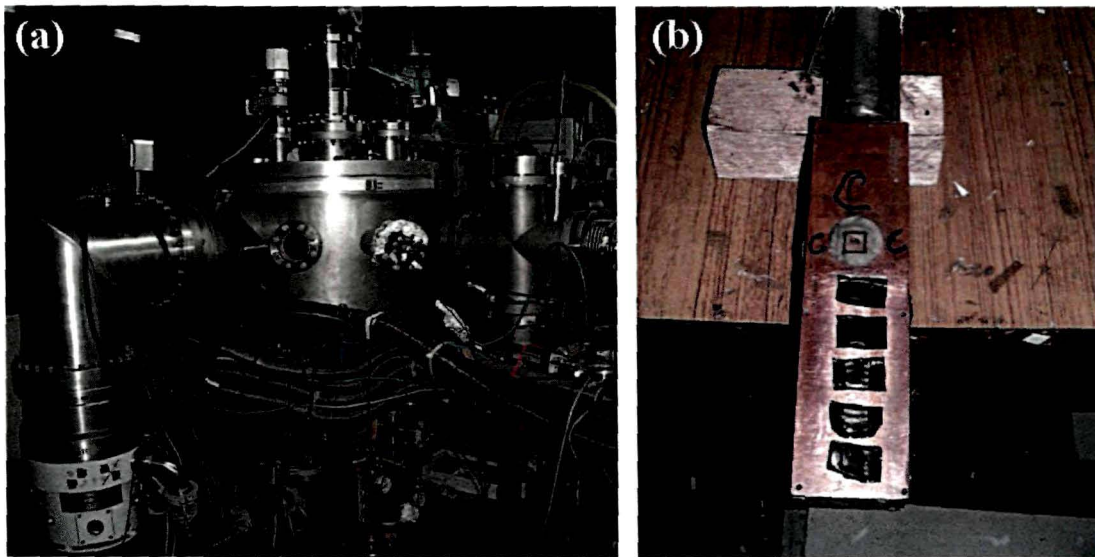


Figure 3.4: Photographs of (a) the high vacuum irradiation chamber in the Materials Science (MS) beam line at IUAC and (b) sample loaded in the ladder used for irradiating the samples

3.4.1. Parameters related to Ion beam

3.4.1.1. Fluence

One of the most important parameter related to ion beams during swift heavy ion (SHI) irradiation is the fluence. Fluence (ϕ) is defined as the total number of irradiating ions incident per square centimeter (ions/cm^2) of the sample. Fluence of an ion beam depends upon the time of irradiation (t), beam current and charge state according to following relation:

$$\text{Fluence } (\phi) = [\text{Time } (t) \times \text{Beam current} \times \text{pnA}] / \text{Charge state} \quad (3.2)$$

Beam currents for ion irradiation experiments are usually taken in the range of 1-5 nA.

$$\begin{aligned} 1 \text{ pA (particle nano-ampere)} &= \frac{10^{-9} \text{ Coul. sec}^{-1}}{1.6 \times 10^{-19} \text{ Coul}} \\ &= 6.25 \times 10^9 \text{ particles/sec} \end{aligned} \quad (3.3)$$

3.4.1.2. Count

The fluences during the irradiation have been recorded by using a counter. Following relation relates the counts and the fluence

$$\text{Counts} = \frac{\phi q e}{S} \quad (3.4)$$

where ϕ is the fluence, q is the charge state of the ion beam, e is the electronic charge (1.6×10^{-19} Coulomb) and S is the scale of the counter.

3.4.1.3. Beam energy

The energy of the accelerated ion beam depends on charge state (q) of the ion and the terminal voltage V_T according to the relation

$$E(\text{MeV}) = (q + 1)V_T + V_{mj} \quad (3.5)$$

For the 15 UD pelletron at Inter University Accelerator Centre, New Delhi, India, the terminal potential V_T is in the range of 10 MV to 15 MV and injector potential (V_{mj}) is in the range of 250 to 350 keV. The projected range of O^{7+} ion beam used in the present work has been calculated using the SRIM-2007 code (SRIM-Stopping Ranges of Ions in Matter) [407].

Table 3.2: SRIM data for O^{7+} ions in different PANi based nanostructured materials

PANi based nanostructured materials	Ion	Energy (MeV)	S_e (eV/Å)	S_n (eV/Å)	Projected Range (μm)
PANi nanostructures			4.739E+01	2.673E-02	124.55
PANi nanofiber reinforced PVA nanocomposites	O^{7+}	90	4.490E+01	2.546E-02	131.78

Table 3.2 gives the incident energy, corresponding electronic energy loss (S_e), nuclear energy loss (S_n) and projected range obtained from SRIM-2007 code for O^{7+} ion beam in the polyaniline (PANi) based nanostructured materials that are investigated in the present work.

3.5. Characterization techniques

3.5.1. *Electron microscopy*

The tremendous advancement in the field of nanoscience and nanotechnology can mainly be associated with the development of sophisticated instruments capable of characterizing the nanomaterials. Electron microscopy is the most efficient technique for investigating the structural and morphological details of nanomaterials.

3.5.1.1. Transmission electron microscopy

Transmission electron microscopy (TEM) is the premier tool for understanding the internal microstructure of materials at the nanometer level. Electrons have an important advantage over X-rays in that they can be focused using electromagnetic lenses. One can obtain real-space images of materials with resolutions on the order of a few tenths to a few nanometers, depending on the imaging conditions, and simultaneously obtain diffraction information from specific regions in the images (e.g. small precipitates) as small as 1 nm [408].

Transmission electron microscope (TEM) uses a high voltage electron beam to create an image. The electrons are emitted by an electron gun, commonly fitted with a tungsten filament cathode as the electron source. The electron beam is accelerated by an anode typically at +100 keV (40 to 400 keV) with respect to the cathode, focused by electrostatic and electromagnetic lenses, and transmitted through the specimen that is in part transparent to electrons and in part scatters them out of the beam. When it emerges from the specimen, the electron beam carries information about the structure of the specimen that is magnified by the objective lens system of the microscope. The spatial variation in this information (the "image") is viewed by projecting the magnified electron image onto a fluorescent viewing screen coated with a phosphor or scintillator material such as zinc sulfide. The image can be photographically recorded by exposing a photographic plate directly to the electron beam, or a high-resolution phosphor may be coupled by means of a lens optical system or a fibre optic light-guide to the sensor of a CCD (charge-coupled device) camera. The image detected by the CCD may be displayed on a monitor or computer. Resolution of the TEM is

limited primarily by spherical aberration, but hardware correction of spherical aberration has allowed the production of images with resolution below 0.5 \AA (50 pm) at magnifications above 50 millions [409].

The TEM studies have been carried out using JEOL JEM 100 CX II transmission electron microscope installed at the Sophisticated Analytical Instrumentation Facility (SAIF), North-Eastern Hill University (NEHU), Shillong, Meghalaya, India shown in Fig. 3.5 (a). The micrographs have been taken at 100 kV accelerating voltage at different magnifications according to need. The samples have been prepared on carbon coated copper grids for viewing under TEM.

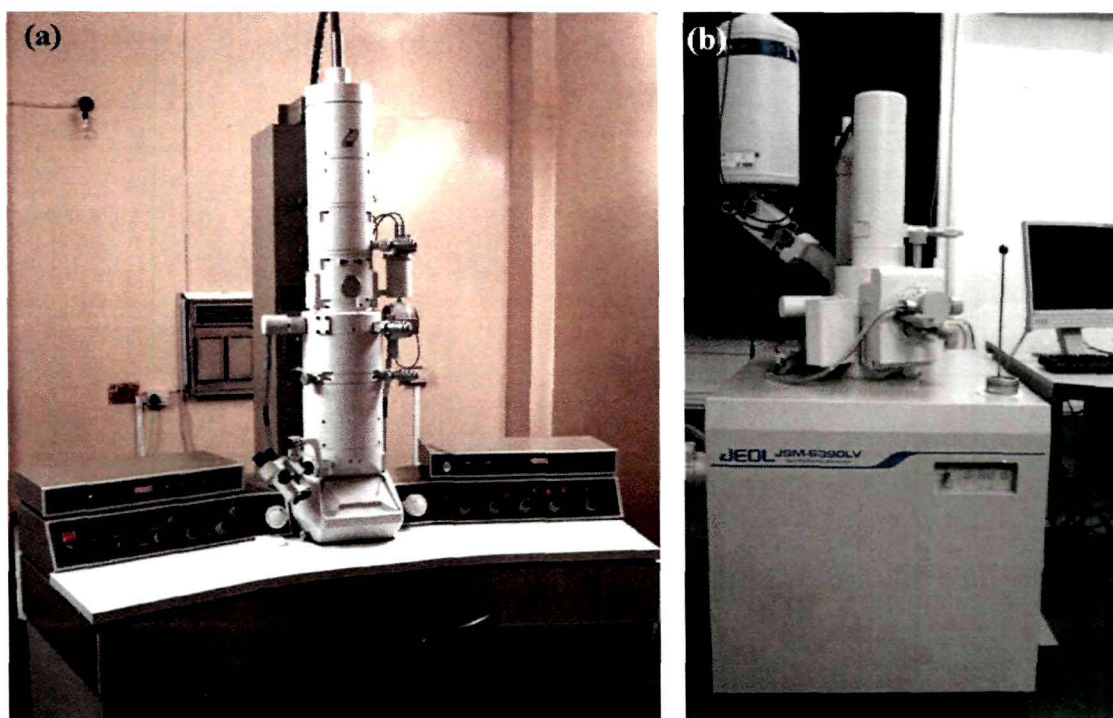


Figure 3.5: (a) Transmission electron microscope (JEOL JEM 100 CXII) at SAIF, NEHU, Shillong and (b) Scanning electron microscope (JEOL JSM 6390 LV) installed at Tezpur University used for acquiring electron micrographs in the present work.

3.5.1.2. Scanning electron microscopy

The scanning electron microscope (SEM) is one of the most widely used instruments in materials research laboratories and is common in various forms in fabrication plants. The SEM study has been carried out using a JEOL JSM 6390 LV model scanning electron microscopy [shown in Fig. 3.5 (b)] installed at Central Instrumentation Facility (CIF), Tezpur University, Assam, India to examine the

surface morphology and porosity. The micrographs have been taken at an accelerating voltage varying between 5-15 kV and magnification is fixed according to need from 2000X to 10000X. The samples have been coated with platinum and placed on carbon tape before viewing.

Scanning electron microscopy is central to microstructural analysis and therefore important to any investigation relating to the processing, properties, and behaviour of materials that involve their microstructure. The SEM provides information relating to topographical features, morphology, phase distribution, compositional differences, crystal structure, crystal orientation, and the presence and location of electrical defects [410]. The SEM electron beam is a focused probe of electrons accelerated to moderately high energy and positioned onto the sample by electromagnetic fields. The SEM optical column is utilized to ensure that the incoming electrons are of similar energy and trajectory. These beam electrons interact with atoms in the specimen by a variety of mechanisms when they impinge on a point on the surface of the specimen. For inelastic interactions, energy is transferred to the sample from the beam, while elastic interactions are defined by a change in trajectory of the beam electrons without loss of energy. Since electrons normally undergo multiple interactions, the inelastic and elastic interactions result in the beam electrons spreading out into the material (changing trajectory from the original focused probe) and losing energy. This simultaneous energy loss and change in trajectory produces an interaction volume within the bulk. The signals resulting from these interactions (e.g. electrons and photons) will each have different depths within the sample from which they can escape due to their unique physical properties and energies.

Lenses in the SEM are not a part of the image formation system but are used to demagnify and focus the electron beam onto the sample surface. This gives rise to two of the major benefits of the SEM: range of magnification and depth of field in the image which allows surfaces at different distances from the lens to appear in focus, and provide three dimensional information [410].

The interaction of high energy electrons with the sample results in the generation of Backscattered electrons (BSEs) and Secondary Electrons (SEs). BSEs are electrons from the incident probe that undergo elastic interactions with the

sample, change trajectory, and escape the sample. These make up the majority of electrons emitted from the specimen at high beam voltage and their average energy is much higher than that of the SEs. The intensity of the BSE signal is a function of the average atomic number (Z) of the specimen, with heavier elements (higher Z samples) producing more BSEs. The BSE intensity and trajectory are also dependent upon the angle of incidence between the beam and the specimen surface. The topography or physical features of the surface are then imaged by using these properties of the BSE signal to generate BSE topographic images. Secondary electrons (SEs) of low energy (typically 2 to 5 eV), on the other hand, are due to inelastic interactions and are influenced more by surface properties than by atomic number. The SE is emitted from an outer shell of a specimen atom upon impact of the incident electron beam. The depth from which SEs escape the specimen is generally between 5 and 50 nm due to their low energy. Secondary electrons are generated by both the beam entering the specimen and BSEs as they escape the specimen; however, SE generation is concentrated around the initial probe diameter. Secondary electron intensity is a function of the surface orientation with respect to the beam and the SE detector and hence produces an image of the specimen morphology [410].

3.5.2. Powder X-ray diffraction (XRD)

X-ray scattering and spectroscopy methods can provide a wealth of information concerning the physical and electronic structure of crystalline and non-crystalline materials in a variety of external conditions and environments. X-ray powder diffraction is one of the most widely used probes for crystal structure determination. This technique is based on the scattering of X-rays by crystals governed by the Bragg's law. Powder X-ray diffraction is used to determine the atomic structure of crystalline, semi-crystalline and amorphous materials without the need for large ($\sim 100 \mu\text{m}$) single crystals. X-ray diffraction patterns give information about crystal structure parameters like crystallite size (domain length in case of semi-crystalline polymers), d -spacing, diffraction planes, structure, phase and lattice constants. In addition to the crystal structure, XRD is applied for various other purposes such as chemical analysis, stress, strain, particle size measurements, phase equilibrium, determination of orientation for single crystals

or the ensemble of orientations in a polycrystalline or polymeric aggregate, order-disorder transformation etc. The intensities and angles of the diffracted X-ray beams are related to the atomic arrangement of the crystal. In case of polymeric materials, XRD is used to determine the proportions of the crystalline and amorphous phases in terms of the degree of crystallinity. X-ray diffraction is also used to determine the domain length in case of polymers. Polymers are semi-crystalline materials. Their crystallinity is attributed to chain folding or to the formation of single or double helices, for at least part of their chain length [411]. This local range of order in polymer chains is referred to as the domain length (L) and can be in the range of angstroms (\AA). The X-ray diffraction patterns for the polyaniline (PAni) based nanostructured materials reported in the present work have been recorded using a Rigaku Miniflex diffractometer with $\text{Cu } K_{\alpha}$ radiation ($\lambda = 1.5406 \text{ \AA}$) shown in Fig. 3.6. The angular range spread over the region between 10° and 70° in 2θ , in steps of 0.05° . The X-ray diffraction patterns have been used to determine the d -spacings, domain length (L), strain (ϵ), and the degree of crystallinity. The methodology adopted for the quantitative estimation of these structural details of the PAni based nanostructured materials specifically the d -spacings, domain length (L), strain (ϵ) and the degree of crystallinity are discussed in the next two subsections (Sections 3.5.2.1 and 3.5.2.2).

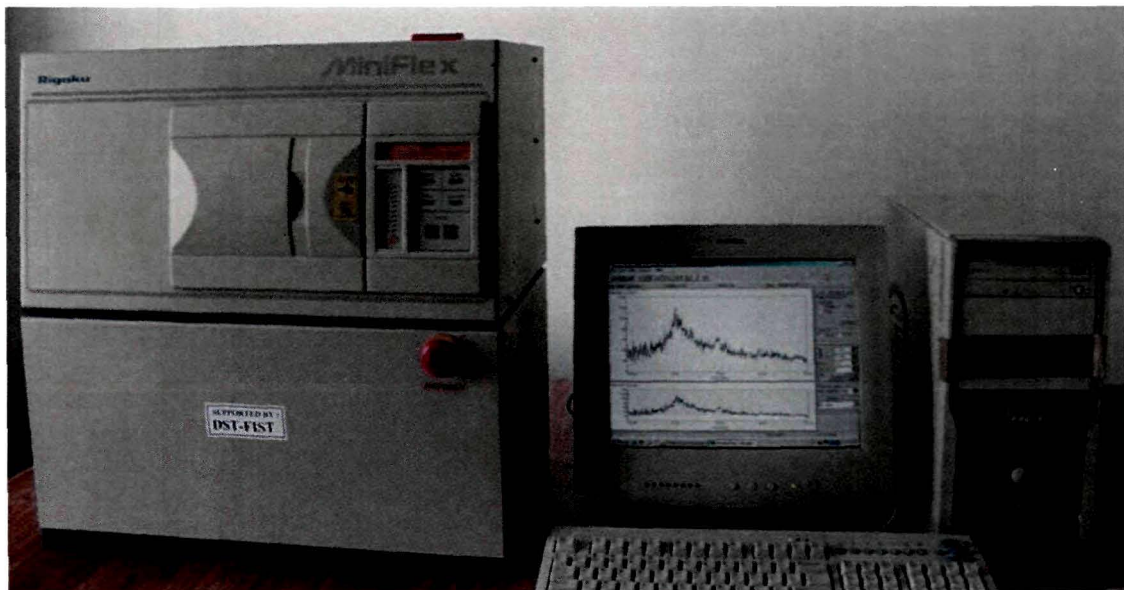


Figure 3.6: Rigaku Miniflex X-ray diffractometer installed at the Department of Physics, Tezpur University

3.5.2.1. Calculation of d -spacing, domain length (L) and strain (ε)

The d -spacings have been deduced from the angular position 2θ of the observed peaks in the X-ray diffraction patterns of the PANi based nanostructured materials, according to the Bragg's formula

$$\lambda = 2d \sin \theta \quad (3.6)$$

Line broadening in the X-ray diffraction patterns may be attributed to two major factors: the size and strain components. The former depends on the size of coherent domains (or incoherently diffracting domains), which is not limited to the grains but may include effects of stacking and twin faults and sub-grain structures (small-angle boundaries, for instance); and the latter is caused by any lattice imperfection (dislocations and different point defects) [412]. The theory is quite general and has been successfully applied to all forms of materials, including oxides and polymers [413].

In the present work, the domain length (L) and strain (ε) of the PANi based nanostructured materials have been calculated using a single line approximation technique employing Voigt function [414]. The measures of dispersion used in earlier studies of crystal imperfections by means of diffraction broadening have been the width of the line profile at half the maximum intensity (FWHM, $2w$) and the integral breadth (β). However, uncertainties arising from the correction of the instrumental broadened in the profile have led to the introduction of the Fourier and variance methods [415]. These methods allow a detailed and accurate analysis of imperfections to be undertaken, but are solely dependent on the quality of the data, necessary expertise and computing facilities that are available to analyse the data.

A limitation in the use of the FWHM or integral breadth is the need to ascribe an analytical function to the line profiles. Earlier workers have assumed that they are Cauchy (Lorentzian) or Gaussian in form, but it has been demonstrated later on [416] that a closer approximation is given by the convolution of these curves, namely the Voigt function. The Voigt function has been adopted by many groups for an analysis of diffraction broadening based on the integral breadth of a single line and the approach has also been used to obtain the domain size and strain in deformed tungsten [414 and refs. therein]. An

explicit equation for the Voigt function has been introduced by Langford in 1978 [417], which shows that the breadths of the Cauchy and Gaussian components can easily be found from the ratio of the FWHM of the broadened profile to its integral breadth ($2w/\beta$). Later on Keijser *et al.* [414] reported that graphical methods or interpolation from tables can be avoided by using empirical formulae and thus the required calculations can be simplified greatly. While it is always desirable to use data from several reflections whenever practicable, the method can be used in single-line analysis.

The measured line profile h is the convolution of the standard profile g with the structurally broadened profile f . Assuming, h , f and g to be Voigt functions [417], we get,

$$h_c = g_c \otimes f_c \text{ and } h_g = g_g \otimes f_g \quad (3.7)$$

where subscripts C and G denote the Cauchy and Gaussian components of the respective Voigt profiles. From Eq. (3.7) it follows that the integral breadths of f_c and f_g , are given by

$$\beta_c^f = \beta_c^h - \beta_c^g \text{ and } (\beta_c^f)^2 = (\beta_c^h)^2 - (\beta_c^g)^2 \quad (3.8)$$

The constituent Cauchy and Gaussian components can be obtained from the ratio $2w/\beta$ for the h and g profiles. However, to avoid graphical methods or interpolation from tables, an empirical formula has been given as [414]:

$$\beta_c = (a_0 + a_1\varphi + a_2\varphi^2)\beta \quad (3.9)$$

and

$$\beta_g = \left[b_0 + b_{12} \left(\varphi - \frac{2}{\pi} \right)^{1/2} + b_1\varphi + b_2\varphi^2 \right] \beta \quad (3.10)$$

where $\varphi = 2w/\beta$, $a_0 = 2.0207$, $a_1 = -0.4803$, $a_2 = -1.7756$, $b_0 = 0.6420$, $b_{12} = 1.4187$, $b_1 = -2.2043$ and $b_2 = 1.8706$.

The maximum error introduced by Eqs. (3.9) and (3.10) is about 1%, and in the majority of cases the error is much less than this. In order to separate size and strain effects, it has been assumed that the size and strain profiles have a Voigtian profile. If two or more reflections are available, size and strain effects can be determined from the variation of β_c^f and β_g^f with hkl [417]. However, in a single-

line analysis it is assumed that the Cauchy component of the f profile is solely due to crystallite size (domain length in case of polymers) and that the Gaussian contribution arises from strain [418]. In a single-line analysis the apparent crystallite or domain length (L) is given by [414]:

$$L = \frac{\lambda}{\beta_C^f \cos \theta} \quad (3.11)$$

and the strain (ε) is given as

$$\varepsilon = \frac{\beta_G^f}{4 \tan \theta} \quad (3.12)$$

where β is measured on a 2θ scale and, if K_α radiation is used, λ and θ are the wavelength and angular position of the α_1 component.

3.5.2.2. Degree of crystallinity

Domain length (L) is a measure of the local range of order (ordering in a single polymer chain) of a polymer whereas the overall ordering in the polymer samples are generally described in terms of the degree of crystallinity. The degree of crystallinity gives quite a good estimation of the amount of crystalline phase present in a polymer sample. A typical X-ray diffractogram for a polymeric material consist of a broad amorphous hump superimposed with some sharp peaks as shown in the Fig. 3.7 (a). The total area under the diffractogram is the sum of the crystalline peaks and broad amorphous hump.

If a typical X-ray diffractogram has two crystalline peaks with areas K_1 and K_2 superimposed on a broad amorphous hump with an area K_3 as shown in Fig. 3.9 (b), then the degree of crystallinity (κ) of the polymer will be

$$\kappa = \frac{\alpha_C(K_1 + K_2)}{\alpha_C(K_1 + K_2) + \alpha_A K_3} \quad (3.13)$$

where α_C and α_A are proportionality constants for the crystalline and amorphous phases, respectively. Assuming $\alpha_C = \alpha_A$ for reasonable accuracy in polymers, the Eq. (3.13) for the degree of crystallinity may be written as

$$\kappa = \frac{K_1 + K_2}{K_1 + K_2 + K_3} = \frac{K}{K_0} \quad (3.14)$$

In order to express the degree of crystallinity in the form of percentage, the above Eq. (3.14) can be modified as

$$\kappa = \frac{K_1 + K_2}{K_1 + K_2 + K_3} \times 100\% = \frac{K}{K_0} \times 100\% \quad (3.15)$$

where K is the sum of the areas of all the crystalline peaks in the diffractogram and K_0 is the total area under the diffractogram. In the present work the area has been calculated by dividing the X-ray diffractogram into minute square grids ($0.5 \times 0.5 \text{ mm}^2$) and counting the number of grids. The degree of crystallinity of a polymer is affected by the secondary valence bonds that can be formed, the structure of the polymer chain (range of order), the physical treatment and the molecular weight of the polymer.

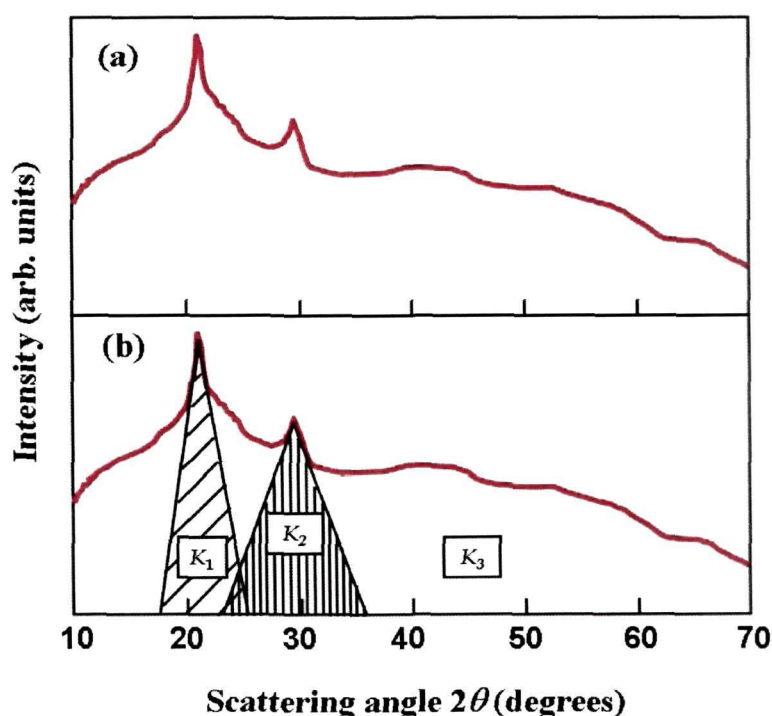


Figure 3.7: (a) Typical X-ray diffractogram of a semi-crystalline polymer and (b) XRD patterns showing the superposition of crystalline peaks and an amorphous hump.

3.5.3. FTIR spectroscopy

Infrared spectroscopy has been a workhorse technique for analysis of materials in the laboratory for over seventy years. Fourier Transform Infrared Spectroscopy (FTIR) is a powerful analytical tool for characterizing and identifying organic molecules, chemical bonds (functional groups) and the molecular structure of organic compounds. Fig. 3.8 describes the layout of a simple FTIR spectrometer. The key modules of a FTIR spectrometer are the

source, the Michelson interferometer and the detector. To use the FTIR instrument, the IR radiation from a continuous source is directed onto the sample of interest and the intensity is measured using an infrared detector. The Michelson interferometer provides the means for the spectrometer to measure all optical frequencies simultaneously. The interferometer modulates the intensity of the individual frequencies of radiation before the detector picks up the signal.

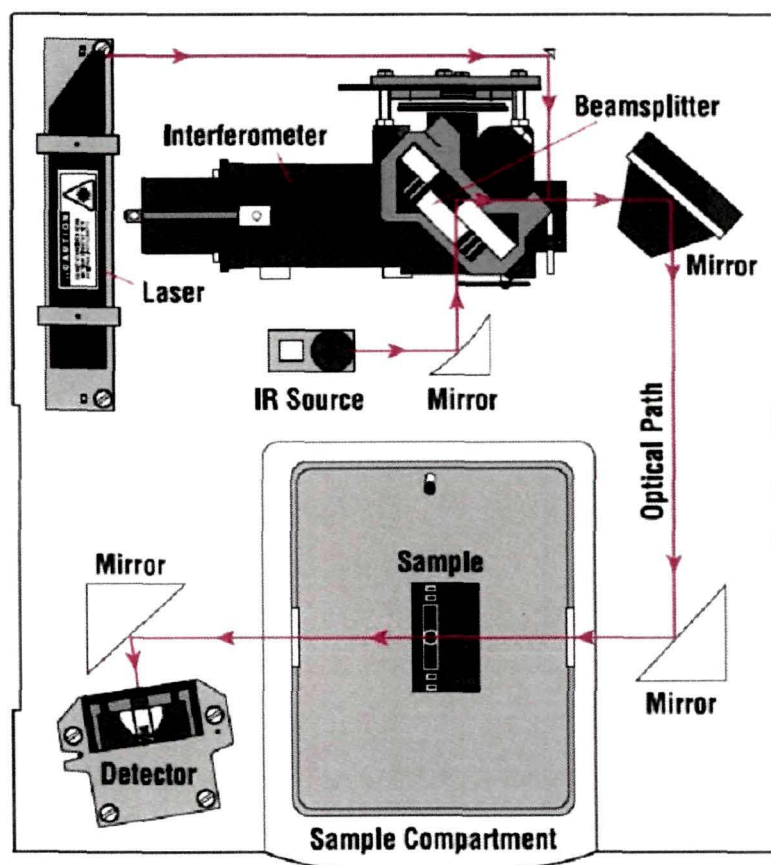


Figure 3.8: Layout of a simple FTIR spectrometer

Part of the infrared radiation is absorbed by the sample and the rest is transmitted. The wavelength of infrared radiation absorbed is characteristic of stretching/bending vibrational modes of a chemical bond. The most useful range for identification of the compounds is the near and mid-infrared region as most of the molecular vibrations lie in these frequency regions. The resulting spectrum represents the molecular absorption and transmission, creating a molecular fingerprint of the sample with absorption peaks which correspond to the frequencies of vibrations between the bonds of the atoms making up the material. Because each material is a unique combination of atoms, no two compounds

produce exactly similar infrared spectra. Therefore, infrared spectroscopy can result in a positive identification (qualitative analysis) of different kind of materials. A single vibrational energy change is accompanied by a number of rotational energy changes, consequently vibrational spectra appear as bands rather than as discrete lines. Band positions are presented as wave numbers (in cm^{-1}). Band intensities are expressed either as transmittance 'T', the ratio of the radiant power transmitted by the sample or the absorbance 'A', logarithm to the base 10 of the reciprocal of the transmittance, $A = \log_{10}(1/T)$. Determination of frequencies, at which the sample absorbs IR radiation, allows the identification of the sample's chemical make-up, since functional groups are known to absorb radiation at specific frequencies. In addition, the size of the peaks in the spectrum is a direct indication of the amount of material present. With modern software algorithms, infrared is an excellent tool for quantitative analysis.

The FTIR spectroscopy study of the polyaniline (PAni) based nanostructured materials have been conducted for understanding the bond structure, compositional and doping studies of the conducting polymers. The FTIR spectra have been recorded using a Perkin Elmer spectrum 100 spectrophotometer installed at Tezpur University, Assam, India.

3.5.4. Ultraviolet-Visible (UV-Vis) spectroscopy

Ultraviolet-visible (UV-Vis) spectroscopy is one of the more ubiquitous analytical and characterization techniques in materials science. Ultraviolet and visible photons are energetic enough to promote valence electrons to higher energy states in molecules and materials. UV-Vis absorption spectroscopy provides key information about the electronic transitions and hence the electronic structure of the material. There is a linear relationship between absorbance and absorber concentration, which makes UV-Vis spectroscopy especially attractive for making quantitative measurements. Ultraviolet-visible absorption spectroscopy involves the absorption of ultraviolet/visible light (wavelengths (λ) between 190 and 900 nm) by a molecule raising electrons from a ground/lower electronic state to an excited/higher electronic state.

In organic molecules and polymers, the UV-Vis spectrum can help in identifying chromophores and the extent of electronic delocalization [419].

information about oxidation states, electronic structure, and metal-ligand interactions. For solid materials, the UV-Vis spectrum can measure the band gap and identify any localized excitations or impurities [410].

There are several types of electronic transitions possible in a molecule including: σ to σ^* (alkanes), σ to π^* (carbonyl compounds), π to π^* (alkenes, carbonyl compounds, alkynes, azo compounds), n to σ^* (oxygen, nitrogen, sulphur and halogen compounds) and n to π^* (carbonyl compounds). Transitions from the highest occupied molecular orbital (HOMO) to the lowest occupied molecular orbital (LUMO) require the least amount of energy and are, therefore, usually the most important. Some electronic transitions are “forbidden” by certain selection rules.

UV-Vis spectroscopy studies of the polyaniline (PAni) based nanostructured materials have been carried out for the study of optical absorption characteristics and hence the energy band structure using a Shimadzu model UV-2450 spectrophotometer as shown in the Fig. 3.9 (a). Pristine and irradiated PAni nanofibers have been dispersed in milli-Q water in a quartz cuvette before taking UV-Vis measurements. The UV-Vis spectra of the PAni nanofibers reinforced nanocomposites films over glass substrates have been acquired after subtraction of glass background.

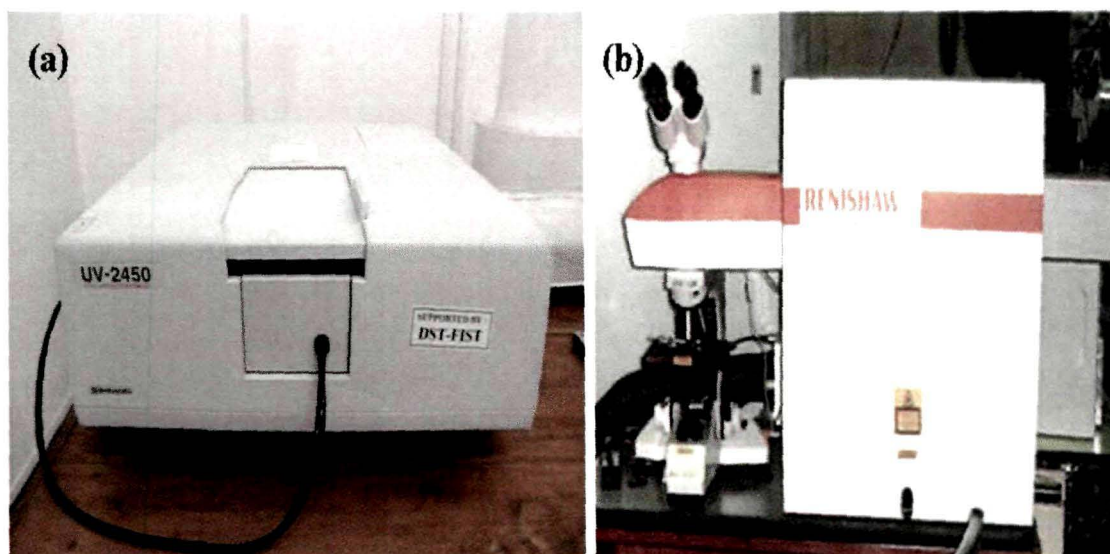


Figure 3.9: Photographs of (a) UV-Visible spectrophotometer (Shimadzu UV-2450) installed at Department of Physics, Tezpur University and (b) The Renishaw in-Via Raman microscope installed at IUAC, New Delhi.

3.5.4.1. Calculation of optical band-gap

The optical absorption coefficient (α) has been calculated from the absorbance (A) using Eqs. (3.16 and 3.17) after correction for reflection:

$$I = I_0 \exp(-\alpha x) \quad (3.16)$$

Eq. (3.16) may be written as

$$\alpha = \frac{2.303}{x} \log\left(\frac{I}{I_0}\right) = \left[\frac{2.303}{x}\right]A \quad (3.17)$$

where x is the thickness of the sample; and A is the absorbance

If we consider d to be the thickness of the quartz cuvette used for the UV-Vis experiments then the equation for the absorption co-efficient [Eq. (3.17)] may be modified as:

$$\alpha = 2.303\left(\frac{A}{d}\right) \quad (3.18)$$

The optical band gap may be evaluated for the values of the absorption coefficient using the following relation:

$$\alpha = \sum \alpha_i = \sum_i \frac{A_i (h\nu - E_{g_i})^{m_i}}{h\nu} \quad (3.19)$$

where the value of E_{g_i} and m_i correspond to the energy and the nature of the particular optical transition with absorption coefficient α_i .

For allowed direct, allowed indirect, forbidden direct and forbidden indirect transitions, the value of m_i corresponds to 1/2, 2, 3/2 and 3, respectively [421]. In an allowed direct transition the electron is simply transferred vertically from the top of the valence band to the bottom of the conduction band, without a change in momentum (wave vector). On the other hand, in materials having an indirect band gap, a transition from the valence to the conduction band must always be associated with a phonon of the right magnitude of crystal momentum.

3.5.5. Micro-Raman (μ R) spectroscopy

In the present work, the micro-Raman (μ R) spectra of the polyaniline (PAni) based nanostructured materials have been acquired using a Renishaw in-Via Raman microscope with Ar ion laser and excitation wavelength of 514.5 nm. The power has been varied from 0.5-1.0 mW and exposure time from 10-20 s

according to the requirement of the sample analysed. Fig. 3.9 (b) shows the Raman microscope installed at Inter University Accelerator Centre (IUAC), New Delhi.

Raman spectroscopy is based on the inelastic scattering of light by matter and is capable of probing the structure of gases, liquids, and solids, both amorphous and crystalline. In addition to its applicability to all states of matter, Raman spectroscopy has a number of other advantages. It can be used to analyze tiny quantities of material (e.g., particles that are ~ 1 μm on edge), as well as samples exposed to a variety of conditions such as high temperature and high pressure and samples embedded in other phases, so long as the surrounding media are optically transparent [410].

Raman scattering results from incident radiation induced transitions in the atoms/molecules of the scattering medium. The transition can be rotational, vibrational, electronic, or a combination (but first-order Raman scattering involves only a single incident photon). In a Raman experiment, the sample is irradiated with monochromatic radiation. If the sample is transparent, most of the light is transmitted, a small fraction is elastically (Rayleigh) scattered, and a very small fraction is inelastically (Raman) scattered. The inelastically scattered light is collected and dispersed, and the results are presented as a Raman spectrum, which plots the intensity of the inelastically scattered light as a function of the shift in wavenumber of the radiation. Each peak in the spectrum corresponds to one or more vibrational modes of the solid. Total number of peaks in the Raman spectrum is related to the number of symmetry- allowed, Raman active modes. Some of the modes may be degenerate and some may have Raman intensities that are too low to be measured, in spite of their symmetry allowed nature. Consequently, the number of peaks in the Raman spectrum will be less than or equal to the number of Raman active modes. The practical usefulness of Raman spectroscopy resides largely in the fact that the Raman spectrum serves as a fingerprint of the scattering material.

The challenge for the so-called nanotechnologies is to achieve perfect control of nanoscale related properties. This obviously requires correlating the parameters of the synthesis process (self assembly, microlithography, sol-gel,

polymer curing, electrochemical deposition, laser ablation) with the resulting nanostructure. Not all conventional techniques are suitable for that purpose but Raman Spectroscopy (RS) has proven to be quite useful for that purpose. For quite a long time this technique has mainly been devoted to fundamental research, but instrumental progress (laser miniaturization, CCD detection, notch filters and data processing softwares) have rendered it a general characterization method. Not only can it provide basic phase identification but subtle spectra alterations can be used to assess nano-scale structural changes and characterize micromechanical behaviour [410].

3.5.6. *Current-Voltage (I-V) characteristics*

The accurate determination of a material's conductivity is critical for understanding material composition or device performance. The method used to determine conductivity depends on whether the material is a bulk sample or a thin film. Two-point measurement using an inexpensive ohmmeter is perhaps the simplest approach for the measurement of conductivity in case of bulk samples, although its accuracy is limited and fairly large samples are required. A current-voltage (I-V) characteristic is a relationship, typically represented as a chart or graph, between an electric current and a corresponding voltage, or potential difference. The conductivity or resistivity of a bulk sample is based on accurate measurement of both resistance and the sample dimensions. The resistance is the ratio of the voltage measured across the sample to the current driven through the sample or of the voltage applied across the sample to the measured current.

For a homogeneous bar of length, L , and uniform cross-section, A , the resistance, R , is related to the resistivity, ρ , by

$$R = \rho L / A \quad (3.20)$$

I-V characteristic curves are used to model the behavior of electronic devices such as bipolar junction transistors (BJTs), heterojunction bipolar transistors (HBTs), junction field effect transistors (JFETs) and various kinds of diodes such as Zener, rectifying, Schottky, laser, light emitting diodes etc. I-V characteristics of the samples investigated in the present thesis have been studied using a Keithley 2400-C source meter interfaced with a PC using a GPIB port as

shown in the Fig. 3.10 (a). The I-V characteristic curves acquired using 2-point probe has been used to determine the resistivity and the conductivity of the samples of a particular thickness and length.

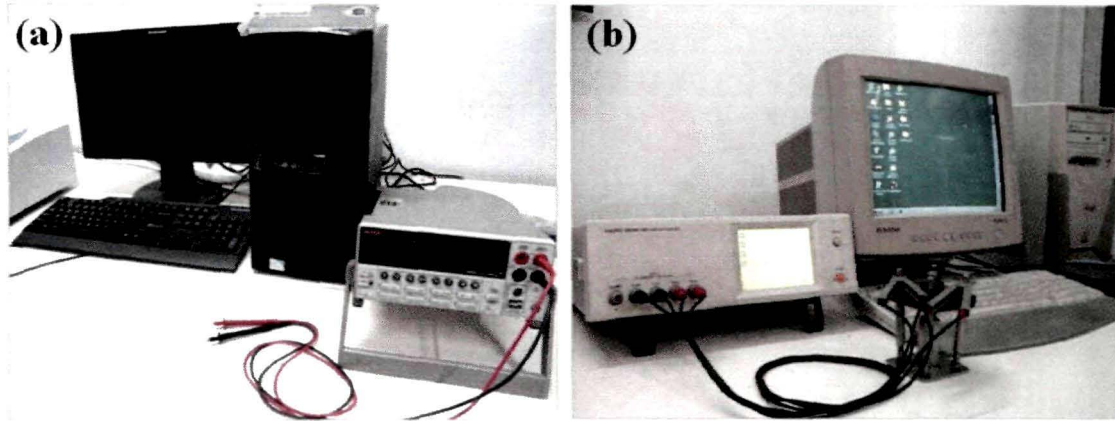


Figure 3.10: Photographs of (a) Keithley 2400-C source meter and (b) HIOKI 3532-50 LCR HiTESTER installed at Materials Research Laboratory, Department of Physics, Tezpur University

3.5.7. Dielectric relaxation spectroscopy

Dielectric relaxation spectroscopy has been widely employed to investigate the charge transport mechanism and relaxation phenomenon in conducting polymers [422, 423]. The overall electric behaviour can be studied by employing different formulations such as the complex impedance Z^* , complex permittivity ϵ^* and complex modulus M^* as discussed in the next subsections. In the present work, a Hioki 3532-50 LCR meter connected with stainless steel circular electrodes (radius=0.5 cm) [Fig. 3.10 (b)] has been used to acquire the data for complex impedance (Z), phase angle (θ), capacitance (C), and other parameters have been calculated from the acquired data using different transformation equations.

In general, the ac electric response is a superposition of the dielectric response of the bound charges (dipoles) along with the hopping of the localized charge carriers and to the response produced by the molecular structure deformations due to the diffusion of charge carriers [422]. Different types of polarization mechanisms can co-exist in the same material. Besides the conductivity and dipolar polarization, there are electrode effects, interfacial effects and space charge relaxations. The correct interpretation of the experiments is obtained by verifying the reliability and physical grounding of the model by

which the fitting procedure is carried out. The dielectric function ε^* is used to study the polarization mechanisms, whereas the complex impedance Z^* and the electric modulus M^* usually are used to describe the conductivity relaxation mechanisms of the materials [424].

3.5.7.1. Permittivity formalism

The real (ε') and imaginary (ε'') part of the complex permittivity (ε^*) is calculated from the measured values of the capacitance (C) and the loss tangent ($\tan \delta$) using the Eqs. 3.21 and 3.22, respectively.

$$\varepsilon' = Cd/\varepsilon_0 A \quad (3.21)$$

$$\varepsilon'' = \varepsilon' \tan \delta \quad (3.22)$$

where C is the measured capacitance, d is the thickness of the sample, A is the area of the pellet and, ε_0 is the permittivity of free space.

3.5.7.2. Impedance formalism

The real (Z') and imaginary part (Z'') of the complex impedance (Z^*) can be written as:

$$Z' = |Z| \cos(\phi) \quad (3.23)$$

and $Z'' = |Z| \sin(\phi) \quad (3.24)$

where, phase angle $\phi = \tan^{-1} \frac{Z''}{Z'}$ and $|Z| = \sqrt{Z'^2 + Z''^2}$.

The real (Z') and imaginary part (Z'') of the complex impedance (Z^*) has been calculated according to the Eqs. (3.23) and (3.24) using the measured values of $|Z|$ and phase angle (ϕ) over the frequency range of 50 Hz -5 MHz acquired by the HIOKI LCR meter.

3.5.7.3. Modulus formalism

Complex electric modulus or inverse complex permittivity (M^*) is defined by the equation,

$$M^* = \frac{1}{\varepsilon^*} = \frac{1}{\varepsilon' - j\varepsilon''} = \frac{\varepsilon'^2}{\varepsilon'^2 + \varepsilon''^2} + j \frac{\varepsilon''}{\varepsilon'^2 + \varepsilon''^2} = M' + jM'' \quad (3.25)$$

where $j = \sqrt{-1}$ and M' and M'' are the real and the imaginary part of complex modulus (M^*), respectively, which have been calculated by transforming the data obtained for the real and imaginary parts of permittivity using the Eq. (3.25).

3.5.8. AC conductivity measurements

The variation in AC conductivity of the PANi based nanostructured materials as a function of frequency and temperature have been derived using the measured values of the conductance $G(\omega)$ according to the Eq. (3.26). The values of conductance have been acquired using the HIOKI LCR meter [Fig. 3.10 (b)].

$$\sigma(\omega) = G(\omega) \cdot \frac{d}{A} \quad (3.26)$$

where d is the thickness and A is the cross-sectional area of the sample.

3.6. Positron Annihilation lifetime spectroscopy

The sensitivity of positrons to lattice defects, particularly vacancy-type defects, in condensed medium has made it possible to use it extensively as an atomic level probe to study defects in a wide variety of solids including polymers [425, 426]. Positron annihilation lifetime (PAL) measurements at room temperature were carried out at Variable Electron Cyclotron Centre (VECC), Kolkata, India. A $4 \mu\text{Ci } ^{22}\text{Na}$ positron source was used as the positron source and was sandwiched between two identical thick films of PANi nanofiber reinforced PVA nanocomposites. The sandwich was then placed in between two ultra fast BaF_2 scintillators (2.5 cm diameter and 2.5 cm thick) coupled to two XP2020Q photomultiplier tubes. These scintillation counters grafted into a slow-fast coincidence assembly constituted the PAL coincidence spectrometer. A time resolution of 190 ps was achieved in this setup. Not less than 0.5 million total coincidence counts were recorded in each of the spectra. The lifetime data were analyzed by using the computer program PATFIT-88.

3.7. Antioxidant activity assay

The antioxidant assays of the material were performed both with respect to time and concentration of the samples following the method of Serpen *et al.* [427]. 0.2–0.8 mg of the material was applied to 3.0 ml of 100 μM DPPH solution in HPLC grade MeOH. The reaction mixture was vortexed for 30 secs and incubated in the dark for 15 min, after which the wavelength scanning was performed using the Shimadzu 2450 UV-Vis spectrophotometer [Fig. 3.9 (a)]. In order to study the time dependence of the antioxidant activity the maximum concentration of each

sample was applied to the 3 ml DPPH solution and the spectra were recorded with 5 min interval from $t = 0$ to 30 min. The DPPH degradation was calculated using the formula:

$$\% \text{ of DPPH scavenging} = \frac{(A_B - A_S)}{A_B} \times 100 \quad (3.27)$$

where A_B is the absorption of the blank and A_S is the absorption of the sample.

3.8. Haemolysis prevention assay

The haemolysis prevention activity was studied following the procedure of Miki *et al.* [428]. Blood was collected from a slaughter house ethically maintained by Tezpur local district administration (Assam, India) using 1/10th volume of 3.8% sodium citrate out of the total blood volume. Blood was then centrifuged in a 50 ml centrifuge tube using an MPW centrifuge at 3000 rpm for 5 min. The supernatant containing platelet-poor plasma was discarded and the pellet containing RBC was suspended in 10 volumes of phosphate buffer saline (PBS) of pH 7.4. The process was repeated two more times to completely remove the buffy coat of RBC. Finally the cells were suspended in PBS to get a uniform suspension of cells. The polyaniline nanofiber samples were suspended in PBS at a concentration of 5 mg/ml and sonicated for 10 min. From the suspension 20 μ l of material was pipetted out into the test tubes. H_2O_2 was added to get 100 μ M concentrations in 3 ml. After allowing the reaction to occur for 5 min, the tubes were subjected to 3 ml blood and incubated for 1 h at 37° C. After incubation, the samples were centrifuged at 3000 rpm for 5 min to pellet out RBC cells. The supernatants were carefully separated using a 1 ml micropipette and used for absorption studies at 540 nm. The percentage of haemolysis prevention was calculated using the relation as follows:

$$\% \text{ of haemolysis prevention} = \frac{A_B - A_S}{A_B} \times 100 \quad (3.28)$$

where A_B is the absorption of the blank and A_S is the absorption of the sample.

3.9. Characterization of QCM based chemical sensors

The characterization of the PANi nanofiber reinforced PVA nanocomposite modified Quartz crystal microbalance (QCM) sensors have been carried out using

a QCM set-up. Fig. 3.12 shows the photograph of the experimental set up of a QCM 200 Quartz crystal microbalance oscillator interfaced with a PC using RS-232 port for on-line data acquisition. The inset of the figure shows a 5 MHz AT-cut quartz crystal coated with gold electrodes.

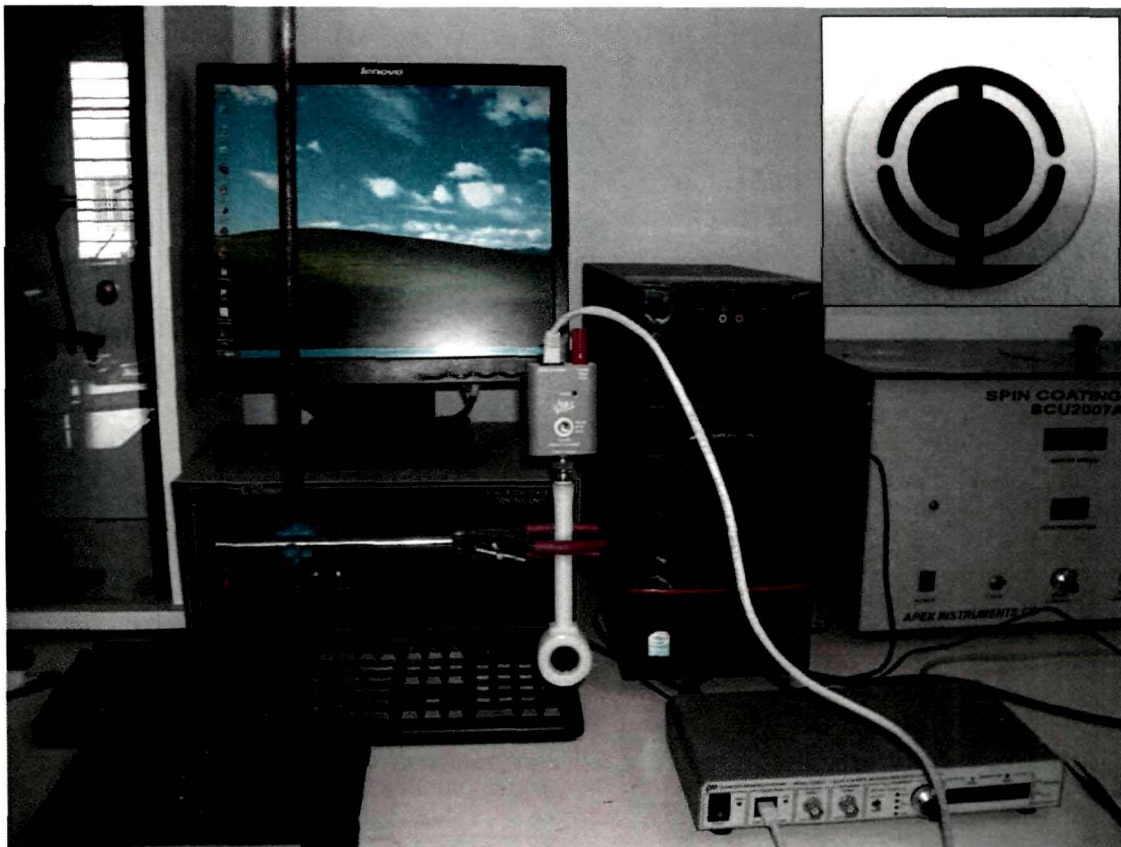


Figure 3.11: Experimental set-up of the Quartz crystal microbalance (QCM) interfaced with a PC. The inset shows a gold coated quartz crystal oscillator.

3.9.1. Response time of the sensor

Sensors do not change output state immediately when an input parameter change occurs. Rather, it will change to the new state over a period of time, called the response time. The response time can be defined as the time required for a sensor output to change from its previous state to a final settled value within a tolerance band of the correct new value. This concept is somewhat different from the notion of the time constant of the system. This term can be defined in a manner similar to that for a capacitor charging through a resistance and is usually less than the response time. The response time of the sensor has been determined using the response characteristic curves for the sensor for different concentration of the analytes.

3.9.2. Linearity of the sensor

The linearity of a sensor is an expression of the extent to which the actual measured curve of a sensor departs from the ideal curve. Linearity is often specified in terms of percentage of nonlinearity, which is defined as:

$$\text{Nonlinearity (\%)} = \frac{D_{m(\max)}}{IN_{f.s.}} \times 100 \quad (3.28)$$

where

Nonlinearity (%) is the percentage of nonlinearity

$D_{m(\max)}$ is the maximum input deviation

$IN_{f.s.}$ is the maximum, full-scale input

The static nonlinearity defined by Eq. (3.28) is often subject to environmental factors, including temperature, vibration, acoustic noise level, and humidity. It is important to know under what conditions the specification is valid and departures from those conditions may not yield linear changes of linearity.

3.9.3. Sensitivity of the sensor

Definitions of sensitivity fall into two contrasting categories. In some fields, sensitivity is the ratio of response to cause. Hence increasing sensitivity is denoted by a progressively larger number. In other fields, sensitivity is the ratio of cause to response. Hence increasing sensitivity is denoted by a progressively smaller number.

Sensitivity is often defined as the ratio of the magnitude of response to the magnitude of the quantity measured. Another definition is taken as the minimum input signal required to produce a specified output signal having a specified signal-to-noise ratio. In general, the sensitivity of the sensor is commonly defined as the slope of the output characteristic curve (dy/dx) or, more generally, the minimum input of physical parameter that will create a detectable output change.

Chapter 4

POLYANILINE NANOFIBERS: SYNTHESIS, SHI IRRADIATION AND CHARACTERIZATION

This chapter deals with the synthesis of Polyaniline (PAni) nanofibers by interfacial polymerization technique and their characterization. A systematic study on the structure-property relationship of PAni nanostructures has been accomplished by means of sophisticated characterization techniques and forms a major portion of this chapter. Morphological, structural and conformational modifications in PAni nanofibers upon swift heavy ion (SHI) irradiation have also been discussed.

4.1. Introduction

Recently, one dimensional (1D) nanostructures such as nanofibers, nanowires, nanorods, nanobelts, and nanotubes have attracted considerable attention of the scientific community owing to their unique applications in mesoscopic physics and fabrication of nanoscale devices. 1D nanostructures are ideal systems for investigating the dependence of electrical, thermal and mechanical properties on quantum confinement and dimensionality. 1D conducting polymer nanostructures deserve a special mention mainly because they combine the advantages of organic conductors with low dimensionality. Polyaniline (PAni) is one of the most extensively studied organic conducting polymers because of its ease of synthesis, environmental stability, ease of doping and good processibility. It has been observed that conventional polyaniline synthesis produces particulate products with irregular shapes. As such many methods have been developed to shape polyaniline into nanostructures by either introducing “structural templates” such as nanoporous membranes and micelles

to the polymerization reaction [146-148, 150, 153, 155, 324] or by post-synthetic polymer fiber processing technologies such as electrospinning [152]. However, it has been very difficult to obtain pure, small diameter polyaniline nanofibers (< 100 nm) in desirable quantities. R. B. Kaner and his group discovered that the basic morphological unit for polyaniline are nanofibers with diameters of tens of nanometers [330]. It has been observed that in the early stages of the polymerization reaction these nanofibers are naturally formed and are much smaller in diameter than most of the templated or electrospun fibers. In conventional polymerization, overgrowth of polyaniline on these nanofiber scaffolds leads to the final irregularly shaped micron sized particulates. In order to separate nanofiber formation from secondary overgrowth two basic approaches viz., interfacial polymerization and rapid mixing polymerization have been developed. In interfacial polymerization, the polymerization reaction is placed in a heterogeneous biphasic system, where the polymerization occurs only at the interface [324, 329]. Since the polyaniline product is synthesized in its hydrophilic emeraldine salt form, it diffuses away from the reactive interface into the water layer. This makes more reaction sites available at the interface and avoids further overgrowth. In this way, the nanofibers formed at the interface are collected in the water layer without severe secondary overgrowth. In rapid mixing polymerization approach, the polymerization is made to stop as soon as the nanofibers are formed by rapidly mixing the monomer and initiator solutions [329]. When the reaction starts, the initiator molecules are consumed rapidly during polymerization and depleted after nanofiber formation. Therefore, the overgrowth of polyaniline is suppressed due to lack of initiator molecules. It has been observed that these nanostructures not only augment the existing properties of the bulk material but also give rise to some novel properties leading to new and exciting applications. Polyaniline nanofibers have been used for a wide range of applications. Chemical sensors fabricated using PANi nanofibers have shown remarkable enhancement in sensitivity and response time [155]. Polyaniline nanofiber based nanocomposites have found applications in novel non-volatile molecular memory device [158]. Such polyaniline based memory devices (PANi-MEM) have switching times in the order of nanoseconds, high on/off ratios and

low manufacturing costs, making them very promising for faster and less expensive data storage media as compared to the currently available flash memories. The nanoscale structure of polyaniline nanofibers produces enhanced polymer functionalities; their polymeric nature also yields new nanoscale physicochemical phenomena that have not been observed in inorganic nanostructured materials [159]. Flash welding is such a phenomenon that has been observed in PANi nanofibers, when they are exposed to light (such as a camera flash) [159]. The high photo-thermal conversion efficiency converts most of the absorbed energy into heat. In PANi nanofibers, the heat generated through photo-thermal processes is confined within the individual nanofibers since PANi is a poor heat conductor. It has been suggested by Kaner and his group that under flash irradiation, polyaniline nanofibers instantly “melt” to form a smooth and continuous film from an originally random network of nanofibers and leads to many exciting potential applications such as creation of a free-standing asymmetric membrane from a nanofiber powder film, industrial separations, for imprinting patterns into nanofiber films by using a photo-mask and for welding PANi to another polymer such as polystyrene or even Teflon (polytetrafluoroethylene) leading to the formation of polymer-polymer nanocomposites [159].

Irradiation of conducting polymers by swift heavy ions (SHI) brings about remarkable and unprecedented variations in the physico-chemical properties of the polymer as discussed earlier in section 1.3 of Chapter 1. However, effects of SHI irradiation on nanostructures of conducting polymers have not been reported earlier. In this study a sincere effort has been made for a systematic study of PANi nanofibers and the physico-chemical modifications in PANi nanofibers upon swift heavy ion (SHI) irradiation. In this chapter, the synthesis of PANi nanofibers using interfacial polymerization has been discussed in details. Characterization by Transmission electron microscopy (TEM), X-ray diffraction (XRD), Fourier Transform Infrared (FTIR) spectroscopy, Micro-Raman (μ R) spectroscopy, UV-Visible spectroscopy, Two probe I-V measurements, Dielectric spectroscopy and AC conductivity measurements have been carried out on PANi nanofibers before

and after irradiation with 90 MeV O^{7+} ions and the results thereof are presented and analyzed in this chapter.

4.2. Synthesis of polyaniline nanofibers

Polyaniline (PAni) nanofibers have been synthesized using the interfacial polymerization technique as described in section 3.2 of chapter 3 [155, 324]. The monomer aniline (p.a. Merck) has been distilled under reduced pressure and kept in darkness at room temperature prior to use. All other chemicals used are analytical grade reagents purchased from Merck and used as received without any further purification. Carbon tetrachloride (CCl_4) has been used as the organic solvent to dissolve aniline. Ammonium peroxydisulfate (APS) is used as the oxidant while hydrochloric acid (HCl) and camphor sulfonic acid (CSA) have been used as dopant acids. The interfacial polymerization reaction has been performed in 30 ml glass vials (Fig 4.1). Aniline (1M) has been dissolved in 10 ml of CCl_4 . Ammonium peroxydisulfate (0.25 M) and the dopant acid (1M) are dissolved in 10 ml of double distilled water. The interface for polymerization is formed by pouring the aqueous solution of the oxidant and the dopant acid very carefully and slowly over the organic solution of the monomer aniline in CCl_4 . The molar ratio of aniline to ammonium peroxydisulfate has been maintained at 4:1. The synthesized PAni nanofibers have then been washed with HPLC grade methanol and filtered several times before further studies.

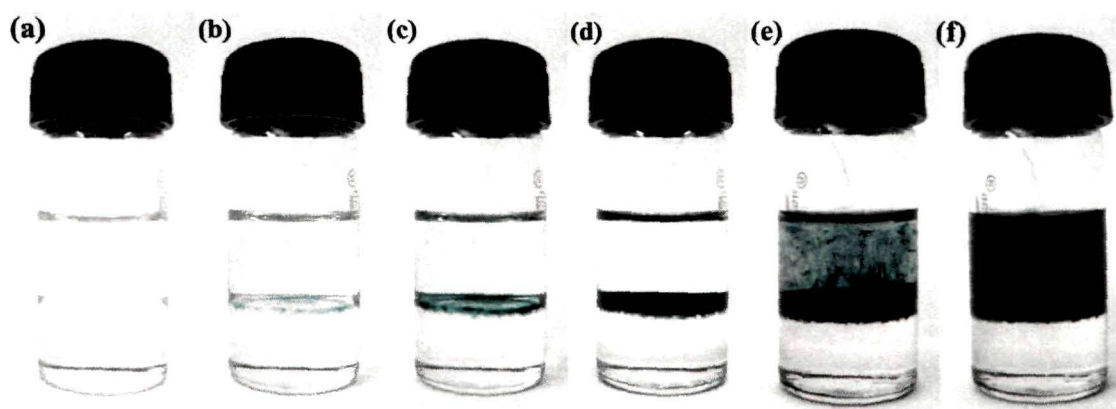


Figure 4.1: Snapshots of the various stages of PAni nanofiber formation at various times (a) $t = 0$, (b) $t = 5$ min, (c) $t = 10$ min, (d) $t = 15$ min, (e) $t = 20$ min and (f) $t = 30$ min.

The purified PAni nanofibers have been dispersed uniformly in a 2% PVA solution for casting thin films (thickness ~ 50 μm) on glass slides of area 1 cm^2 for

irradiation purpose. Small amount of PVA acts as a matrix and does not affect the properties of the PANi nanofibers. Thin films of the nanofibers have been irradiated with 90 MeV O^{7+} ions with a mean projected range ($\sim 120 \mu\text{m}$) much larger than the thickness of the films. The irradiation fluence has been varied from 3×10^{10} to 1×10^{12} ions cm^{-2} using the 15UD Pelletron accelerator at the Inter University Accelerator Centre (IUAC), New Delhi. The vacuum inside the irradiation chamber has been maintained with the help of rotary and turbomolecular pumps at $\sim 10^{-6}$ Torr during irradiation. All the samples have been irradiated at normal beam incidence.

4.3. Characterization of pristine and SHI irradiated polyaniline nanofibers

4.3.1. Transmission Electron microscopy

Figures 4.2 (a) & (b) show the transmission electron micrographs of polyaniline (PANi) nanofibers doped with 1M hydrochloric acid (HCl) [Fig. 4.2 (a)] and 1M camphor sulfonic acid (CSA) [Fig. 4.2 (b)]. Interfacial polymerization is a technique wherein the secondary overgrowth is restricted resulting in pure nanofibers as evident from the TEM micrographs.

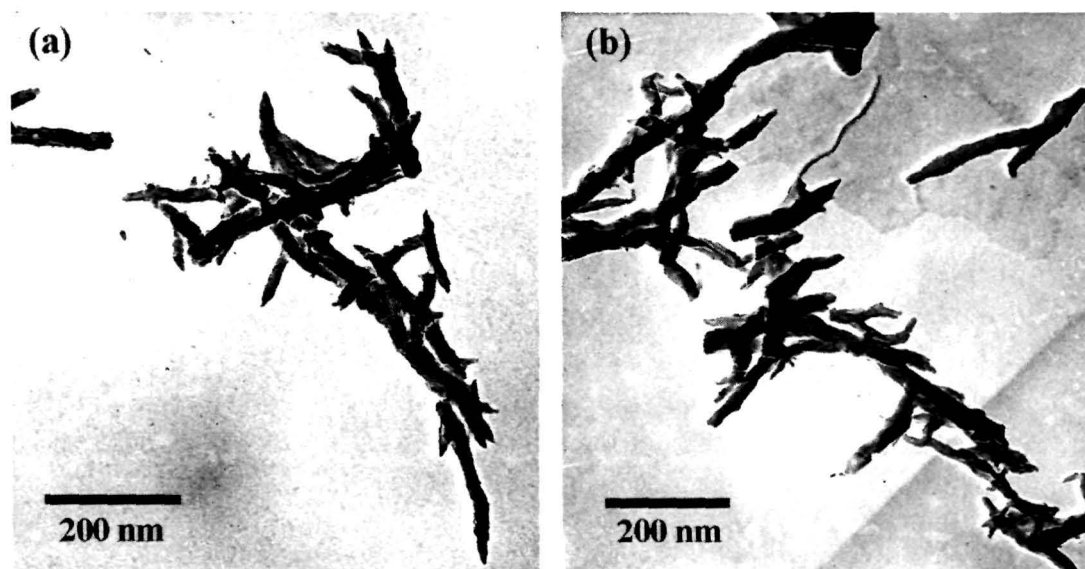


Figure 4.2: Transmission electron micrographs of PANi nanofibers doped with (a) 1M HCl and (b) 1M CSA

It is also observed that the nature of the dopant acid plays an important role in determining the diameter of the polyaniline nanofibers. The distribution of

diameters of the HCl and CSA doped PANi nanofibers are shown in the Figs 4.3 (a) and (b). The diameter distribution of the PANi nanofibers have been determined from the TEM micrographs. The bars shown in the Figs. 4.3 (a) and (b) represent the number of PANi nanofibers with the corresponding diameters shown on the abscissa as determined from the TEM micrographs. The distribution of diameters of the PANi nanofibers have been fitted with a Gaussian distribution function using Origin 8.5 software which calculates the average diameter of the distribution. The average diameter of the PANi nanofibers doped with HCl is 28.42 nm, whereas that for the nanofibers doped with CSA is 46.63 nm, indicating that less secondary growth takes place in HCl-doped PANi nanofibers.

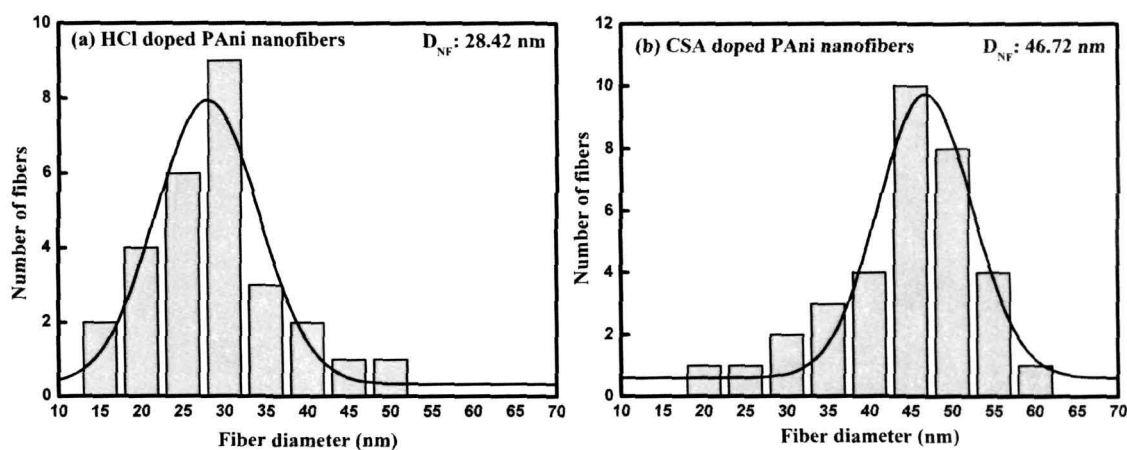


Figure 4.3: Diameter distribution of PANi nanofibers doped with (a) 1M HCl and (b) 1M CSA.

Swift heavy ions interacting with materials are known to leave a damage trail known as the “Latent track” [400]. Track formation in polymers, have been investigated by TEM experiments [429] but track formation mechanism in polymers is poorly understood. Two phenomenological models are generally used to describe the formation of tracks and the conversion mechanism of the energy of the excited electrons into the kinetic energy of the target atoms in materials. The Coulomb-explosion model is based on the assumption that the intense ionization and excitation along the ion path leads to an unstable zone in which atoms are ejected into the non-excited part of the solid by Coulomb explosion [402]. In the thermal-spike model, the energy deposited by the ion leads to a transient temperature increase and the cylindrical volume around the ion path melts due to electron-phonon coupling, which is subsequently quenched by

thermal conduction [430, 431]. The effects of swift heavy ions (SHI) on the structural and morphological features of PANi nanofibers have been investigated using Transmission electron microscopy (TEM). Figures 4.4 (a)-(d) and 4.5 (a)-(d) are the transmission electron micrographs of the pristine and 90 MeV O^{7+} ion irradiated PANi nanofibers doped with HCl and CSA, respectively. The TEM micrographs reveal a continuous decrease in the length as well as the diameter of the PANi nanofibers with increasing ion fluence.

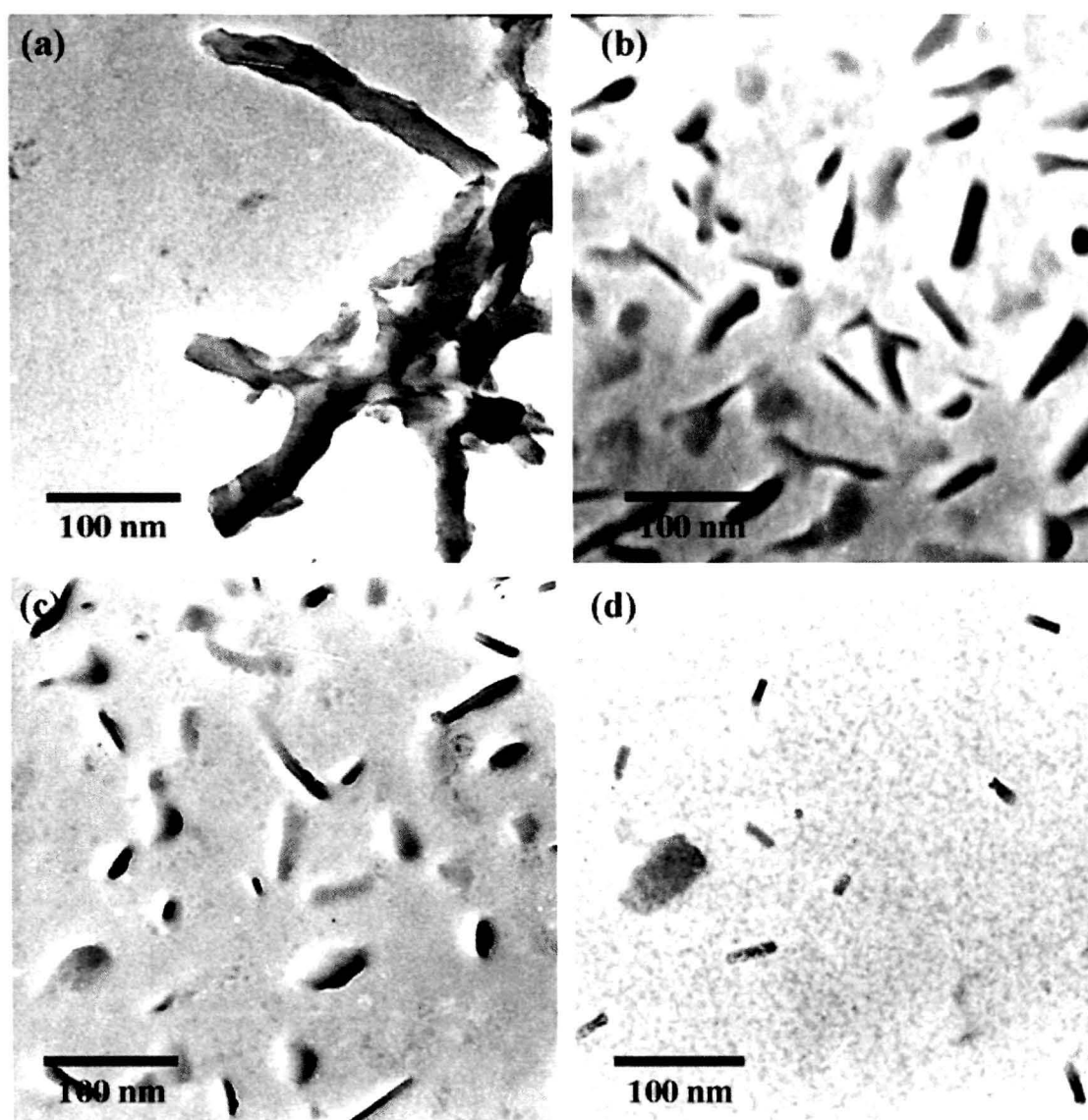


Figure 4.4: Transmission electron micrographs of HCl doped polyaniline nanofibers (a) before irradiation; and after irradiation with 90 MeV O^{7+} ions at fluences (b) 3×10^{10} , (c) 3×10^{11} and (d) 1×10^{12} ions cm^{-2} .

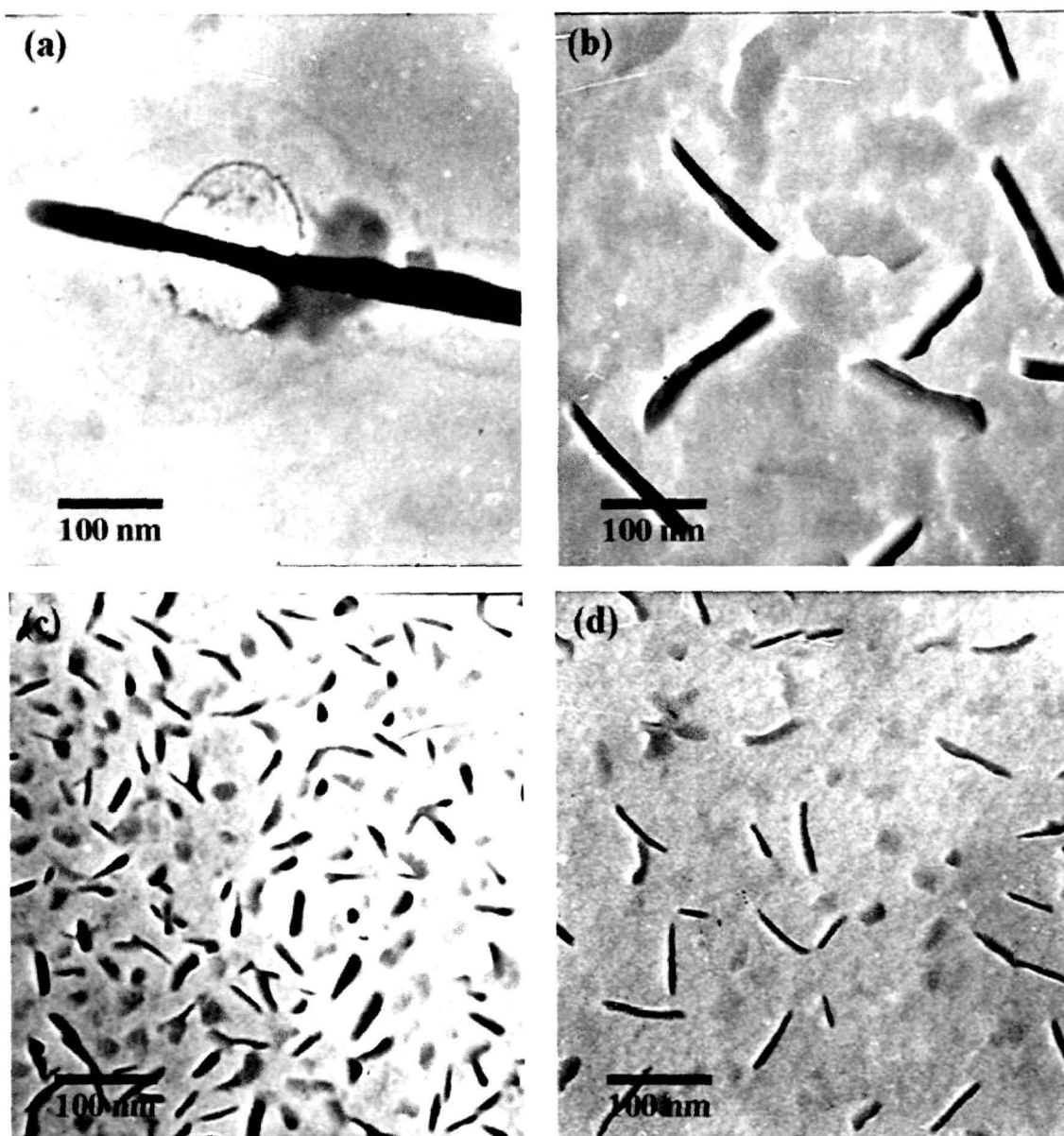


Figure 4.5: Transmission electron micrographs of CSA doped polyaniline nanofibers (a) before irradiation; and after irradiation with 90 MeV O^{7+} ions at fluences (b) 3×10^{10} , (c) 3×10^{11} and (d) 1×10^{12} ions cm^{-2} .

The diameter distributions of the pristine and irradiated PANi nanofibers doped with HCl and CSA have been determined from the TEM micrographs and are presented in Figs. 4.6 (a)-(d) and Figs. 4.7 (a)-(d). The average diameters of the pristine and 90 MeV O^{7+} ion irradiated PANi nanofibers have been determined in the same way as mentioned earlier. It is observed from the Gaussian fitting of the diameter distribution that with the increase in irradiation fluence the average diameter of the HCl doped PANi nanofiber decreases from 29.35 nm to about 9.45

nm, whereas for the CSA doped PANi nanofibers the average diameter decreases monotonically from 50 nm to 11.38 nm with increasing irradiation fluence.

Conjugated (conducting) polymers are organic materials that conduct when doped. Depending upon the degree of doping, the carrier concentration in conducting polymers is comparable to that of semiconductors/metals; the carrier mobility, however, is very low ($\sim 10^{-4} \text{ cm}^2 \text{ V}^{-1} \text{ s}^{-1}$) as compared to that of semiconductors/metals ($\sim 10^2\text{--}10^5 \text{ cm}^2 \text{ V}^{-1} \text{ s}^{-1}$). Therefore, in conjugated polymers the charge neutrality cannot be re-established upon SHI irradiation on the timescale of lattice vibrations (10^{-13} s), as is required in thermal spike model, which is used to explain the SHI irradiation effects on semiconductors/metals.

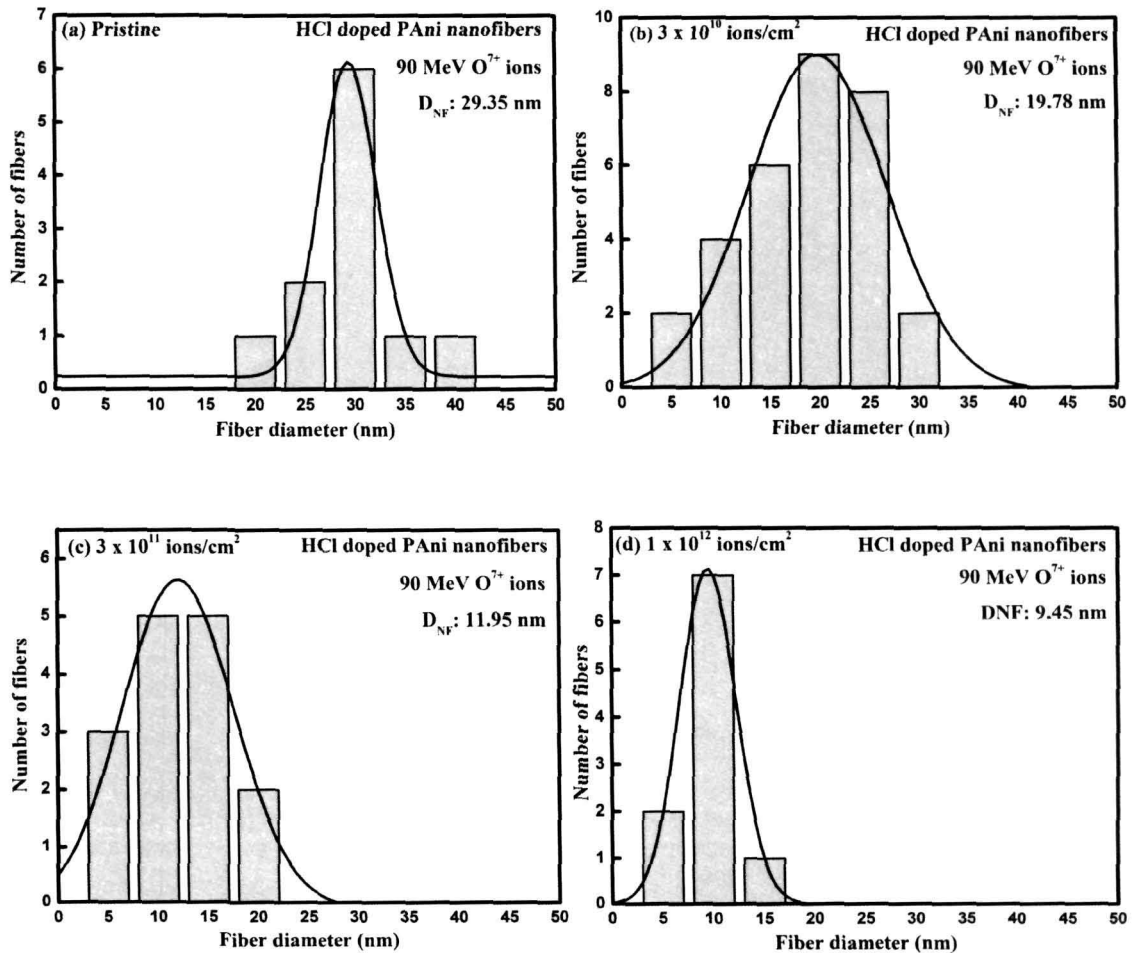


Figure 4.6: Diameter distribution of HCl doped polyaniline nanofibers (a) before irradiation; and after irradiation with 90 MeV O^{7+} ions at fluences (b) 3×10^{10} , (c) 3×10^{11} and (d) $1 \times 10^{12} \text{ ions cm}^{-2}$.

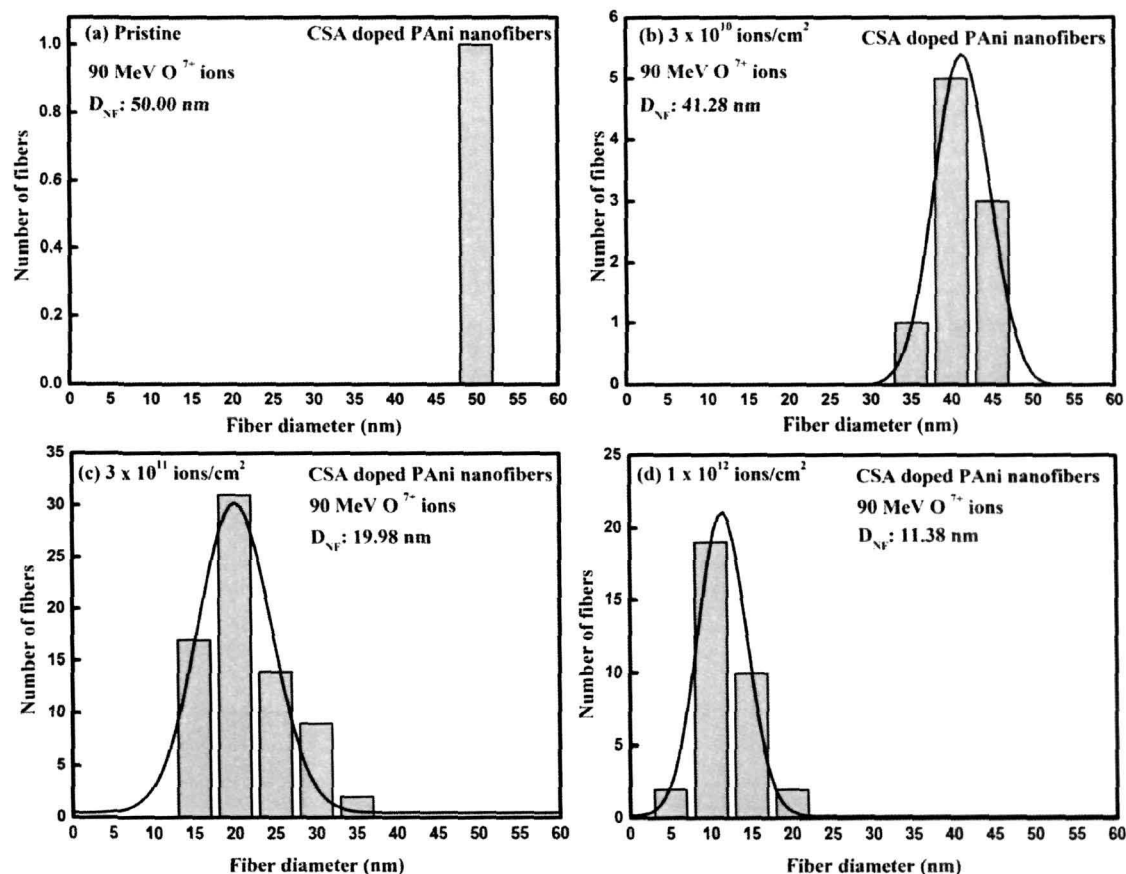


Figure 4.7: Distribution of diameters for the CSA doped polyaniline nanofibers (a) before irradiation; and after irradiation with 90 MeV O^{7+} ions at fluence (b) 3×10^{10} , (c) 3×10^{11} and (d) 1×10^{12} ions cm^{-2} .

According to the Coulomb explosion model, a highly ionized zone of active chemical species, cations, anions, radicals and electrons is created along the ion track on the timescale of $\sim 10^{-12}$ s. Since the charge neutrality cannot be re-established by mobile charge carriers on this timescale, the electrostatic interactions among these active species cause violent bond stretching; segmental motion in the polymer chains; and a rapid expansion of the material in the charged domain, resulting in the formation of shock waves. These shock waves generated in the material are responsible for the creation of tremendous strain leading to fragmentation. Keeping this in view, Coulomb explosion seems to be more appropriate model for explaining the observed fragmentation of PANi nanofibers upon SHI irradiation. However, there are no reports of Coulomb explosion occurring in materials except for alkali halides. On the other hand, Thermal-spike model has been successfully used for analysing the evolution of latent tracks in insulating polymers such as PVdF [432] and Polycarbonate [433].

Even if Coulomb explosion occurs in conducting polymers, it will inevitably be followed by a thermal spike due to local temperature rise. Formation of Latent tracks is a salient feature of interaction of swift heavy ions (SHIs) with materials but in case of conducting polymers it seems to be physically complicated to correlate the track formation mechanism with any particular one of the established models. However, in order to explain the fragmentation of PANi nanofibers upon SHI irradiation, it can certainly be assumed that upon SHI irradiation the PANi nanofibers are amorphized within the core of the tracks, which leads to their fragmentation. As the ion fluence increases, the tracks overlap and fragmentation increases leading to a reduction in the size of the PANi nanofibers as evident from the TEM micrographs.

4.3.2. X-ray diffraction analysis

Figure 4.8 (a) shows the X-ray diffraction patterns of polyaniline bulk, CSA doped PANi nanofibers and the HCl-doped PANi nanofiber samples over the 2θ range from 10° to 60° . Polyaniline exists in two different crystalline forms depending upon the method of preparation, namely Emeraldine salt I (ES I) and Emeraldine salt II (ES II). The ES I form can be indexed with a pseudo-orthorhombic cell with lattice parameters $a = 4.3 \text{ \AA}$, $b = 5.9 \text{ \AA}$, $c = 9.6 \text{ \AA}$ and $V = 245 \text{ \AA}^3$ [130]. All the main reflections observed in the X-ray pattern of bulk polyaniline at $2\theta = 15.5^\circ$, 20° , 25.5° , 27.6° and 30.2° resemble the ES I crystalline form. However, in the case of the HCl and CSA doped PANi nanofibers, only the (100) and (110) reflections are observed. The (100) and (110) reflection peaks which are observed at $2\theta = 20^\circ$ and 25.5° for the PANi bulk exhibits a shift towards lower 2θ values and is clearly evident from the Fig. 4.8 (a). The absence of other reflections in the PANi nanofibers can be interpreted as the absence of corresponding planes as a result of particle size reduction.

Fig. 4.8 (b) shows the comparison of the most intense (110) reflection peak of polyaniline for polyaniline bulk, CSA doped PANi nanofiber and the HCl-doped PANi nanofiber samples. Broadening of the (110) reflection peak as particle size decreases is evident from Fig. 4.8 (b). It is also observed that the (110) reflection for the PANi nanofiber doped with HCl [Fig. 4.8(b)] shows a shift in the peak position towards lower 2θ values.

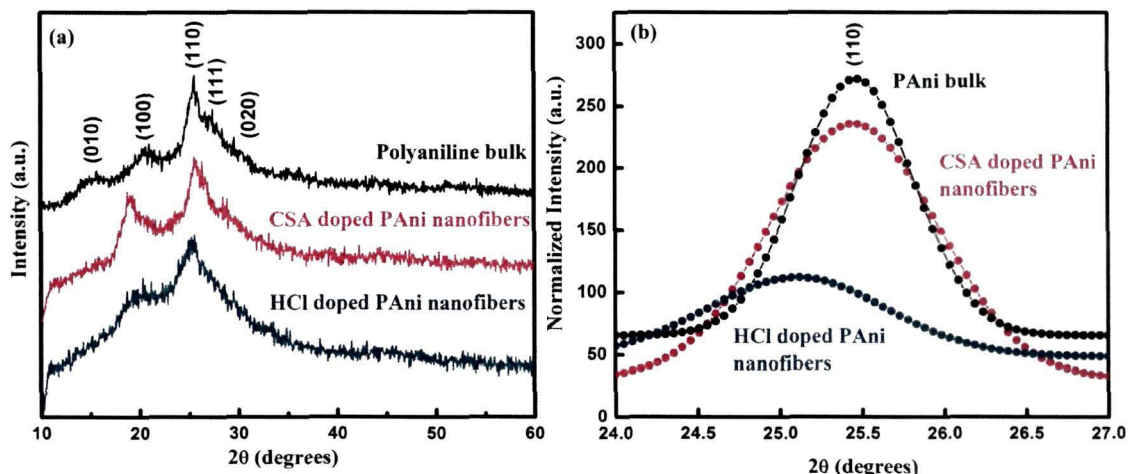


Figure 4.8: (a) X-ray diffraction patterns of polyaniline (PAni) bulk, CSA doped PAni nanofibers and HCl doped PAni nanofibers within 2θ ranging from 10° to 60° and (b) Comparison of the (110) reflection peak for polyaniline (PAni) bulk, CSA doped PAni nanofibers and HCl doped PAni nanofibers

The origin of line broadening in the X-ray diffraction pattern has been analyzed using a single-line approximation method employing Voigt function [414] as described in details in section 3.5.2.1 of Chapter 3. A well-annealed Cu powder sample was used for the correction of instrumental broadening. The contribution of crystallite size (referred to as domain length or the range of order (L) in the case of polymers) and strain towards line broadening has been separately calculated and is given in Table 4.1. The domain length and the strain have been calculated according to the Eqs. 3.11 and 3.12 as given in section 3.5.2.1 of Chapter 3. Table 4.1 also includes the values of the d spacings deduced from the angular positions 2θ of the observed reflections using Bragg's formula.

The domain length for (110) reflection in the case of ES I varies from 20 to 70 \AA , depending upon the Cl/N ratio [130]. In the case of polyaniline (PAni) bulk it has been found to be 39.86 \AA which decreases to 19.80 \AA [Table 4.1] for the HCl doped PAni nanofibers. Since the Cl/N ratio has been kept constant for all the samples, the decrease in the domain length can be interpreted as a result of the reduction in particle size. The contribution of strain in the observed x-ray line broadening is also given in Table 4.1. As observed from Table 4.1 the strain corresponding to the (110) reflection increases from polyaniline bulk to the HCl doped PAni nanofiber. Thus, the broadening of the most intense (110) reflection can be attributed to the decrease in the domain length along with the increasing

strain in the samples. The increase in the strain component as the particle size varies from sub-micron range for the PANi bulk to the nanometer range for the PANi nanofibers indicates that reduction in particle size leads to an enhancement in lattice imperfections such as dislocations and point defects.

Table 4.1: (hkl) pseudo-orthorhombic indexation, d spacing, domain length (L) and strain of polyaniline (PANi) bulk, CSA doped PANi nanofiber and HCl doped PANi nanofiber

Sample	$(hkl)^a$	$d, \text{Å}$	Intensity	$L, \text{Å}$	Strain (ϵ) (%)
Polyaniline bulk	(010)	5.824	Weak	---	---
	(100)	4.349	Strong	---	---
	{(110)}	3.495	Very strong	39.86	0.78
	{(111)}	3.275	Very weak	---	---
	(020)	2.957	Very weak	---	---
CSA doped PANi nanofiber	(100)	4.655	Strong	---	---
HCl doped PANi nanofiber	{(110)}	3.495	Very strong	32.55	1.17
HCl doped PANi nanofiber	(100)	4.362	Weak	---	---
HCl doped PANi nanofiber	{(110)}	3.552	Very strong	19.80	1.9

^a (hkl) means a set of reflections with permutations of the sign of the indices (they are equivalent in an orthorhombic symmetry, but not in a triclinic one).

Furthermore, the increase in the d spacing from 3.495 to 3.552 Å, in the case of HCl doped PANi nanofibers, suggests an increase in the angle at which the chains tilt with respect to the (a, b) basal plane of polyaniline [130]. The x-ray patterns thus reveal that the conformation of the PANi backbone chain in the case of the HCl doped PANi nanofibers is different than that of the other samples.

X-ray diffraction patterns of the pristine and irradiated PANi nanofibers doped with HCl and CSA are shown in Figs. 4.9 (a) and (b). The x-ray spectra reveals that the peak due to the (100) reflection centered at $2\theta = 20^\circ$ is the most prominent peak. This peak is ascribed to the parallel periodicity of PANi. The (110) reflection peak centered at 25.5° attributed to the perpendicular periodicity of PANi is of very low intensity. The fact that the PANi nanofibers have been dispersed in a 2% PVA matrix before irradiation might have induced this effect. However, the peaks at 20° and around 25° are the signature of the ES I crystalline structure of PANi.

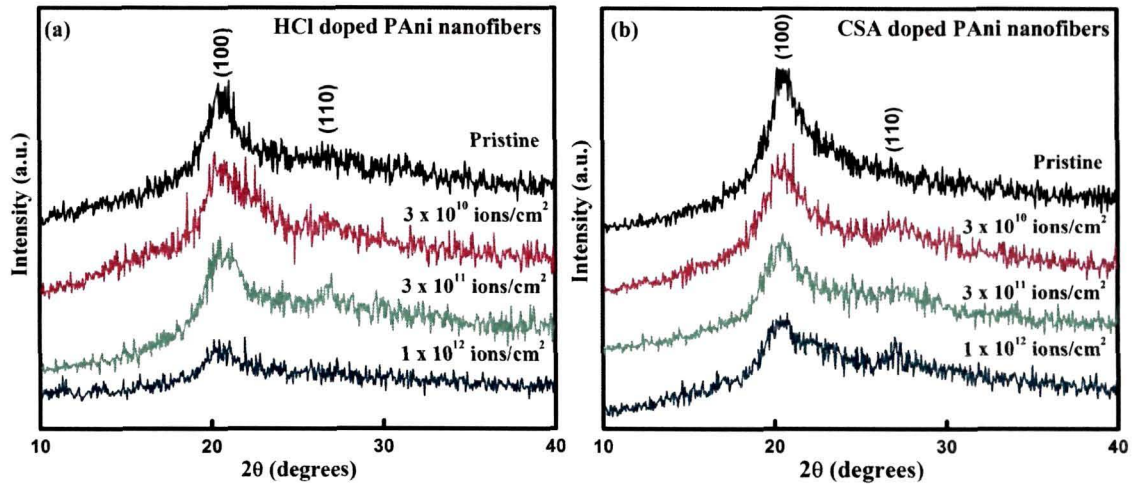


Figure 4.9: X-ray diffraction patterns of pristine and irradiated polyaniline nanofibers doped with (a) HCl and (b) CSA

Figure 4.10 (a) and (b) reveals the changes in the most intense (100) reflection peak for the HCl doped and CSA doped PANi nanofibers, respectively as a function of increasing ion fluence. Full width at half maxima (FWHM) of the (100) peak for both the samples (PANi nanofibers doped with HCl and CSA) is observed to increase as the irradiation fluence is increased. The observed increase in the FWHM in the XRD patterns with increasing fluence has been analyzed by employing the single-line approximation method [414] in order to separate the contributions of the crystallite size (referred to as domain length or the range of order (L) in case of polymers) and the strain towards the line broadening.

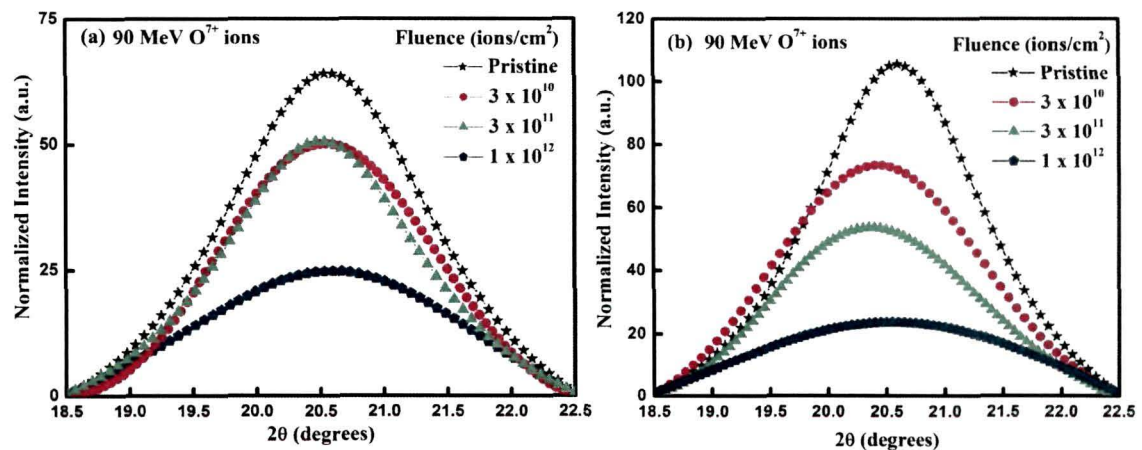


Figure 4.10: X-ray diffraction patterns of the pristine and irradiated PANi nanofibers doped with (a) HCl and (b) CSA showing the most intense (100) peak of PANi.

The variations in d -spacings, domain length (L), strain (ϵ) and normalized integral intensity (I/I_0) of the HCl and CSA doped PANi nanofibers with the

increase in irradiation fluence are shown in Fig. 4.11 (a)–(d). The increase in d -spacing from 4.31 Å to 4.38 Å for the CSA doped PANi nanofibers and from 4.28 Å to 4.36 Å for the HCl doped PANi nanofibers [Fig. 4.11 (a)] with increasing ion fluence indicates an increase in the angle at which the chains tilt with respect to the (a, b) basal plane of polyaniline.

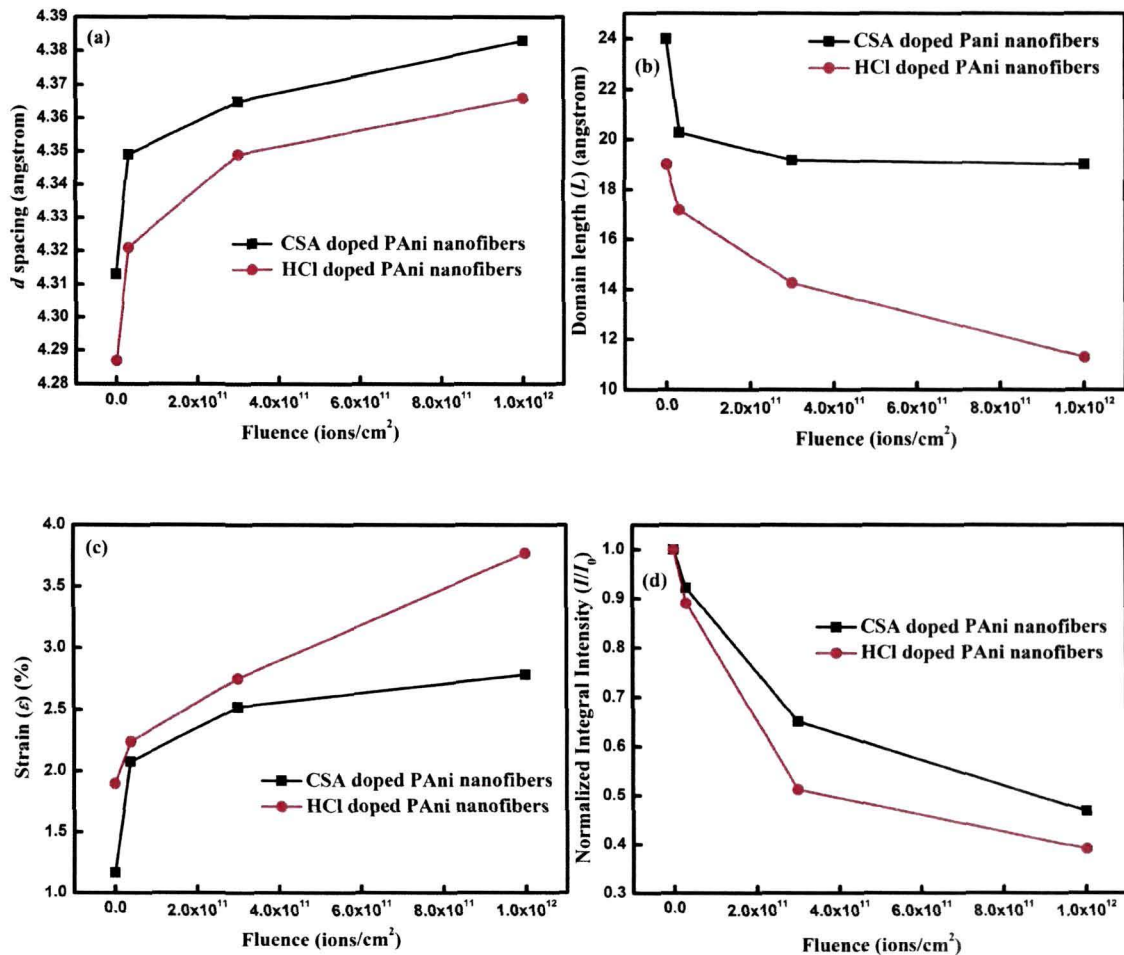


Figure 4.11: Variation of d -spacing, domain length (L), strain (ϵ) and normalized integral intensity (I/I_0) of PANi nanofibers as a function of irradiation fluence.

Furthermore, the increase in the d -spacings may also be interpreted as a reduction in π -stacking and a corresponding decrease in the Cl/N ratio [130]. The primary phenomena associated with the interaction of ion beam and polymers are cross-linking, chain scission and emission of atoms, molecules and molecular fragments. Thus, a variation in the Cl/N ratio of the PANi nanofibers upon SHI irradiation is very much a possibility. It is observed that domain length (L) decreases with increasing fluence [Fig. 4.11 (b)] for both the CSA doped and HCl doped PANi nanofibers, which reveals a decrease in the local range of order in the

polymer chains. The decrease in domain length may be attributed to the fragmentation of the PANi nanofibers upon SHI irradiation as is observed from the TEM micrographs [Fig. 4.4 and 4.5] combined with a decrease in the Cl/N ratio or in other words the degree of doping in the PANi nanofibers upon SHI irradiation. Thus, the x-ray diffraction analysis suggests that PANi nanofibers may be dedoped upon SHI irradiation.

The increase in the strain in the material with increasing irradiation fluence [Fig. 4.11 (c)] may be attributed to the creation of dislocations and point defects due to the tremendous amount of electronic energy deposition in the material. In order to analyze the degree of amorphization, the x-ray patterns of all the samples have been fitted with Lorentz function by fixing the most intense (100) peak's position and FWHM. The integral intensities I (area) of the diffraction peak of PANi nanofibers irradiated with different ion fluence have been extracted and normalized with respect to the unirradiated integral intensity (I_0). The decrease in the normalized integral intensity (I/I_0) with the increase in fluence [Fig. 4.11 (d)] implies that PANi nanofibers are amorphized upon SHI irradiation, which corroborates with the proposed reason for the observed fragmentation of PANi nanofibers upon SHI irradiation.

4.3.3. Vibrational Spectroscopy

4.3.3.1. Fourier Transform Infrared (FTIR) Spectroscopy

Figures 4.12 (a) and (b) show the FTIR spectra of the pristine and irradiated PANi nanofibers doped with HCl and CSA, respectively. The vibrational band around 3400 cm^{-1} is attributed to the N-H stretching vibrations while that at 1650 cm^{-1} is a signature of the N-H bending vibration of polyaniline (PANi). The strong band observed at 1140 cm^{-1} and the band at 1200 cm^{-1} are due to the C-C stretching and C-C twisting of the alkyl chain [411]. The C-Cl stretching vibration observed around 600 cm^{-1} confirms the fact that the PANi nanofibers are in doped states. The peaks at 1400 and 1460 cm^{-1} are assigned to the C=C stretching vibrations of the benzenoid and quinoid units of PANi, respectively. The peak at 660 cm^{-1} is assigned to the C-H out of plane deformations. It has been observed that the prominent vibrational bands of PANi nanofibers decrease in intensity upon SHI irradiation.

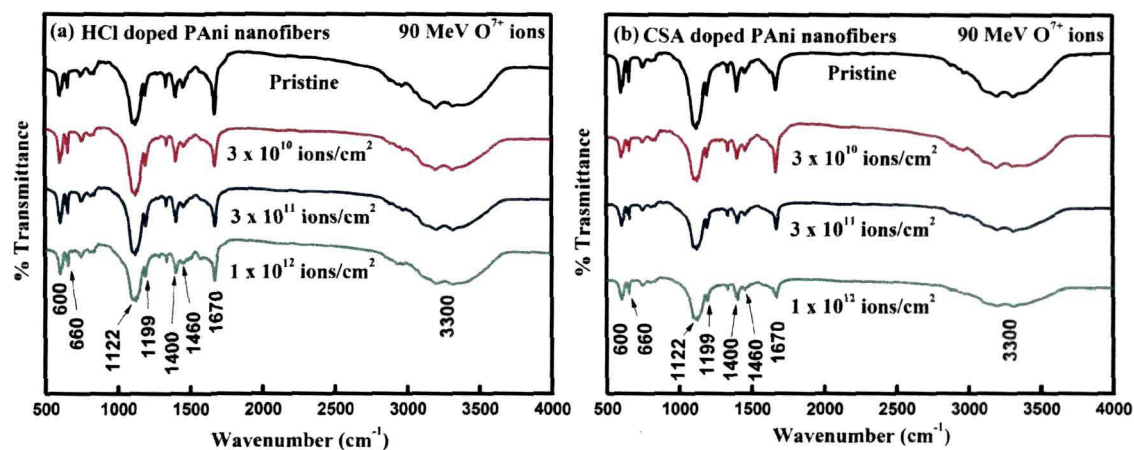


Figure 4.12: FTIR spectra of pristine and irradiated (a) HCl doped and (b) CSA doped PANi nanofibers.

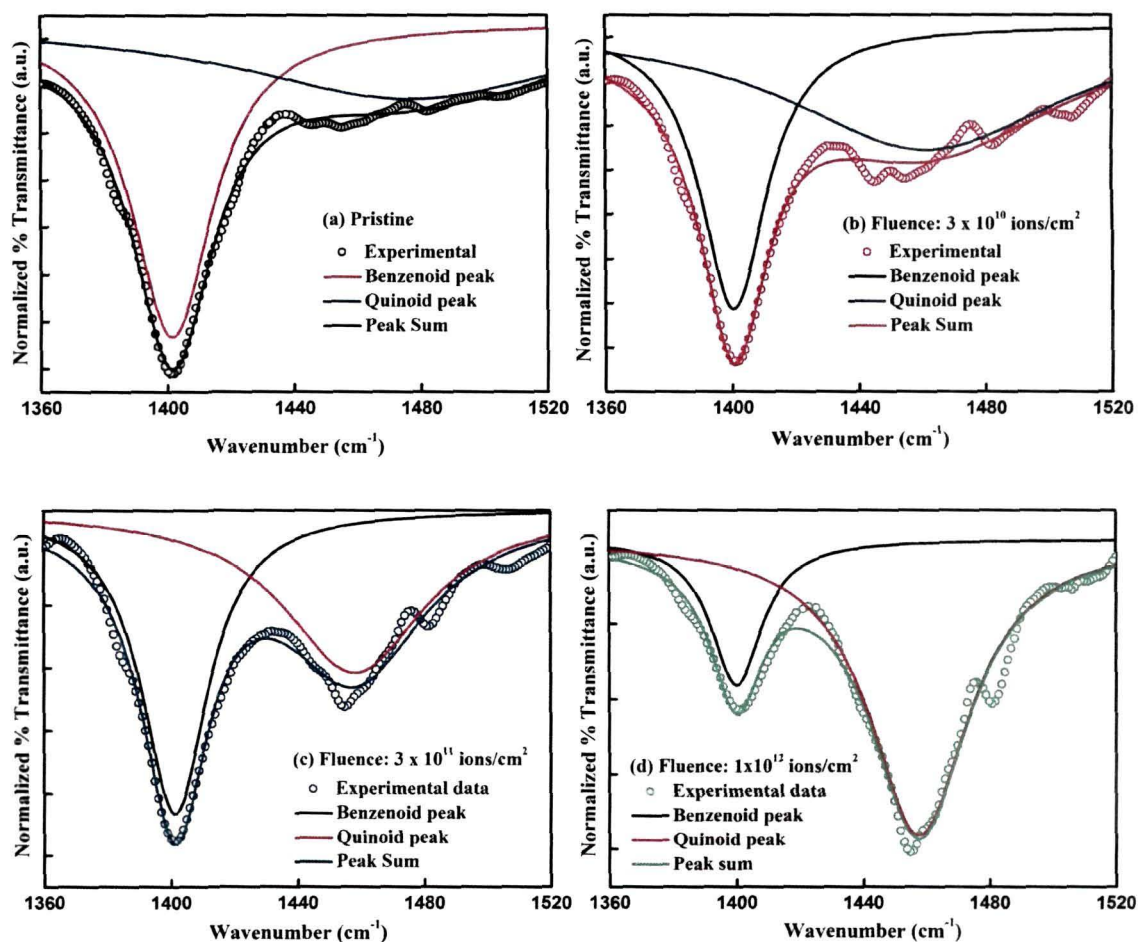


Figure 4.13: Lorentzian deconvolution of the FTIR spectra within 1360–1520 cm^{-1} for (a) pristine HCl doped PANi nanofibers and those irradiated at a fluence of (b) 3×10^{10} , (c) 3×10^{11} and (d) 1×10^{12} ions cm^{-2} .

The variations in the band widths and band shifts have been studied quantitatively by deconvoluting the FTIR spectra of the pristine and 90 MeV O^{7+} ion beam irradiated PANi nanofibers using Lorentzian oscillation curves corresponding to the IR-active modes of PANi nanofibers, in the range of 500-4000 cm^{-1} . Each FTIR spectra has been normalized with respect to the maximum value prior to deconvolution. The deconvolution of the vibrational peaks for the benzenoid and quinoid structures for the pristine and irradiated HCl and CSA doped PANi nanofibers are shown in the Figs. 4.13 (a-d) and 4.14 (a-d), respectively. The detailed position, intensity and band widths of the deconvoluted peaks are listed in Table 4.2. Although there is a negligible change in the peak positions, the intensity and band widths show remarkable variations with the increase in the irradiation fluence.

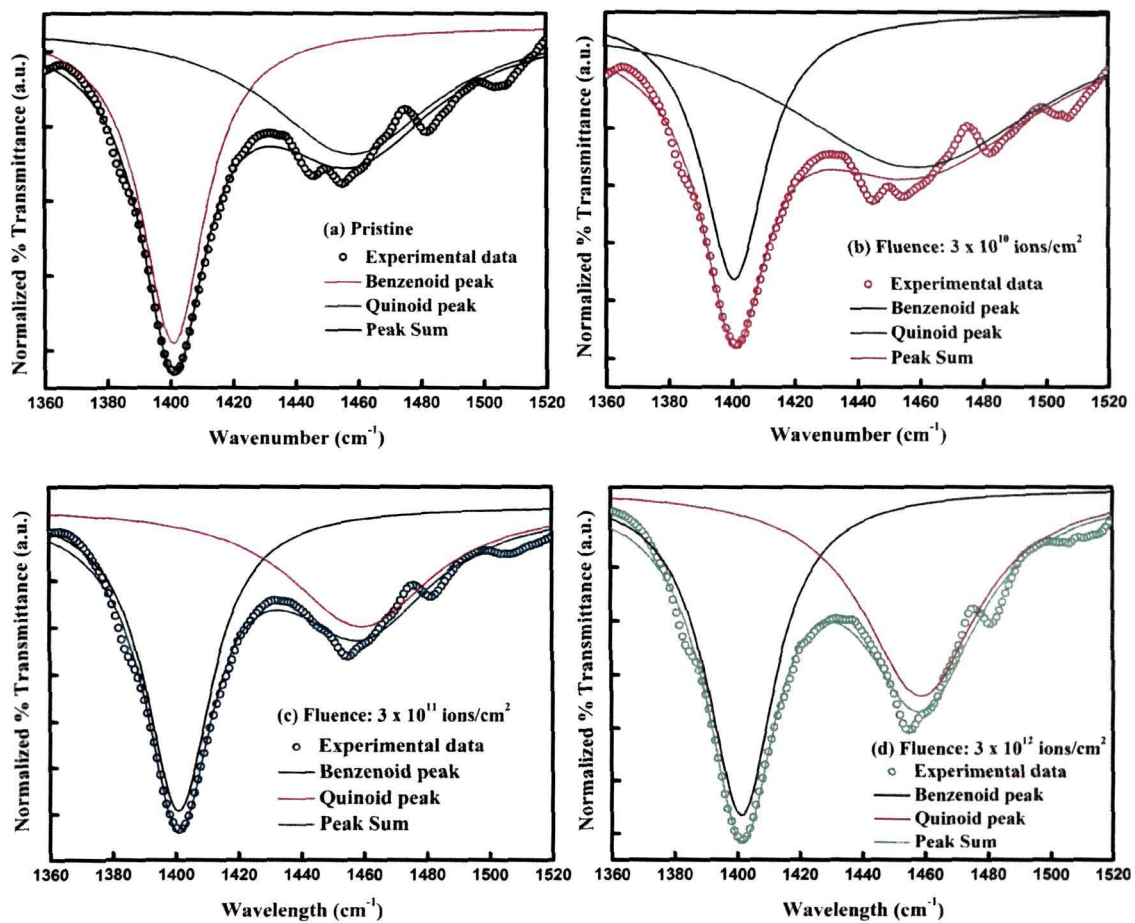


Figure 4.14: Lorentzian deconvolution of the FTIR spectra within 1360–1520 cm^{-1} for (a) pristine CSA doped PANi nanofibers and those irradiated at a fluence of (b) 3×10^{10} , (c) 3×10^{11} and (d) 1×10^{12} ions cm^{-2} .

Table 4.2: Position, Intensity and FWHMs of the prominent FTIR peaks of pristine and 90 MeV O⁷⁺ ion beam irradiated PAni nanofibers doped with HCl and CSA

Peak (cm ⁻¹)	Designation of the peaks	Samples	Lorentzian deconvolution of the FTIR peaks for pristine and irradiated samples at different fluences											
			Position				Intensity				FWHM			
			Pristine	3x10 ¹⁰	3x10 ¹¹	3x10 ¹²	Pristine	3x10 ¹⁰	3e10 ¹¹	1x10 ¹²	Pristine	3x10 ¹⁰	3x10 ¹¹	1x10 ¹²
600	C-H out of plane deformation	S1 ^a	603.3	602.9	603.4	602.9	23.8	13.5	12.7	10.2	30.2	33.9	34.5	36.71
		S2 ^b	603.1	605.7	603.0	601.7	16.7	15.0	12.0	5.0	27.1	30.0	31.7	40.68
1122	C-H in plane deformation	S1	1122.4	1121.0	1119.8	1122.4	49.4	31.5	29.9	26.3	99.5	102.3	106.5	109.29
		S2	1121.6	1119.2	1118.6	1119.6	34.5	31.5	27.5	12.9	89.8	98.7	105.8	108.11
1400	C=C stretching vibration of benzenoid ring	S1	1401.0	1401.0	1401.3	1401.9	19.2	12.1	10.1	9.7	24.5	24.9	25.5	27.20
		S2	1400.7	1400.9	1400.9	1401.3	13.1	12.3	9.3	4.2	24.3	24.5	25.4	26.22
1460	C=C stretching vibration of quinoid ring	S1	1459.9	1459.2	1460.6	1458.9	3.9	4.9	7.2	7.8	67.8	48.4	45.0	44.97
		S2	1459.3	1458.8	1458.2	1457.9	1.7	5.2	5.4	7.8	101.1	64.4	54.8	44.42
1670	Due to N-H stretching vibration of polyaniline	S1	1669.0	1666.9	1669.6	1668.4	23.9	18.4	15.1	9.3	27.9	28.6	34.9	40.25
		S2	1669.1	1669.0	1668.4	1669.7	23.8	15.4	14.9	6.0	24.	27.2	28.4	29.7
3350		S1	3277.9	3296.4	3286.4	3279.8	55.1	36.7	25.1	22.3	731.1	911.1	940.9	945.98
		S2	3287.3	3286.3	3271.8	3273.5	35.1	25.3	24.6	9.0	703.7	714.0	718.2	879.69

^a S1 stands for the HCl doped PAni nanofibers and ^b S2 stands for the CSA doped PAni nanofibers

The decrease in the intensity of almost all the prominent peaks in the FTIR spectra indicates that the interaction of the highly energetic ion beams with the PANi nanofibers induces chain scissions that increases with increasing ion fluence leading to a reduction in the crystalline nature and induces fragmentation of the PANi nanofibers upon ion beam treatment. The FTIR results corroborates with the X-ray diffraction and TEM results.

4.3.3.2. Micro-Raman (μ R) spectroscopy

The micro-Raman (μ R) spectra of the PANi nanofibers doped with CSA and HCl, respectively obtained with an Ar ion laser of 0.5 mW power and 514.5 nm excitation are presented in the Figs. 4.15 (a, b). In the μ R spectra, the C-H benzene deformation modes at 1182.63 cm^{-1} indicate the presence of quinoid rings. The band at 1248.11 cm^{-1} can be assigned to the C-N stretching mode of the polaronic units. The absorption band at 1375.28 cm^{-1} corresponds to the C-N⁺ stretching modes of the delocalized polaronic charge carrier, which indicates that the PANi nanofibers are in doped ES I form. The band at 1328.51 cm^{-1} is a characteristic of the semiquinone radical cation. The bands at 1451.30 and 1417.18 cm^{-1} correspond to the C=N stretching mode of the quinoid units. The absorption peak at 1528.78 cm^{-1} corresponds to the N-H bending deformation band of protonated amine. The C=C deformation bands of the benzenoid ring positioned at 1601.75 cm^{-1} are characteristic of the semiquinone rings.

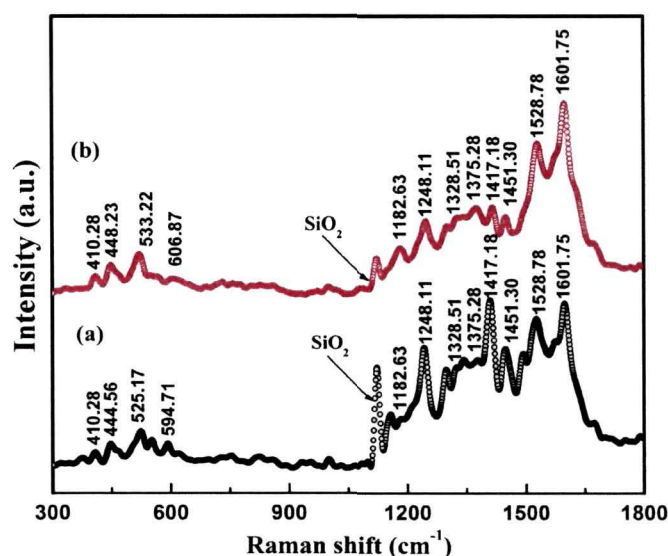


Figure 4.15: MicroRaman (μ R) spectra of PANi nanofibers doped with (a) CSA and (b) HCl.

It is well known that the Raman bands of PANi at wavenumbers higher than 1000 cm^{-1} are sensitive to its oxidation and protonation state, but it is difficult to correlate any change with the crystallinity or morphology aspects [434]. Colombari *et al.* [435] demonstrated that the Raman spectrum of PANi at low wavenumbers is sensitive to the kind of crystallinity arrangement of PANi. The shift of the bands at 444.56 , 525.17 and 594.71 cm^{-1} in CSA doped PANi nanofibers [Fig. 4.15(a)] to 448.23 , 533.22 and 606.87 cm^{-1} , respectively, in HCl doped PANi nanofibers [Fig. 4.15(b)] indicate a change in the crystallinity arrangement. Cochet *et al.* [436, 437], in an extensive study on the influence of the conformational changes over the vibrational spectra of PANi, showed that mainly the bands at about $200\text{--}500\text{ cm}^{-1}$ are very sensitive to the conformational changes. The shift of the bands to higher wavenumbers indicates the increase of the torsion angles of the $C_{ring}\text{--}N\text{--}C_{ring}$ segments [436, 437]. Thus, the shifts of the bands in the range between 300 and 600 cm^{-1} , as in the case of the HCl doped PANi nanofibers, are due to the conformational changes in the PANi backbone. This increase in the torsion angles is due to the loss of the π stacking among the PANi rings, leading to the reduction of crystallinity of the HCl doped PANi nanofibers, which is corroborated by the XRD results. The μR spectra and the x-ray diffraction patterns confirm that the PANi nanofibers doped with HCl and CSA are not only different in terms of particle size but also in terms of their structural conformation.

Figure 4.16 (a) and (b) shows the micro-Raman (μR) spectra of the pristine and 90 MeV O^{7+} ion irradiated PANi nanofibers doped with HCl and CSA, respectively within the range of $1200\text{--}1650\text{ cm}^{-1}$. The insets of Fig. 4.16 (a) and (b) show the Raman active modes of the pristine and irradiated PANi nanofibers doped with HCl and CSA, respectively in the range of $300\text{--}700\text{ cm}^{-1}$. It is observed that all the Raman active modes in the material decrease in intensity with increasing irradiation fluence. The decrease in the intensity of the Raman active modes in the low wave number region indicate changes in the crystallinity arrangement of the PANi nanofibers upon SHI irradiation, specifically increase of the torsion angles of the $C_{ring}\text{--}N\text{--}C_{ring}$ segments [435-437]. This increase in the torsion angles is due to the loss of π -stacking among the PANi rings, leading to amorphization of the nanofibers, which is also supported by the XRD results. The

results indicate that the electronic interaction between the electron rich C–N site in the aromatic rings of PANi chains and the ion beam might have induced distortion of the polymeric chains leading to conformational modifications of the PANi nanofibers. In order to perform a quantitative analysis of the SHI induced conformational modifications and peak shifts in the μ R spectra of PANi nanofibers upon SHI irradiation the μ R spectra of PANi nanofibers doped with HCl and CSA have been deconvoluted by using Lorentzian oscillation curves corresponding to the PANi nanofiber Raman modes, in the range of 1200–1650 cm^{-1} . In order to compare the deconvoluted peaks quantitatively, each micro-Raman spectra of the pristine and irradiated PANi nanofiber samples has been normalized with respect to the maximum value.

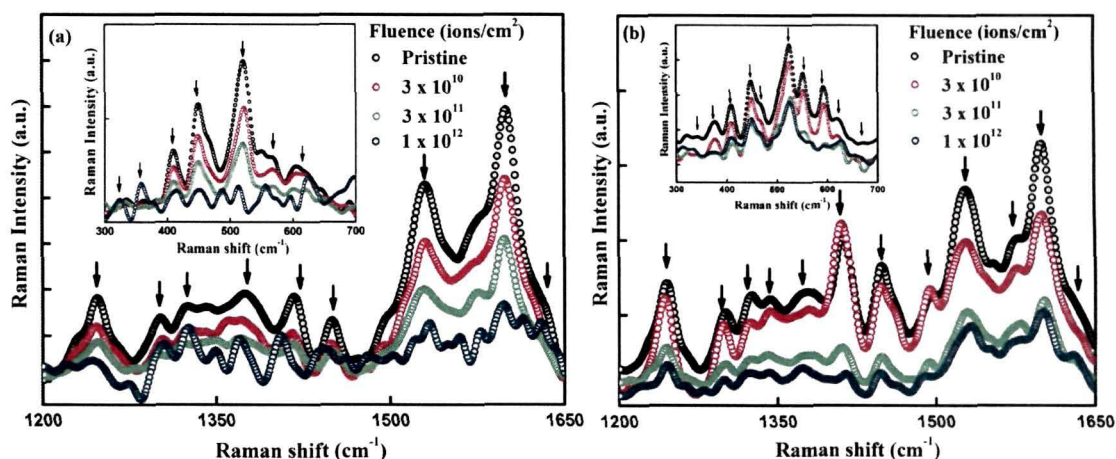


Figure 4.16: Micro-Raman spectra of pristine and irradiated PANi nanofibers doped with (a) HCl and (b) CSA in the range 1200–1650 cm^{-1} . Inset shows the micro-Raman spectra of the pristine and irradiated PANi nanofibers doped with (a) HCl and (b) CSA at lower wavelength (300–700 cm^{-1}).

Figs. 4.17 (a)-(d) show the deconvoluted Raman spectra of the pristine and 90 MeV O^{7+} ion irradiated HCl doped PANi nanofibers with a fluence of 3×10^{10} , 3×10^{11} and 1×10^{12} ions cm^{-2} , respectively. The variations in the position, line widths (FWHM) and intensity of the prominent peaks along with their assignments to different Raman active vibrational modes in the PANi nanofibers have been tabulated in the Table 4.3. On the other hand, the deconvoluted Raman spectra of the pristine and 90 MeV O^{7+} ion irradiated CSA doped PANi nanofibers with a fluence of 3×10^{10} ions cm^{-2} , 3×10^{11} ions cm^{-2} and 1×10^{12} ions cm^{-2} , respectively are shown in Figs. 4.18 (a)-(d). The details of the positions, FWHM

and intensity of the deconvoluted Raman active modes are presented in the Table 4.4.

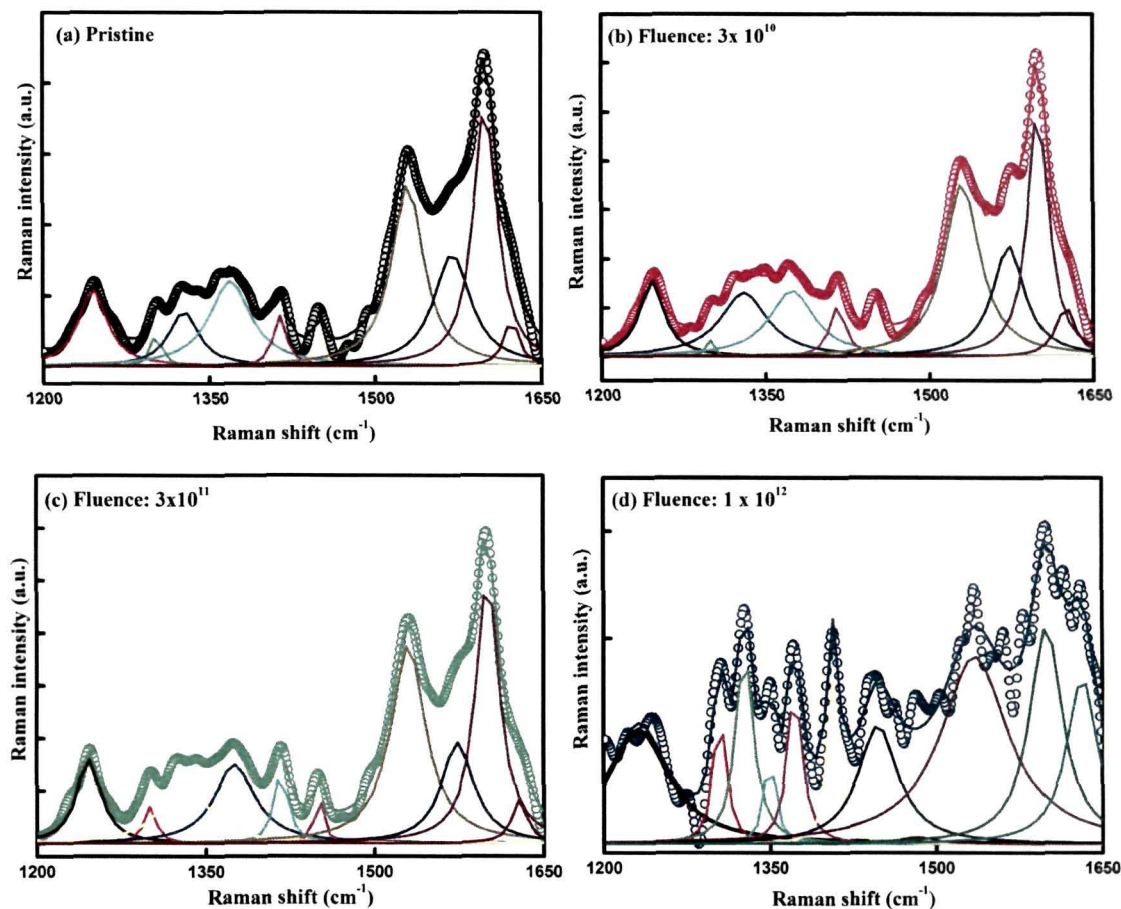


Figure 4.17: Lorentzian deconvolution of micro-Raman spectra of HCl doped polyaniline nanofibers (a) before irradiation; and after irradiation with 90 MeV O^{7+} ions at fluences (b) 3×10^{10} , (c) 3×10^{11} and (d) 1×10^{12} ions cm^{-2} .

It is clearly evident from the Table 4.3 and 4.4 that the interaction of swift heavy ions (SHIs) brings about remarkable changes in the position, intensity and FWHM of the Raman peaks observed in the wavenumber range within 1200 cm^{-1} to 1650 cm^{-1} . The Raman peak for the C-N stretching of the polaronic units at 1245 cm^{-1} shift from 1245.3 to 1247.2 cm^{-1} and from 1241.6 to 1243.7 cm^{-1} for the PANi nanofibers doped with HCl and CSA, respectively. The intensity of the peak at 1245 cm^{-1} for both the HCl and CSA doped PANi nanofibers after SHI irradiation decreases to about 4 times the value for the pristine sample. On the other hand, the FWHMs of the peak at 1245 cm^{-1} for the HCl and CSA doped PANi nanofibers show a gradual increase. The Raman bands at 1325 , 1344 and 1375 cm^{-1} attributed to the C-N⁺ stretching modes of the delocalized polaronic charge carrier also

exhibits noticeable variations in position, intensity and FWHM with the increase in irradiation fluence. All the peaks corresponding to the C–N⁺ stretching of the delocalized polaronic charge carrier shifts to higher wave numbers and broaden while the intensity of the peaks decreases. The variations in the Raman active modes corresponding to the polaronic charge carriers indicate that interaction of SHIs with the doped PANi nanofibers may have induced a transition from doped to dedoped states in the PANi nanofibers. Thus, both Raman and FTIR spectral analysis reveal chain-scissioning and de-doping events to be dominant in PANi nanofibers upon irradiation with the highly energetic oxygen ions.

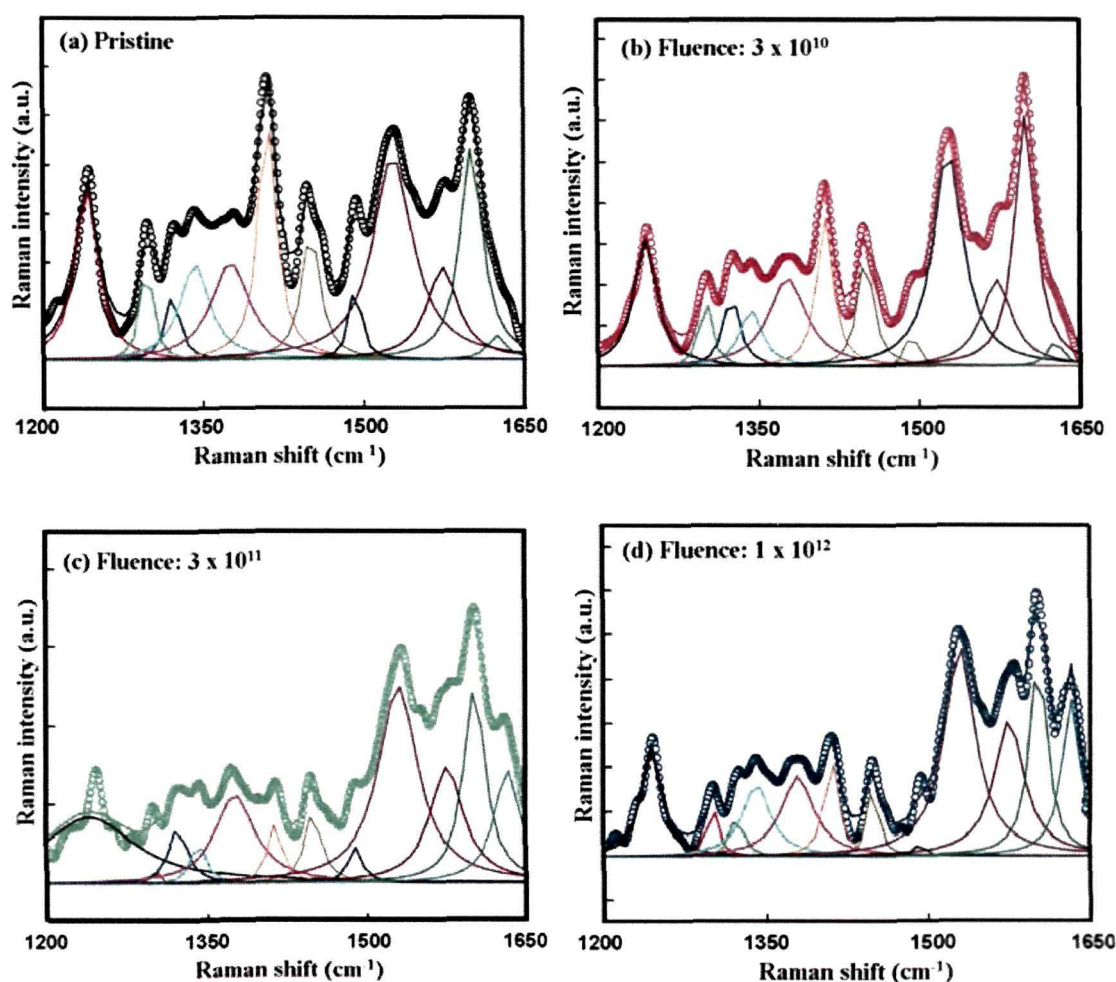


Figure 4.18: Lorentzian deconvolution of micro-Raman spectra of CSA doped polyaniline nanofibers (a) before irradiation; and after irradiation with 90 MeV O⁷⁺ ions at fluences (b) 3×10^{10} , (c) 3×10^{11} and (d) 1×10^{12} ions cm⁻².

Table 4.3: Deconvolution of the micro-Raman (μR) peaks for pristine and 90 MeV O^{7+} ion irradiated PANi nanofibers doped with HCl at different fluences.

Peaks (cm^{-1})	Description of the vibrations	Decomposition of the Raman peaks for pristine and irradiated samples at different fluences											
		Position				Intensity				FWHM			
		Pristine	3×10^{10}	3×10^{11}	1×10^{12}	Pristine	3×10^{10}	3×10^{11}	1×10^{12}	Pristine	3×10^{10}	3×10^{11}	1×10^{12}
1245	C-N stretching mode of polaronic units	1245.3	1245.9	1246.0	1247.2	318.52	217.45	155.12	77.43	25.89	26.73	31.13	37.56
1325	C-N ⁺⁺ stretching modes of the delocalized polaronic charge carrier	1322.5	1323.7	1324.0	1325.4	337.03	281.58	134.05	73.54	14.90	17.14	19.98	22.23
1344		1342.4	1342.6	1342.9	1342.9	428.08	312.98	203.69	119.67	13.63	23.45	29.80	37.02
1375		1375.8	1376.3	1376.9	1379.6	432.64	408.45	291.73	193.01	54.27	59.12	61.68	65.47
1527	N-H bending deformation of protonated amine	1526.4	1527.2	1529.9	1530.1	1215.1	1031.34	639.29	453.90	32.45	34.32	42.35	45.70
1595	Symmetric C=C stretching	1601.8	1602.5	1602.6	1603.1	1038.92	772.35	519.86	279.72	16.43	21.52	25.61	28.33
1626		1625.3	1628.5	1632.2	1633.4	57.61	104.52	291.83	384.91	15.01	19.64	22.14	25.50

Table 4.4: Deconvolution of the micro-Raman (μ R) peaks for pristine and 90 MeV O⁷⁺ ion irradiated PANi nanofibers doped with CSA at different fluences.

Peaks (cm ⁻¹)	Description of the vibrations	Decomposition of the Raman peaks for pristine and irradiated samples at different fluences											
		Position				Intensity				FWHM			
		Pristine	3 x 10 ¹⁰	3 x 10 ¹¹	1 x 10 ¹²	Pristine	3 x 10 ¹⁰	3 x 10 ¹¹	1 x 10 ¹²	Pristine	3 x 10 ¹⁰	3 x 10 ¹¹	1 x 10 ¹²
1245	C-N stretching mode of polaronic units	1241.6	1242.3	1243.5	1243.7	706.99	621.00	242.69	167.84	23.31	25.02	25.18	25.24
1325	C-N ⁺⁺ stretching modes of the delocalized polaronic charge carrier	1322.1	1322.4	1323.0	1324.2	352.03	275.58	140.05	93.734	13.08	15.68	17.61	21.11
1344		1341.4	1341.6	1342.9	1342.9	398.68	280.41	161.53	106.54	16.16	24.77	26.96	30.51
1375		1375.8	1376.8	1376.3	1379.6	432.64	398.45	223.57	179.06	35.81	42.31	43.43	44.75
1527	N-H bending deformation of protonated amine	1527.4	1528.0	1529.9	1530.1	1050.1	831.02	502.04	466.90	33.45	34.82	41.40	44.79
1595	Symmetric C=C stretching	1600.8	1600.2	1601.5	1602.9	1228.0	872.74	499.28	450.34	18.68	22.62	24.23	24.84
1626		1624.3	1628.1	1632.1	1632.9	97.56	124.85	283.65	353.85	16.01	19.73	20.19	23.30

4.3.3.3. SHI induced benzenoid to quinoid transformation in polyaniline nanofibers

The most significant variation in the vibrational spectra of the HCl and CSA doped PANi nanofibers can be observed in the C=C stretching vibration mode of the para di-substituted benzene (benzenoid) and quinone di-imine (quinoid) structures. The deconvoluted sub-peaks representing the C=C stretching of two kinds of resonant structures: the benzenoid and the quinoid ring in the FTIR spectra within the range 1360-1530 cm^{-1} for the pristine and irradiated PANi nanofibers doped with HCl and CSA, respectively are shown in the Fig. 4.19 (a) and (b). The intensity of the peak at 1400 cm^{-1} due to the C=C stretching of the benzenoid ring for the HCl doped PANi nanofibers irradiated at the fluence of 1×10^{12} ions/ cm^2 decreases as compared to that for the pristine, while in case of the CSA doped PANi nanofibers the intensity of the peak decreases almost to 3 times than that of the pristine. The FWHMs for the HCl doped and CSA doped PANi nanofibers increases by 2.69 cm^{-1} and 1.85 cm^{-1} , respectively with increasing ion fluence. On the other hand, the peak at 1460 cm^{-1} due to the C=C stretching of the quinoid ring intensifies for both the HCl and CSA doped PANi nanofibers upon SHI irradiation as observed from the Table 4.2. This suggests that there is a partial transformation from the benzenoid to the quinoid structure in the PANi chains upon SHI irradiation.

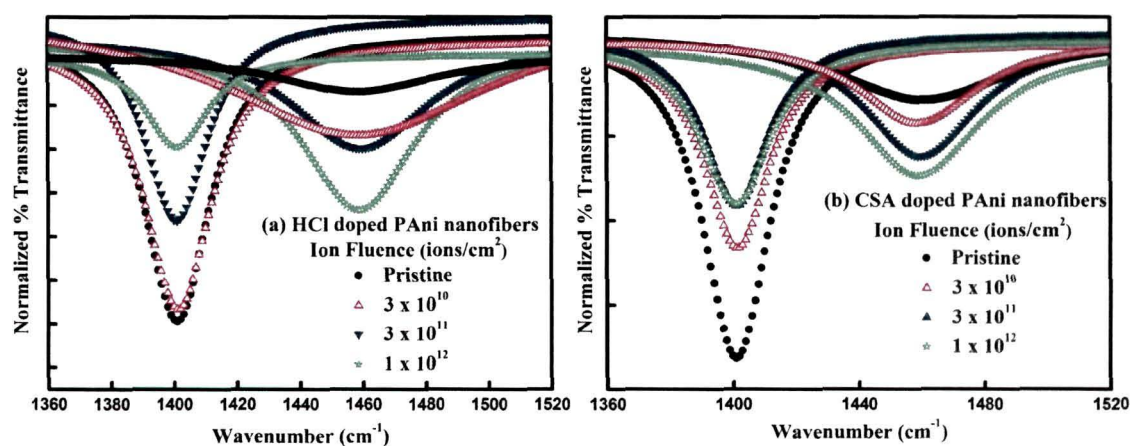


Figure 4.19: Comparison of the deconvoluted sub-peaks representing the C=C stretching vibration of the benzenoid and quinoid rings of pristine and 90 MeV O^{7+} ion irradiated PANi nanofibers doped with (a) HCl and (b) CSA.

In the micro-Raman (μ R) spectra of both the HCl and CSA doped PANi nanofibers after SHI irradiation it has been observed that the symmetric C=C stretching peak at 1595 cm^{-1} can be deconvoluted into two sub-peaks, which can be clearly observed from the Fig. 4.20 (a) and (b). The sub-peaks indicate two kinds of resonant structures: the main peak is due to the benzenoid structure and the shoulder peak is due to the quinoid structure of the PANi nanofibers. In case of the HCl doped PANi nanofibers, the main peak of the symmetric C=C stretching mode is up-shifted from 1601.8 to 1603.1 cm^{-1} and the intensity is found to decrease from 1038.92 to 279.72 upon irradiation [Table 4.3]. The shoulder peak of the symmetric C=C stretching mode also shows an up-shift from 1625.3 to 1633.4 cm^{-1} and is intensified more than 6 times from 57.61 to 384.91 upon irradiation [Table 4.3]. The FWHMs of both the main and shoulder of the HCl doped PANi nanofibers increases to 11.9 cm^{-1} and 10.49 cm^{-1} , respectively upon SHI irradiation.

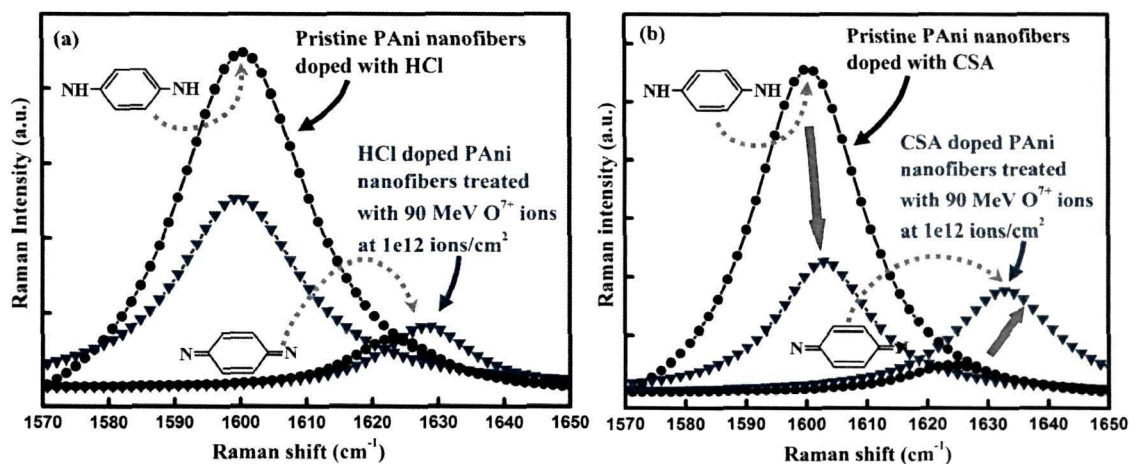


Figure 4.20: A comparison of the decomposed sub-peaks corresponding to the symmetrical C=C stretching modes of the pristine PANi nanofiber and that irradiated with a fluence of 1×10^{12} ions/cm² for (a) HCl doped PANi nanofibers and (b) CSA doped PANi nanofibers.

Similar variations in the position, intensity and FWHM have also been observed for the CSA doped PANi nanofibers as is evident from Fig. 4.20 (b) and Table 4.4. The main peak of the symmetric C=C stretching mode is up-shifted from 1600.8 to 1602.9 cm^{-1} and the intensity decreases from 1228 to 450.34 . The shoulder peak of the symmetric C=C stretching mode is up-shifted from 1624.3 to 1632.9 cm^{-1} and intensifies more than 3 times. This is again an indication of the

fact that there is a transformation from benzenoid to quinoid structure in the PANi chains upon SHI irradiation.

The fact that there is a transition from the benzenoid to the quinoid structure in the PANi chains is further corroborated by the decrease in the intensity of the peaks corresponding to the N-H stretching at 1670 cm^{-1} as can be observed from the Figs. 4.21 (a)-(b). The intensity of the N-H stretching peak at 1670 cm^{-1} decreases from 23.9 to 9.3 for the HCl doped PANi nanofiber whereas from 23.8 to 6.0 for the CSA doped PANi nanofibers [Table 4.2]. A similar decrement in the intensity is also observed for the N-H stretching peak centered at 3300 cm^{-1} . The band is also found to broaden with increasing ion fluence and the band width increases by 214.83 cm^{-1} for the HCl doped PANi nanofibers and by 175.95 cm^{-1} for the CSA doped PANi nanofibers.

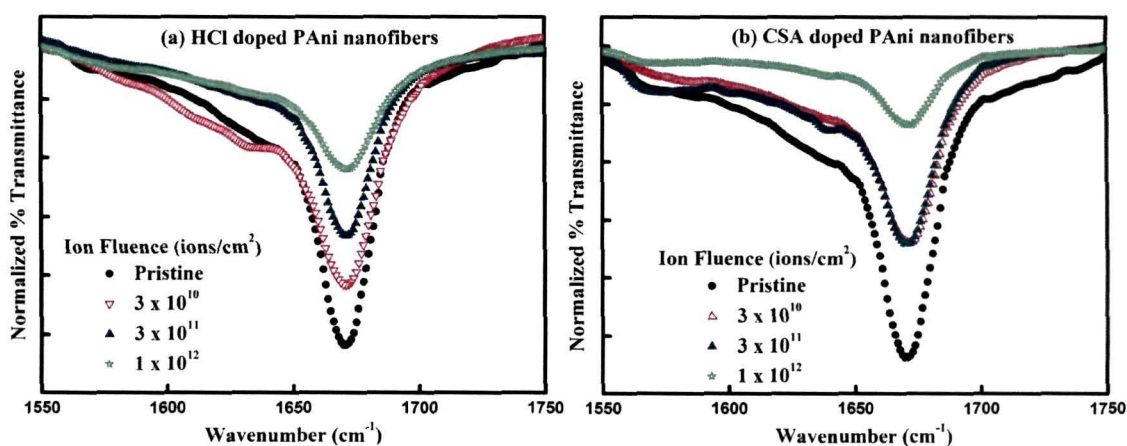


Figure 4.21: Comparison of the N-H stretching band at 1670 cm^{-1} for the pristine and 90 MeV O^{7+} ion irradiated PANi nanofibers doped with (a) HCl and (b) CSA.

Both the FTIR and the Raman spectra point out to the fact that the intercylic rings of the PANi nanofibers become distorted upon SHI irradiation; the proportion of the para di-substituted benzene rings (benzenoid) decreases, while there is a corresponding increase in that of the quinone di-imine rings (quinoid) upon SHI irradiation. The distortion of PANi chains may influence their π -conjugation length, which is associated with π -electron delocalization, resulting in the reduced coplanarity of the aromatic ring. The observed up-shifting of the symmetric C=C stretching mode is due to the shortening of π -conjugation length (i.e., π -electron delocalization) of PANi nanofibers upon SHI irradiation. This implies that SHI irradiation induces defects and distortions in the PANi main

chains, resulting in reduced coplanarity of the aromatic ring and π -conjugation length [438].

It is, however, interesting to note that both FTIR and Raman spectra of PANi exhibit peaks which bear the signatures of para di-substituted benzene (benzenoid) and the quinone di-imine (quinoid) structures although generally FTIR and Raman active modes are mutually exclusive. Inelastic light scattering from condensed matter is due to fluctuations of the dielectric susceptibility which, in turn, is related to the spectrum of dynamic excitations of the system. In crystals, momentum conservation during the scattering event only allows zone-center phonons to be Raman-active while acoustic modes are inactive. Structure disorder such as stacking fault induces the Brillouin zone folding; hence, some optical phonons become active [435]. These restrictions are removed in amorphous solids, and all modes could be active. Essentially it is the local disorder of amorphous materials which leads to the electrical and mechanical fluctuations. These fluctuations destroy the symmetry rules which account for the acoustic modes giving rise to Raman scattering.

Doping induces very intense Infra-Red (IR) bands, which was ascribed to mysterious Raman active modes; however, it was shown later that the new modes arise from the breakdown of the electrical symmetry by the removal or injection of charges [439]. The intensity of the IR modes is due to the very large charge fluxes and a longer conjugation length. The modes with high IR intensity tend to have the highest electron phonon coupling. The vibrations giving rise to the maximum electron-phonon coupling are also the ones responsible for the highest Raman intensity modes in the undoped conjugated materials [435-440]. Only in the case of conjugated molecules terminated by a donor (D) and acceptor (A) groups forming a D- π -A system, the intra-molecular charge transfer creates a strong link between IR and Raman active modes. In the present case, the most prominent features in the Raman spectrum are also strongly active in the IR [440].

Raman scattering is a resonant process, so that the spectral line shapes change with varying excitation energy. This depicts that the similarity between the FTIR and Raman spectra taken at visible excitation is purely accidental. However, the apparent similarity between the Raman and IR spectra, in

particular, the presence of two main peaks representing the same structures in PANi nanofibers can be explained as follows: Raman spectrum at a given excitation energy weights those configurations resonant with that energy. Thus Raman spectra excited with lower IR photons resonate with the most delocalized sp^2 phases, with the lowest gap. Therefore, it can be assumed that the IR spectra and the Raman spectra excited in limit of low energy will probe the same sp^2 structures. Thus, the transformation of the para di-substituted benzene (benzenoid) structure to the quinone di-imine (quinoid) structure in PANi nanofibers upon SHI irradiation can be probed by FTIR as well as Raman spectroscopy.

4.3.4. *UV-Visible (UV-Vis) absorption spectroscopy*

Figures 4.22 (a, b) show the absorption spectra of the pristine and irradiated PANi nanofibers doped with HCl and CSA, respectively plotted in the wavelength range 200–900 nm. The pristine sample shows three prominent peaks which are the signature of PANi in the emeraldine salt form. In case of conducting polymers, there are always two distinct defect bands within the band gap, arising from a destabilization of the highest occupied band (HOMO), which leads to the lower defect band and a stabilization of the lowest unoccupied band (LUMO) leading to the highest defect band [27]. Stafström *et al.* [121] have suggested that unlike other conducting polymers, in case of PANi the doubly charged spinless bipolarons become unstable on a polyemeraldine chain resulting in the formation of two polarons, which separates to yield a polaron lattice. The fact that the Pauli susceptibility increases linearly with the degree of protonation in PANi confirms the existence of a polaron lattice in PANi. Thus, in PANi, instead of two bands, a single broad polaron band appears deep in the gap, which is also supported by band structure calculations [121].

The absorption peak occurring at $\lambda = 290$ nm can be attributed to the $\pi-\pi^*$ band transition. There are two visible region bands, one at around $\lambda = 440$ nm and the other, a broad peak centered on $\lambda = 800$ nm. The peak at 440 nm is ascribed to the transitions between the π and polaron bands, and the second peak centered at 800 nm is due to the polaron- π^* band transitions. It is observed that with the increase in irradiation fluence, the peak at 290 nm is further blue-shifted. The blue

shift observed in the UV-Visible spectra [Fig 4.22 (a) and (b)] may be attributed to the reduction in particle size of the PANi nanofibers, which has been clearly observed from TEM micrographs [section 4.2].

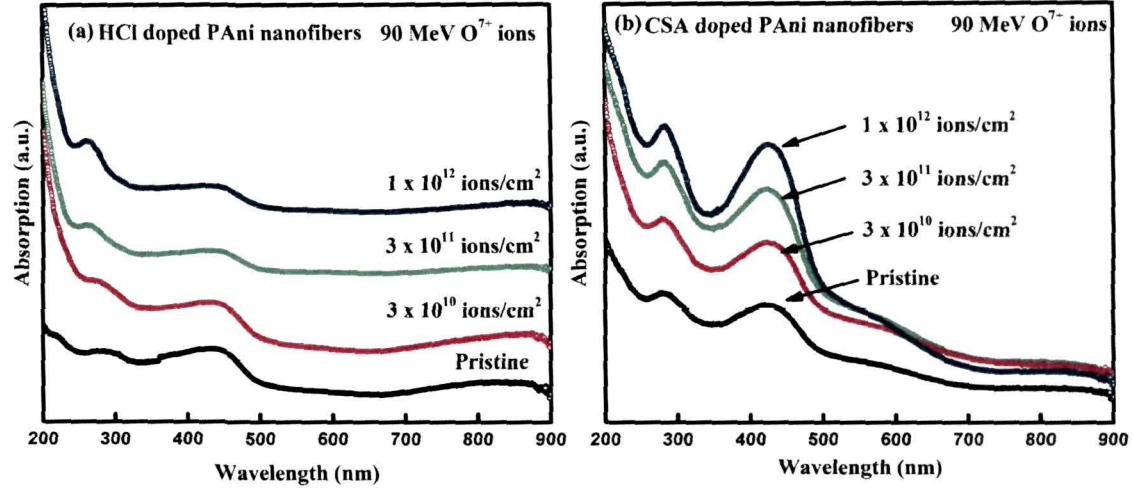


Figure 4.22: UV-Visible spectra of pristine and irradiated PANi nanofibers doped with (a) HCl and (b) CSA.

4.3.4.1. Optical band-gap

The optical absorption coefficient (α) has been determined from the absorption spectra using Eq. (4.1). After correction for reflection, the absorption coefficient (α) has been calculated from the absorbance (A), using the relation:

$$I = I_0 \exp(-\alpha x) \quad (4.1)$$

The Eq. (4.1) may be written as

$$\alpha = \frac{2.303}{x} \log\left(\frac{I}{I_0}\right) = \left[\frac{2.303}{x}\right] A, \quad (4.2)$$

where, x is the thickness of the sample;

$$\alpha = 2.303 \left(\frac{A}{d}\right) \quad (4.3)$$

where, A is the absorbance d is the thickness of the quartz cuvette used for the UV-Vis experiments.

The optical band gap may be evaluated for the values of the absorption coefficient using the following relation [Eq. (4.4)]:

$$\alpha = \sum \alpha_i = \sum_i \frac{A_i (h\nu - E_{gi})^{m_i}}{h\nu}, \quad (4.4)$$

where, the value of E_{gi} and m_i correspond to the energy and the nature of the particular optical transition with absorption coefficient α_i . For allowed direct, allowed indirect, forbidden direct and forbidden indirect transitions, the value of m_i corresponds to $1/2$, 2 , $3/2$ and 3 , respectively [421]. In an allowed direct transition the electron is simply transferred vertically from the top of the valence band to the bottom of the conduction band, without a change in momentum (wave vector). On the other hand, in materials having an indirect band gap, the bottom of the conduction band does not correspond to zero crystal momentum and a transition from the valence to the conduction band must always be associated with a phonon of the right magnitude of crystal momentum. In the present work, since we are dealing with nanostructures viz., PANi nanofibers, we have attempted to determine the value of m_i without pre-assuming the nature of the optical transition in the PANi nanofibers.

Now, the Eq. (4.4) can be written as

$$\frac{d[\ln(\alpha h\nu)]}{d(h\nu)} = \frac{m}{(h\nu - E)} \quad (4.5)$$

for a particular value of m_i and E_{gi} (say $m_i = m$ and $E_{gi} = E$). The plot of $d[\ln(\alpha h\nu)]/d(h\nu)$ vs. $h\nu$ will show a discontinuity at a particular value $h\nu = E$ where a possible optical transition might have occurred corresponding to a particular band-gap $E = E_{g1}$.

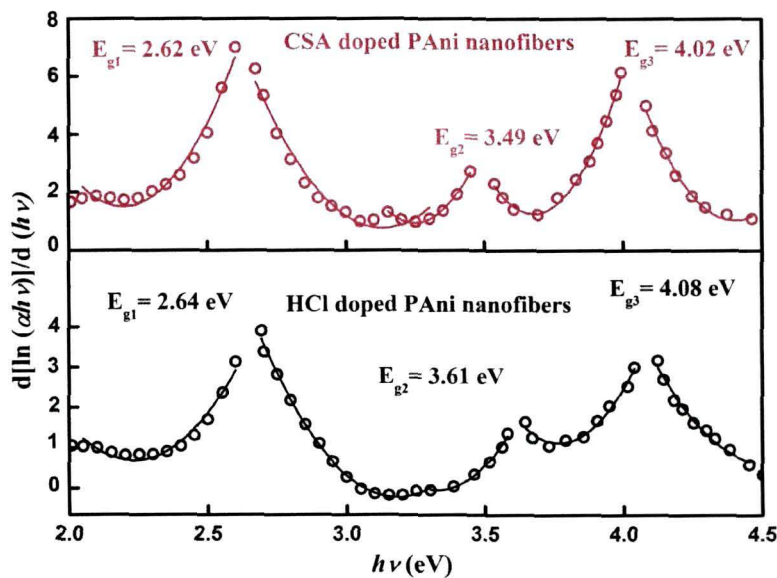


Figure 4.23: Plots of $d[\ln(\alpha h\nu)]/d(h\nu)$ vs. $h\nu$ for the pristine HCl and CSA doped PANi nanofibers.

Fig. 4.23 shows the plot of $d [\ln (\alpha h\nu)]/d (h\nu)$ vs. $h\nu$ for the pristine HCl and CSA doped PANi nanofibers. It is observed that there are three discontinuities corresponding to three possible optical transitions (at $E = E_{g1}$, $E = E_{g2}$ and $E = E_{g3}$) in both the pristine PANi nanofibers doped with HCl and CSA. In case of HCl doped PANi nanofibers the transitions have been observed at 2.64, 3.61 and 4.08 eV, while for the CSA doped PANi nanofibers the three discontinuities where the possible optical transition might have occurred are at 2.62, 3.49 and 4.02 eV. However, the Fig. 4.23 does not give us any idea about the nature of the optical transition as to whether it is direct or indirect.

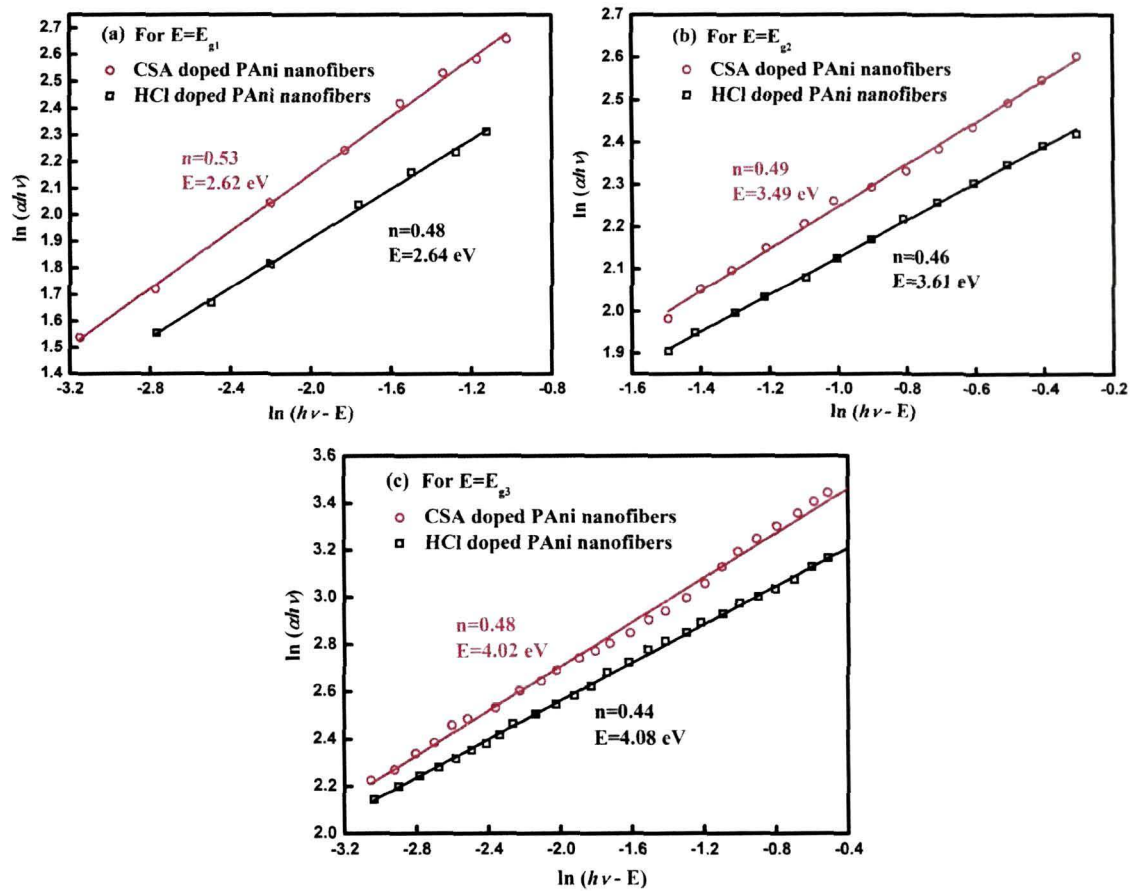


Figure 4.24: (a) Linear fit of $\ln (\alpha h\nu)$ vs. $\ln (h\nu-E)$ where $E = E_{g1}$ and (b) Linear fit of $\ln (\alpha h\nu)$ vs. $\ln (h\nu-E)$ where $E = E_{g2}$ and (c) Linear fit of $\ln (\alpha h\nu)$ vs. $\ln (h\nu-E)$ where $E = E_{g3}$ for both the HCl and CSA doped PANi nanofibers.

The nature of the optical transitions can be evaluated by determining the value of m associated with each transition. In order to get the m values corresponding to the three optical transitions at 2.64, 3.61 and 4.08 eV for HCl doped PANi nanofibers and 2.62, 3.49 and 4.02 eV for the CSA doped PANi

nanofibers, we plot $\ln(\alpha h\nu)$ as a function of $\ln(h\nu - E)$, where $E = E_{g1}, E_{g2}$ and E_{g3} for the three types of optical transitions as shown in Figs. 4.24 (a-c). The slopes of the plots have been determined by performing a linear fitting of the experimental data. It has been observed that for all the three types of optical transitions at $E = E_{g1}, E = E_{g2}$ and $E = E_{g3}$ for the HCl and CSA doped PANi nanofibers the slope is quite near to 0.5. This confirms that the three types of optical transitions in both the HCl and CSA doped PANi nanofibers are of allowed direct nature.

The direct optical band gap of the pristine HCl and CSA doped PANi nanofiber samples have also been determined by plotting $(\alpha h\nu)^2$ against the photon energy ($h\nu$). The relation between the optical absorption coefficient (α) for a direct transition and the photon energy ($h\nu$) was given by Fahrenbruch and Bude [Eq. (4.6)] [441]:

$$\alpha h\nu = A(h\nu - E_g)^{1/2} \quad (4.6)$$

where, A is a constant, h is Planck's constant, ν is the frequency of the radiation and E_g is the optical energy gap for direct transition.

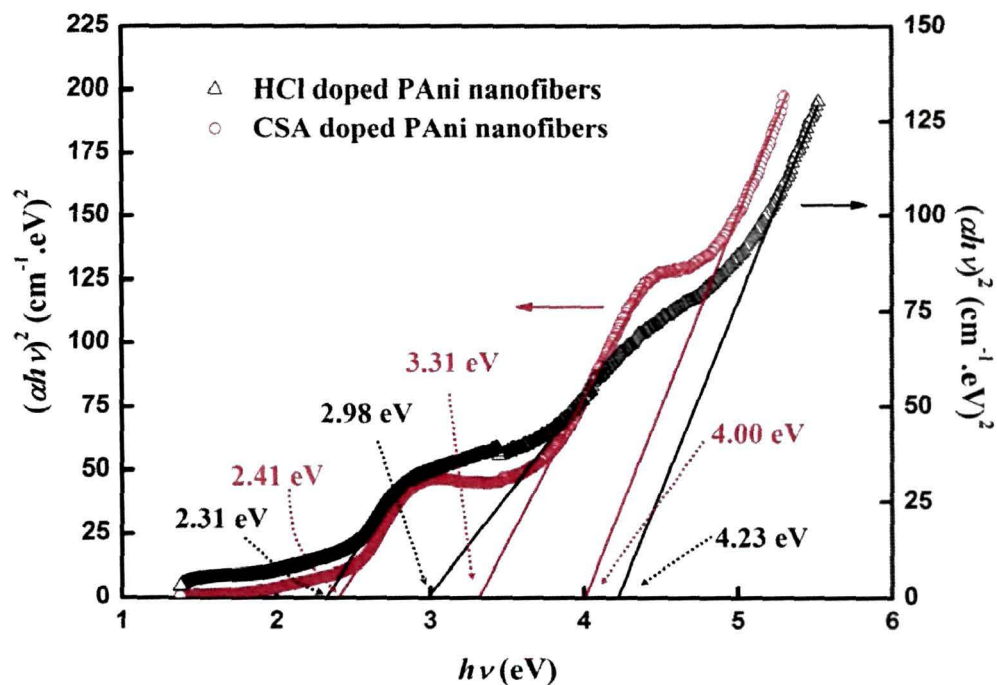


Figure 4.25: $(\alpha h\nu)^2$ vs. $h\nu$ plots for the pristine PANi nanofibers doped with HCl and CSA.

The plot of $(\alpha h\nu)^2$ versus photon energy ($h\nu$) for the pristine HCl and CSA doped PANi nanofibers has been presented in Fig. 4.25. The value of the optical

energy gap E_g is determined from the intersection of the extrapolated line with the photon energy axis (at $\alpha = 0$). The direct optical band gap of the pristine sample is found to be 4.23 eV and 4.00 eV for the PANi nanofibers doped with HCl and CSA, respectively, which is similar to the values (E_{g3}) obtained from the $d[\ln(\alpha h\nu)]/d(h\nu)$ vs. $h\nu$ plots for the same samples. Extrapolating two straight line portions of the plots to $\alpha = 0$, one can get two more activation energies viz., 2.31 eV and 2.98 eV for the PANi nanofibers doped with HCl and 2.41 eV and 3.31 eV, corresponding to the doping induced polaron defect levels present within the band gap in the samples, which also correspond to the energies (E_{g1} and E_{g2}) of the other two discontinuities observed in Fig. 4.23.

The direct optical band gap for the irradiated samples have been determined directly from the plot of $(\alpha h\nu)^2$ versus photon energy ($h\nu$), since the optical transitions in PANi nanofibers have been found to be of the allowed direct nature. Figs. 4.26 (a) and (b) show the $(\alpha h\nu)^2$ vs. $h\nu$ plots for the HCl and CSA doped PANi nanofibers, respectively, irradiated at a fluence of 3×10^{10} , 3×10^{11} and 1×10^{12} ions/cm². The optical band gaps (E_g) determined from these plots have been tabulated in Table 4.5.

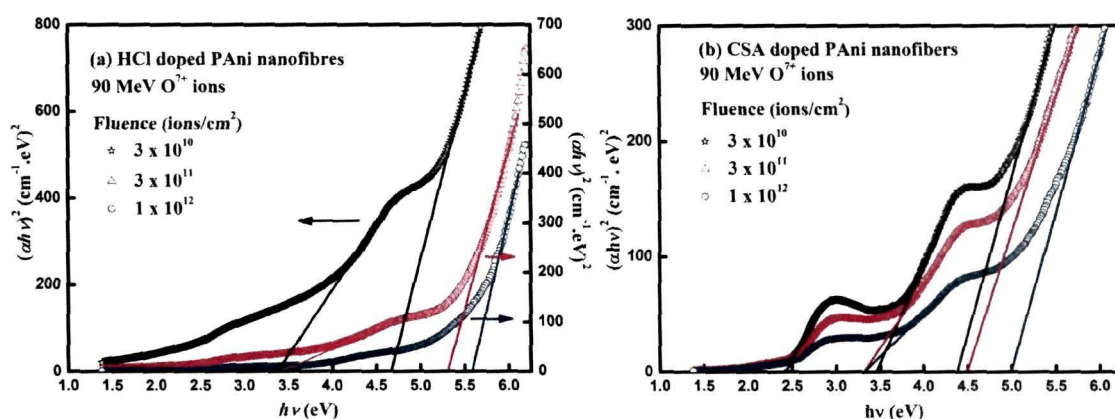


Figure 4.26: $(\alpha h\nu)^2$ vs. $h\nu$ plots for the irradiated PANi nanofibers (a) doped with HCl and (b) doped with CSA.

It is observed that the optical band gap increases with increasing irradiation fluence. This increase in the direct optical band gap values can be attributed to two factors: (a) the fragmentation of the PANi nanofibers upon SHI irradiation, and (b) a decrease in the extent of conjugation which suggests that the adjacent phenyl rings of the polymer have larger torsion angles with respect to the

plane of the nitrogen atoms [13]. This result is corroborated by the FTIR results, which show that there is a benzenoid to quinoid transition in the PANi nanofibers upon SHI irradiation that is an evidence of the decrease in the conjugation length of PANi nanofibers. It has also been observed from the $(\alpha h\nu)^2$ vs. $(h\nu)$ plots of the irradiated PANi nanofibers doped with HCl [Fig. 4.26 (a)], that the defect level observed at 2.31 eV for the pristine material cannot be detected for the irradiated samples. This suggests that the defect must have annealed out upon SHI irradiation.

SHI irradiation can anneal out defects as well as create defects within the forbidden energy gap of materials depending upon the nature of the material irradiated and the ion beam parameters such as fluence, energy and charge state of the ion. The defect level at 2.98 eV observed in the $(\alpha h\nu)^2$ vs. $(h\nu)$ plot for the pristine PANi nanofiber is found to shift to about 3.38 eV and remains almost similar for the samples irradiated at different fluences. However, both the defect levels in the CSA doped PANi nanofiber samples still continue to exist at almost the same positions (~ 2.41 eV and ~ 3.31 eV) even after irradiation. In fact, the defect levels in CSA doped PANi nanofibers become more prominent upon SHI irradiation, which is an indication of an increase in the density of states in the defect levels. The reason as to why the defect level at 2.41 eV still persists after SHI irradiation in the CSA doped PANi nanofibers is not clear. One might assume that the parameters of the ion beam being exactly same for both the samples, the observed phenomenon as discussed above has to do with the property of the dopant CSA, which is quite different from HCl since CSA has a long side chain and is much bulkier than HCl.

4.3.4.2. Urbach's tail

In case of non-crystalline materials there can be dense localized energy states, near the valence (HOMO) and conduction (LUMO) band edges, known as "Urbach energy bands". The absorption coefficient below the fundamental absorption edge for the non-crystalline materials show an exponential dependence on the photon energy ($h\nu$) which follows the Urbach formula given by Eq. 4.7 [442]:

$$\alpha(\nu) = \alpha_0 \exp\left(\frac{h\nu}{E_u}\right) \quad (4.7)$$

where α_0 is a constant, E_u is an energy which is interpreted as the width of the tail of localized states in the forbidden band gap, ν is the frequency of radiation and h is Planck's constant. This region is attributed to the electronic transition between a localized band tail and an extended band. The origin of E_u is considered as thermal vibrations in the lattice [443]. The above relation has been first proposed by Urbach [442] to describe the absorption edge in alkali halide crystals. This relation has also been found to be applicable for amorphous materials.

Figures 4.27 (a) and (b) show the logarithm of the absorption coefficient α plotted as a function of the photon energy ($h\nu$) for the pristine and irradiated HCl and CSA doped PANi nanofibers. The values of the Urbach energies (E_u) for the pristine and irradiated PANi nanofibers doped with HCl and CSA have been calculated by taking the reciprocal of the slopes of the linear portion of these curves and are listed in Table 4.5.

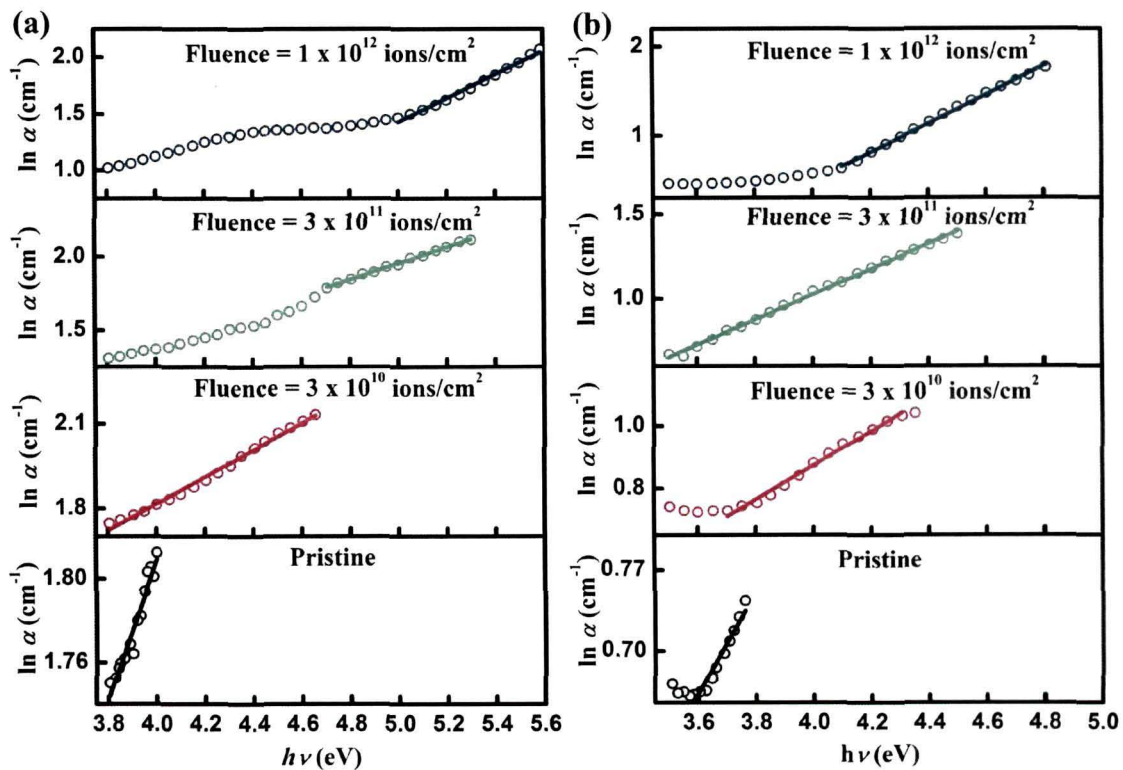


Figure 4.27: Plot of $\ln \alpha$ vs. $h\nu$ for the pristine and irradiated PANi nanofibers (a) doped with HCl and (b) doped with CSA. The reciprocal of the slopes of the linear portion of these curves have been used to calculate the Urbach's energy.

Table 4.5: Optical band gap (E_{opt}/E_{g3}), defect levels (E_{g1} and E_{g2}) and Urbach tail width (eV) of PANi nanofibers

Fluence	E_{opt} (E_{g3}) (eV)		E_{g2} (eV)		E_{g1} (eV)		Urbach energy (eV)	
	S1 ^a	S2 ^b	S1 ^a	S2 ^b	S1 ^a	S2 ^b	S1 ^a	S2 ^b
Pristine	4.08	4.02	2.98	3.31	2.31	2.41	3.01 ± 0.22	2.23 ± 0.09
3 × 10 ¹⁰	4.66	4.37	3.37	3.45	—	2.44	2.09 ± 0.05	1.82 ± 0.04
3 × 10 ¹¹	5.31	4.50	3.38	3.32	—	2.45	1.81 ± 0.03	1.34 ± 0.02
1 × 10 ¹²	5.59	4.81	3.38	3.31	—	2.42	0.95 ± 0.09	0.65 ± 0.17

^a S1 stands for PANi nanofibers doped with HCl

^b S2 stands for PANi nanofibers doped with CSA

Values of E_{opt} , E_{g2} and E_{g1} have errors upto ±5%.

According to Cody's model the Urbach tail width (ε) can be written as:

$$\varepsilon(T, X) = \frac{K_B \theta}{2\sigma_0} + \frac{K_B \theta}{\sigma_0} \left[\frac{1}{\exp(\theta/T) - 1} \right] + \frac{K_B \theta X}{2\sigma_0} \quad (4.8)$$

where, K_B is the Boltzmann constant, X is a dimensionless parameter called structural disorder parameter and θ is related to the Debye temperature (θ_D) by $\theta_D \approx 4\theta/3$. The second term in the Eq. (4.8) represents the contribution of electron-phonon and exciton-phonon interactions and the third term originates due to the mean square deviation of the atoms from a perfectly ordered lattice due to structural disorder. In the present work, since all the optical absorption spectra have been recorded at room temperature, the decrease in the Urbach tail width in PANi nanofibers upon SHI irradiation is supposed to be only due to the decrease in structural disorder.

The optical band gap calculated using UV-Vis spectroscopy is actually less than the actual band gap of the material. It is due to the band tailing that we are only able to measure the apparent band gap and not the actual one. It is observed that the Urbach's tail width decreases with increasing ion fluence, which indicates that the localized states due to disorder are annealed out upon SHI irradiation.

This leads to the further separation of the valence and the conduction band edges and hence the band gap of the material increases. Similar type of annealing out of disorders and subsequent increase in the band gap has been reported earlier [444]. However, the increase in band gap may be a combined effect of the decrease in the Urbach tail width and the quantum confinement effect, which has been discussed in the following section (Section 4.3.5.3.).

4.3.4.3. Quantum confinement effect

Another probable reason for the increase in the band gap upon SHI irradiation is the reduction in the fiber diameter upon SHI irradiation, which is clearly evident from the TEM micrographs [Figs. 4.2 (a-d) and Figs. 4.3 (a-d)]. Thus, it may be assumed that the observed increase in the band gap is a consequence of the existence of quantum confinement effect.

According to the theoretical treatment for this small fiber size, the electron and hole wave functions are individually confined. The gap energy, E , is inversely proportional to the square of the particle radius, R , as follows [445]:

$$E = E_g + \frac{\hbar^2 \pi^2}{2\mu R^2} \quad (4.9)$$

where E_g is the bulk band gap of PANi nanofibers, $\hbar = h/2\pi$, h is Planck's constant, and μ is the reduced mass of electrons and holes ($\sim 0.08 m_0$).

It is observed from the Table 4.5 that the absorption edge energy increases as the irradiation fluence is increased. On the other hand, it is clearly evident from the TEM micrographs and the size distribution curves described in the section 4.3.1 that the diameter as well as the length of both the HCl and CSA doped PANi nanofibers decreases with increasing ion fluence. If the absorption edge energy and the inverse of the square of the average particle radius of the pristine as well as irradiated PANi nanofibers exhibit a linear relationship, then one can associate the observed increase in the optical band gap with the quantum confinement effect. Fig. 4.28 shows the absorption edge energy as a function of the inverse of the square of the average particle radius. A linear relationship confirms the quantum size effect in PANi nanofibers leading to the enhancement of the optical band gap upon SHI irradiation. The corresponding bulk band-gap energy

obtained by interpolating the straight line at $1/R^2=0$ is found to be 3.89 for the HCl doped PANi nanofibers whereas for the CSA doped is 3.96 eV.

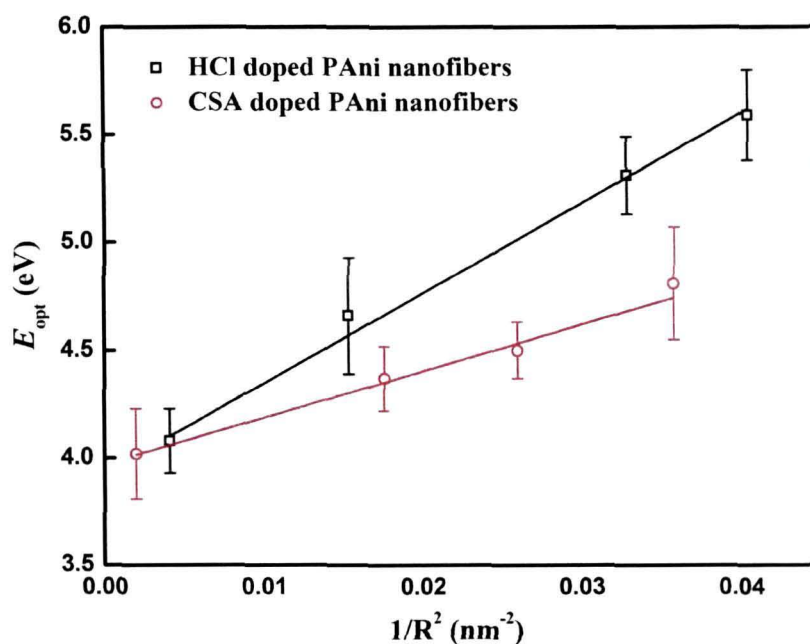


Figure 4.28: Band-gap versus the inverse of the square of the radius of the pristine and irradiated nanofibers illustrating the quantum confinement effect in PANi nanofibers.

4.3.5. Dielectric relaxation spectroscopy

Dielectric relaxation spectroscopy has been done for the pristine and irradiated HCl and CSA doped PANi nanofibers in order to understand the variations in the dielectric and conductivity relaxation processes in PANi nanofibers upon interaction with highly energetic ions. Dielectric relaxation spectroscopy has been widely employed to investigate the charge transport and relaxation phenomena in conducting polymers [422-424]. In general, the ac electric response is a superposition of the dielectric response of the bound charges (dipoles) along with the hopping of the localized charge carriers and the response produced by the molecular structure deformations due to the diffusion of charge carriers. The overall electric behaviour can be understood by employing different formulations such as the complex impedance (Z^*), complex permittivity (ϵ^*) and complex modulus (M^*). The experimental data acquired in the present work is presented in different formalisms viz., the permittivity formalism, the impedance formalism and the electric modulus formalism to investigate different relaxation processes taking place in the pristine and SHI irradiated HCl and CSA

doped PANi nanofibers. The dielectric function (ϵ^*) has been used to study the polarization mechanisms, whereas the complex impedance (Z^*) and the electric modulus (M^*) have been used to describe the conductivity relaxation mechanisms of the materials.

4.3.5.1. Permittivity formalism

Figures 4.29 (a, b) depicts the overall frequency dependence of the real part (ϵ') of the dielectric function ($\epsilon^* = \epsilon' - j\epsilon''$) for the HCl and CSA doped PANi nanofibers, respectively within the temperature range of 303–373 K. The real part (ϵ') of the dielectric function (ϵ^*) has been calculated from the measured values of capacitance using the formula:

$$\epsilon' = Cd/\epsilon_0 A \quad (4.10)$$

where, C is the measured capacitance of the sample, d is the thickness of the sample, A is the area of the pellet and ϵ_0 is the permittivity of free space.

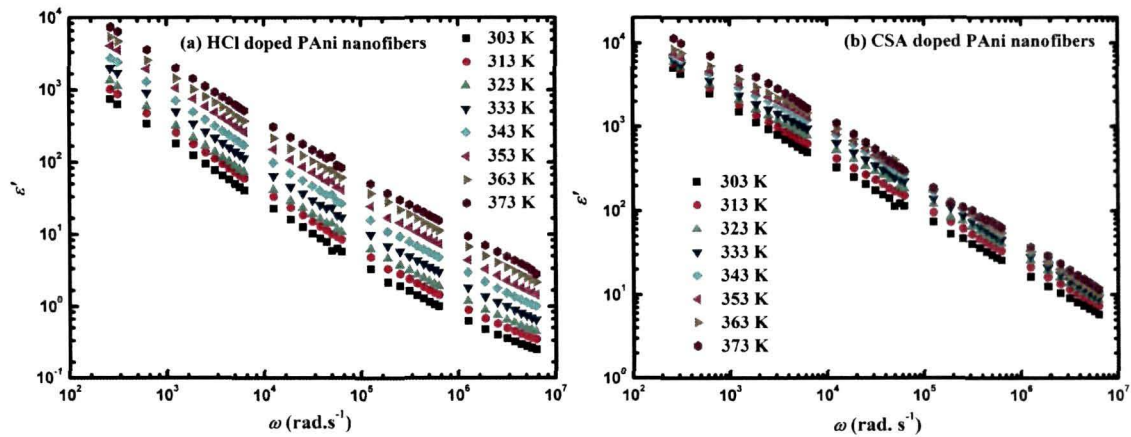


Figure 4.29: Frequency dependent variation of the real part (ϵ') of the complex permittivity (ϵ^*) for the PANi nanofiber doped with (a) HCl and (b) CSA within the temperature range of 303–373 K.

The frequency and temperature dependent variation in the imaginary part (ϵ'') of the complex dielectric function (ϵ^*) for the PANi nanofibers doped with HCl and CSA are shown in the Figs. 4.30 (a, b). The imaginary part (ϵ'') of the complex impedance has been measured as:

$$\epsilon'' = \epsilon' \tan \delta \quad (4.11)$$

where $\tan \delta$ is the loss factor that can be measured using the Hioki LCR meter and values of (ϵ') can be obtained according to the Eq. (4.10) by measuring the capacitance (C) using the LCR meter and the sample dimensions d and A .

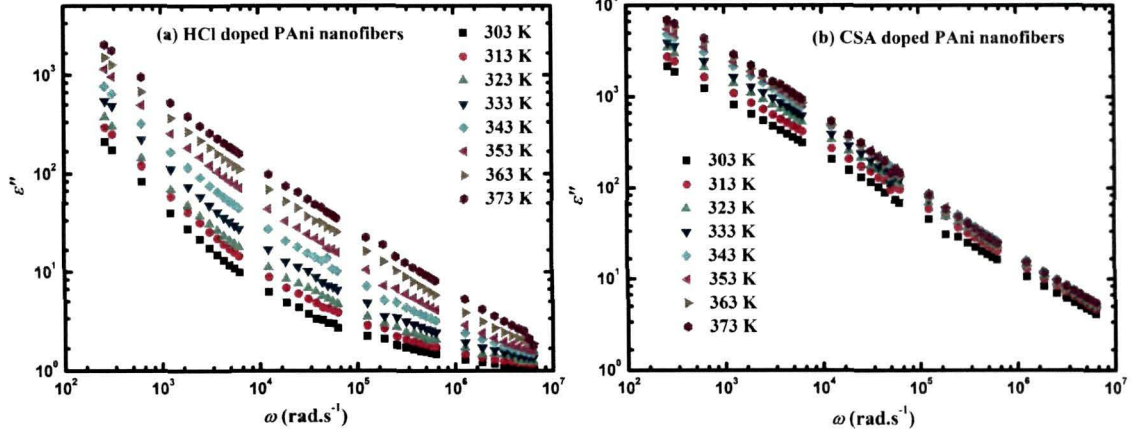


Figure 4.30: Frequency dependent variation of the imaginary part (ϵ'') of the complex permittivity (ϵ^*) for the PANi nanofiber doped with (a) HCl and (b) CSA in the temperature range of 303–373 K.

It is observed in Figs. 4.29 (a, b) and 4.30 (a, b) that the values of (ϵ') and (ϵ'') increase with increasing temperature in the low frequency (LF) region of the permittivity spectra. At frequencies (~ 10 kHz), a dielectric like relaxation can be recognized in the (ϵ'') spectra, which is more prominent in case of the HCl doped PANi nanofibers. The ϵ'' spectra of the HCl and CSA doped PANi nanofibers have been fitted to the following equation:

$$\epsilon'' = A\omega^{-s} + \frac{\Delta\epsilon' \sin(\beta\varphi)}{\left[1 + 2(\omega\tau_0)^{1-\alpha} \sin(\pi\alpha/2) + (\omega\tau_0)^{2(1-\alpha)}\right]^{\beta/2}}, \quad (4.12)$$

where

$$\varphi = \tan^{-1} \left[\frac{(\omega\tau_0)^{1-\alpha} \cos(\pi\alpha/2)}{1 + (\omega\tau_0)^{1-\alpha} \sin(\pi\alpha/2)} \right] \quad (4.13)$$

where A ($=\sigma/\epsilon_0$) and s are curve-fitting parameters and $\omega(=2\pi f)$ is the angular frequency. The first term of Eq. (4.12) describes the contribution of the dc conductivity to the ϵ'' losses. The second term of the Eq. (4.12), is the Havriliak–Negami (H–N) empirical relation. Parameters $\alpha(0 \leq \alpha < 1)$ and $\beta(0 < \beta \leq 1)$ depict the symmetric and asymmetric deviation from simple relaxation time, respectively. The H–N equations coincide with the respective Debye equations for

real and imaginary part of the complex dielectric function (ϵ^*) when $\alpha = 0$ and $\beta = 1$.

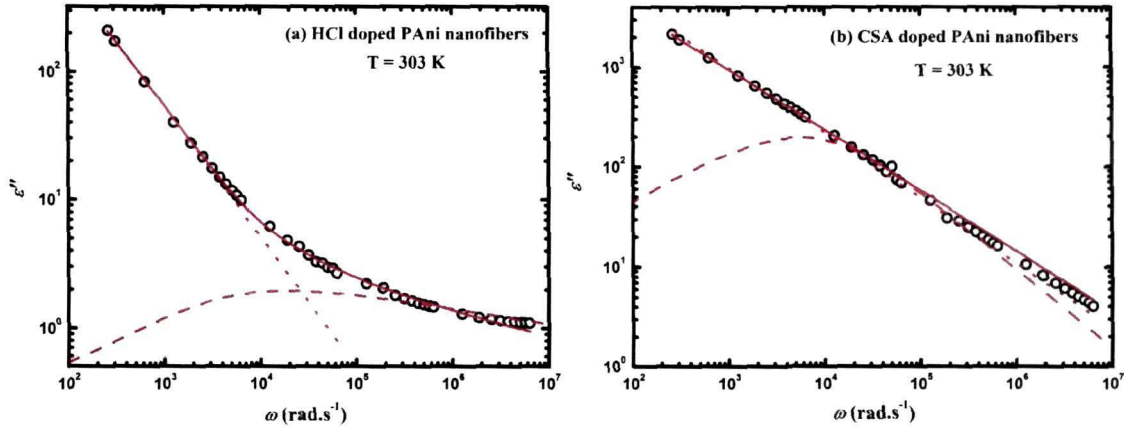


Figure 4.31: The imaginary part ϵ'' of the dielectric function (ϵ^*) vs. frequency for the PANi nanofibers doped with (a) HCl and (b) CSA at 373 K. The solid line is the best fit of Eq. (4.12) to the experimental data. The dotted line (.....) shows the contribution of dc conductivity and the dashed line (- - -) line shows the contribution of H-N function to the dielectric losses ϵ'' .

The best fit of Eq. (4.12) on a representative diagram of $\log \epsilon''$ versus $\log \omega$ concerning the HCl and CSA doped PANi nanofibers at 303 K are presented in Figs. 4.31 (a) and (b), respectively. The contributions of the dc conductivity and of the H-N function to the dielectric losses ϵ'' can be clearly marked from the same figure. The average values of the parameters α and β as obtained from the best fits of the experimental data are $\alpha = 0.245$ and $\beta = 0.834$ for the HCl doped PANi nanofibers and $\alpha = 0.345$ and $\beta = 0.657$ for the CSA doped PANi nanofibers. It is evident that the values of the fitting parameters α and β lie between 0 and 1, which indicates that the relaxation is non-Debye type and there is a distribution of relaxation times.

The strong low frequency (LF) dispersion for ϵ' and ϵ'' is a characteristic of materials in which charge carrier hopping is the dominating conduction mechanism [446]. In the LF region, the ϵ'' spectra exhibit no loss peaks even at higher temperatures and increase almost linearly with decreasing frequency due to the increased contribution of dc conductivity. At low temperatures and at a frequency around 10^4 Hz, a change in slope is observed in ϵ'' spectra [Figs. 4.30

(a) & (b)]. In conducting polymers there are no permanent dipoles. However, there is strong charge (polaron) trapping and its localized (short range) motion under the application of an external electric field serves as an “effective” electric dipole [447–449]. The dielectric relaxation in presence of such an alternating electric field is a result of charge hopping among available localized sites [365]. Polarons and bipolarons formed during doping are the relevant charge species for PANi nanofibers. At low frequencies such charge hopping could extend throughout the sample in the absence of strong pinning leading to a continuous current. Increasing temperature has the effect of mobilizing the polymer chains, reducing pinning and leading to larger number of charges participating in the relaxation process for a given frequency. With increasing temperature the ϵ'' spectra for both the HCl and CSA doped nanofibers exhibit almost linear behaviour with frequency and no relaxation mechanism can be noticed. This may be attributed to shorter time constants associated with increased chain movement. However, it must be stated that increased chain movement does not imply efficient charge transport as there is a concomitant reduction in polymer conjugation at higher temperatures increasing the barrier potentials for charge transport. At higher temperatures, the change in slope due to dielectric relaxation is not observed as the contribution of dc conductivity is higher. Since the polymer under investigation is non-polar, the observed relaxation in Figs. 4.30 (a, b) is not associated with a structural relaxation and a dynamic glass transition (i.e., the α - relaxation) [450]. This relaxation process has, therefore, been assigned to the hopping and/or oscillations of charges around fixed pinning centers.

Figure 4.32 (a-d) depict a comparison of the real part (ϵ') of complex permittivity (ϵ^*) as a function of temperature for the pristine and 90 MeV O^{7+} ion irradiated HCl doped PANi nanofibers at different frequencies. It is observed that ϵ' for the pristine and irradiated PANi nanofibers increases with the increase in temperature at any particular frequency and follows almost a similar trend for the pristine as well as the irradiated samples. At low temperatures, the rate of increase in ϵ' with temperature is smaller; however above 343 K (70^o C) the rate of increase in ϵ' is enhanced. It can be clearly observed that the real part of the complex permittivity or the dielectric constant of the HCl doped PANi nanofibers

at a particular frequency and temperature decreases as the irradiation fluence increases. Similar results have also been obtained for the pristine and irradiated CSA doped PANi nanofibers.

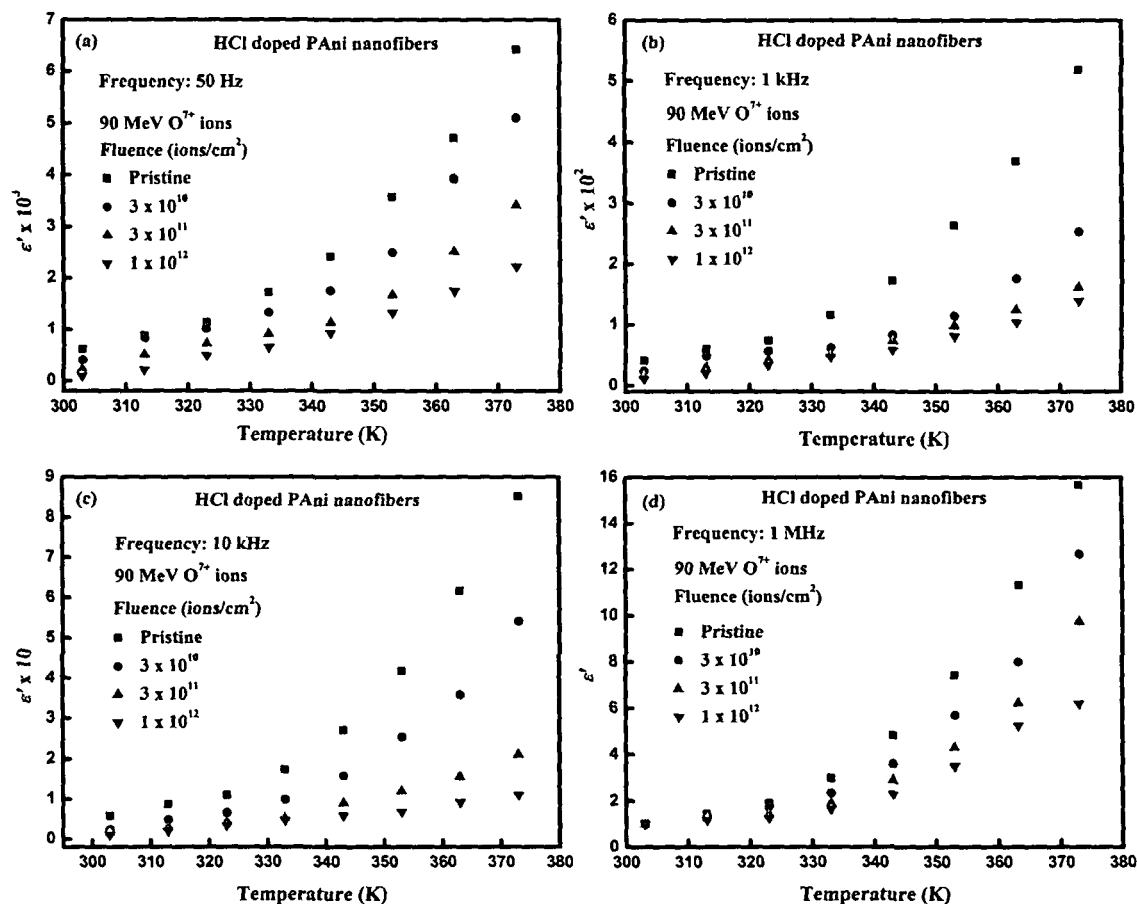


Figure 4.32: Variation of the real part (ϵ') of the complex permittivity (ϵ^*) as a function of temperature for the pristine and 90 MeV O^{7+} ion irradiated PANi nanofibers doped with HCl at frequencies of (a) 50 Hz, (b) 1 kHz, (c) 10 kHz and (d) 1 MHz.

It has been reported that the dielectric constant of polyaniline is proportional to the square of the crystalline domain coherence length and increases with increase in crystallinity of the macroscopic metallic domains [353]. The noticeable decrease in dielectric constant of both the HCl and CSA doped PANi nanofibers upon SHI irradiation can thus be ascribed to the decrease in crystallinity of the PANi nanofibers upon SHI irradiation. As discussed in section 4.3.2, X-ray investigations of the pristine and SHI irradiated PANi nanofibers show that the domain length and overall the degree of crystallinity of the PANi nanofibers decreases upon SHI irradiation. The dielectric relaxation in the irradiated PANi nanofibers shows almost similar behaviour to that of the

unirradiated sample, however, the contribution of the dc conductivity to the Eq. (4.12) defining the relaxation process in PANi nanofibers decreases with increasing irradiation fluence and the contribution of the H-N term becomes more prominent.

4.3.5.2. Impedance formalism

Fig. 4.33 (a-b) displays the variation of the real part (Z') of the complex impedance (Z^*) for the HCl and CSA doped PANi nanofibers as a function of frequency at different temperatures. Fig. 4.34 (a-b) shows the variation of the imaginary part (Z'') of the complex impedance (Z^*) of the HCl and the CSA doped PANi nanofibers as a function of frequency at different temperatures.

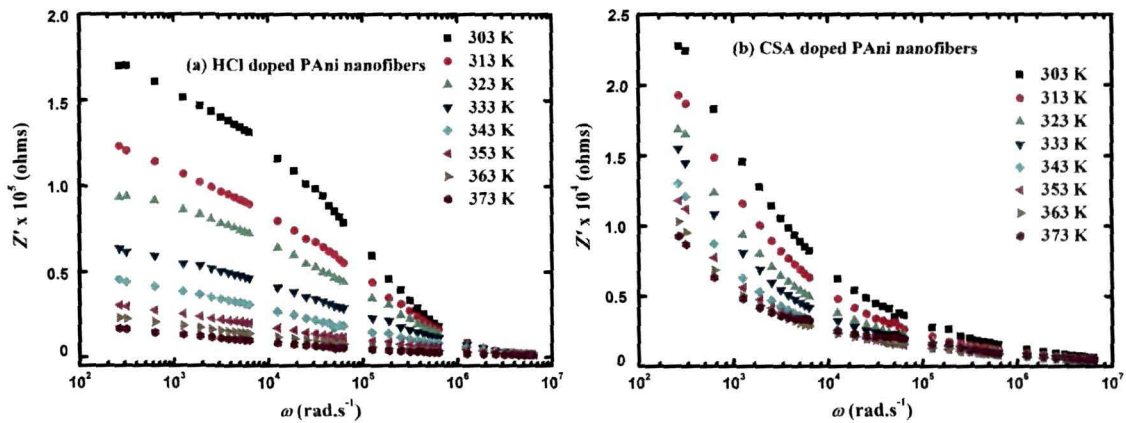


Figure 4.33: Variation of real part (Z') of complex impedance (Z^*) of PANi nanofibers doped with (a) HCl and (b) CSA

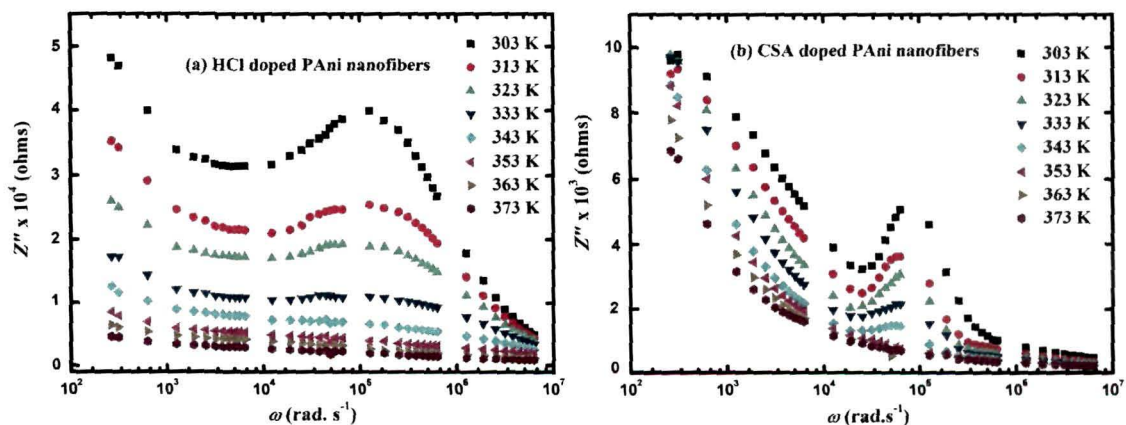


Figure 4.34: Variation of imaginary part (Z'') of complex impedance (Z^*) of PANi nanofibers doped with (a) HCl and (b) CSA

It is observed that the real part (Z') of the complex impedance (Z^*) decreases with the increase in frequency as well as temperature for both the HCl and CSA doped PANi nanofibers. The conductivity relaxation mechanisms in the HCl and CSA doped PANi nanofibers have been studied by considering the variations of the imaginary part (Z'') of the complex impedance (Z^*) as a function of frequency and temperature. Two relaxation mechanisms corresponding to a weak peak at high frequency and a probable strong peak at low frequency are observed. However, the phenomenon is not prominent at higher temperatures. (Z'') versus $\log \omega$ can be fitted to a sum of two Cole-Cole equations [390]:

$$Z'' = \sum_{i=1}^2 \frac{\Delta Z'_i [(\omega\tau_{0i})^{1-\alpha_i} \cos(\pi\alpha_i/2)]}{1 + 2(\omega\tau_{0i})^{1-\alpha_i} \sin(\pi\alpha_i/2) + (\omega\tau_{0i})^{2(1-\alpha_i)}} \quad (4.14)$$

where, $\Delta Z'_i$ is the contribution of each conductivity relaxation mechanism to the real part of the complex impedance, $\Delta Z'_i = R_i$. ω is the angular frequency, α_i is a parameter correlated with the mean width of the curve of each mechanism and obtains values of $0 \leq \alpha < 1$. The conductivity mechanism is described by a single relaxation time in case of $\alpha = 1$, while when $\alpha > 0$, this mechanism is described by symmetrical distribution of relaxation times. The parameter $\tau_{0i} (= 1/2\pi f_{0i})$ describes the mean relaxation time of each conductivity relaxation mechanism and corresponds to the frequency of maximum Z'' value. Figs. 4.35 (a, b) depict the respective fitting of Eq. (4.14) to the experimental Z'' data for the HCl and CSA doped PANi nanofibers, respectively acquired at 303 K.

Figs. 4.35 (a, b) also show the simulated curves depicting the contribution of two conductivity relaxation mechanisms having different relaxation times as obtained from the fitting parameters. The occurrence of two relaxation peaks in the Z'' spectra is not caused by any crystalline structure in the PANi nanofibers as the PANi nanofibers are mostly amorphous as is evident from the x-ray diffraction analysis presented in the section 4.3.2. The appearance of two relaxation peaks may be considered to be due to the two-phase structure in the PANi nanofibers. The lower frequency peak can be attributed to the phase of oxidized repeat units (quinoid) and the higher frequency peak to the phase of reduced repeat units (benzenoid) of PANi nanofibers [451, 452]. A comprehensive decrease in the value

of impedance has been observed with the increase in temperature, which may be attributed to increasing charge transfer between the two phases of the PANi nanofibers, since the charge transfer is a thermally activated process.

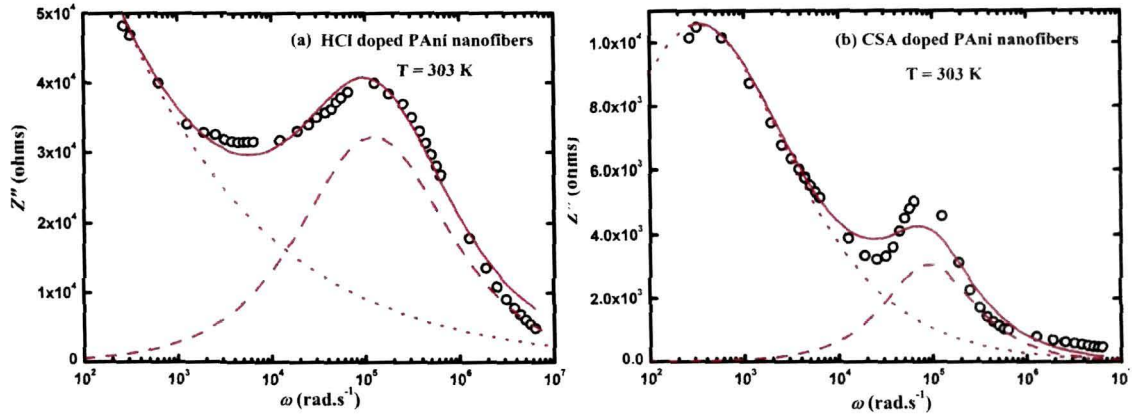


Figure 4.35: The imaginary part Z'' of the complex impedance (Z^*) as a function of frequency for PANi nanofibers doped with (a) HCl and (b) CSA at 303 K. The solid line (—) is the best fit according to Eq. (4.14). The dot lines (....) and the dashed lines (----) show the contribution of the two conductivity relaxation mechanisms to Z'' .

The variation of the real part (Z') of the complex impedance (Z^*) for the irradiated PANi nanofibers doped with HCl and CSA are shown in the Figs. 4.36 (a, b), respectively. The inset in the figures show the variation of real part of the complex impedance of the pristine HCl and CSA doped PANi nanofibers at 303 K for a better comparative view.

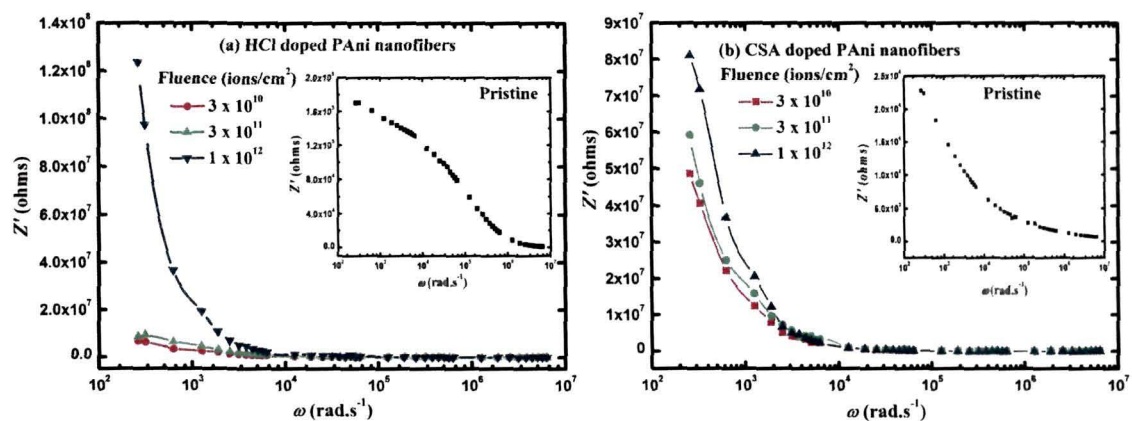


Figure 4.36: Variation of real part (Z') of complex impedance (Z^*) of 90 MeV O^{7+} ion irradiated PANi nanofibers doped with (a) HCl and (b) CSA. Inset shows the real part of complex impedance for the HCl and CSA doped PANi nanofibers at 303 K.

Figs. 4.37 (a, b) show the variation of the imaginary (Z'') part of the complex impedance for the 90 MeV O^{7+} ion irradiated PANi nanofibers doped with HCl and CSA, respectively. The inset shows the imaginary part of the complex impedance of the pristine HCl and CSA doped PANi nanofibers at 303 K. It can be clearly observed that in the SHI irradiated samples only one relaxation peak with a high value of impedance is observed at low frequency. The experimental data for the imaginary part of the complex impedance for the irradiated samples have thus been fitted to a single Cole-Cole equation resembling Eq. (4.14) but with the summation sign removed. This result is quite significant as it once again confirms that SHI irradiation leads to the transformation of the benzenoid units in the PANi nanofibers into quinoid units, which shows a peak at low frequency. The peak due to the benzenoid unit at higher frequency and with a low value of impedance as can be observed from the inset of the Figs. 4.37 (a, b) is no longer observed in the SHI irradiated PANi nanofibers indicating a transformation from the benzenoid to quinoid structure as has also been observed from the vibrational spectroscopy analysis.

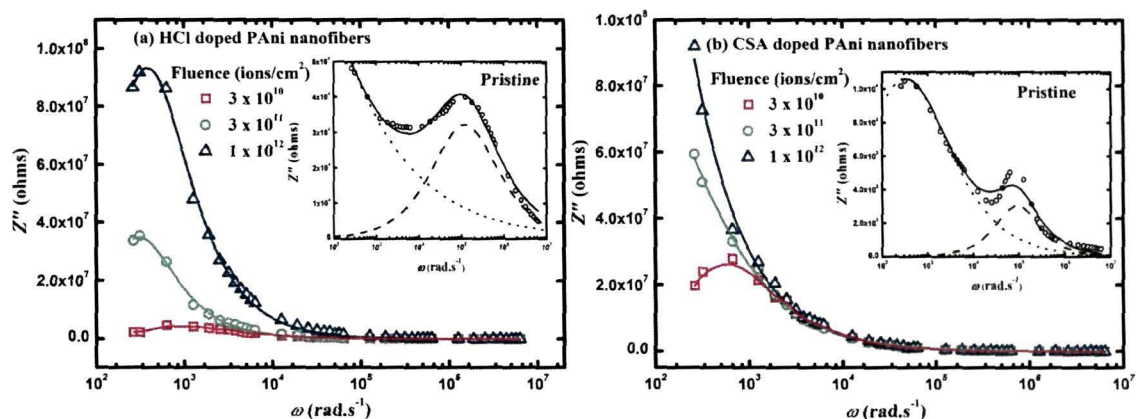


Figure 4.37: Variation of imaginary part (Z'') of complex impedance (Z^*) of 90 MeV O^{7+} ion irradiated PANi nanofibers doped with (a) HCl and (b) CSA. Inset shows the imaginary part of complex impedance for the HCl and CSA doped PANi nanofibers at 303 K. The solid lines are fit of the experimental data to a single Cole-Cole equation.

4.3.5.3. Electric modulus formalism

The term electrical conductivity relaxation (ECR) is often used to describe the frequency-dependent movement of charge carriers. The analysis of conductivity relaxation in HCl and CSA doped PANi nanofibers have been

undertaken in the complex electric modulus formalism M^* . Figs. 4.38 (a, b) show the variation of the real part (M') of the complex modulus (M^*) obtained by transforming the data of the complex permittivity for the HCl and CSA doped PANi nanofibers as a function of frequency at different temperatures ranging from 303-373 K according to the Eq. (2.86) in section 2.6.2 in Chapter 2. It is evident from the Figs. 4.38 (a, b) that the influence of electrode polarization is effectively suppressed for the electric modulus data since highly capacitive phenomena are suppressed in the M^* formalism.

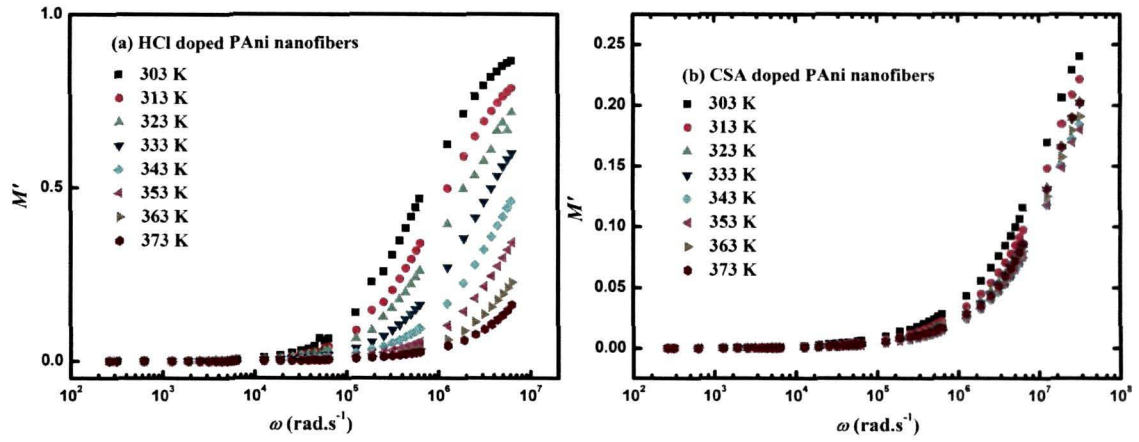


Figure 4.38: Frequency dependence of the real part M' part of the electric modulus function M^* at different temperatures for PANi nanofibers doped with (a) HCl and (b) CSA.

The generalization introduced by Havriliak and Negami [392, 424], in the permittivity mode can also be expressed in terms of M' and M'' as:

$$M' = M_{\infty} M_S \times \frac{[M_S B^{\gamma} + (M_{\infty} - M_S) \cos \gamma \varphi] B^{\gamma}}{M_S^2 B^{2\gamma} + 2B^{\gamma} (M_{\infty} - M_S) M_S \cos \gamma \varphi + (M_{\infty} - M_S)^2} \quad (4.15)$$

$$M'' = M_{\infty} M_S \times \frac{[(M_{\infty} - M_S) \sin \gamma \varphi] B^{\gamma}}{M_S^2 B^{2\gamma} + 2B^{\gamma} (M_{\infty} - M_S) M_S \cos \gamma \varphi + (M_{\infty} - M_S)^2} \quad (4.16)$$

where

$$B = \left[1 + 2(\omega\tau)^{1-\alpha} \sin \frac{\pi\alpha}{2} + (\omega\tau)^{2(1-\alpha)} \right]^{1/2} \quad (4.17)$$

and φ is given in Eq. (4.13). For $\gamma = 1$ and $\alpha = 0$, the corresponding Debye equations are obtained, for $\gamma = 1$ and $\alpha \neq 0$ the Cole-Cole equations and for $\gamma \neq 1$ and $\alpha = 0$, the Davidson-Cole equations for M' and M'' are obtained.

Figs. 4.39 (a, b) show the variation in the imaginary part M'' of the complex electric modulus (M^*) for the HCl and CSA doped PANi nanofibers as a function of frequency at different temperatures. The solid lines are the best fits of the experimental data according to the Eq. (4.16). The average values of the parameters α and γ as obtained from the best fits of the M'' spectra at different temperatures are $\alpha = 0.292$, $\gamma = 0.714$ for the PANi nanofiber doped with HCl and $\alpha = 0.312$, $\gamma = 0.809$ for the PANi nanofiber doped with CSA.

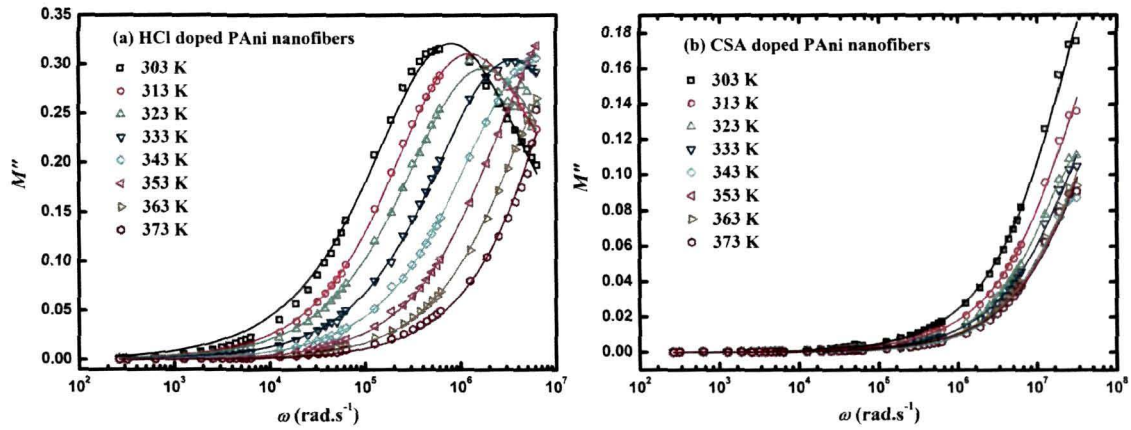


Figure 4.39: Frequency dependence of the real part M' part of the electric modulus function M^* at different temperatures for PANi nanofibers doped with (a) HCl and (b) CSA. The solid lines represent the best fits of the experimental data to Eq. (4.16) at different temperatures.

It is observed from the Fig. 4.38 (a, b), that $M'(\omega)$ shows a dispersion tending toward M_∞ , i.e. the asymptotic value of $M'(\omega)$ at higher frequencies approaches to zero at low frequencies, indicating that the electrode polarization makes a negligibly low contribution to $M'(\omega)$ and may be ignored when the permittivity data are expressed in this form. Figs. 4.39 (a, b) show the frequency dependence of the imaginary part of electric modulus M'' of the PANi nanofibers. In Fig. 4.39 (a), a peak is observed which shifts to higher frequencies with increasing temperature. However, in case of the PANi nanofibers doped with CSA the peak is not observed and might evolve if the measurement is done at frequencies higher than those in the present work. Although the physical meaning of this type of representation is still not fully understood [453, 454], the M^* formalism is frequently used in the analysis of dielectric data in relation to

conductivity effects [455]. The peak frequency ω_{\max} in the M'' versus $\log \omega$ spectra is an indication of a transition from short range to long range mobility at decreasing frequency along conductivity paths [456]. The low frequency side of the peak represents the range of frequencies in which charge carriers can move over long distances. The high frequency side of the M'' peak represents the range of frequencies in which charge carriers are spatially confined to their potential wells and can only make localized motion within the wells. The increase in $M'(\omega)$ and the subsequent development of peaks in the $M''(\omega)$ plot is a characteristic behaviour of dielectric dispersion [457].

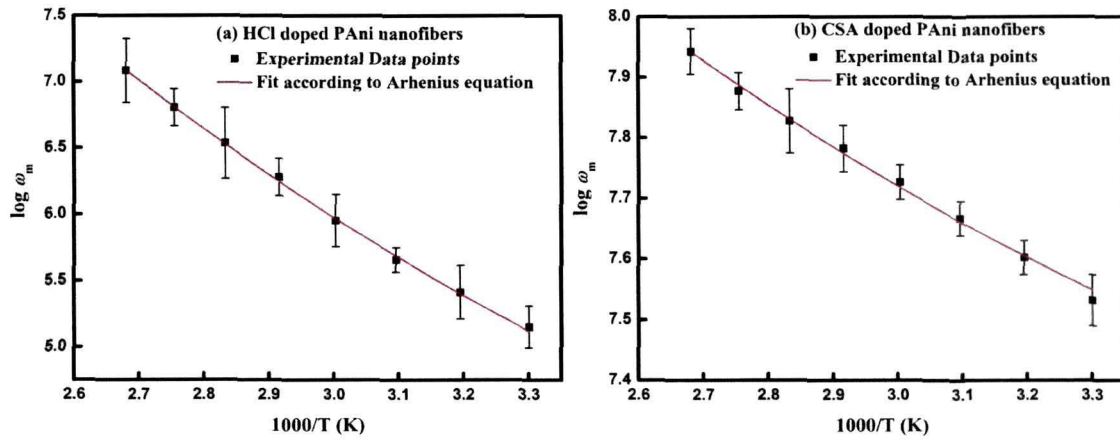


Figure 4.40: Temperature dependence of the most probable relaxation frequency obtained from the modulus formalism for PANi nanofibers doped with (a) HCl and (b) CSA. The solid line represents the best fit according to Eq. (4.18).

The peak angular frequency ω_{\max} is the characteristic frequency of the conductivity relaxation and defines the most probable conductivity relaxation time by $\omega_{\max} \tau_M = 1$. The values of ω_{\max} have been calculated by taking the inverse of the corresponding values of τ_M as obtained from the best fits of the experimental M'' data. The most probable relaxation time obeys the Arhenius relation given by:

$$\omega_{\max} = \omega_0 \exp\left[\frac{E_a}{k_B T}\right] \quad (4.18)$$

where ω_0 is the pre-exponential factor, k_B is the Boltzmann's constant, T is the absolute temperature, and E_a is the activation energy. Figs. 4.40 (a, b) show plots of $\log \omega_m$ versus $10^3/T$ for the HCl and CSA doped PANi nanofibers. The

activation energy E_a calculated from the best fit to the data points according to Eq. (4.18) are 0.24 eV for the HCl doped PANi nanofibers and 0.30 eV for the CSA doped PANi nanofibers.

Figs. 4.41 (a, b) show the plot of M'' measured at different temperatures ranging from 303–373 K, in which each frequency is scaled by the peak frequency ω_{\max} and M'' is scaled by the magnitude of the peak M''_{\max} . It can be observed that almost all the curves at different temperatures overlap on a single master curve, which is an indication of the fact that the dynamic processes occurring at different frequencies exhibit the same activation energy, so that a distribution of activation energies should not be considered as the origin of non exponential response [365]. However, a little deviation is observed for temperatures higher than 353 K, which may be attributed to the temperature induced modifications in the PANi nanofibers.

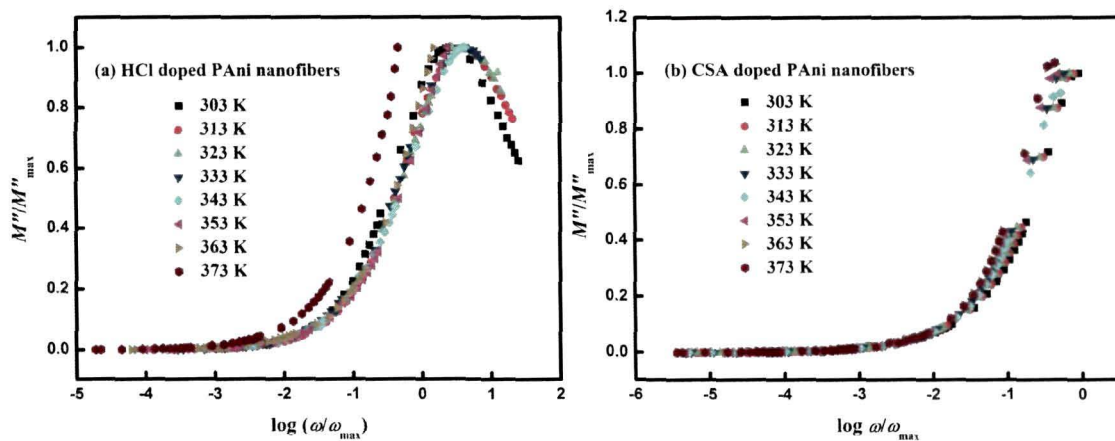


Figure 4.41: Scaling behaviour of M'' at various temperatures for PANi nanofibers doped with (a) HCl and (b) CSA

The variation in the imaginary part M'' of the complex modulus function M^* of the HCl and CSA doped PANi nanofibers upon irradiation with 90 MeV O^{7+} ions at different fluences are shown in the Figs. 4.42 (a, b). The experimental data points have been fitted with the Eq. 4.16. The parameters α , γ and relaxation time τ have been determined from the best fits and are tabulated in Table 4.6. It has been observed that the values of the parameters α and γ for the pristine as well as the irradiated PANi nanofibers lie between 0 and 1. This is an indication of the fact that relaxation in the pristine as well as the irradiated PANi

nanofibers is of the non-Debye type and that there is a distribution of relaxation times. The relaxation time, however, increases with increasing fluence.

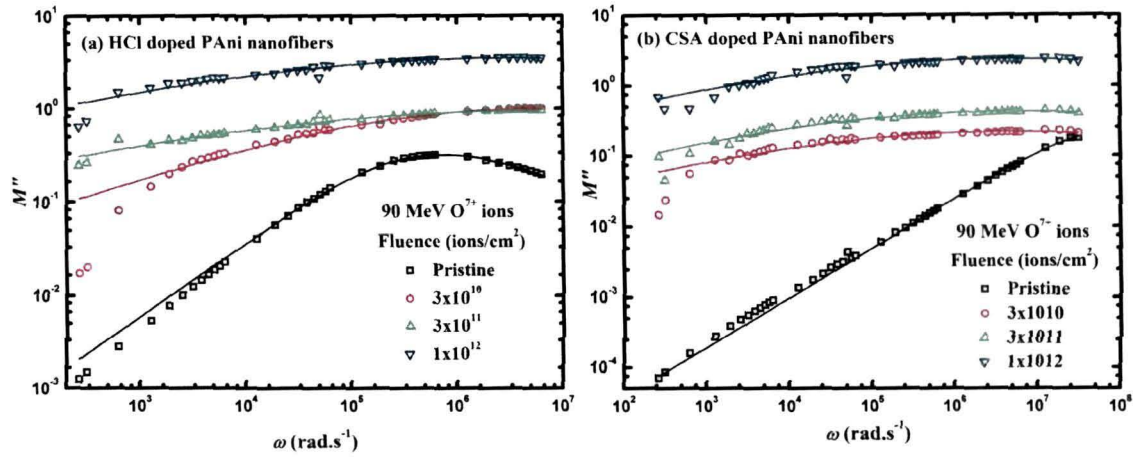


Figure 4.42: Variation of M'' for the pristine and 90 MeV O^{7+} ion irradiated PANi nanofibers doped with (a) HCl and (b) CSA as a function of frequency. Solid lines are the best fits to the experimental points according to the Eq. (4.16).

Table 4.6: Best fit parameters for M'' spectra at 303 K for the pristine and irradiated PANi nanofibers doped with HCl and CSA [Figs. 4.42 (a, b)]

Fluence (ions/cm ²)	α		γ		τ (secs)	
	S1	S2	S1	S2	S1	S2
0 (Pristine)	0.282	0.318	0.709	0.812	6.03×10^{-6}	2.83×10^{-8}
3×10^{10}	0.309	0.362	0.692	0.803	7.23×10^{-7}	3.45×10^{-8}
3×10^{11}	0.292	0.388	0.717	0.752	7.89×10^{-7}	5.35×10^{-8}
1×10^{12}	0.351	0.417	0.613	0.825	6.15×10^{-8}	8.91×10^{-8}

4.3.6. AC conductivity and charge transport mechanism

Figs. 4.43 (a, b) show the variations in ac conductivity as a function of frequency at different temperatures for the HCl and CSA doped PANi nanofibers, respectively. The ac conductivity $\sigma(\omega)$ of the PANi nanofibers over the entire frequency and temperature range has been calculated using the measured values of conductance $G(\omega)$ according to the Eq. 3.30 mentioned in the section 3.5.9 in Chapter 3. The ac conductivity of amorphous semiconductors and disordered

systems, in general, exhibit a universal behaviour and follow a power law with frequency [365] according to the Eq. 4.19 as:

$$\sigma(\omega) = \sigma_{d.c.} + A\omega^s \quad (4.19)$$

where s is the frequency exponent and $\sigma_{d.c.}$ is the frequency independent dc conductivity.

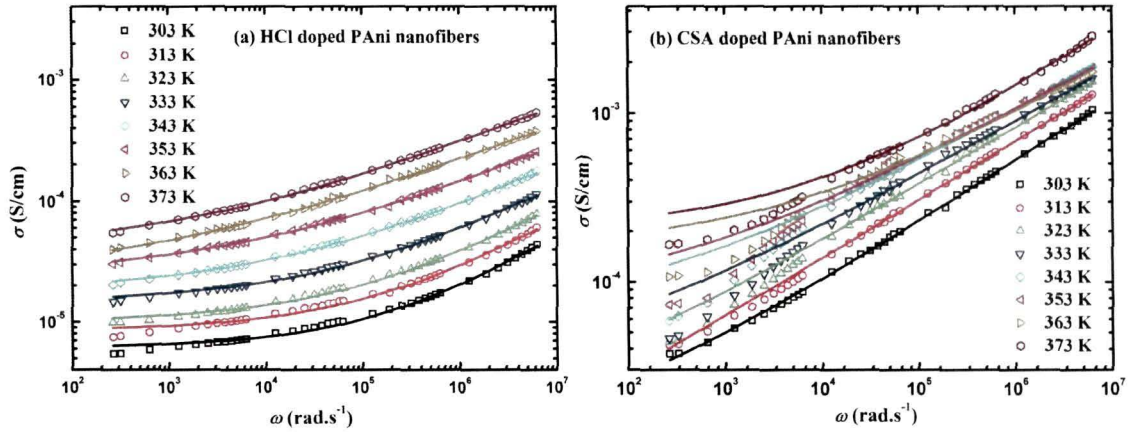


Figure 4.43: Variation of ac conductivity $\sigma(\omega)$ as a function of frequency and temperature (303-373 K) for PANi nanofibers doped with (a) HCl and (b) CSA. Solid lines are the best fits to the experimental data according to the Eq. (4.19).

The experimental data of ac conductivity acquired for the HCl and CSA doped PANi nanofibers as a function of frequency and temperature have been fitted to the Eq. (4.19). Solid lines in the Fig. 4.43 (a, b) are the best fits of the experimental values to the Eq. (4.19). The values of dc conductivity and the exponent “ s ” have been determined from the best fits. In general, the ac conductivity of disordered semiconductor and polymeric materials exhibits a common phenomenon characterized by a transition above a critical frequency ω_c from a frequency independent plateau in the low frequency region to a dispersive high frequency region [365]. Free charges available in the system contribute to the first trend observed in the curve whereas the frequency dependent conductivity is due to trapped charges, which are activated at higher frequencies. However, it can be observed from the Figs. 4.43 (a, b) that the experimental data in the lower frequency region especially for the CSA doped PANi nanofibers does not fit perfectly to the Eq. (4.19). This may be ascribed to electrode polarization effects often observed during dielectric measurements. However, the values of dc

conductivity obtained from the best fits indicate that the conductivity of the PANi nanofibers increases with increasing temperature. This can be attributed to the fact that with increasing temperature the polymer chains mobilize and pinning is reduced. Thus charge transport may become easier as more and more charges can take part in conduction.

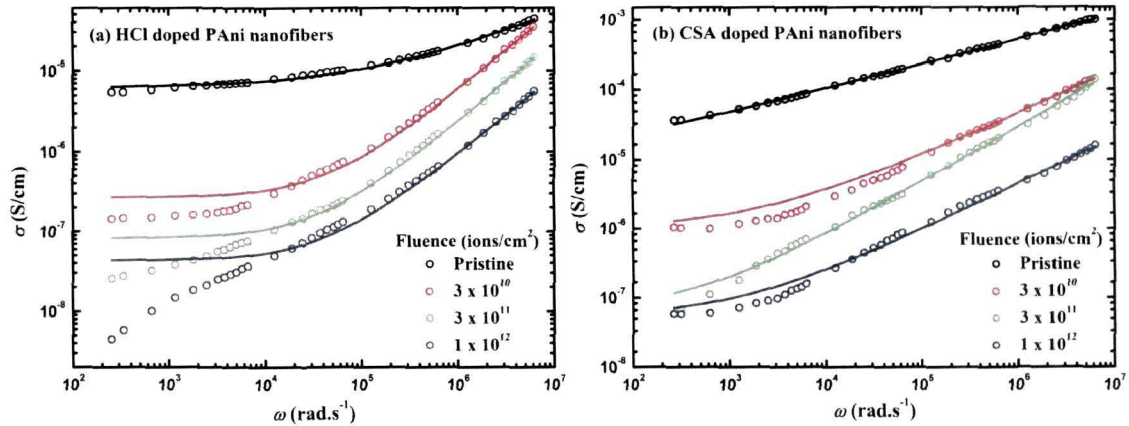


Figure 4.44: Frequency dependent ac conductivity of the pristine and irradiated PANi nanofibers doped with (a) HCl and (b) CSA

Figs. 4.44 (a, b) show the variation in the ac conductivity for the pristine and SHI irradiated PANi nanofibers doped with HCl and CSA, respectively. The experimental curves have been once again fitted with the Eq. (4.19) and the values of dc conductivity and the frequency exponent “ s ” have been determined. It has been observed that the deviation from the ideal curve according to the Eq. (4.19) in the low frequency region is greater for the irradiated samples than that for the pristine PANi nanofibers, which may be attributed to increased electrode polarization effects. The increase in the electrode polarization may be due to the decrease in the dc conductivity. The temperature dependent variation in the frequency exponent “ s ” as obtained from the best fits of the experimental data for the pristine and irradiated HCl and CSA doped PANi nanofibers are shown in the Figs. 4.45 (a, b). The exact nature of charge transport is obtained experimentally from the temperature variation of the frequency exponent “ s ” [366]. It is evident from the Figs. 4.45 (a, b) that the s -parameter for the pristine as well as the irradiated PANi nanofibers doped with HCl and CSA varies inversely with temperature. This behaviour observed for both the pristine and irradiated PANi nanofibers can be explained by the correlated barrier hopping model for charge

transport [366]. Thus, one can assume that the charge transport mechanism in PANi nanofibers remains unaltered upon SHI irradiation though the frequency independent dc conductivity decreases with the increase in irradiation fluence as observed in Figs. 4.44 (a, b).

Figs. 4.45 (a, b) show the variation of the frequency exponent “s” determined from the best fits of the ac conductivity data for the pristine and the SHI irradiated PANi nanofibers doped with HCl and CSA as a function of temperature.

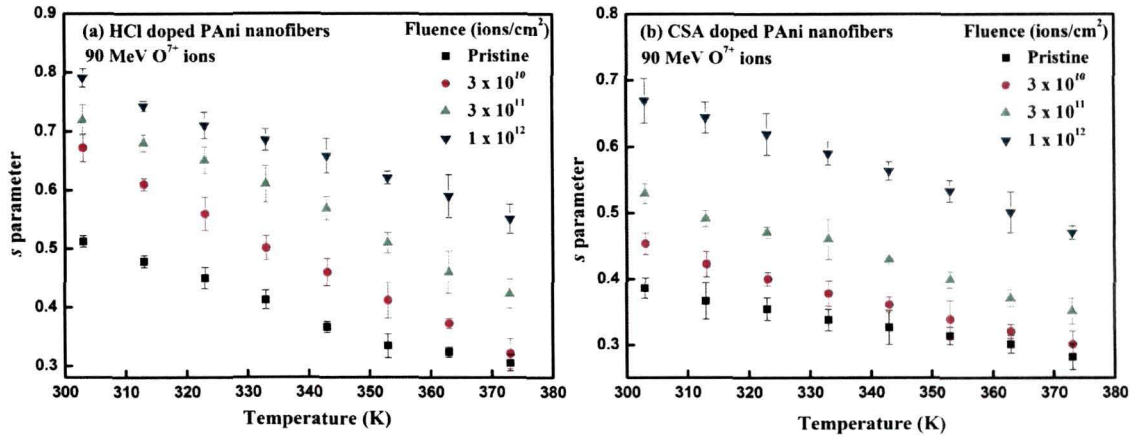


Figure 4.45: Variation in the frequency exponent “s” as a function of temperature for PANi nanofibers doped with (a) HCl and (b) CSA.

The temperature dependence of “s” according to the correlated barrier hopping model is given by:

$$s = 1 - \frac{6kT}{W_M - kT \ln[1/\omega\tau_0]} \quad (4.20)$$

where W_M is the polaron binding energy and τ_0 is the characteristic relaxation time. For large values of $W_M = kT$; Eq. (4.20) may be written as

$$1 - s = \frac{6kT}{W_M} \quad (4.21)$$

The values of W_M for the pristine and SHI irradiated PANi nanofibers at 303 K and 100 Hz calculated using the values of “s” determined from the best fits of the experimental data of ac conductivity are shown in Table 4.7. It can be clearly seen from the Table 4.7 that the value of W_M lies between 0.30–0.80 indicating that single polarons, and not bipolarons are the major charge carriers in the PANi nanofibers since the value for W_M must be almost four times higher for

bipolaronic transport [366]. Thus, it is not only the mechanism of charge transport but also the nature of charge carriers in PANi nanofibers that are not altered upon irradiation with 90 MeV O^{7+} ions.

The values of the hopping distance R_w calculated according to the correlated barrier hopping model using the Eq. (4.22) at the same frequency and temperature for the pristine and irradiated PANi nanofibers doped with HCl and CSA are also presented in Table 4.7:

$$R_w = \frac{e^2}{\pi\epsilon\epsilon_0[W_M - kT \ln\left(\frac{1}{\omega\tau_0}\right)]} \quad (4.22)$$

The expression for ac conductivity $\sigma(\omega)$ according to the correlated barrier hopping model is given by the relation:

$$\sigma(\omega) = \frac{1}{24} \pi^3 N^2 \epsilon\epsilon_0 \omega R_w^6 \quad (4.23)$$

where $N = kTN(E_F)$ and $N(E_F)$ is the density of states at the Fermi level. Table 4.7 also shows the values of $N(E_F)$ for the pristine and irradiated PANi nanofibers at 100 Hz and 303 K calculated by putting the experimental values of $\sigma(\omega)$ and ϵ for the particular frequency and temperature in the Eq. (4.23).

Table 4.7: Values of polaron binding energy (W_M), hopping distance (R_w) and density of states $N(E_F)$ calculated using the correlated barrier hopping model.

Fluence (ions/cm ²)	W_M (eV)		R_w (Å)		$N(E_F) 10^{24} \text{ eV}^{-1} \cdot \text{cm}^{-3}$	
	S1 ^a	S2 ^b	S1 ^a	S2 ^b	S1 ^a	S2 ^b
0 (Pristine)	0.32	0.26	2.16	2.71	1.24	0.95
3×10^{10}	0.47	0.28	1.52	2.05	2.92	1.53
3×10^{11}	0.56	0.33	1.02	1.47	4.35	2.92
1×10^{12}	0.75	0.47	0.65	0.76	6.76	4.13

It is due to the disorder in conducting polymers that they exhibit a finite density of states at the Fermi level (E_F) thereby facilitating hopping in conducting polymers [335]. The increase in the density of states with increasing irradiation

fluence corresponds to a decrease in delocalization of the electronic states impeding hopping charge transport upon SHI irradiation.

4.4. Summary

Polyaniline (PAni) nanofibers doped with hydrochloric acid (HCl) and camphor sulfonic acid (CSA) have been successfully synthesized using interfacial polymerization and irradiated with 90 MeV O^{7+} ions at different fluences and the physico-chemical modifications in the nanofibers have been investigated employing different characterization techniques. Transmission electron microscopy of the pristine and irradiated PAni nanofibers reveals fragmentation of the PAni nanofibers. It has been observed that upon SHI irradiation the average diameter of the PAni nanofibers decreases from 29.35 to 9.45 nm for the nanofibers doped with HCl and from 50 nm to 11.38 nm for the nanofibers doped with CSA. XRD analysis shows that as the irradiation fluence increases, the crystalline domain size decreases while the strain increases. The decrease in the integral intensity (area) for the (100) reflection peak with increasing fluence suggests that the PAni nanofibers are amorphized. Enhancement in the strain in the material may be attributed to the creation of dislocations and defects in the material upon SHI irradiation. The increase in d -spacing indicates an increase in the $C_{ring}-N-C_{ring}$ tilt angle with respect to the (a, b) basal plane of PAni. This has been associated with the reduction in π -stacking among the PAni chains and de-doping of the doping states of PAni nanofibers upon SHI irradiation. De-doping and amorphization of PAni nanofibers have been confirmed by micro-Raman (μ R) spectroscopy. Vibrational spectra of the pristine and SHI irradiated PAni nanofibers investigated using FTIR and μ R spectroscopic techniques brings out a very significant result i.e., a benzenoid to quinoid transition in the PAni nanofibers upon SHI irradiation. The benzenoid to quinoid transition leads to a decrease in the π -conjugation length. It has been observed that PAni nanofibers exhibit three allowed direct transitions at ~ 2.64 , 3.61 and 4.08 eV for HCl doped and at ~ 2.62 , 3.49 and 4.02 eV for the CSA doped PAni nanofibers. The slight variations in the energies of the allowed optical transitions has been attributed to different fiber diameters in case of the two types of PAni nanofibers (HCl doped ~ 30 nm and CSA doped ~ 50 nm). The optical band gap determined from the

$(ah\nu)^2$ against photon energy $h\nu$ plot is consistent with the energy discontinuities observed in the plot of $d[\ln(ah\nu)]/d(h\nu)$ vs. $h\nu$, where the possible optical transition might take place. Upon irradiation an increase in the optical band gap is observed which has been attributed to the fragmentation of the PANi nanofibers upon SHI irradiation and also a decrease in the extent of conjugation which suggests that the adjacent phenyl rings of the polymer have larger torsion angles with respect to the plane of the nitrogen atoms, which is also corroborated by the μ R and FTIR results that indicate a partial benzenoid to quinoid transition resulting in reduction in π -conjugation. The structural disorders have been found to anneal out as a result of SHI irradiation as confirmed by the decreasing value of Urbach tail width with increasing ion fluence that enhances the band gap. Dielectric spectroscopy of PANi nanofibers reveals that relaxation in PANi nanofibers is of the non Debye type and there is a distribution of relaxation times. The disappearance of the peak due to benzenoid units of PANi nanofibers in the impedance spectra as a result of SHI irradiation also indicates a benzenoid to quinoid transition in the PANi nanofibers upon SHI irradiation. Existence of a master curve in the modulus spectra reveals that the dynamic processes occurring at different frequencies exhibit the same activation energy. These results indicate that there is an increased coupling among the localized short range dipolar motion in the PANi nanofibers. The decrease of the s -parameter with increasing temperature for the pristine and SHI irradiated PANi nanofibers suggests that correlated barrier hopping (CBH) is the dominant charge transport mechanism. Low values of polaron binding energy (0.30–0.80 eV) calculated using the experimental values of the frequency exponent s confirms the existence of single polarons as the major charge carriers in both the pristine and SHI irradiated PANi nanofibers. Although there is little variation in the charge transport mechanism and the nature of charge carriers in the PANi nanofibers upon SHI irradiation but there is a significant decrease in the conductivity of the PANi nanofibers upon SHI irradiation. The increase in the density of states in PANi nanofibers with increasing irradiation fluence reveals a decrease in delocalization, which is responsible for the observed decrease in the conductivity.

Chapter 5

POLYANILINE NANOFIBER REINFORCED PVA NANOCOMPOSITES: SYNTHESIS, SHI IRRADIATION AND CHARACTERIZATION

This chapter describes the details of the synthesis of polyaniline (PAni) nanofiber reinforced polyvinyl alcohol (PVA) nanocomposites employing in-situ rapid mixing polymerization technique and the effect of SHI irradiation on the physico-chemical properties of the nanocomposites. Modifications in the morphology, conformation and the charge transport properties of the nanocomposites have been investigated and analyzed using sophisticated characterization tools. The discussions of the results obtained constitute the core of this chapter.

5.1. Introduction

Modernization of existing technologies requires new materials. The movement towards nanodimensions in many areas of technology during the past few decades have aroused tremendous interest in nanostructured materials. Future progress in such fields of technology as actuators, microelectronics, sensors, biosensors, drug delivery systems, chemical and biochemical engineering depends greatly on the development of the available knowledge on nanostructured materials. Conducting polymers have been in the forefront of research and development for the last three decades and have found application in diverse areas of research [38-49]. Conducting polymer based nanostructured materials offer the advantage of being low dimensional organic conductors and has often been more efficient in certain applications where surface to volume ratio plays an important role [155].

Nanocomposites of intrinsically conducting polymers (ICPs) are materials that utilize conjugated polymers and at least one secondary component in the nano-dimension that can be inorganic, organic materials or biologically active species. The goal is to produce a composite material that has distinct properties not observed in the individual components. A special class of these nanocomposites viz., the Organic in Organic (O-O) nanocomposites have the advantages of better processibility, light weight, low cost and environmental stability. Carbon nanotubes reinforced polymer composites, carbon fiber reinforced polymer composites are examples of nanocomposites belonging to this class of materials [218, 225]. This class of nanocomposites have potential for being used as biomaterials. These materials possess much higher stiffness and mechanical strength and as such are more desirable for device applications.

Conducting polymer nanostructures generally have poor film formability and it is only under special circumstances that we can obtain a stable film of PAni nanofibers [155]. The lack of film formability and the requirement of a film substrate restrict the application of these nanostructures in certain specific applications such as actuators and sensors where a stable free standing film is often a primary requirement. As such it seems that developing nanocomposites of conducting polymer nanostructures with other insulating polymers having good mechanical strength can lead us to the realization of some device applications, which otherwise may not be possible with the pristine nanostructures of conducting polymers. In this chapter of the thesis, we present a synthesis technique based on rapid mixing polymerization [148] to synthesize nanocomposites of conducting polymer nanostructures in general and PAni nanofibers in particular with an insulating but mechanically strong water soluble polymer to yield free standing (self supporting) films of PAni nanofiber reinforced polymer nanocomposites. The advantage of this technique is that the synthesis is carried out in a single pot and the polymerization takes place *in-situ*, which reduces the risk of phase separation as is generally observed when conducting polymer nanostructures are mixed with another polymer *ex-situ*. In the following sections and sub-sections we present a detailed discussion of the advantages and limitations of the synthesis technique and the results obtained

after the characterization of the pristine and SHI irradiated PANi nanofiber reinforced PVA nanocomposites using different characterization techniques.

5.2. Synthesis of polyaniline nanofiber reinforced PVA nanocomposites

Processible PANi nanofiber reinforced PVA nanocomposite films have been synthesized by *in-situ* rapid mixing polymerization in a medium consisting of the water-soluble non-conducting polymer [polyvinyl alcohol (PVA)] and a plasticizer. A plasticizer (in this case Glycerol) has been added at a certain concentration to confer plasticity and flexibility to the films. PVA has been dissolved in milli-Q water after heating at 80° C. Glycerol is added after the solution cools down to room temperature. After that the monomer (aniline), oxidant and dopant are added all at the same time and the solution is rapidly mixed (>2000 rpm) for 24 hours. The solution gradually turns green indicating the formation of PANi nanofibers. After 24 hours the solution is heated to make it viscous and cast on glass slides and Petri dishes. Ultra thin films of the nanocomposites have also been prepared using spin-coating and dip-coating techniques for certain specific characterizations. The films have high stability and are also free standing (self supporting). Hydrochloric acid (HCl) has been used as the dopant while ammonium peroxydisulfate [APS, (NH₄)₂S₂O₈] as the oxidant during the synthesis. The ratio of the monomer to the oxidant has been maintained at 2:1. HCl has been added to the solution to maintain a pH<3. Table 5.1 shows the composition of the PANi nanofiber reinforced PVA nanocomposites synthesized in the present study.

Table 5.1: Composition of the PANi nanofiber reinforced PVA nanocomposites

Sample Code	PVA (wt. %)	Glycerol (wt. %)	Aniline (wt. %)	Thickness (μm)
G1	80	20	2	31.72 ± 0.28
G2	80	20	4	33.67 ± 0.51
G3	80	20	6	30.13 ± 0.62

Other compositions have also been studied varying the aniline wt.%, however, in the present study we have considered only three samples with aniline content varying from 2 wt.% to 6 wt.% as these compositions showed good and repeatable results.

5.3. Characterization of pristine and SHI irradiated polyaniline nanofiber reinforced PVA nanocomposites

5.3.1. Electron microscopy

Fig 5.1 shows the transmission electron micrograph of the PANi nanofiber reinforced PVA nanocomposite (sample G3). It is observed that PANi nanofibers having average diameters in the range of 30 nm have been formed after the rapid mixing polymerization reaction. In this case HCl is used as dopant and it has been reported that PANi nanofibers doped with HCl have diameters within this range (~ 30 nm) whether they are synthesized by interfacial polymerization or rapid mixing polymerization technique [155]. However, the mixing speed is an important factor since if the solution is mixed at very high speeds then there is a probability of obtaining agglomerated structures and not nanofibers.

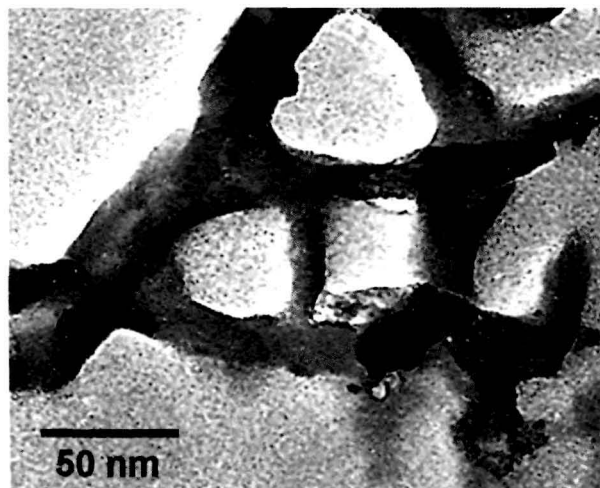


Figure 5.1: Transmission electron micrograph of the PANi nanofiber reinforced PVA nanocomposite with 6 wt. % of aniline content (sample G3)

Figs. 5.2 (a-c) show the scanning electron micrographs of the PANi nanofiber reinforced PVA nanocomposites viz., sample G1, G2 and G3 with 2 wt. %, 4 wt. % and 6 wt. % of aniline content, respectively. The micrographs display that the surface morphology of the nanocomposites becomes rougher and the porosity decreases as the aniline content in the nanocomposites increases. Fig. 5.2 (c) clearly indicates randomly oriented fiber like structures of PANi evolving in the surface of the PANi nanofiber reinforced PVA nanocomposites.

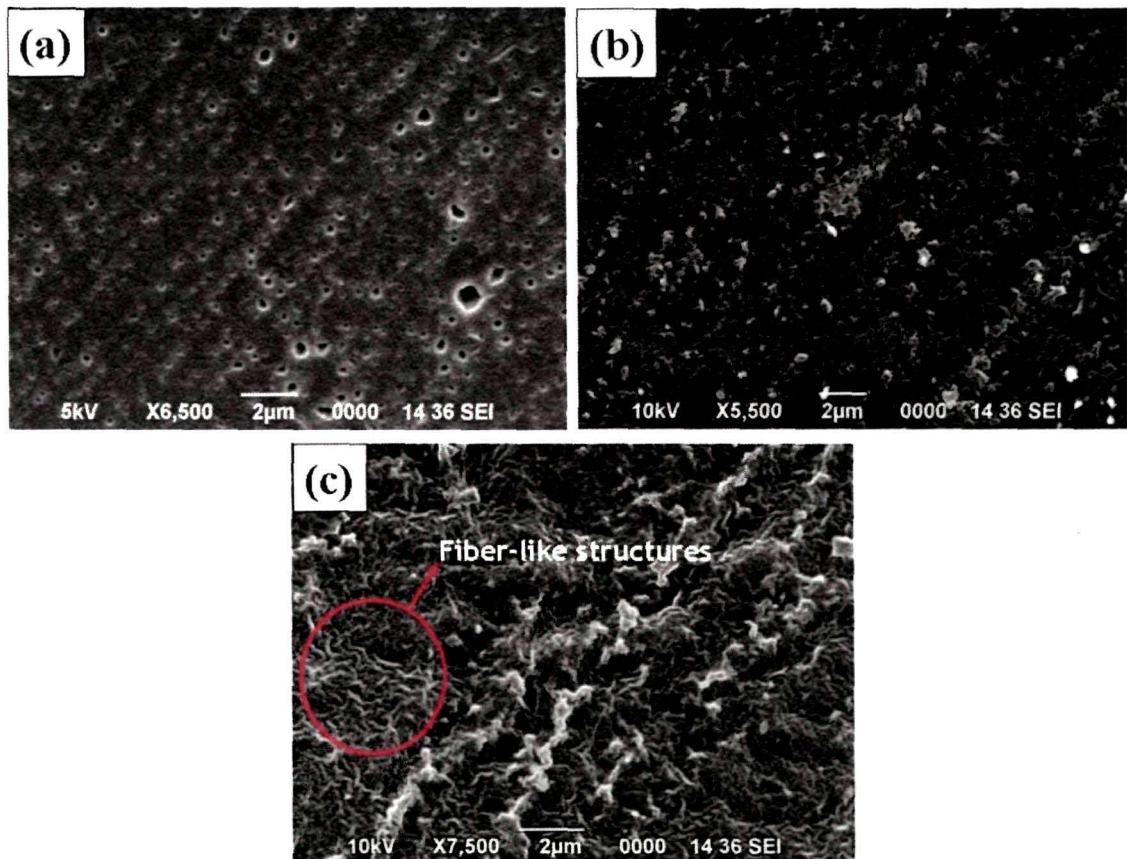


Figure 5.2: Scanning electron micrographs of the PANi nanofiber reinforced PVA nanocomposites with (a) 2 wt. % (sample G1), (b) 4 wt. % (sample G2) and (c) 6 wt. % (sample G3) of aniline content

The effect of 90 MeV O^{7+} ion irradiation on the surface morphology of the PANi nanofiber reinforced PVA nanocomposite is evident from the Figs. 5.3 (a-d). It is observed that after irradiation the surface of the PANi nanofiber reinforced PVA nanocomposite films become smoother and the fibrous structure of PANi nanofibers visible in Fig. 5.3 (a) vanishes. The fact that there are no visible pores in the SEM micrographs suggests that the density of the PANi nanofiber reinforced PVA nanocomposites increases upon interaction with the 90 MeV O^{7+} ions. The improvement in the surface morphology and density of the PANi nanofiber reinforced PVA nanocomposite can be attributed to the displacement of the polymer chains from the hilly to the valley regions due to the deposition of huge amount of electronic energy under the impact of swift heavy ions incident [228, 411] on the PANi nanofiber reinforced PVA nanocomposites.

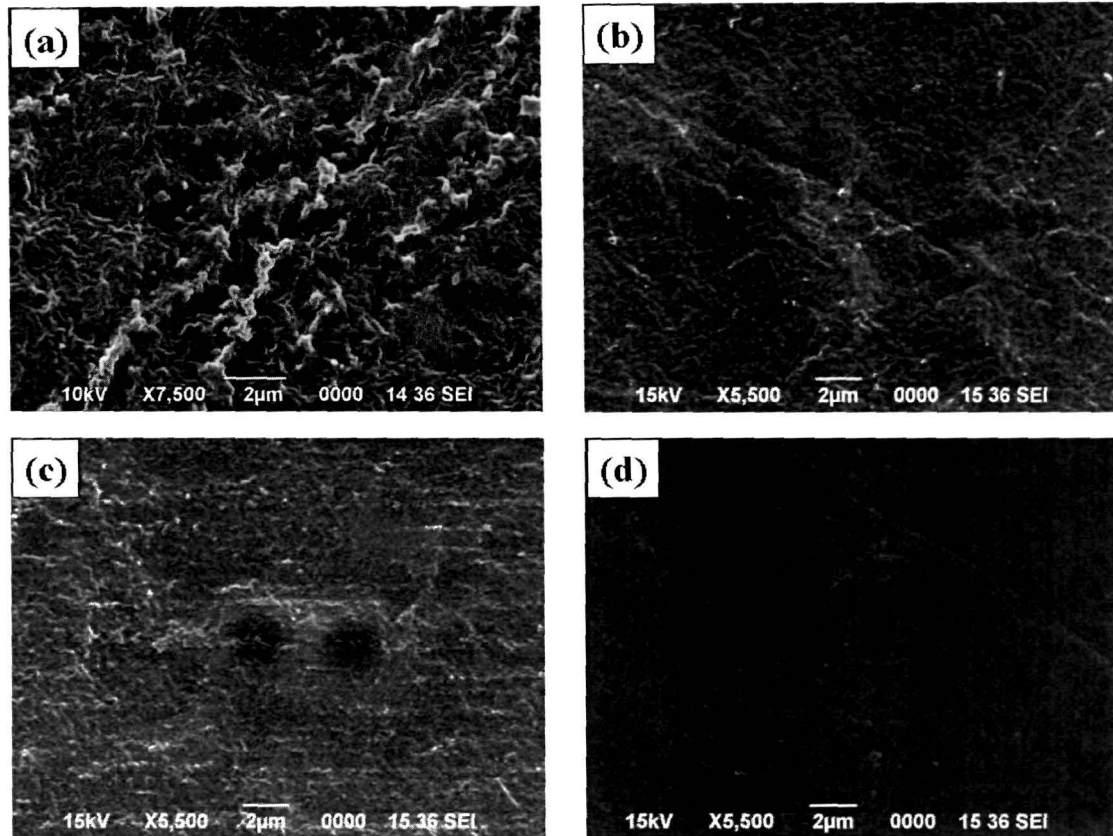


Figure 5.3: Scanning electron micrographs of the PANi nanofiber reinforced PVA nanocomposites with 6 wt.% (sample G3) of aniline content (a) before and after irradiation with 90 MeV O^{7+} ions at fluences of (b) 3×10^{10} , (c) 3×10^{11} and (d) 1×10^{12} ions cm^{-2} .

5.3.2. X-ray diffraction analysis

Fig. 5.4 (a) shows the X-ray diffraction pattern of the PANi nanofiber reinforced PVA nanocomposites in the 2θ range of 10° - 40° . It has been observed that the (100) reflection peak of PANi (at $2\theta = 20^\circ$), which is attributed to the parallel periodicity of PANi is the most intense peak. With increase in aniline content the (100) reflection peak intensifies and sharpens up. Figure 5.4 (b) is the X-ray diffraction patterns of the three nanocomposite samples G1, G2 and G3 within the 2θ range of 18° - 21° which shows the variations in the (100) reflection peak of polyaniline nanofiber reinforced PVA nanocomposites. The size and strain components are the two major factors leading to line broadening in an X-ray diffractogram. Size broadening is governed by the size of coherent domains (or incoherently diffracting domains) and may include effects of stacking and

twin faults and sub-grain structures such as small-angle boundaries. Broadening due to strain, on the other hand, is caused by lattice imperfections [412, 413].

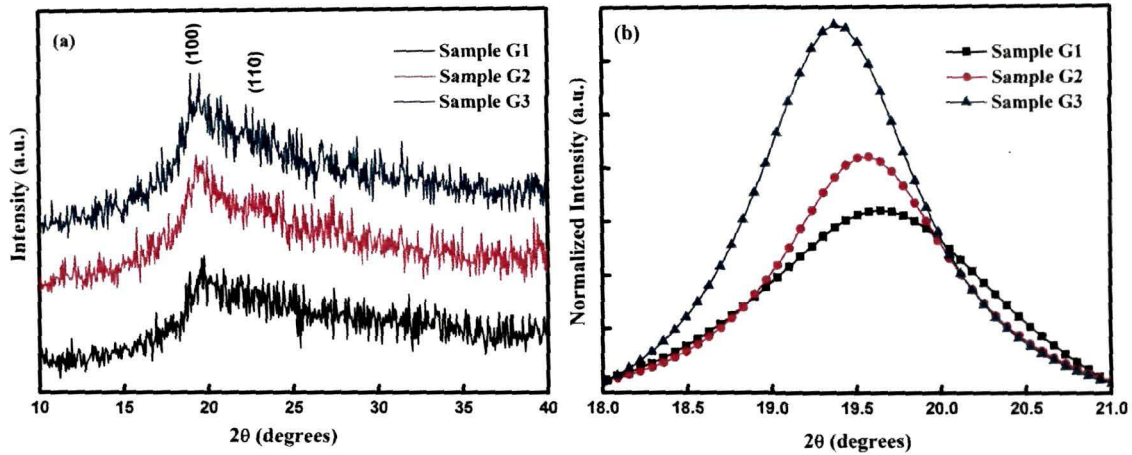


Figure 5.4: X-ray diffraction patterns of polyaniline nanofiber reinforced PVA nanocomposite samples with 2 wt.% (sample G1), 4 wt.% (sample G2) and 6 wt.% (sample G3) of aniline content in the 2θ range from (a) 10° to 60° and (b) $18-21^\circ$ showing the comparison of the (110) reflection peak for polyaniline (PAni) in the PAni nanofiber reinforced PVA nanocomposites.

The line broadening in the X-ray diffractogram has been studied employing the single-line approximation method using Voigt function [414] as described in the section 3.5.2 of Chapter 3. The technique has been used to separate the contributions of the crystallite size (referred to as domain length or the range of order (L) in case of polymers) and the strain towards the line broadening. The domain length (L) and strain (ϵ) of the nanocomposite films are tabulated in the Table 5.2.

Table 5.2: Variation of domain length (L) and strain (ϵ)

Samples	Domain length (L) in Å	Strain (ϵ)
G1	20.05	1.50
G2	20.25	1.38
G3	22.66	1.16

It is observed from the Table 5.2 that the range of order (domain length) within the nanocomposite films increases as the aniline content is increased while the strain decreases. This indicates that the periodicity of the PAni chains within the nanofibers, which is caused mainly due to chain folding and formation of

single or double helices, increases with increasing aniline contents, while the contribution of lattice defects decreases considerably.

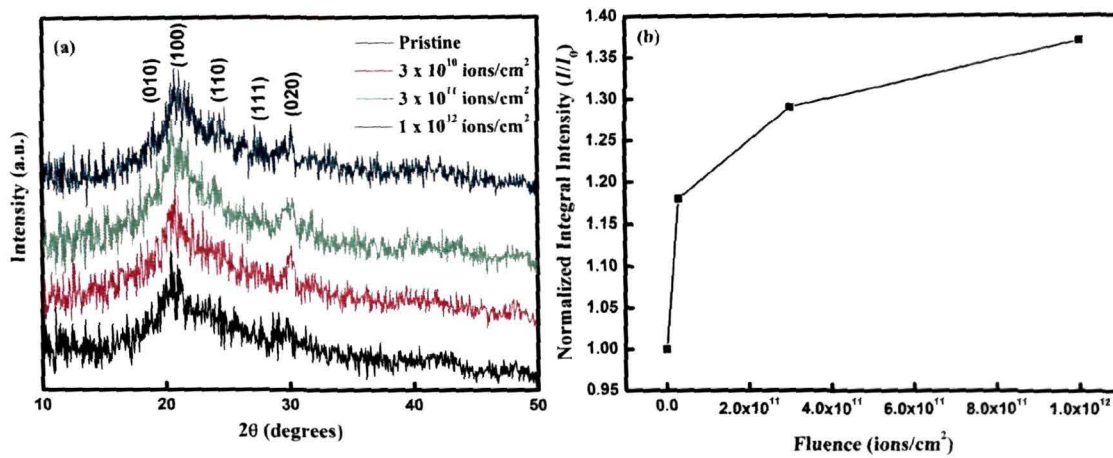


Figure 5.5: (a) X-ray diffraction patterns of the pristine and 90 MeV O^{7+} ion irradiated PANi nanofiber reinforced PVA nanocomposite with 6 wt.% aniline (sample G3) and (b) shows the variation of the normalized integral intensity (I/I_0) of the sample G3 as a function of irradiation fluence.

Fig. 5.5 (a) shows the X-ray diffraction patterns of the pristine and the 90 MeV O^{7+} ion irradiated PANi nanofiber reinforced PVA nanocomposite (sample G3) at different fluences. Reflection peaks corresponding to the (010), (100), (110), (111) and (020) planes of PANi can be identified in all the samples. It is observed that the intensity of the reflection peaks increases with the increase in irradiation fluence. The (100) reflection peak of PANi, in particular intensifies with the increase in the irradiation fluence. The degree of crystallinity can be determined from the variation of the normalized integral intensity (I/I_0) as a function of fluence that is depicted in the Fig. 5.5 (b). It is observed that the normalized integral intensity of the PANi nanofiber reinforced PVA nanocomposites increases as the irradiation fluence in increased. This is an indication of the fact that the PANi nanofiber reinforced PVA nanocomposite becomes more crystalline as the irradiation fluence in increased. The observed enhancement in the degree of crystallinity of the PANi nanofiber reinforced PVA nanocomposites with the increase in the irradiation fluence can be ascribed to cross-linking events occurring in the nanocomposite films as a result of the tremendous electronic energy deposition due to the interaction of the highly energetic ions with the polymer.

5.3.3. Fourier Transform Infrared (FTIR) Spectroscopy

FTIR spectra of the PANi nanofiber reinforced PVA nanocomposite samples with different aniline contents (sample G1, G2 and G3) are shown in Fig. 5.6. The band around 3400 cm^{-1} is attributed to the N-H stretching vibrations while that at 1650 cm^{-1} is a signature of the N-H bending vibration of polyaniline (PANi). The peak observed at 815 cm^{-1} is ascribed to the N-H out of plane bending vibration. The strong bands observed at 1140 cm^{-1} and 1200 cm^{-1} are due to the C-C stretching and C-C twisting of the alkyl chain, respectively [411]. The C-N stretching peak of the polymer is observed at 1336 cm^{-1} . The peak near 2930 cm^{-1} is due to the C-H stretching absorption. The C-Cl stretching vibration observed around 600 cm^{-1} confirms the fact that the PANi nanofibers are in doped states. The vibrational bands around 1460 and 1400 cm^{-1} are assigned to C=C stretching vibration of the quinoid and benzenoid ring of PANi, respectively. It is evident from the FTIR spectra that almost all the vibrational bands increase in intensity with the increase in aniline content in the nanocomposites.

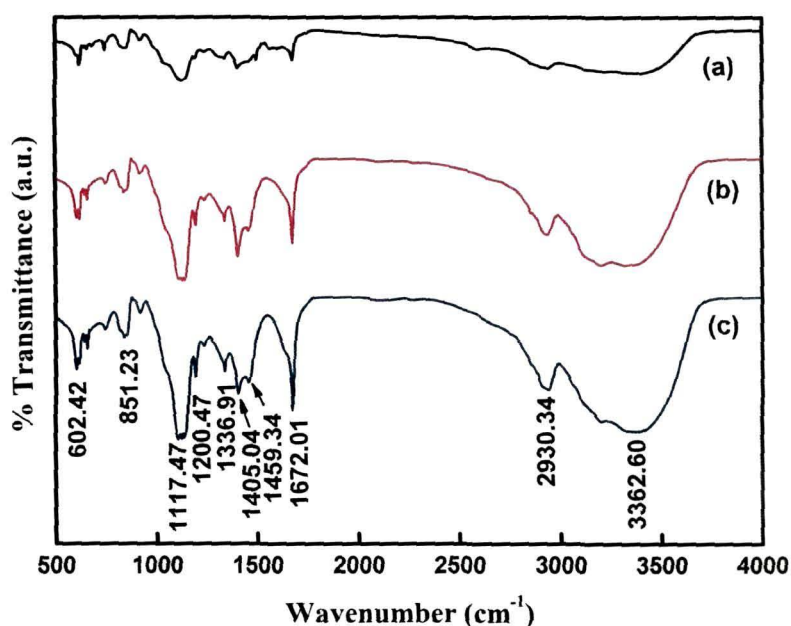


Figure 5.6: FTIR spectra of PANi nanofiber reinforced PVA nanocomposite with different concentration of aniline (a) 2 wt. % (sample G1), (b) 4 wt. % (sample G2) and (c) 6 wt. % (sample G3).

The peaks due to the C=C stretching of the benzenoid and quinoid units for all the three PANi nanofiber reinforced PVA nanocomposite samples with

different concentration of aniline have been deconvoluted using Lorentzian oscillation curves. Figs. 5.7 (a-c) show the deconvolution of the peaks due to the C=C stretching of the benzenoid and quinoid units of the PANi nanofiber reinforced PVA nanocomposites.

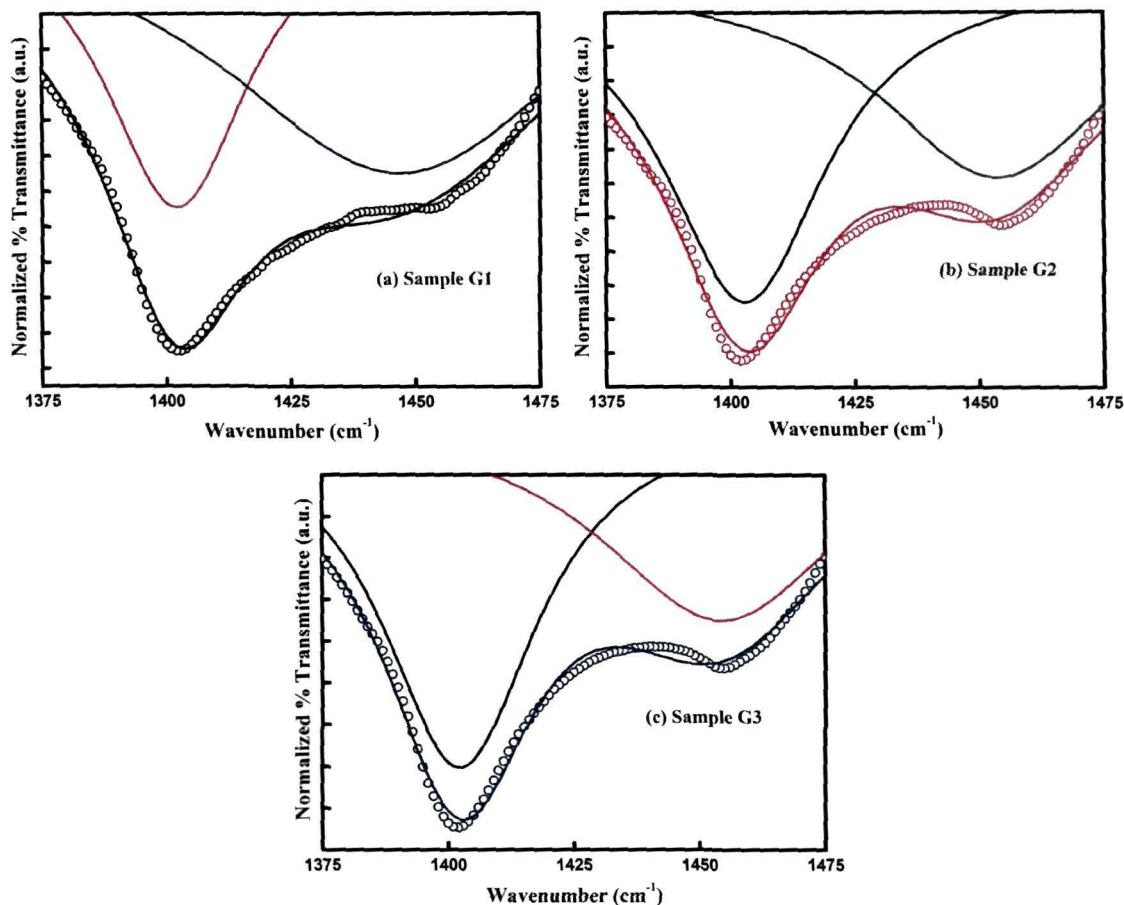


Figure 5.7: Lorentzian deconvolution of the C=C stretching peaks for the benzenoid and quinoid units of the PANi nanofiber reinforced PVA nanocomposites (a) sample G1, (b) sample G2 and (c) sample G3

Fig. 5.8 presents the comparison of the deconvoluted sub-peaks due to the C=C stretching corresponding to the two types of structures: the benzenoid (para di-substituted benzene) and quinoid (quinine diimine) in the PANi chains. It is observed that the peaks corresponding to the C=C stretching of both benzenoid and quinoid rings increase in intensity with the increase in the concentration of aniline (G1→G3). However, the band due to the C=C stretching of the benzenoid ring around 1400 cm^{-1} is far more intense than that for the quinoid ring at around 1460 cm^{-1} , which indicates that there are more benzenoid units than quinoid units in the PANi nanofiber reinforced PVA nanocomposites. This is further

corroborated by the simultaneous increase in the intensity of the band at 1671 cm^{-1} due to N-H stretching with increasing aniline concentration (G1→G3) as can be clearly observed from the Fig. 5.6. The fact that there are more benzenoid units than quinoid units in the PANi chains is an indication of better conjugation within the chains. Thus, it can be inferred from the FTIR analysis that the conjugation length of PANi nanofibers increases with the increase in aniline concentration in the nanocomposites.

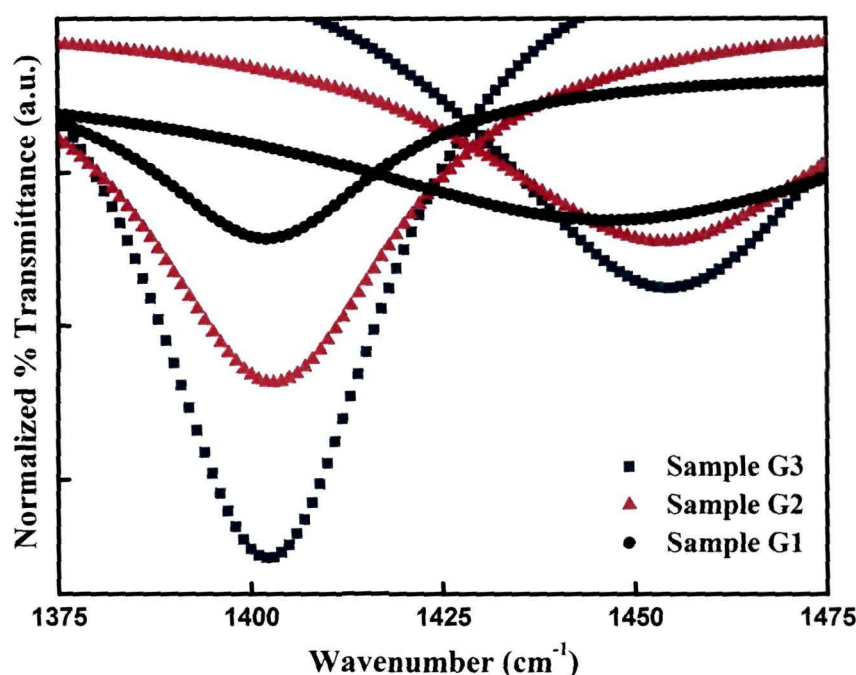


Figure 5.8: Comparison of the deconvoluted sub-peaks for the C=C stretching corresponding to the benzenoid (*para* disubstituted benzene) and quinoid (quinine diimine) structures in the PANi chains

Fig. 5.9 shows the comparison of the FTIR spectra of the pristine and 90 MeV O^{7+} ion irradiated PANi nanofiber reinforced PVA nanocomposites. It has been observed that almost all the peaks observed in the pristine PANi nanofiber reinforced PVA nanocomposites are also present in the irradiated samples. This indicates that there is no change in the basic chemical structure of the polymer upon SHI irradiation. However, some specific changes in the FTIR spectra have been found. The band due to C-C stretching of the alkyl chain observed at 1140 cm^{-1} intensifies, which is an indication of cross-linking events occurring in the PANi nanofiber reinforced PVA nanocomposites upon SHI irradiation. However, the band at 1200 cm^{-1} has been found to decrease in intensity upon SHI

irradiation, which may be due to the fact that twisting vibrational modes may not be possible if cross-linking is occurring in the sample upon SHI irradiation.

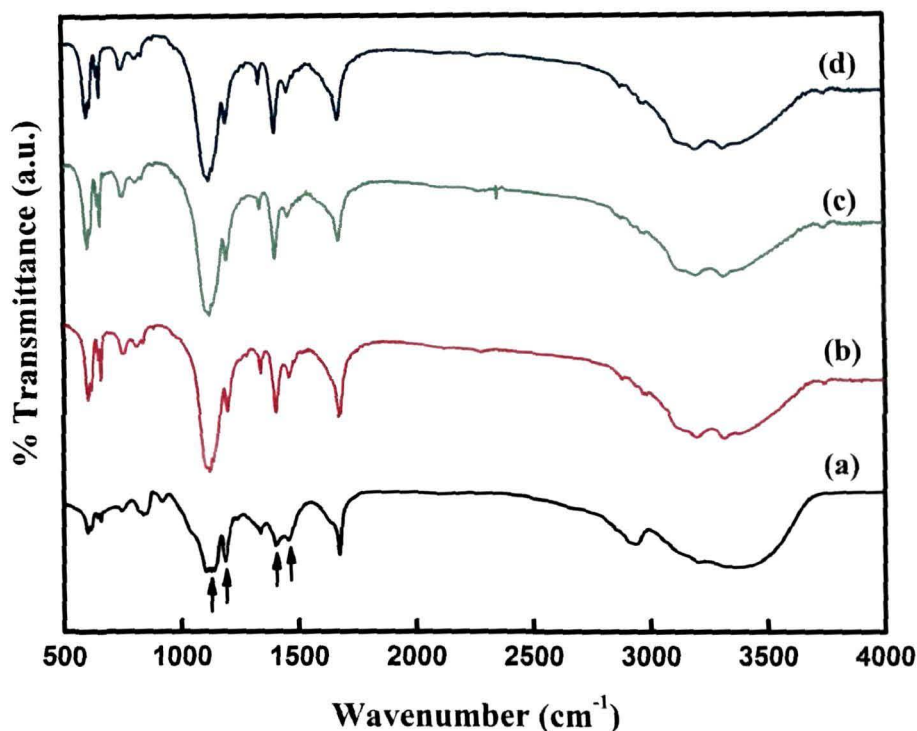


Figure 5.9: FTIR spectra of PANi nanofiber reinforced PVA nanocomposites (a) before and after irradiation with 90 MeV O^{7+} ions at a fluence of (b) 3×10^{10} , (c) 3×10^{11} and (d) 1×10^{12} ions/cm²

Another important variation in the FTIR spectra of PANi nanofiber reinforced PVA nanocomposites can be observed considering the bands at 1400 and 1460 cm^{-1} due to the C=C stretching vibrations of the benzenoid and quinoid rings. In order to extract more information from the FTIR spectra the bands due to the C=C stretching vibrations of the benzenoid and quinoid units have been deconvoluted. Fig. 5.10 shows the deconvoluted bands corresponding to the C=C stretching of the benzenoid and quinoid structures. It has been observed that the intensity of the C=C stretching peak centered around 1400 cm^{-1} intensifies with the increase in irradiation fluence. This indicates that some of the quinoid rings present in the pristine material has been reduced to the benzenoid structure or it might be a case that hydrogen from the polyvinyl alcohol matrix has led to the reduction of the quinoid ring to the benzenoid rings upon SHI irradiation. However, the band due to the C=C stretching of the quinoid structures at 1460 cm^{-1} has also been found to increase in intensity after SHI irradiation. With the

increase in fluence this band decreases in intensity slightly. Thus, it is evident that although some of the quinoid structures might have been reduced to the benzenoid form, the transformation is partial. It may also be inferred that it is not only that the quinoid rings are reduced to benzenoid; there is also a possibility of oxidation of the benzenoid rings to form the quinoid structures. However, it seems that in the case of PANi nanofiber reinforced PVA nanocomposites due to the presence of a hydrogen rich polyvinyl alcohol (PVA) matrix, the probability of the quinoid structure being reduced to the benzenoid structure upon SHI irradiation is more as can be observed from the Fig. 5.10. A transformation from the quinoid to the benzenoid structures indicate the possibility of having better conjugation within the polymer chains, which might allow better charge transport through the material upon SHI irradiation.

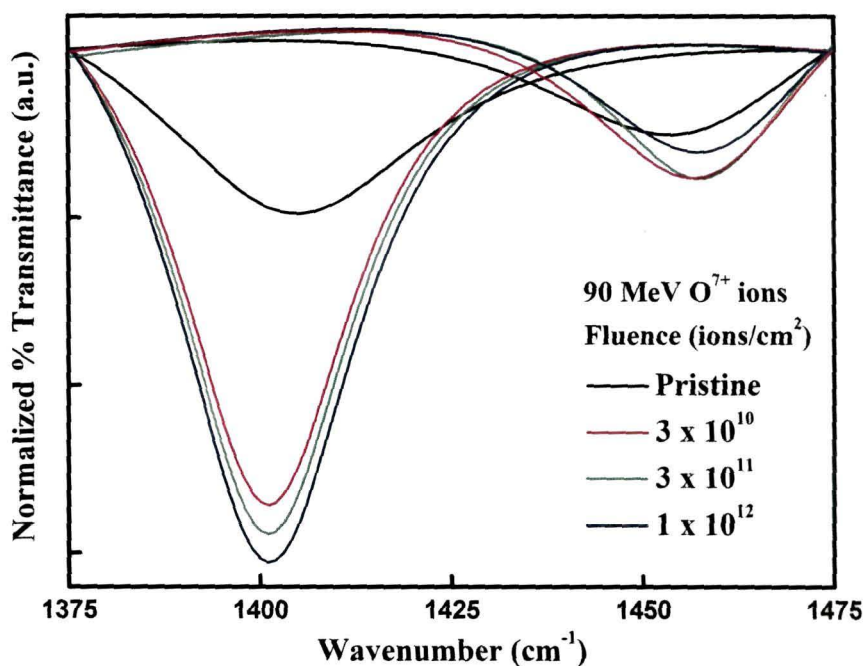


Figure 5.10: Comparison of the FTIR peaks for the C=C stretching vibrations of the benzenoid rings at 1400 cm^{-1} and the quinoid rings at 1460 cm^{-1} for the pristine and irradiated PANi nanofiber reinforced PVA nanocomposites.

5.3.4. UV-Visible (UV-Vis) absorption spectroscopy

The UV-Visible spectra of the PANi nanofiber reinforced PVA nanocomposite samples with different aniline content viz., 2 wt.% (sample G1), 4 wt.% (sample G2) and 6 wt.% (sample G3) are shown in the Fig. 5.10. Three prominent bands can be clearly observed from the Fig. 5.11. The band appearing

around 290 nm is attributed to the π - π^* transition while the bands appearing at 400 nm and 800 nm are due to the π -polaron and polaron- π^* transitions in PANi [126]. The intensity of the absorption bands seems to increase with the increase in aniline concentration indicating an increase in the density of states.

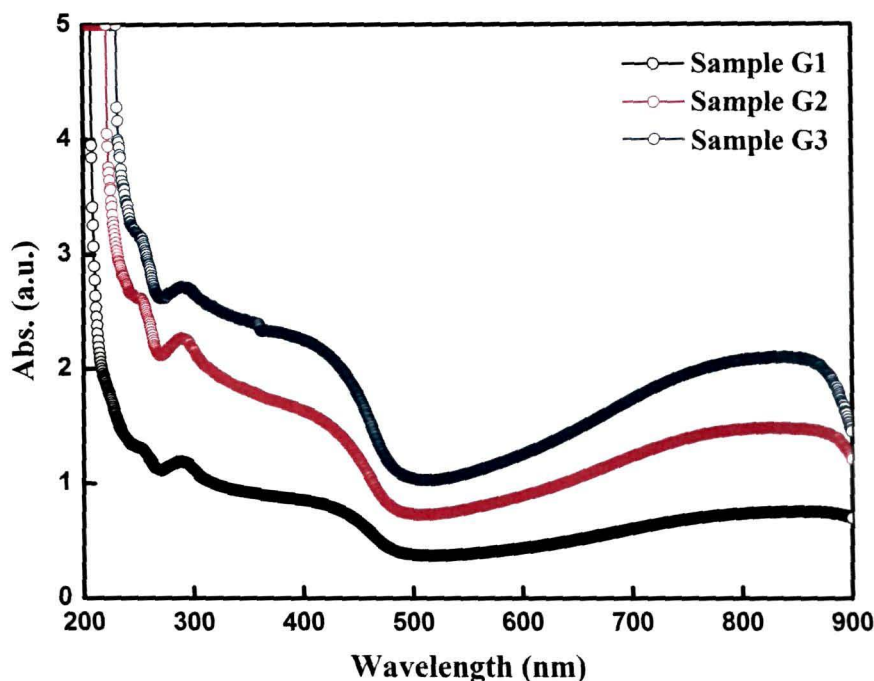


Figure 5.11: UV-Visible spectra of the PANi nanofiber reinforced PVA nanocomposites with 2 wt. % (sample G1), 4 wt. % (sample G2) and 6 wt. % (sample G3).

Fig. 5.12 shows the UV-Visible spectra of the PANi nanofiber reinforced PVA nanocomposite films before and after irradiation with 90 MeV O^{7+} ions at different fluences. The three primary absorption bands that are generally observed in polyaniline are prominently observed in both the pristine and SHI irradiated PANi nanofiber reinforced PVA nanocomposites. In case of the PANi nanofiber reinforced PVA nanocomposites films the polaron- π^* is observed at around 600 nm which has also been attributed in earlier studies to the π - π^* transition of the quinoid ring of oxidized polyaniline [458, 459]. The peak centered around 350 nm is actually observed to be composed of two sub-peaks as can be seen from the Fig. 5.12. These peaks represent transitions from the π -polaron band and confirm the existence of a single broad polaron band in the polymer. It has been observed that upon SHI irradiation the intensity of the carrier absorption peaks specifically the peaks due to the π -polaron and polaron- π^* transitions

centered around 350 and 600 nm increase with the increase in fluence. This is an indication that the density of states in the polaron band located deep inside the band-gap of the nanocomposites increases upon SHI irradiation.

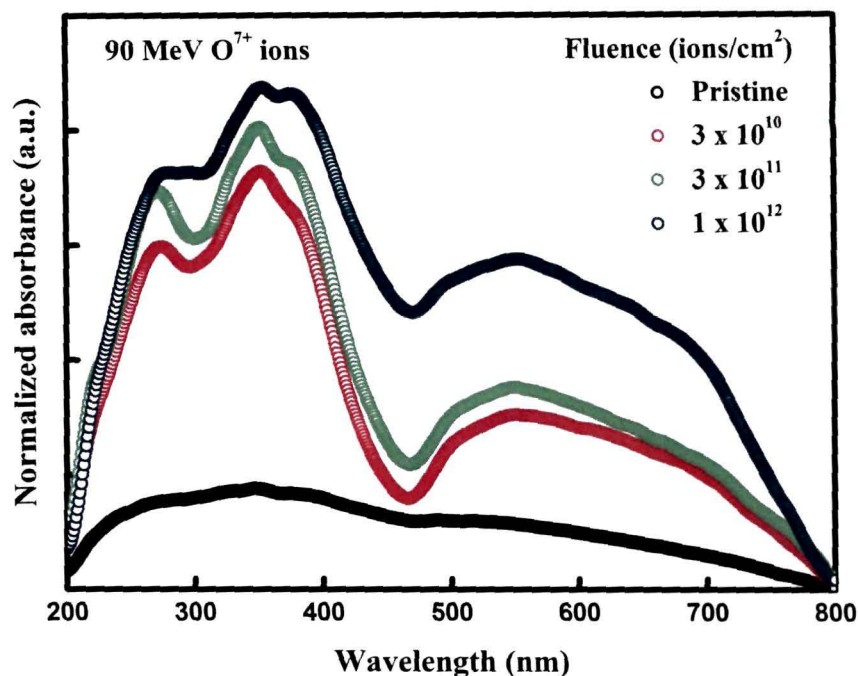


Figure 5.12: UV-Visible spectra of the PANi nanofiber reinforced PVA nanocomposites (sample G3) before and after SHI irradiation with 90 MeV O^{7+} ions.

5.3.5. I-V characteristics

Fig. 5.13 shows the I-V characteristics of the PANi nanofiber reinforced PVA nanocomposite sample with different weight percentage of aniline (2 wt.%, 4 wt.% and 6 wt.%). The figure shows that the I-V curves for the nanocomposites are non-linear and the non-linearity increases with the increase in aniline concentration in the nanocomposites. The existence of non-linearity in the current-voltage characteristic of conducting polymers has been investigated by several research groups [460, 461]. It has been recently proposed by Kaiser *et al.* [460] that the non-linearity observed in the current voltage characteristic curves of conducting polymers can be explained using an extended fluctuation induced tunneling (FIT) and a thermal excitation model. In this model Kaiser *et al.* also proposed a generic expression based on numerical calculations for metallic conduction interrupted by small barriers, and showed that the expression could give a very good description of the observed nonlinearities in conducting polymers. The equation suggested by Kaiser *et al.* by means of which the

conduction through small barriers between metallic regions, according to the fluctuation induced tunneling (FIT) and thermal excitation model, can be explained is written as [460]:

$$G = \frac{I}{V} = \frac{G_0 \exp\left(\frac{V}{V_0}\right)}{1 + h \left[\exp\left(\frac{V}{V_0}\right) - 1 \right]} \quad (5.1)$$

where G_0 is the temperature-dependent zero bias conductance; V_0 is the voltage scale factor, which depends strongly on the barrier energy and $h = G_0/G_h$ ($h < 1$) and G_h is the saturation value of G at high field.

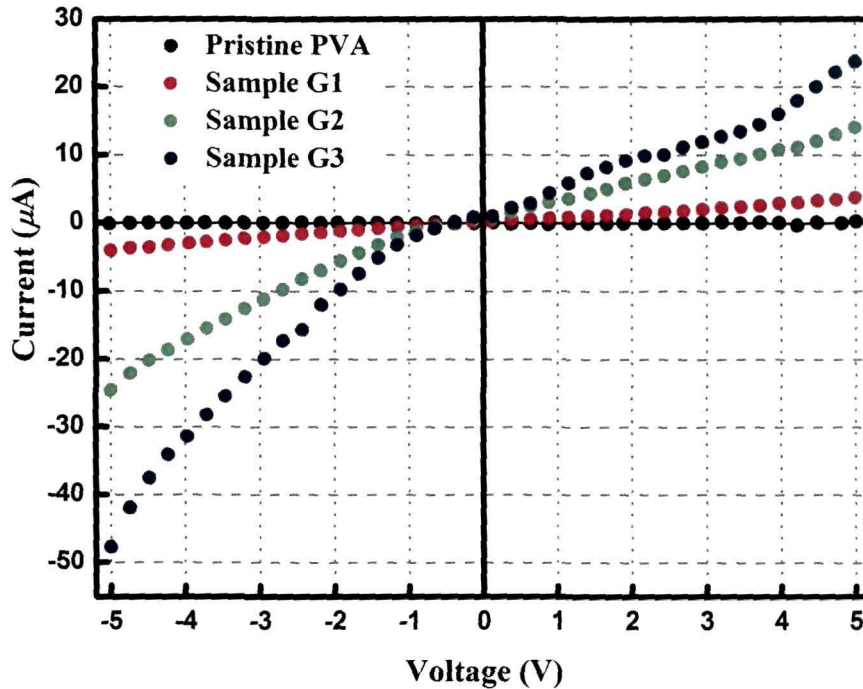


Figure 5.13: I-V characteristics for the pristine polyvinyl alcohol (PVA) and the PANi nanofiber reinforced PVA nanocomposites with 2 wt. % (sample G1), 4 wt. % (sample G2) and 6 wt. % (sample G3) of aniline content.

The complex structures of conducting polymers, which are quasi-one dimensional systems, can be considered as ordered metallic regions in series with disordered conduction barriers. Thus, the nonlinear I-V behaviour can be attributed to the charge carrier tunneling through conduction barriers and thermal activation over the barriers. It can be concluded that with the increase in aniline content in the PVA matrix, the probability of a fluctuation induced tunneling or thermally activated hopping of charge carriers between two metallic

regions formed by the PANi nanofibers within the PVA matrix increases and as such the resistance of the material decreases and the current-voltage characteristic becomes non-linear. The enhancement in conductivity is also corroborated by the UV-Visible studies, which indicate that the density of charge carriers increases in the material with the increase in aniline content.

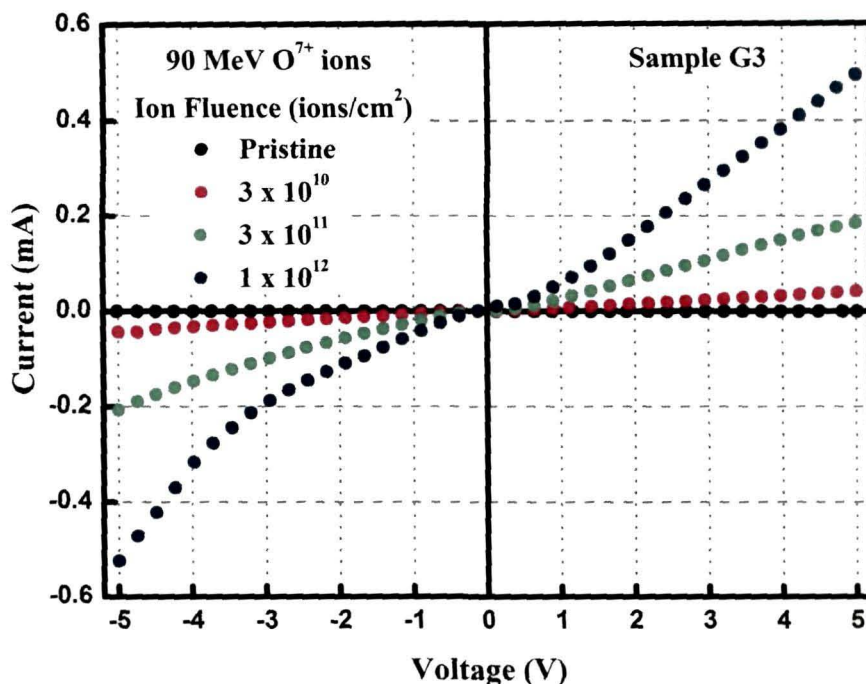


Figure 5.14: I-V characteristics of PANi nanofiber reinforced PVA nanocomposites (sample G3) before and after irradiation with 90 MeV O^{7+} ions at fluences of 3×10^{10} , 3×10^{11} and 1×10^{12} ions cm^{-2} .

Fig. 5.14 shows the I-V characteristics of the pristine and SHI irradiated PANi nanofiber reinforced PVA nanocomposites (sample G3). From the figure, it is evident that the non-linearity in the current-voltage characteristics of the PANi nanofiber reinforced PVA nanocomposites increases and the resistance of the nanocomposites decreases upon SHI irradiation. This might be attributed to the fact that charge carrier transport via fluctuation induced tunneling or thermally activated hopping increases in the nanocomposites after SHI irradiation. This phenomenon is corroborated by the fact that upon SHI irradiation the material has been found to become more crystalline and the surface of the nanocomposites becomes smoother and denser leading to reduced scattering of charge carriers and enhancement in conduction through the material. Increase in the probability of thermally activated hops or a fluctuation induced tunneling is also supported by

the UV-Visible studied [Fig. 5.12], which shows that the intensity of the carrier absorption peak increases with the increase in irradiation fluence leading to an enhancement in the density of states.

5.3.6. Dielectric spectroscopy

Dielectric spectroscopy studies using three different formalisms viz., permittivity, impedance and modulus formalisms have been carried out for the PANi nanofiber reinforced PVA nanocomposites in order to analyze the dielectric and conductivity relaxations in the nanocomposites and any probable variations in the relaxation mechanisms of the nanocomposite films upon SHI irradiation. The results of dielectric spectroscopy for the pristine and SHI irradiated PANi nanofiber reinforced PVA nanocomposites are discussed in the following sub-sections.

5.3.6.1. Permittivity formalism

Figs. 5.15 (a) and (b) present the frequency dependent variation of the real (ϵ') and the imaginary (ϵ'') parts of the complex permittivity (ϵ^*) for the three different compositions of the PANi nanofiber reinforced PVA nanocomposites with varying concentrations of aniline calculated using the Eq. (4.10) mentioned in section 4.3.5.1 of Chapter 4.

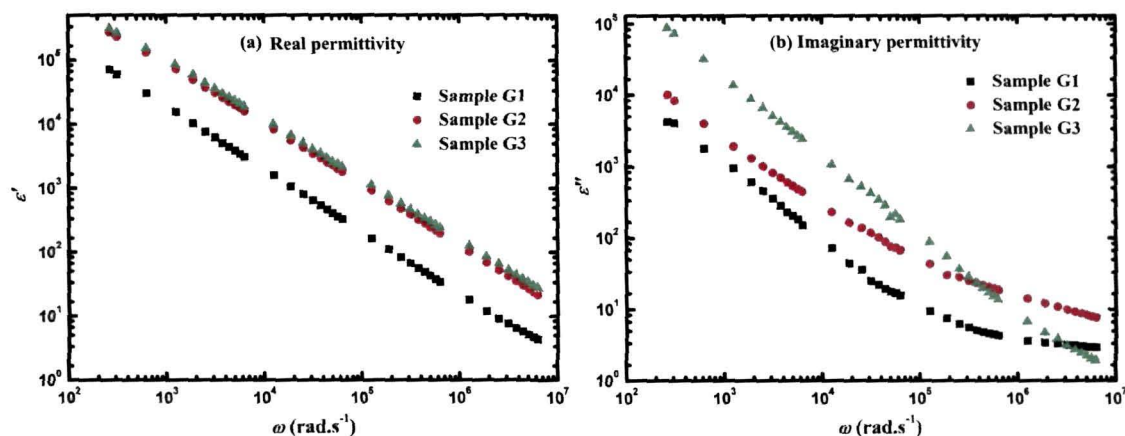


Figure 5.15: Variation of (a) the real part (ϵ') and (b) imaginary part (ϵ'') of the complex permittivity (ϵ^*) for the PANi nanofiber reinforced PVA nanocomposites with varying aniline content viz., 2 wt. % (sample G1), 4 wt. % (sample G2) and 6 wt. % (sample G3).

The low frequency (LF) dispersion in the values of ϵ' and ϵ'' can be clearly observed from the Figs. 5.15 (a, b). This reveals that the charge carrier hopping is

the dominant conduction mechanism in the nanocomposites. A dielectric like relaxation can be clearly observed from the Fig. 5.15 (b) for the PANi nanofiber reinforced PVA nanocomposites, which becomes less prominent as the aniline content increases in the nanocomposites. The ε'' spectra for the PANi nanofiber reinforced PVA nanocomposites have also been fitted to the generalized Havriliak-Negami (H-N) equation [Eq. (4.12)] mentioned in section 4.3.5.1 of Chapter 4.

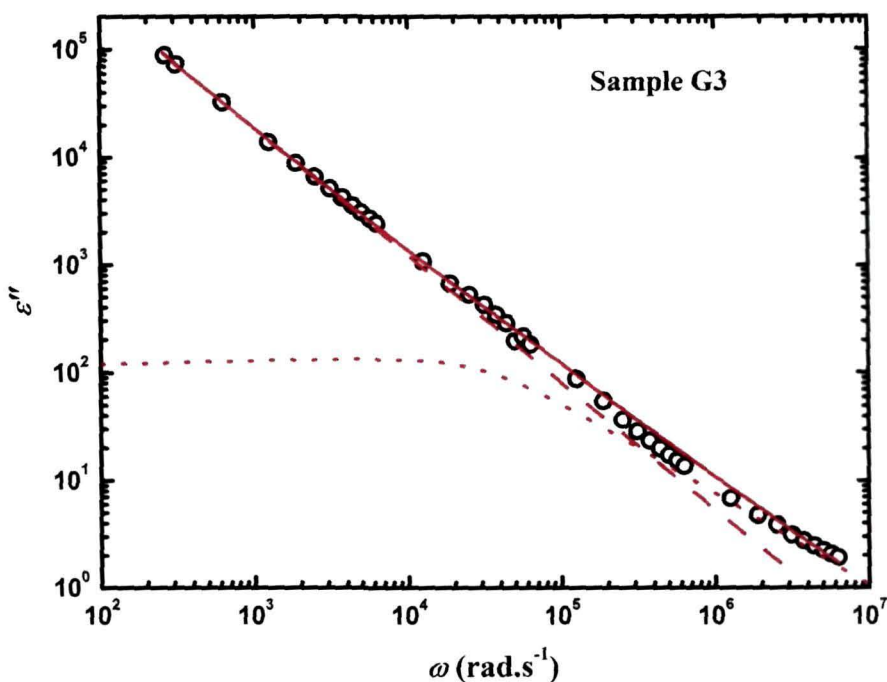


Figure 5.16: The imaginary part ε'' of the complex dielectric function ε^* vs. frequency for the PANi nanofiber reinforced PVA nanocomposites with 6 wt. % of aniline content. The solid line is the best fit of Eq. (4.12) to the experimental data. The dotted line (.....) shows the contribution of the dc conductivity and the dashed line (- - -) shows the contribution of H-N function to the dielectric loss ε'' .

Fig. 5.16 shows the best fit of the experimental data of the imaginary permittivity ε'' for the sample G3 according to the H-N equation [Eq. (4.12)]. The contributions of dc conductivity and H-N function to the dielectric losses ε'' can be clearly marked from the Fig. 5.16. The average values of the parameters α and β have been found to be 0.8941 and 0.8734, respectively. This indicates that the relaxation in the PANi nanofiber reinforced PVA nanocomposites is non-Debye type with a distribution of relaxation times. However, it can be clearly noticed from the Fig. 5.15 that the relaxation is prominently observed in the sample with

lower concentration of aniline. With the increase in aniline content the conductivity of the material increases and as such the contribution of the first term in the Eq. 4.12 due to dc conductivity dominates over the H-N term.

Fig. 5.17 shows the variation of the real part (ϵ') and the imaginary part (ϵ'') of the complex permittivity (ϵ^*) for the sample G3 as a function of frequency at different temperatures. It is observed that both ϵ' and ϵ'' increase with increasing temperature. This increase can be attributed to the increased polymer chain motions leading to larger number of charge carriers participating in the relaxation process.

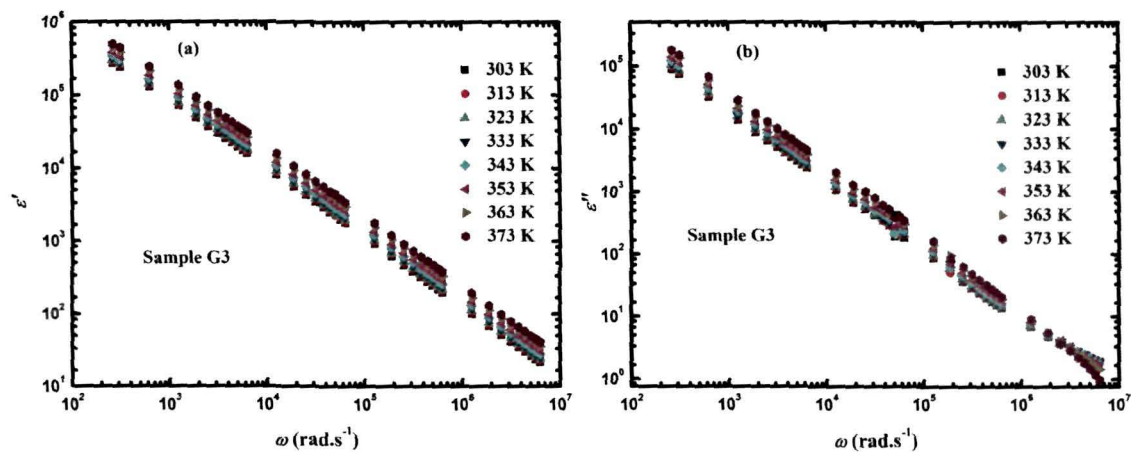


Figure 5.17: Variation of (a) the real part (ϵ') and (b) imaginary part (ϵ'') of the complex permittivity (ϵ^*) for the sample G3 as a function of frequency at different temperatures.

The effect of 90 MeV O^{7+} ion irradiation upon real (ϵ') and the imaginary (ϵ'') parts of the complex permittivity (ϵ^*) of the PANi nanofiber reinforced PVA nanocomposites (sample G3) can be observed from the Figs. 5.18 (a) and (b). It is observed that the value of ϵ' and ϵ'' for every value of frequency increases with the increase in fluence. The enhancement in the dielectric constant of the PANi nanofiber reinforced nanocomposites films upon SHI irradiation can be attributed to the increase in the degree of crystallinity as observed from the X-ray diffraction analysis. Similar trends are observed in the frequency dependent variation of ϵ' and ϵ'' for the pristine and irradiated PANi nanofiber reinforced PVA nanocomposites. However, the contribution of the dc conductivity term to the dielectric loss [Fig. 5.18 (b)] increases with the increase in irradiation fluence. This indicates that the conductivity of the nanocomposites increases with the increase

in the irradiation fluence. The result is well corroborated by the X-ray diffraction, SEM and I-V studies. The enhancement in the degree of crystallinity and the improvement of the structural morphology reduces scattering of charge carriers that leads to the enhancement in the conductivity of the nanocomposites.

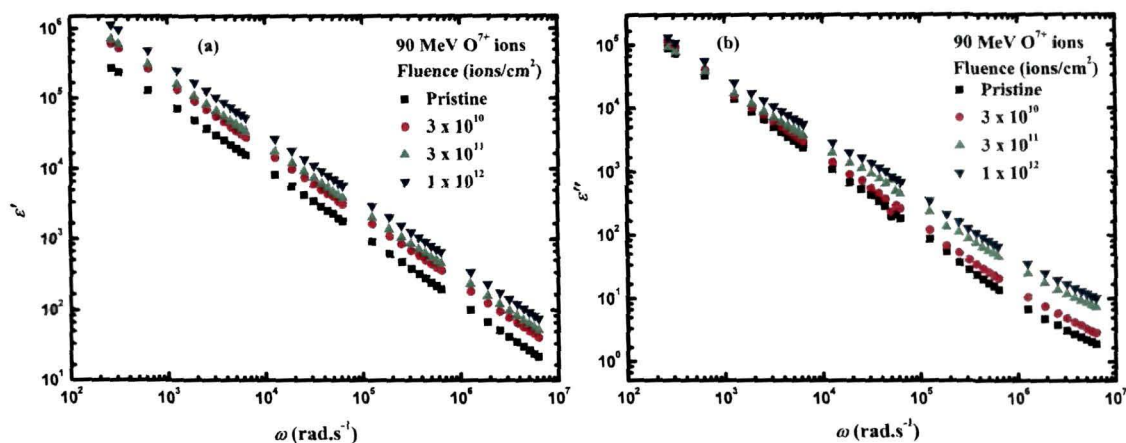


Figure 5.18: Variation of the (a) real part (ϵ') and (b) the imaginary part (ϵ'') of the complex permittivity (ϵ^*) as a function of frequency for the sample G3 at different fluences.

5.3.6.2. Impedance formalism

Fig. 5.19 shows the Cole-Cole plots of the PANi nanofiber reinforced PVA nanocomposite samples with varying content of aniline. All the plots comprise of a depressed semicircular/semi-elliptical arc in the high frequency region and an oblique line in the low frequency region. It is widely accepted that the high frequency semicircle is due to the bulk resistance of the sample, whereas the low frequency spike is ascribed to the charge transfer resistance and capacitance of electric double layer formed at the electrode interface [462]. The occurrence of a depressed semicircular/semi-elliptical arc implies that the PANi nanofiber reinforced PVA nanocomposite samples are of non-Debye type with a distribution of relaxation times. The bulk resistance is determined from the point where the semicircular arc intersects the ordinate. It has been observed that the intersection point of the semicircular arc moves towards lower value of Z' with the increase in aniline content. Thus the bulk resistance of the nanocomposite films decreases with the increase in aniline content. With the increase in aniline content, more PANi nanofibers are formed within the PVA matrix and there is better

connectivity among the conducting nanofibers that reduces the bulk resistance of the nanocomposites samples.

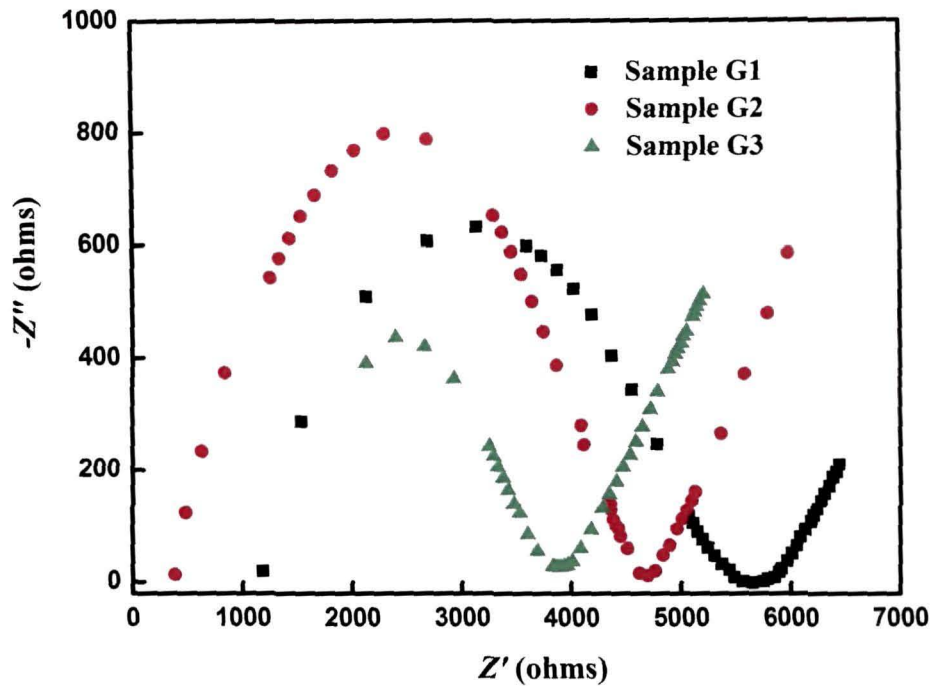


Figure 5.19: Cole-Cole (Nyquist) plots of the PANi nanofiber reinforced PVA nanocomposite samples with 2 wt. % (sample G1), 4 wt. % (sample G2) and 6 wt. % (sample G3) of aniline content.

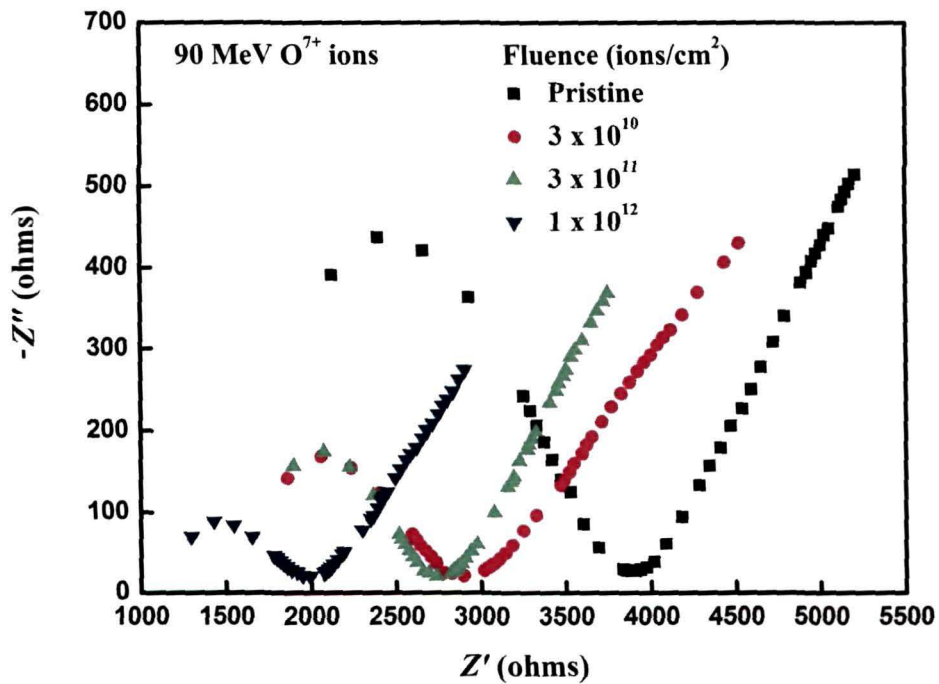


Figure 5.20: Cole-Cole (Nyquist) plots of the pristine and 90 MeV O^{7+} ion irradiated PANi nanofiber reinforced PVA nanocomposite (sample G3 with 6 wt. % aniline content).

The Cole-Cole (Nyquist) plots for the pristine and SHI irradiated PANi nanofiber reinforced PVA nanocomposite samples (sample G3) are shown in the Fig. 5.20. It is clearly evident from the figure that the bulk resistance of the nanocomposite samples decreases with the increase in irradiation fluence. The result is consistent with those of the I-V characteristics which also indicate that the resistance of the nanocomposites decreases upon SHI irradiation. The decrease in the resistance can also be attributed to the enhanced degree of crystallinity of the nanocomposite samples observed from the X-ray diffraction analysis due to cross-linking events occurring in the nanocomposites upon SHI irradiation.

5.3.6.3. Modulus formalism

Figs. 5.21 (a, b) show the variation of the real part (M') and the imaginary part (M'') of the complex modulus (M^*) for the PANi nanofiber reinforced PVA nanocomposites with varying aniline content that have been calculated using Eq. (3.29) mentioned in section 3.5.8.3 of Chapter 3.

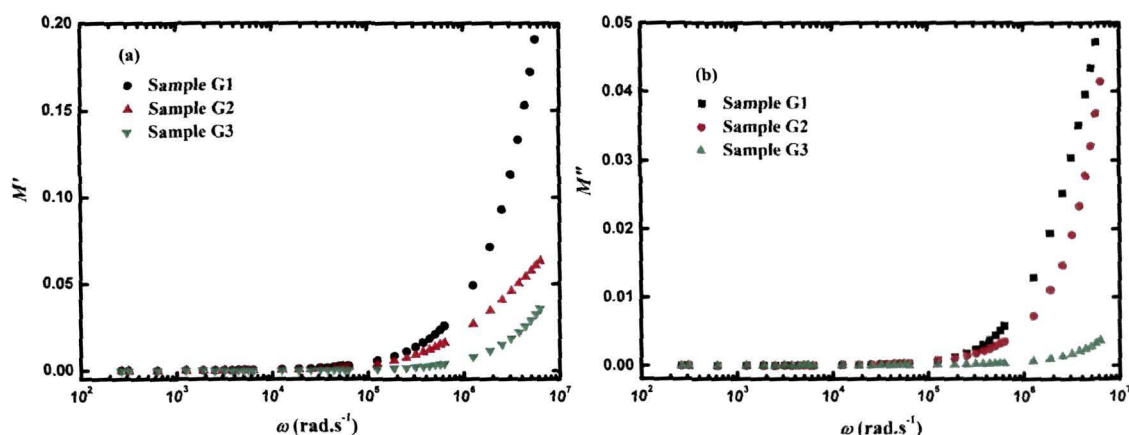


Figure 5.21: Variation of the (a) real part (M') and (b) the imaginary part (M'') of the complex modulus (M^*) for the PANi nanofiber reinforced PVA nanocomposites with varying aniline content.

The appearance of long tail in the low frequency region for all compositions is attributed to the large capacitance associated with the electrode at lower frequencies. In the Fig. 5.21 (b), modulus peak is not observed for the PANi nanofiber reinforced PVA nanocomposites in the frequency range employed. However, it can be mentioned that the modulus peak representing the bulk relaxation may occur at higher frequencies. The existence of long tail at low

frequencies and the shape of the curves imply that the nanocomposite systems are non-Debye in nature.

Figs. 5.22 (a, b) depict the variation in the real and imaginary part of the electric modulus as a function of frequency for the pristine and irradiated PANi nanofiber reinforced PVA nanocomposites (sample G3 with 6 wt. % aniline content). As for the pristine sample peaks are not observed for the M'' spectra in case of the irradiated samples as well and it seems that peak may appear at higher frequency beyond the measured frequency of 5 MHz. However, the nature of the modulus curves remain the same indicating that the nanocomposites whether in the pristine or irradiated forms are of non-Debye type having a wide distribution of relaxation times.

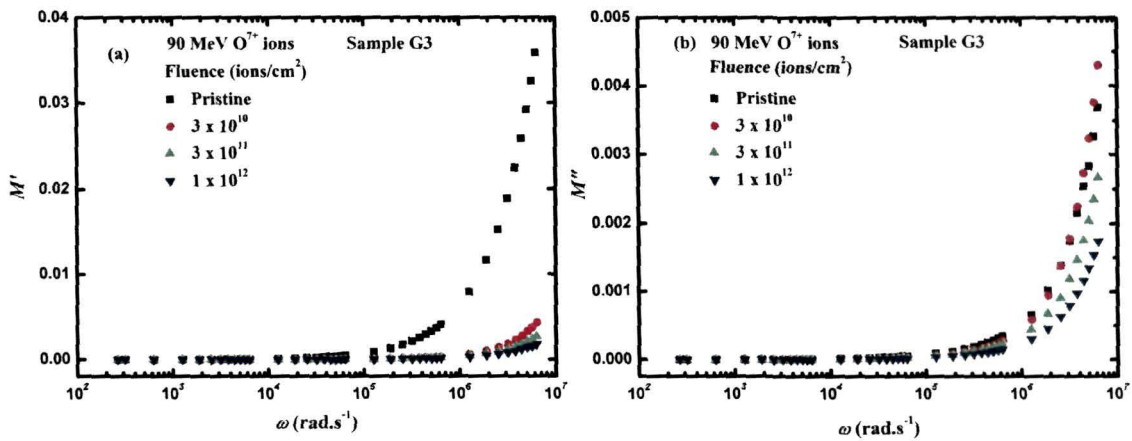


Figure 5.22: Variation of the (a) real part (M') and (b) the imaginary part (M'') of the complex modulus (M^*) for the pristine and irradiated PANi nanofiber reinforced PVA nanocomposites (sample G3).

5.3.7. AC conductivity and charge transport mechanism

Fig. 5.23 (a) shows the variation of ac conductivity as a function of frequency for the PANi nanofiber reinforced PVA nanocomposites with different aniline concentration viz., 2 wt.% (sample G1), 4 wt.% (sample G2) and 6 wt.% (sample G3). On the other hand, the effect of SHI irradiation upon the ac conductivity of PANi nanofiber reinforced PVA nanocomposite with the highest concentration of aniline (sample G3) is depicted in the Fig. 5.23 (b). Ac conductivity in amorphous and disordered materials obeys a Universal law as

discussed in section 2.3 of Chapter 2. The experimental data acquired for the ac conductivity have accordingly been fitted to the power law equation [Eq. (4.19)].

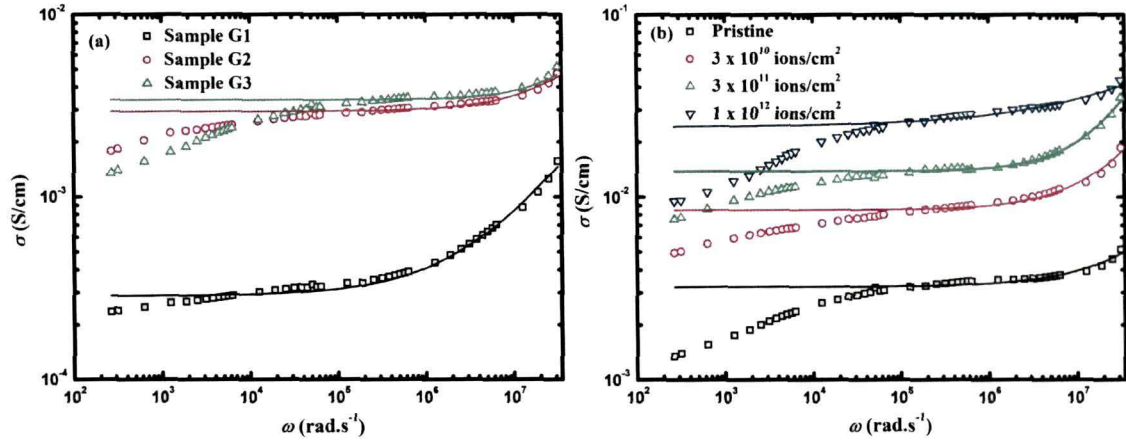


Figure 5.23: Variation of ac conductivity for (a) PANi nanofiber reinforced PVA nanocomposites with varying aniline content and (b) pristine and irradiated PANi nanofiber reinforced PVA nanocomposites

The solid lines in the above figures are the best fit of the experimental data to the Eq. (4.19). The dc conductivity and the frequency exponent have been determined from the best fit results. It is observed that dc conductivity increases with the increase in aniline content as can also be observed from the Fig. 5.23 (a). SHI irradiation also leads to an increase in the value of dc conductivity which is consistent with other results. However, it has been observed that the experimental data does not fit well to the theoretical curve at low frequencies. This may be attributed to the electrode polarization effects that creep in during the dielectric measurements.

The variation of the frequency exponent 's' as a function of temperature for the pristine and irradiated PANi nanofibers reinforced PVA nanocomposite samples are displayed in Figs. 5.24 (a, b). Fig. 5.24 (a) shows the temperature dependent variation of the frequency exponent 's' for the PANi nanofiber reinforced PVA nanocomposites with varying aniline concentration while the temperature dependent variation of the frequency exponent for the pristine and irradiated samples have been shown in the Fig. 5.24 (b). It can be clearly observed that the variation of the s-parameter for the pristine and irradiated PANi nanofiber reinforced PVA nanocomposites show similar variation as a function of temperature.

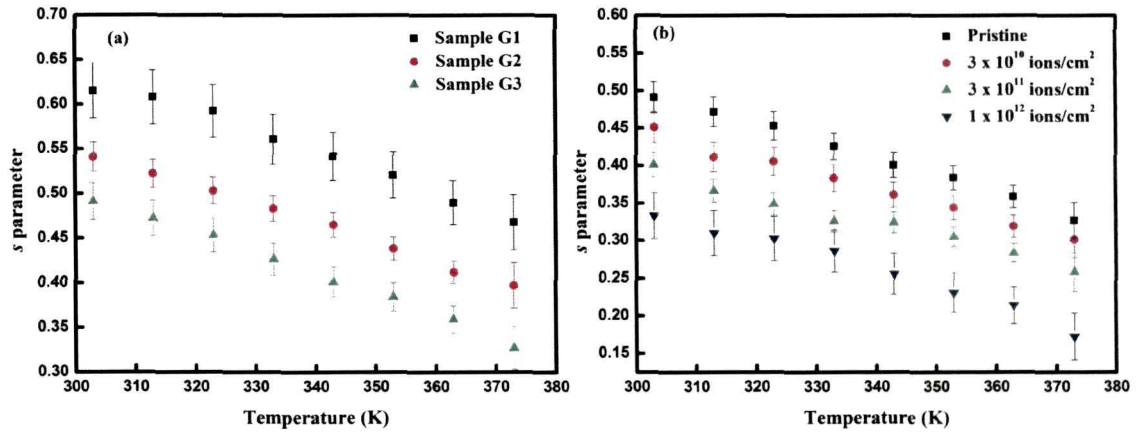


Figure 5.24: Temperature dependent variation of the frequency exponent 's' for (a) PANi nanofiber reinforced PVA nanocomposites with varying aniline content and (b) pristine and irradiated PANi nanofiber reinforced PVA nanocomposites

Although the dc conductivity of the nanocomposites increases with the increase in aniline content as well as upon SHI irradiation but the 's' parameter in all the samples decreases with the increase in temperature. This feature shown by the pristine and SHI irradiated PANi nanofiber reinforced PVA nanocomposites fits well to the correlated barrier hopping (CBH) model [366]. Thus, it is evident that although the conductivity of the nanocomposites increases upon SHI irradiation, it has no effect on the charge transport mechanism of the nanocomposites.

5.3.8. Positron annihilation lifetime spectroscopy (PALS)

Positron annihilation lifetime spectroscopy (PALS) has been performed for the PANi nanofiber reinforced PVA nanocomposites in order to investigate the SHI irradiation effects upon the electron density in its bulk and lattice structure. PALS is also an excellent technique to investigate the generation of defects such as cation vacancies upon SHI irradiation that can trap positrons and give rise to a longer lifetime component [463, 464]. Variation in the Positron annihilation lifetime can also be correlated with the variation in conductivity of conducting polymers upon SHI irradiation. PALS has been used in the present work for investigating the variation in the conductivity of the PANi nanofiber reinforced PVA nanocomposite samples upon SHI irradiation.

Figs. 5.25 (a, b) show the variation of the shortest and intermediate lifetime components, τ_1 and τ_2 , respectively. Although, the three component analysis of

positron annihilation lifetime spectra in polymers is generally accepted, for the PANi nanofiber reinforced PVA nanocomposites almost no positronium have been found to be formed in the samples, which is consistent with the PALS results reported for conducting polymers [465]. It is observed from the Fig. 5.25 (a) that the shortest lifetime component that includes annihilation of free positrons and para-positronium (p -Ps) decreases sharply when we go from the pristine PANi nanofiber reinforced PVA nanocomposite to that irradiated with a fluence of 3×10^{10} ions/cm². But as we go on increasing the fluence further not much variation in the lifetime is observed. The inset of Fig. 5.25 shows the intensity (I_1) of the shortest lifetime component which reveals that the intensity is almost constant. Fig. 5.25 (b) shows the variation of the intermediate lifetime component τ_2 and the inset shows its intensity. The intermediate lifetime that has been attributed to positrons annihilating from trapped states in vacancies is also found to decrease sharply upon SHI irradiation but with the increasing fluence not much variation is noticed in the lifetimes of positrons. The intensity (I_2) of the intermediate lifetime is again found to be almost constant.

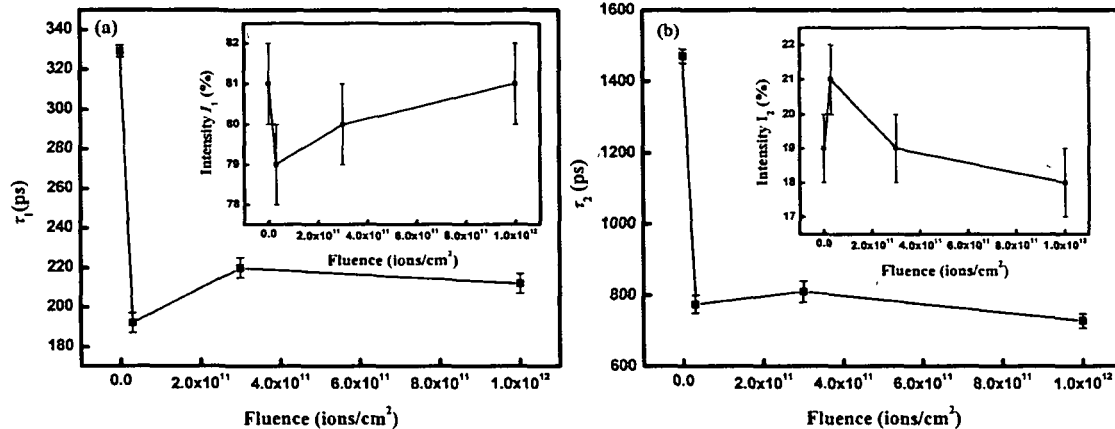


Figure 5.25: Variation of the positron lifetime components for PANi nanofiber reinforced PVA nanocomposites (a) shortest lifetime component τ_1 and (b) intermediate lifetime component τ_2 . The insets in the Fig. 5.25 (a) and (b) are the respective intensities of the lifetime components.

Swift heavy ion irradiation can cause certain phenomenon such as cross-linking, chain scissions, creation of radicals and defects, molecular fragmentation etc. due to the huge amount of electronic energy deposition in the material within a very short time-span. SHI irradiation can easily perturb the intermolecular

forces in the vicinity of the ion track within the PANi nanofiber reinforced PVA nanocomposites leading to the creation of local lattice distortions (polarons) in a manner so as to create local negatively charged regions that localize positrons. The polarons, which are chemically named semiquinone radical cations, are the charge carriers in conducting polymers. Other than polaron defects, SHI can also create chain defects which can be formed by the coiling, bending or overlapping of the polymer chains. During their passage through the PANi nanofibers reinforced PVA nanocomposite, swift heavy ions (SHIs) cause a tremendous enhancement of local temperature in the vicinity of their trail. Once the ion passes through, the nanocomposite cools down and quenches within a very short span of time creating chain defects in the PANi nanofiber reinforced PVA nanocomposites. The increment in the trapping sites for positrons in PANi nanofiber reinforced PVA nanocomposites can be a combined effect of both these phenomenon. Thus it is evident that both the shortest and the intermediate lifetime of positrons decrease with increasing irradiation fluence. However, the reason as to why the intensities of these lifetime components are constant is not very clear. The increase in the conductivity of the PANi nanofiber reinforced PVA nanocomposites upon SHI irradiation is well supported by the fact that the positron lifetimes in the nanocomposites decrease with increasing fluence since this is an indication of an increase in the low momentum π -electron density in the polymer [466].

5.4. Summary

Polyaniline nanofibers reinforced PVA nanocomposites have been synthesized using in-situ rapid mixing polymerization technique and irradiated with 90 MeV O^{7+} ions. Transmission electron microscopy of the PANi nanofiber reinforced PVA nanocomposites reveal that PANi nanofibers of average diameter around 30 nm are formed within the PVA matrix. Scanning electron microscopy shows that surface morphology of the nanocomposite gets rougher and the porosity decreases as the aniline content in the nanocomposites increases. It has been observed that upon SHI irradiation the porosity of the nanocomposite decreases and the surface becomes dense and smooth. The observed variations in the surface morphology of the PANi nanofibers reinforced PVA nanocomposite has been ascribed to the displacement of the polymer chains from the hilly to the

valley regions due to the deposition of huge amount of electronic energy under the impact of swift heavy ions. Irradiation of PANi nanofiber reinforced PVA nanocomposites induces enhancement in crystallinity of the material which might be due to the cross-linking of PANi nanofibers within the PVA matrix as is observed from the X-ray diffraction analysis. FTIR results show that there is no change in the basic polymer structure upon SHI irradiation, however, some specific bands such as the C-C stretching band intensify while the intensity of the band associated with the C-C twisting vibration decreases. This indicates that the polymer undergoes cross-linking upon SHI irradiation since twisting vibrations are generally not observed in cross-linked polymers. The analysis for the evolution of the C=C stretching vibrations corresponding to the benzenoid and the quinoid structures indicate that there is a partial deformation from the quinoid to the benzenoid induced by SHI irradiation unlike that in case of the pure polyaniline nanofibers in which SHI irradiation leads to a benzenoid to quinoid transition. This has been attributed to the availability of the hydrogen rich polyvinyl alcohol matrix in the nanocomposites unlike that in case of the polyaniline nanofibers. UV-Visible studies indicate that the density of states in the polaron band associated deep inside the band-gap of the nanocomposites increases upon SHI irradiation. The conductivity of the material also increases with the increase in irradiation fluence which is observed from the I-V characteristics of the pristine and irradiated PANi nanofiber reinforced PVA nanocomposites and are also corroborated by dielectric spectroscopy. The ac conductivity results indicate that although there is an increase in the dc conductivity but the charge transport mechanism follows the correlated barrier hopping (CBH) model. Positron annihilation lifetime spectroscopy (PALS) results reveal that there is a sharp decrease in the shortest and the intermediate lifetime components after irradiation but with the increase in the ion fluence the lifetime components almost show similar values. The sharp decrease in the lifetime components has been attributed to the perturbation caused by irradiation in the intermolecular forces in the vicinity of the ion track. This perturbation leads to the creation of local lattice distortions (polarons) in a manner so as to create local negatively charged regions that localize positrons and as such the life time

decreases. The decrease in the positron lifetimes upon SHI irradiation suggests an increase in the π -electron density in the nanocomposites leading to an enhancement in conductivity of the nanocomposites that has been observed from I-V characteristics, dielectric spectroscopy and ac conductivity measurements. SHI irradiation effects upon PVA have not been prominently observed from the characterizations of the sample. However, there are reports that irradiation of PVA leads to a shift in the optical absorption edges, which indicate a lowering of the energy gap due to the formation of carbonaceous clusters [411].

Chapter 6

ANTIOXIDANT ACTIVITY AND BIOCOMPATIBILITY STUDIES ON POLYANILINE BASED NANOSTRUCTURED MATERIALS

This chapter focuses on the application potential of polyaniline (PAni) based nanostructured materials as biocompatible antioxidants for applications in the rubber and polymer industry and in the field of biomedicine. The effect of SHI irradiation on the antioxidant activity and biocompatibility of these materials have also investigated and are presented in this chapter.

6.1. Introduction

Free-radical-mediated oxidation by molecular oxygen is an important chemical process. Many important industrial processes in the petrochemical industry are based on the controlled oxidation of hydrocarbons. In biological systems, free radicals are generated as by-products of complex biochemical reactions taking place inside living beings. External factors like high energy radiation, xenobiotics and oxidative stress also contribute to the generation of free radicals inside the body [467]. The free radical damage to the living tissue is already well established and recent studies indicate that the progression of various diseases such as inflammation, infection, cardiac and cerebral ischemia, reperfusion injury, neurodegenerative diseases, cardiovascular diseases, cancer and ageing are caused by the uncontrolled oxidation of lipids, proteins and DNA in biological systems [468, 469]. Prevention of many oxidant dependent diseases is possible by supplementing antioxidants externally. Free-radical-mediated

oxidation has also been found to be the main cause of deterioration of foodstuffs, oils and polymers [470]. Phenolic antioxidants in the diet are thought to offer protection against cardiovascular diseases and cancers where the onset of the disease involves oxidative damage caused by excessive levels of free radicals; however, even a balanced diet cannot provide an adequate amount of antioxidants required for maintaining a desired low level of free radicals in the body. As such, there is an increasing interest in antioxidants, particularly in those intended to prevent the presumed deleterious effects of free radicals in the human body and to prevent the deterioration of fats and other constituents of food stuffs. Inhibition of this oxidation by various natural and synthetic antioxidants has been explored. Given that conducting polymers are redox-active, they are potential materials to act as reducing agents and scavenge free radicals. Polyaniline and substituted polyanilines have already been examined for their use as antioxidants in rubber materials [471]. However, their antioxidant ability in biological media needs to be examined to assess their likely activity in biomedical applications [256]. In recent years, one-dimensional (1D) polyaniline nanostructures, including nanorods, nanotubes and nanofibers, have been studied in view of the fact that such materials possess the advantages of both low-dimensional systems and organic conductors. These nanostructured materials are expected to perform better wherever there is an interaction between the material and the surrounding environment. The high surface to volume ratio of the nanostructures make them potential candidates for acting as better free radical scavengers than that their bulk counterparts. The antioxidant activity of PAni nanofibers has been previously studied by Wang *et al.* [472], wherein the effects of different dopant acids on the average diameter and antioxidant activity of PAni nanofibers have been reported. In the present work, a sincere effort has been made to present a comparative study of the antioxidant activity of PAni in bulk and nanofiber forms doped with two different dopants viz., hydrochloric acid (HCl) and camphorsulfonic acid (CSA) as a function of sample weight and time of reaction. The biocompatibility of these materials in real biological media *in-vitro* and the variation in the antioxidant activity and biocompatibility of the materials upon SHI irradiation and has also been investigated.

6.2. Antioxidant activity of polyaniline nanofibers

The antioxidant activity of PANi bulk and nanofibers doped with CSA and HCl has been investigated using the methodology adopted by Serpen *et al.* [427] that has been discussed in section 3.6 in Chapter 3. Reactions of fixed amount of samples S1 (PANi bulk), S2 (CSA doped PANi nanofiber) and S3 (HCl doped PANi nanofiber) with 1, 1-diphenyl-2-picrylhydrazyl (DPPH) have been carried out and the UV-visible spectra of the solutions have been recorded after 15 min. The results of the reaction [Fig. 6.1] reveal a progressive decrease in the absorption peak of DPPH at 516 nm. The DPPH scavenging activities for the three samples S1, S2 and S3 have been found to be in the order: $A_{S3} > A_{S2} > A_{S1}$, where A_{S1} , A_{S2} and A_{S3} are the DPPH scavenging activities for samples S1 (PANi bulk), S2 (CSA doped PANi nanofiber) and S3 (HCl doped PANi nanofiber), respectively. The observed antioxidant property is due to the neutralization of the free radical character of DPPH by transfer of an electron [473]. A single unit of the emeraldine salt has two benzenoid units which are capable of donating one hydrogen atom each, thereby eliminating DPPH free radicals. This leads to the decrease in the peak intensity at 516 nm. The greater the decrease in the peak intensity, higher is the antioxidant activity of the material.

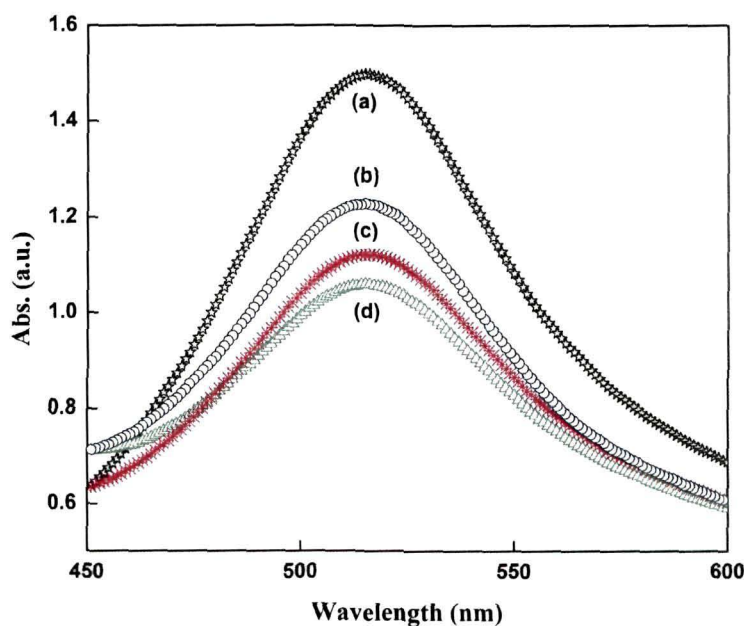


Figure 6.1: UV-Vis spectra of DPPH solutions in methanol after 15 min incubation in dark with (a) no material (blank), (b) 0.5 mg of PANi bulk, (c) 0.5 mg of CSA doped PANi nanofibers and (d) 0.5 mg of HCl doped PANi nanofibers.

The variation of antioxidant activity as a function of the weight of the PANi bulk and PANi nanofibers doped with CSA and HCl has been estimated and is shown in Fig. 6.2. All the samples quenched DPPH in a dose dependent manner; the greater the amount of material better is the DPPH scavenging ability. This is obvious because the greater the amount of the substance present, greater is the number of hydrogen atoms that can be donated for eliminating DPPH. It is observed that the antioxidant activity exhibits almost a linear variation with the amount of antioxidant present in the reaction mixture. HCl-doped PANi nanofibers (sample S3) have smaller average diameter as is observed from the Figs. 4.2 (a) and 4.3 (a) in the section 4.3.1 in Chapter 4 and exhibit better DPPH scavenging efficiency for a given amount of sample as compared to that for CSA-doped PANi nanofibers (sample S2) and bulk PANi (sample S1). The phenomenon is attributed to the increased surface area and availability of more reaction sites for a given weight of the sample.

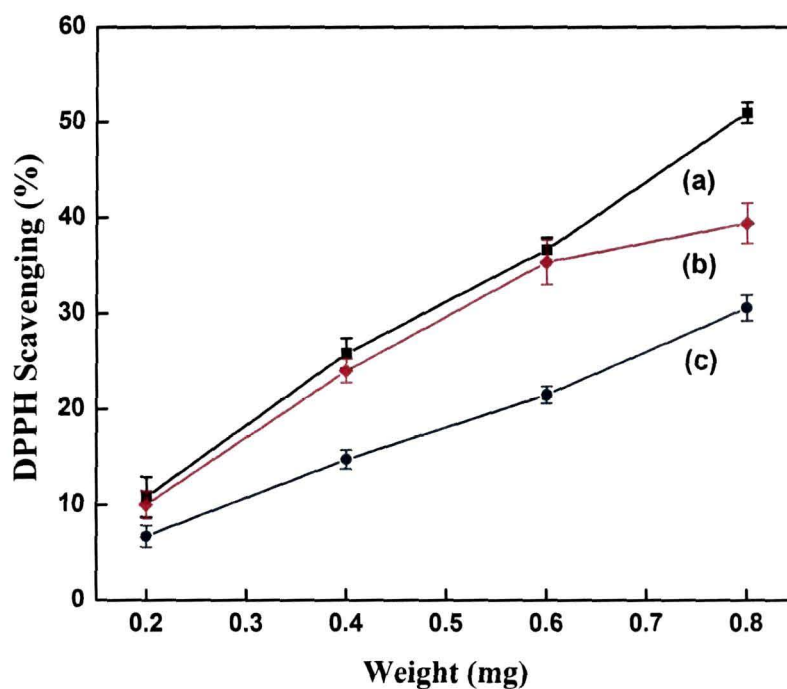


Figure 6.2: Variation of antioxidant activity as a function of weight of (a) S3, (b) S2 and (c) S1 samples. The higher the percentage of DPPH scavenging better is the antioxidant activity of the material.

The time dependence of antioxidant activity of a material provides important information about the reaction mechanism. Figure 6.3 shows the time dependence of the antioxidant activity of polyaniline bulk (sample S1), CSA

doped PANi nanofibers (sample S2) and HCl doped PANi nanofibers (sample S3). It is observed for all the samples that the antioxidant activity increases linearly up to a certain time, after which the slope of the line decreases, indicating that the material has been used up and there are no more hydrogen atoms that can be donated for quenching DPPH free radicals. This marks the completion of the reaction. The time-dependent antioxidant activity of S3 shows that the DPPH scavenging efficiency for the HCl doped PANi nanofibers (sample S3) is better than that of both the CSA doped PANi nanofibers (sample S2) and PANi bulk (sample S1).

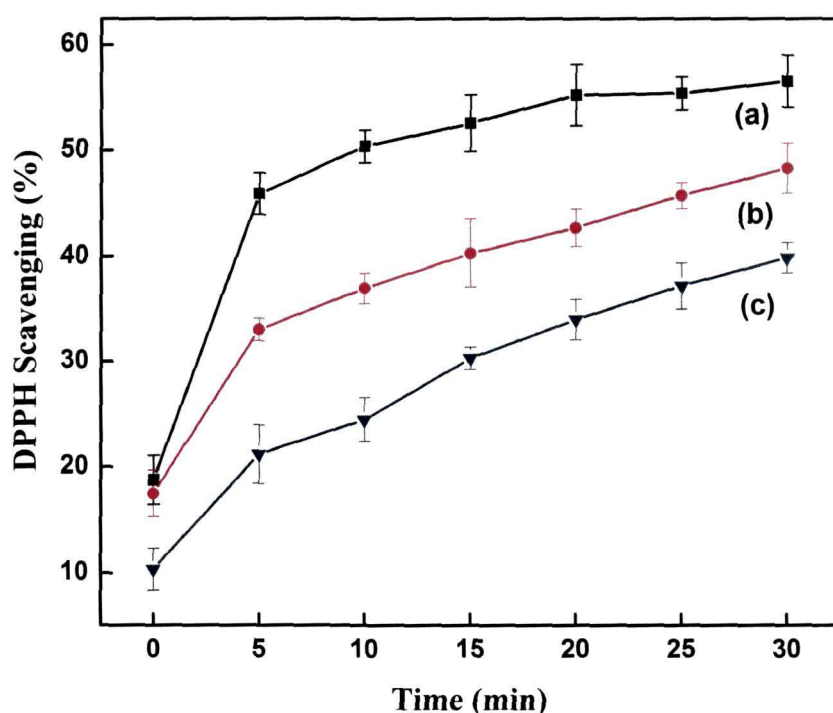


Figure 6.3: Time-dependent antioxidant activity of 0.3 mg of (a) S3, (b) S2 and (c) S1 samples. The results presented are average values of three repetitions.

6.3. Swift heavy ion irradiation induced enhancement in the antioxidant activity of polyaniline nanofibers

Figures 6.4 (a) and (b) show the UV-Visible spectra of solutions consisting of fixed amounts of the pristine and irradiated PANi nanofibers doped with HCl and CSA respectively, and DPPH recorded after 15 min. The results for the reaction [Fig. 6.4 (a) and 6.4 (b)] reveal a progressive decrease in the absorption band of DPPH at 516 nm. This indicates that the DPPH scavenging activity for the irradiated PANi nanofibers is better than that of the pristine samples and increases

with the increase in irradiation fluence for both the CSA and HCl doped PANi nanofibers.

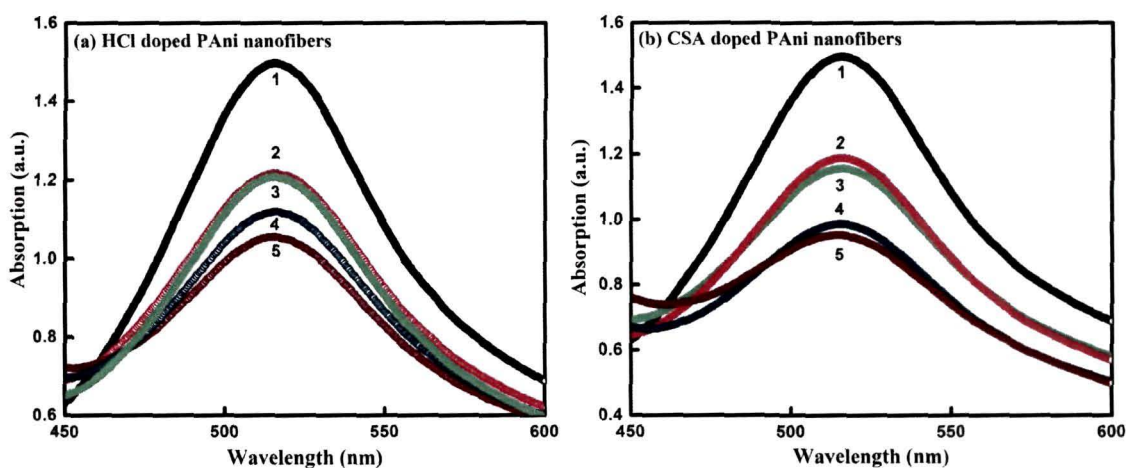


Figure 6.4: UV-Vis spectra of DPPH solutions in methanol after 15 min incubation in the dark with 0.5 mg of pristine and irradiated (a) HCl doped and (b) CSA doped PANi nanofibers. Spectra labelled 1-5 correspond to solutions of DPPH containing no PANi nanofibers, pristine PANi nanofibers and nanofibers irradiated with fluences of 3×10^{10} , 3×10^{11} and 1×10^{12} ions cm^{-2} , respectively.

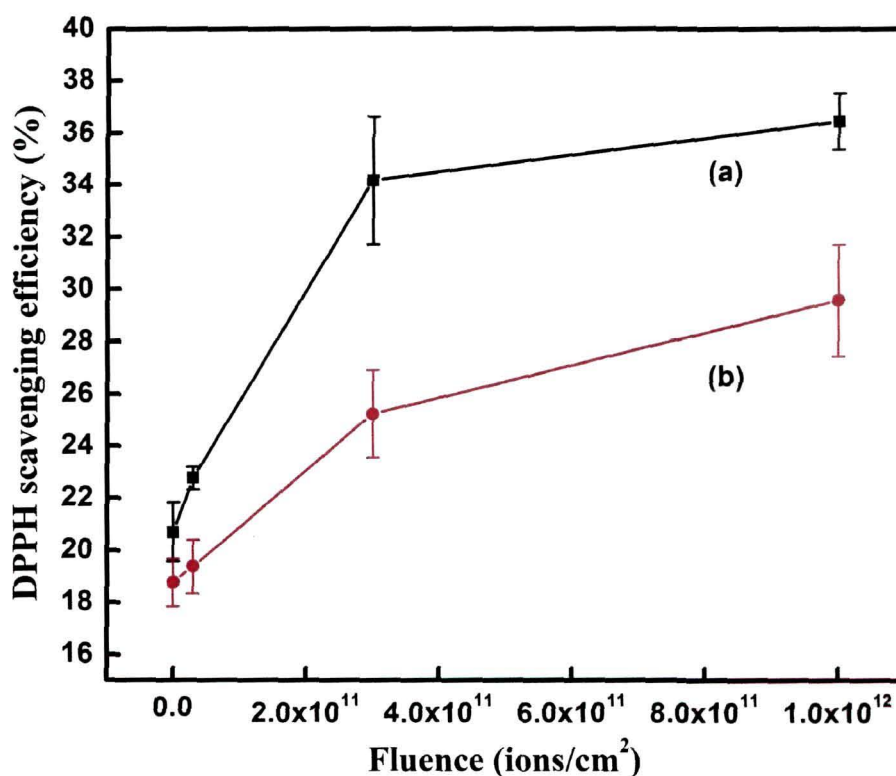


Figure 6.5: Variation of antioxidant activity of the PANi nanofibers (a) doped with HCl and (b) doped with CSA as a function of irradiation fluence.

The dependence of antioxidant activity upon irradiation fluence is depicted in the Fig. 6.5. It clearly shows that the free radical scavenging efficiency of polyaniline nanofibers increases upon SHI irradiation. This can be attributed to the fact that with increasing irradiation fluence the PANi nanofibers get fragmented as has been elucidated in section 4.3.1 in Chapter 4. Due to fragmentation of the PANi nanofibers more reaction sites are available at the surface that can act to reduce DPPH by donating hydrogen atoms and as such the free radical scavenging efficiency increases with increasing irradiating fluence.

Figs. 6.6 (a, b) show the weight dependent free radical scavenging efficiency of the pristine and irradiated PANi nanofibers doped with HCl and CSA, respectively. It is observed that all the samples quenched DPPH in a dose dependent manner; the more the amount of material, the better is the DPPH scavenging ability. This is obvious because there is more substance present and a higher number of hydrogen atoms that can be donated for eliminating DPPH.

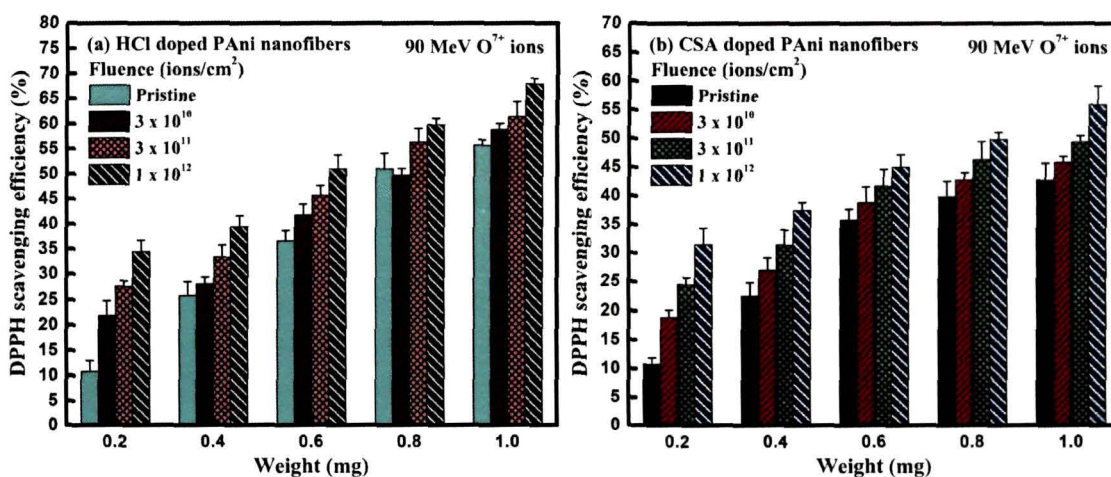


Figure 6.6: Weight dependent free radical scavenging efficiency of pristine and irradiated PANi nanofibers doped with (a) HCl and (b) CSA.

6.4. Mechanism behind free radical scavenging by polyaniline nanofibers

A solution of DPPH on reacting with that of a substance capable of donating a hydrogen atom gives rise to the reduced form with the loss of violet colour (although there would be expected to be a residual pale yellow colour from the picryl group still present). Representing the DPPH radical by Z^{\bullet} and the donor molecule by AH, the primary reaction is:



where ZH is the reduced form and A^{\bullet} is a free radical produced in this first step. This latter radical undergoes further reactions which control the overall stoichiometry, i.e. the number of molecules of DPPH reduced (decolorized) by one molecule of the reductant. The reaction in Eq. (6.1) is therefore intended to provide the link with the reactions taking place in an oxidizing system, such as the auto-oxidation of a lipid or other unsaturated substance; the DPPH molecule Z^{\bullet} is thus intended to represent the free radicals formed in the system whose activity is to be suppressed by the molecule AH .

The mechanism of the reaction between aniline and DPPH has been investigated by many researchers [474, 475]. Polyaniline in the emeraldine oxidation state is comprised of half amine and half imine groups. The observed antioxidant property is due to the neutralization of the free-radical character of DPPH by transfer of an electron [473]. The benzenoid unit of polyaniline (PAni) has the capability of donating hydrogen to reduce the DPPH free radical and in turn get oxidized itself to form a quinoid structure. After the reaction with DPPH, the emeraldine salt form gets converted into the fully oxidized pernigraniline state of polyaniline which is no longer effective for scavenging DPPH. Fig. 6.7 is a schematic diagram showing the possible mechanism of free radical scavenging by PAni nanofibers.

The variation of the antioxidant activity of polyaniline (PAni) bulk (sample S1), PAni nanofiber doped with CSA (sample S2) and PAni nanofiber doped with HCl (sample S3) with time shown in Fig. 6.3 reveals the fact that the scavenging of DPPH free radical increases almost linearly up to a certain point in time, after which the rate of increase in the DPPH scavenging activity decreases. This is indicative of the fact that the emeraldine salt form has been fully oxidized to pernigraniline and has lost its free radical scavenging activity. In the case of nanofibers there are more active sites on the surface as compared to those in the bulk and, as such, more reaction sites are available. This is the reason as to why the antioxidant activity of polyaniline nanofibers (S2 and S3) is found to be much better than the bulk polyaniline.

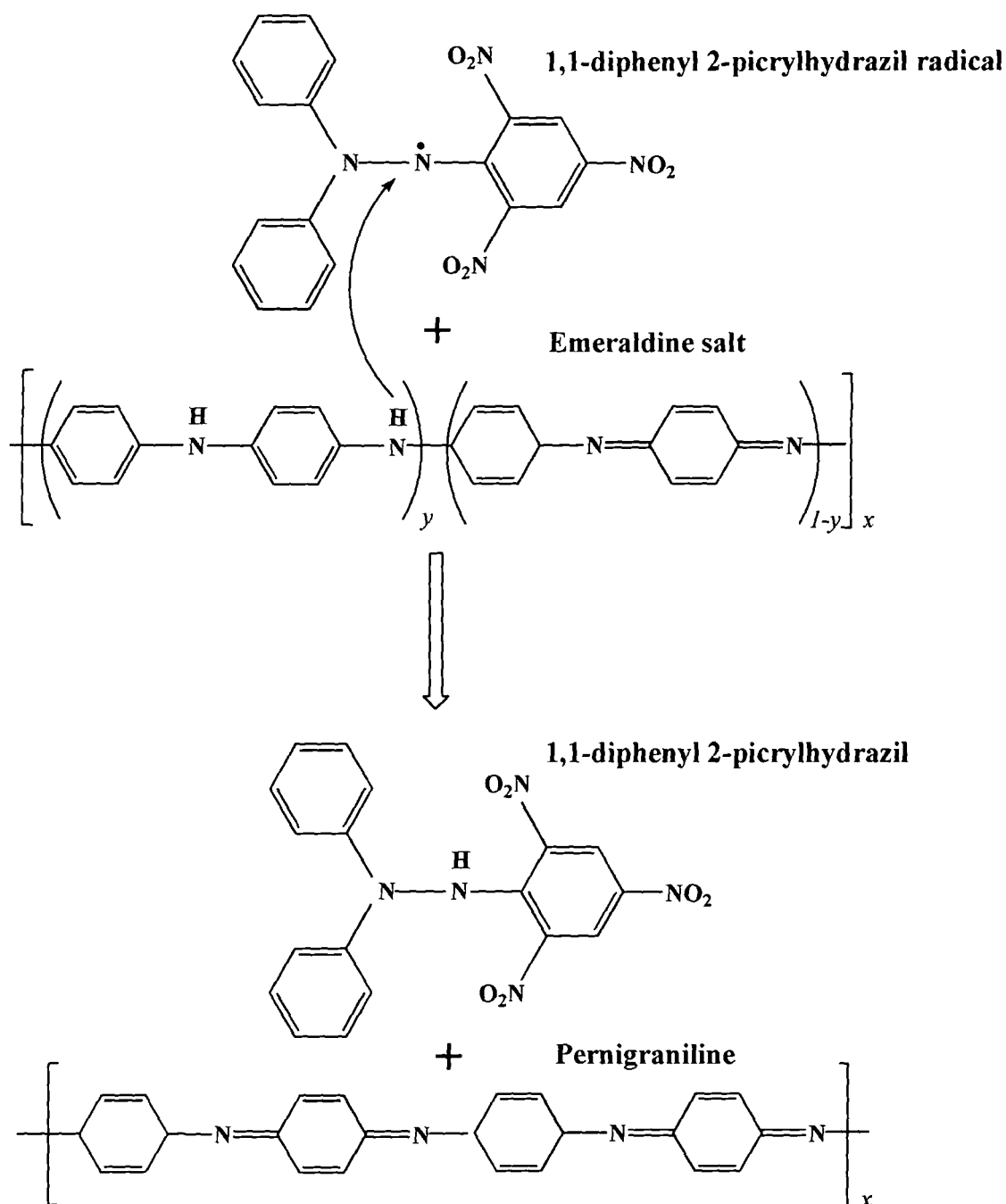


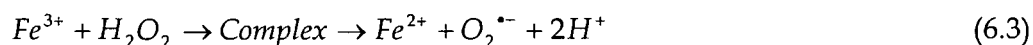
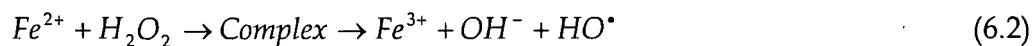
Figure 6.7: Schematic diagram depicting the most probable mechanism for free radical scavenging by PANi nanofibers.

The same mechanism also accounts for the free radical scavenging by the 90 MeV O^{7+} ion irradiated PANi nanofibers. However, it is observed from the FTIR and micro-Raman (μR) spectral analysis that there is a transition from the benzenoid to quinoid structures in the PANi chain as the irradiation fluence is increased as is elucidated in the sections 4.3.3 and 4.3.4 in Chapter 4. The quinoid form has no hydrogen that can be donated to DPPH for scavenging it, and as such

the antioxidant activity should actually decrease after irradiation. But the experimental data reveal an increase in the antioxidant activity of both the HCl and CSA doped PANi nanofibers after irradiation. This may be attributed to the fragmentation of PANi nanofibers upon SHI irradiation. Fragmentation of the nanofibers leads to an increase in the surface to volume ratio. The enhancement in the surface to volume ratio corresponds to the availability of more reaction sites for DPPH scavenging. Availability of more reaction sites as a result of fragmentation of the nanofibers compensates for the lack of hydrogen for DPPH scavenging due to the transition from benzenoid to quinoid structures as a result of SHI irradiation and as such an enhancement in the free radical scavenging efficiency is observed upon SHI irradiation.

6.5. Biocompatibility studies on polyaniline nanofibers

For biomedical applications the biocompatibility of polyaniline (PANi) needs to be investigated in real biological media. It is expected that the toxicity of polyaniline decreases as we go from bulk to nanofibers form. In the present thesis, we have studied the biocompatibility of PANi nanofibers by employing haemolysis prevention assay as described in section 3.7 of Chapter 3. Hydrogen peroxide (H_2O_2) is capable of damaging the red blood cells (erythrocytes) by causing haemolysis. Reaction of hydrogen peroxide with iron causes the formation of free radicals and other charged species [Eqs. (6.2) and (6.3)]. Gutteridge [476-478] found that incubation of commercial haemoglobin (presumably largely methaemoglobin) with H_2O_2 causes formation of hydroxyl radical (OH^\bullet) and releases iron ions from the heme-protein causing deformation of red blood cells.



Figures 6.8 (a)-(c) are scanning electron micrographs showing the morphology of erythrocytes (RBCs) and the effect of H_2O_2 on erythrocytes in the absence and presence of polyaniline nanofibers, respectively. The deformation of erythrocytes caused by H_2O_2 is evident from the scanning electron micrograph [Fig. 6.8 (b)] in which one can clearly see irregularities in the cellular surface of the

RBCs. However, it is observed [Fig. 6.8 (c)] that in the presence of polyaniline nanofibers, the damage caused by H_2O_2 in the erythrocytes is significantly reduced.

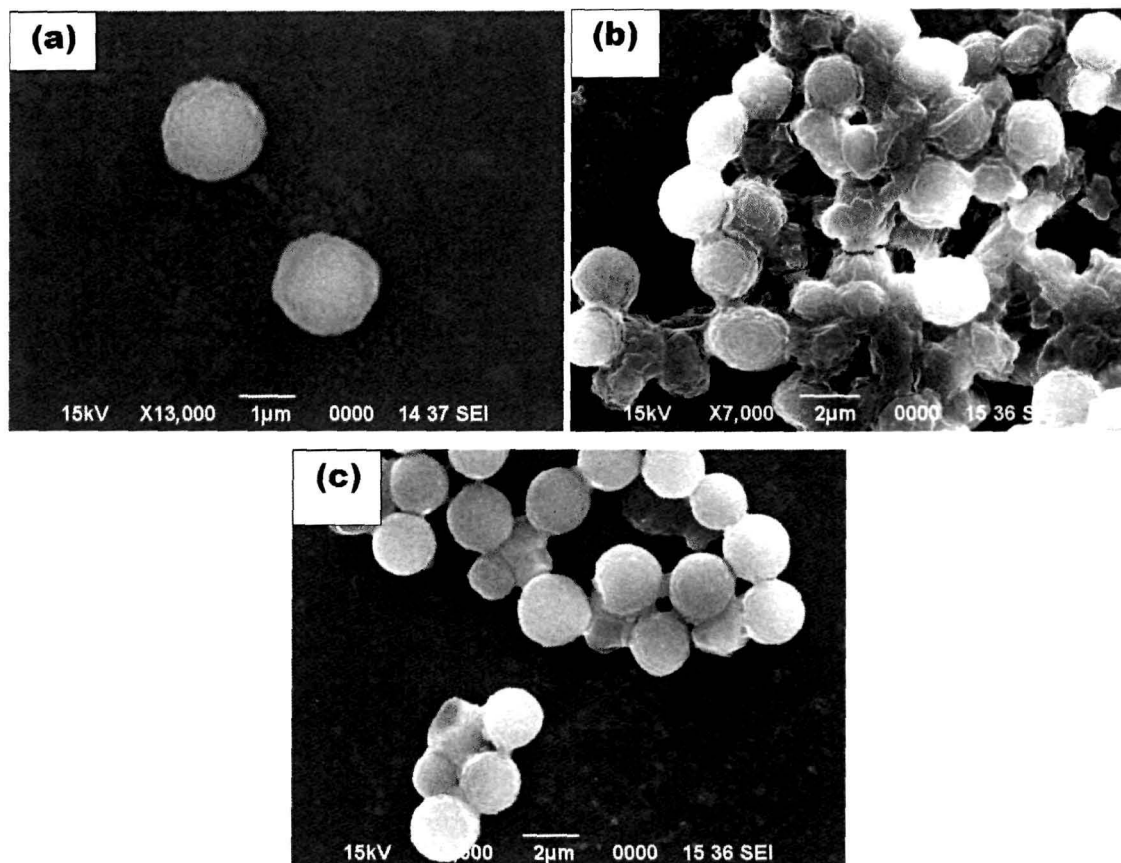


Figure 6.8: Scanning electron micrographs showing (a) morphology of the erythrocytes (RBCs) and the damage caused to the erythrocytes by (b) H_2O_2 and (c) H_2O_2 in the presence of HCl-doped polyaniline nanofibers.

The above phenomenon of haemolysis prevention exhibited by the polyaniline nanofibers can be explained on the basis of their antioxidant nature. Since H_2O_2 is an oxidant, it has the tendency of oxidizing the polyaniline nanofiber in the half-oxidized emeraldine salt form to the fully oxidized pernigraniline form. As a result the H_2O_2 molecule itself gets reduced and loses its potency to damage blood cells. In order to verify this fact, we have investigated the antioxidant activity of HCl doped PANi nanofibers before and after treatment with H_2O_2 employing the DPPH assay. The results presented in Fig. 6.9 show that, after reaction with H_2O_2 , the polyaniline nanofibers that show very high antioxidant activity prior to it, are rendered almost inactive. These results confirm the fact that the emeraldine form of the nanofibers after reacting with the H_2O_2

molecule gets oxidized to form pernigraniline and loses its antioxidant activity. In the process, H_2O_2 gets reduced itself and loses its haemolytic activity.

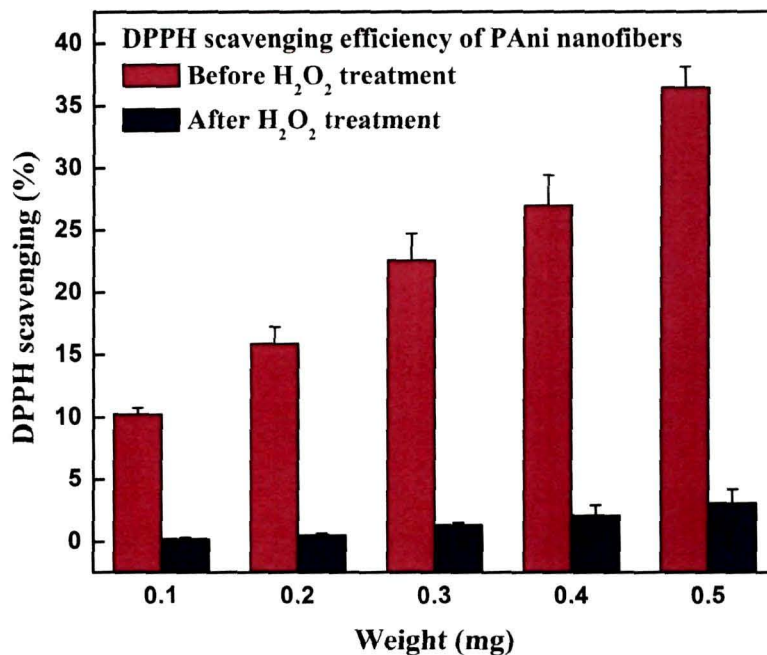


Figure 6.9: DPPH scavenging efficiency of HCl doped polyaniline nanofibers before and after reacting with H_2O_2 .

Figure 6.10 shows a graphical representation of the weight dependent haemolysis prevention activity of CSA doped (sample S2) and HCl doped (sample S3). From the Fig. 6.10, it is evident that the HCl doped PANi nanofiber (sample S3) shows better haemolysis prevention than that of the CSA doped PANi nanofiber (sample S2) for a particular amount of material taken. Reduction in the size leads to the increase in the surface-to-volume ratio, giving rise to more reaction sites. Therefore, for a given amount of the material the nanofiber with the minimum size is more effective for preventing haemolysis. The conformational changes between (sample S2) and (sample S3) as observed from micro-Raman (μR) spectroscopy and XRD analysis discussed in section 4.3.4 in Chapter 4 might also be responsible for the observed enhancement in haemolysis prevention activity. The efficiency of the PANi nanofibers (both samples S2 and S3) to prevent haemolysis shows remarkable enhancement as the amount of nanofibers is increased. This is due to the fact that, as the amount of the material is increased, more and more H_2O_2 is scavenged, therefore, reducing the extent of haemolysis, a phenomenon observed for both the CSA and HCl doped PANi nanofibers.

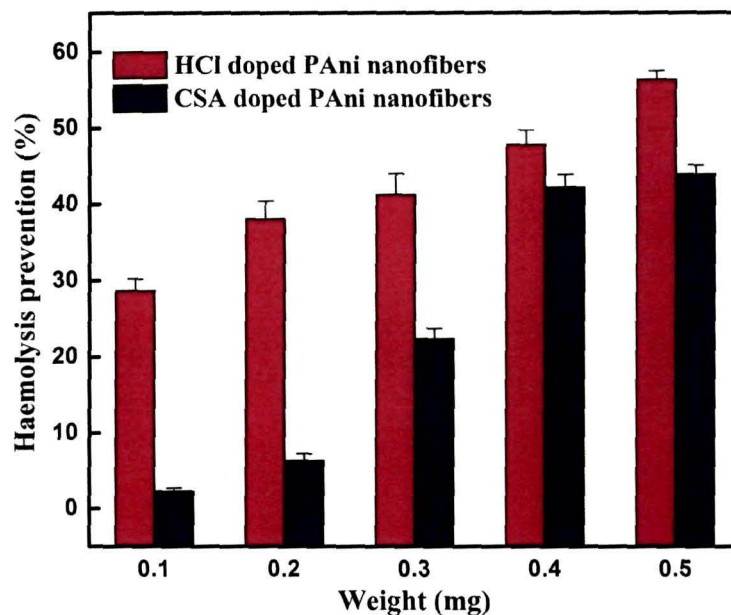


Figure 6.10: Haemolysis prevention efficiency of HCl doped and CSA doped PANi nanofibers

6.6. Swift heavy ion induced enhancement in the biocompatibility of PANi nanofibers

Figure 6.11 shows the haemolysis prevention activity of HCl and CSA doped PANi nanofibers before and after irradiation. It is observed that the haemolysis prevention efficiency of PANi nanofibers increases as the irradiation fluence is increased. The phenomenon of haemolysis prevention exhibited by the polyaniline nanofibers has been explained on the basis of their antioxidant nature. H_2O_2 being an oxidant has the tendency of oxidizing the PANi nanofiber, which is in the half-oxidized emeraldine salt form to the fully oxidized pernigraniline. As a result the H_2O_2 molecule itself gets reduced and loses its potency to damage blood cells. Thus the enhancement in haemolysis prevention activity, and thereby, the biocompatibility of the PANi nanofibers with the increase in irradiation fluence, can be interpreted as the reduction in the particle size and a corresponding increase in the antioxidant activity due to SHI irradiation. The haemolysis prevention activity indicates that the PANi nanofibers become more biocompatible after irradiation with 90 MeV O^{7+} ions at different fluences.

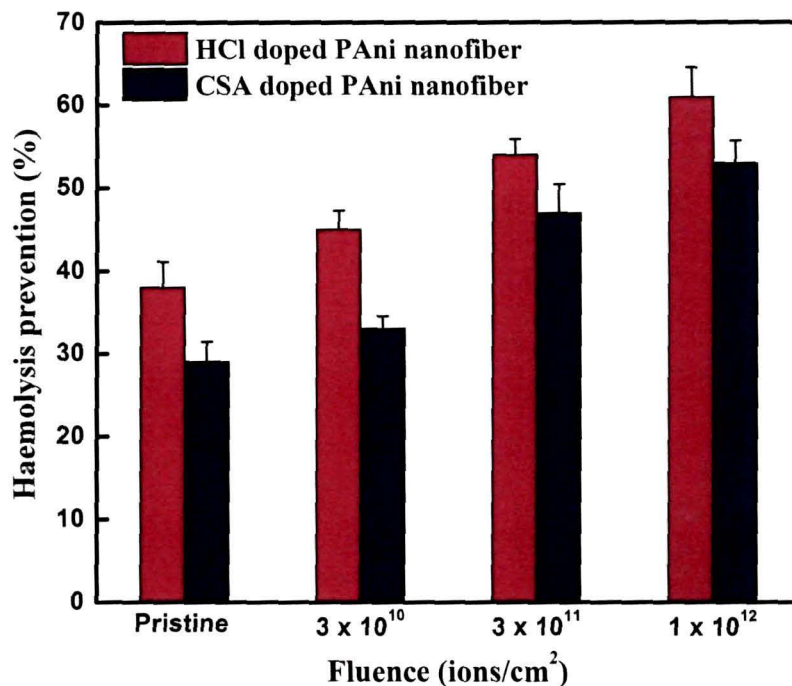


Figure 6.11: Haemolysis prevention activity of pristine and irradiated PANi nanofibers doped with CSA and HCl.

6.7. Antioxidant activity and biocompatibility studies of polyaniline nanofiber reinforced PVA nanocomposites

It is obvious from the experimental results described in the previous sections that PANi nanofibers possess excellent free radical scavenging capability and are also biocompatible as can be inferred from the fact that PANi nanofibers can prevent haemolysis. Although under certain conditions of temperature and pH, PANi nanofibers can form pure colloids and can be cast in the form of thin films, in general we have found that the film formability and stability of PANi nanofibers are poor. In order to enhance the film formability of PANi nanofibers we have adopted the rapid mixing polymerization technique to reinforce the PANi nanofibers in a passive water soluble polymer matrix to render it with mechanical strength which may be useful for some practical device applications. In the present thesis, polyvinyl alcohol (PVA) has been used as the polymer to render PANi nanofibers with mechanical stability. Although PVA is known to be biocompatible, it is interesting to study the variations in the antioxidant activity and the biocompatibility of the PANi nanofiber reinforced PVA nanocomposites as compared to that of pure PANi nanofibers. The antioxidant activity of the PANi

nanofiber reinforced PVA nanocomposites have been determined using the same methodology as for PANi nanofibers as described in the section 3.6 in Chapter 3.

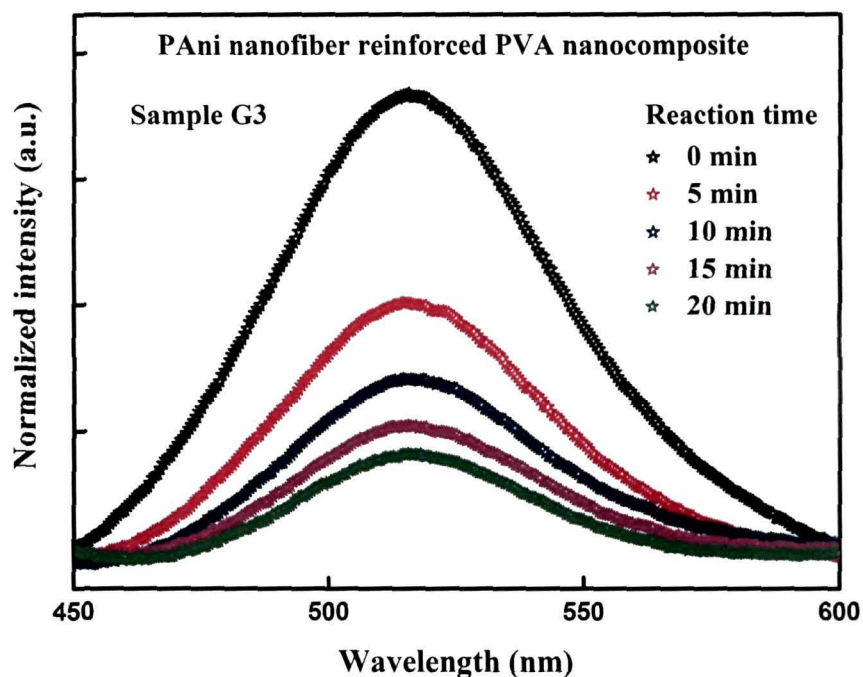


Figure 6.12: Time dependent scavenging of the free radical (DPPH) by PANi nanofiber reinforced PVA nanocomposite with 6 wt. % of aniline content (sample G3)

Reaction of the PANi nanofiber reinforced PVA nanocomposite with the highest concentration of aniline (~ 6 wt. %) (referred to as sample G3 in the Chapter 5) have been carried out with DPPH and the UV-visible spectra of the solutions have been recorded as a function of time. Fig. 6.12 shows the results of the reaction as a function of time, which reveals a decrease in the absorption peak at 516 nm indicating that the free radical DPPH is scavenged by the PANi nanofiber reinforced PVA nanocomposites. This is expected because PANi nanofibers have been found to be highly antioxidant. The weight dependent free radical scavenging efficiency of the PANi nanofiber reinforced PVA nanocomposites with 2 wt. % (sample G1) and 4 wt. % (sample G2) of aniline have also been compared with the sample G3 and it has been observed that the free radical scavenging efficiency of the PANi nanofiber reinforced PVA nanocomposites for a fixed weight of the material taken increases with the increase in aniline content as can be observed from the Fig. 6.13. It is evident from the Fig. 6.8 and Fig. 6.13 that compared to pure PANi nanofibers the free radical scavenging efficiency of PANi nanofiber reinforced PANi nanocomposites is less

for a fixed amount of both the materials taken. This can be attributed to the fact that PVA though is a biocompatible polymer; it is not known to be an antioxidant material.

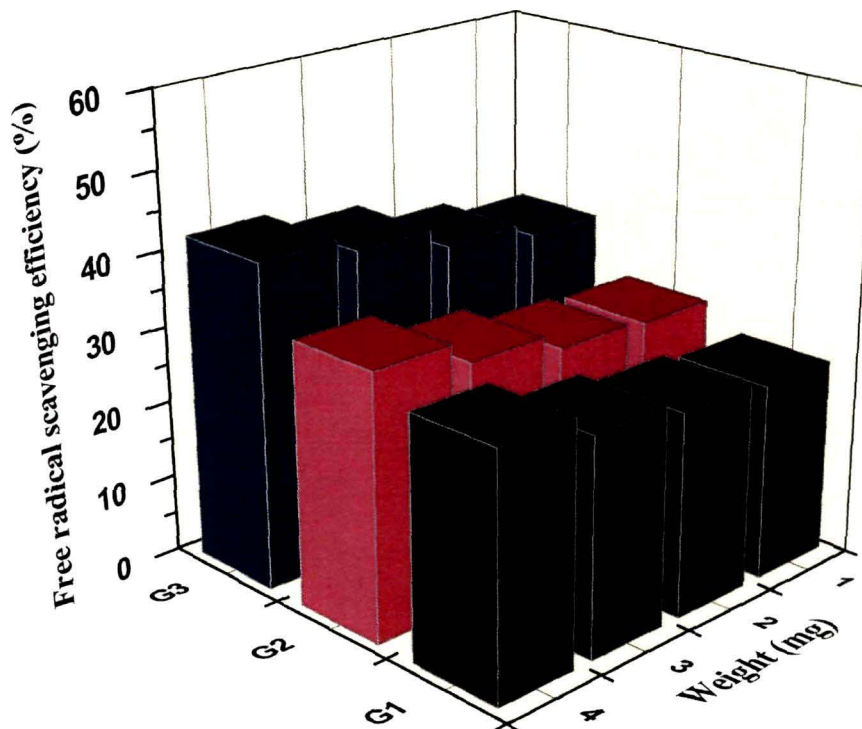


Figure 6.13: Weight dependent free radical scavenging efficiencies (antioxidant activities) of the PANi nanofiber reinforced PVA nanocomposites with 2 wt. % (sample G1), 4 wt. % (sample G2) and 6 wt. % (sample G3) of aniline content. The results presented are average values of 10 repetitions.

The biocompatibility of the PANi nanofiber reinforced PVA nanocomposites have also been investigated by studying the haemolysis prevention efficiency of the nanocomposites following the methodology of Miki *et al.*, as described in section 3.7 of Chapter 3. Fig. 6.14 shows the haemolysis prevention efficiency of the PANi nanofiber reinforced PVA nanocomposites (samples G1, G2 and G3) as a function of weight of the material. Similar trend as observed for the free radical scavenging efficiency is observed with the sample G3 having 6 wt.% of aniline exhibiting better haemolysis prevention as compared to the other two samples with 2 wt.% (sample G2) and 4 wt.% (sample G3) for a fixed weight of the material taken. However, it is observed that the biocompatibility of PANi nanofiber reinforced PVA nanocomposites seems to be better than that of the pure PANi nanofibers. This must be due to the polyvinyl

alcohol (PVA) which is biocompatible and comprises 80 wt. % of the PANi nanofiber reinforced PVA nanocomposites.

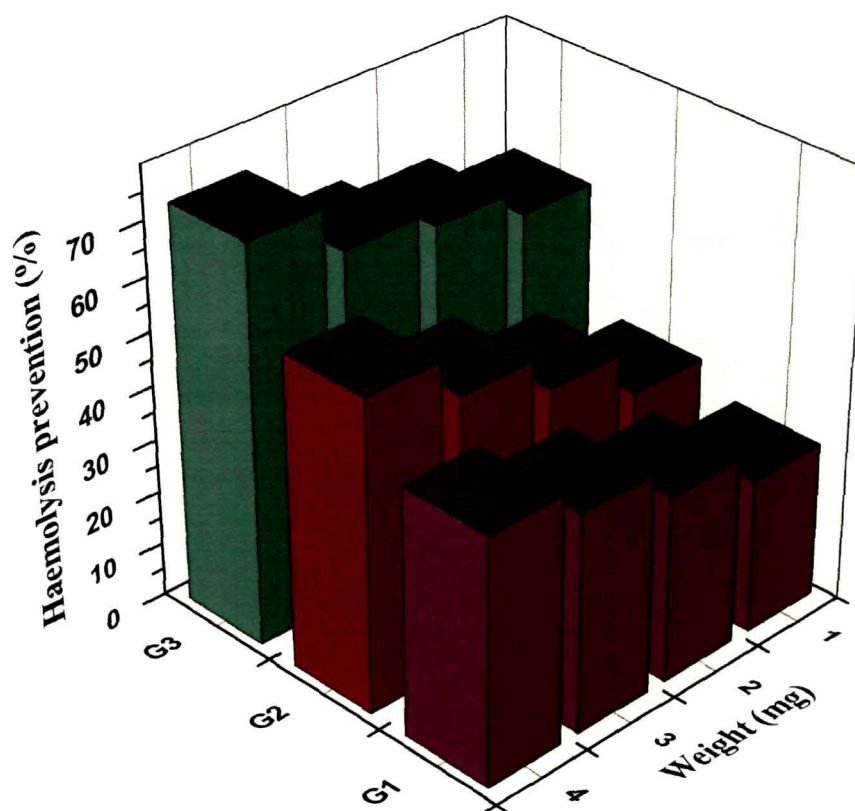


Figure 6.14: Weight dependent haemolysis prevention efficiency of the PANi nanofiber reinforced PVA nanocomposites with 2 wt.% (sample G1), 4 wt.% (sample G2) and 6 wt.% (sample G3) of aniline content. The results presented are average values of 10 repetitions.

6.8. Summary

The antioxidant activity and biocompatibility of PANi nanofibers and PANi nanofiber reinforced PVA nanocomposites have been studied employing well established biochemical assays. The antioxidant and haemolysis prevention efficiencies of HCl-and CSA-doped polyaniline nanofibers, aside from their better processibility, are much better as compared to that of the bulk counterpart. In case of the PANi nanofiber reinforced PVA nanocomposites it has been observed that the antioxidant activity and the biocompatibility increase with the increase in aniline content in the nanocomposites. The observed enhancement in the antioxidant and haemolysis prevention activities of the PANi nanofibers and the PANi nanofiber reinforced PVA nanocomposites have been attributed to the

reduction in particle size and changes in structural conformation, as evident from TEM, XRD and micro-Raman (μ R) and FTIR spectroscopy.

The antioxidant activity of the PANi nanofibers increases as the irradiation fluence is increased. This result conflicts with the fact that after SHI irradiation there is a benzenoid to quinoid transformation in the PANi main chain and as such the antioxidant activity should decrease since the quinoid unit does not have any hydrogen to scavenge DPPH. However, the observed enhancement in the antioxidant activity may be attributed to the decrease in size of the PANi nanofibers after SHI irradiation, which implies availability of more active reaction sites for DPPH scavenging. The increase in the availability of surface reaction sites overcome the lack of hydrogen due to the benzenoid to quinoid transition. The haemolysis prevention capability and subsequently the biocompatibility of the PANi nanofibers are also found to increase with irradiation fluence. The results indicate the possibility of using SHI irradiation as a potential technique for enhancement in the antioxidant activity and the biocompatibility of conducting polymer nanostructures for biomedical applications.

Reduction in particle size and changes in structural conformation, namely the change in torsion angle of $C_{ring}-N-C_{ring}$, are found to be major factors determining the availability of active surface sites for reaction which greatly affects the antioxidant and haemolysis prevention activities of PANi nanofibers. Increase in the surface-to-volume ratio due to the reduction in particle size and change in the $C_{ring}-N-C_{ring}$ torsion angle is a major factor contributing towards the enhancement in the antioxidant as well as the haemolysis prevention activity of PANi nanofibers. Conducting polymer nanostructures having good biocompatibility combined with antioxidant and haemolysis prevention property can lead to tremendous development in the fields of biomedicine and controlled drug release, the latter of which can be immensely useful for cancer treatment. Although the present investigations reveal that polyaniline (PANi) nanofibers have excellent antioxidant and haemolysis prevention activity, further *in vivo* studies for their compatibility in biological media are very essential before exploiting the fabulous scope of these synthetic antioxidants in biomedical applications.

Chapter 7

POLYANILINE NANOFIBER REINFORCED PVA NANOCOMPOSITE COATED QUARTZ CRYSTAL MICROBALANCE SENSORS

This chapter embodies the details of fabrication of quartz crystal microbalance (QCM) based sensors coated with polyaniline nanofibers reinforced PVA nanocomposites for sensing some specific analytes viz., free radicals and hydrochloric acid. The polyaniline nanofibers reinforced PVA nanocomposite coated QCM sensors have been characterized and several important device parameters have been determined. This chapter also includes a discussion on the most probable mechanism governing the sensing of the above mentioned analytes by the fabricated sensors.

7.1. Introduction

In comparison with sensors based on metal oxides that are operated at high temperatures, the sensors made of conducting polymers have many improved characteristics such as high sensitivities and short response time even at room temperature. Likewise conducting polymers such as polypyrrole (PPy), polyaniline (PAni), polythiophene (PTh) and their derivatives, have been used as active layers for different type of sensors since early 1980s [259-269]. Conducting polymers are easy to be synthesized through chemical or electrochemical processes, and their molecular chain structure can be modified conveniently by copolymerization or structural derivations. Furthermore, conducting polymers have good mechanical properties, which allow facile fabrication of sensors. The fact that conducting polymers exhibit changes in colour, conductivity, volume, mass, mechanical properties and ion permeability upon doping makes them efficient sensing materials. As a result, increasing attention has been paid to the sensors fabricated from conducting polymers.

The quartz crystal microbalance (QCM) comprises of a thin vibrating AT-cut quartz wafer sandwiched between two metal excitation electrodes. When a small amount of mass is adsorbed at the quartz electrode surface, the frequency of the quartz is changed according to the well-known Sauerbrey equation [479]:

$$\Delta F = \frac{-2f_0^2 \Delta m}{A(\mu_q d_q)^{1/2}} \quad (7.1)$$

where ΔF is the measured frequency shift, f_0 the original oscillation frequency of the dry crystal, Δm the mass change, A the piezo-electrically active area of the excitation electrodes, d_q the density of quartz and μ_q the shear modulus.

When the surface of a quartz crystal electrode is coated by a material capable of interaction with the environment of interest, a sensor sensitive to this component can be constructed. The performance characteristics of the QCM sensor (such as selectivity, response time and reversibility) depend on the chemical nature and physical properties of the coating material. Quartz crystals, coated with various coatings, have been used for adsorption and determination of various compounds [309-311]. In the present study, 5 MHz AT-cut quartz resonators coated with polyaniline nanofiber reinforced PVA nanocomposites have been applied for the continuous monitoring of free radical and hydrochloric acid concentrations in a liquid medium. The effects of increasing analyte concentration on the physico-chemical properties of the PANi nanofiber reinforced PVA nanocomposite have been investigated using XRD, FTIR, ac conductivity measurements and dielectric spectroscopy to have a better insight into the mechanism of sensing of these analytes by the PANi nanofiber reinforced PVA nanocomposite modified quartz resonators.

7.2. Fabrication of Polyaniline nanofiber reinforced PVA nanocomposite coated QCM sensor

Polyaniline nanofiber reinforced PVA nanocomposites have been synthesized using *in-situ* rapid mixing polymerization technique as mentioned in Chapter 5. Thin films of the PANi nanofiber reinforced PVA nanocomposites have been coated over the 5 MHz AT cut quartz crystals with gold coated electrodes purchased from Stanford Research Systems. On-line monitoring of different

analytes viz., free radicals and hydrochloric acid in solution have been performed using the experimental set-up for quartz crystal microbalance [Fig. 3.11] based sensors as elucidated in section 3.8 of Chapter 3.

7.3. Polyaniline nanofiber reinforced PVA nanocomposite modified QCM sensors for sensing free radicals

As has been discussed in section 6.1 of Chapter 6, free radicals are harmful chemical species that can lead to the progression of several acute diseases in living beings and can also deteriorate fats, oils, rubber and polymer products by free radical mediated oxidation. Thus, detection of free radicals both in-vitro and in-vivo has become very important in medical science. Several techniques employing spin trapping using electron spin resonance (ESR) [480] and NMR [481] have been employed for detection of free radicals. Scientists have also used chemical labelling by quenching with free radicals, e.g. with nitric oxide (NO) or DPPH (1,1-diphenyl-2-picrylhydrazyl), followed by spectroscopic methods like X-ray photoelectron spectroscopy (XPS) or absorption spectroscopy for the determination of free radicals [482]. But all these techniques are very sophisticated, expensive and time consuming. Thus, the development of cheap and reliable sensors for the detection of very small levels of free radicals is highly desirable and can have immense application in biomedical science, petroleum, polymer and rubber industries.

Being redox active, conducting polymers have the capability of neutralizing free radicals. As discussed in Chapter 6, the emeraldine salt form of polyaniline (PAni) has been found to exhibit excellent free radical scavenging property since they can neutralize the free radical by donating hydrogen atom and thereby changing their oxidation state from emeraldine to pernigraniline. It has been observed that as compared to the bulk, PAni nanofibers have better free radical scavenging property that has been attributed to the availability of more surface reaction sites for scavenging free radicals.

7.3.1. Characterization of the sensor

Quartz crystals with gold electrodes have been coated using an aqueous solution of polyaniline (PAni) nanofiber reinforced PVA nanocomposites

employing spin coating technique. The morphology of the PANi nanofiber reinforced PVA nanocomposite films coated on the quartz crystals have been investigated by scanning electron microscopy. It has already been observed from electron microscopy that PANi nanofibers of average diameter around 30 nm are formed within the PVA matrix. The polymer-coated electrodes have been exposed to different concentrations (500-900 ppb) of a standard stable free radical viz., 1, 1 diphenyl 2-picrylhydrazil (DPPH) dissolved in HPLC grade methanol (MeOH). The response curve of a quartz crystal coated with PANi nanofiber reinforced PVA nanocomposite for different concentration of free radicals in methanol solution is shown in Fig. 7.1.

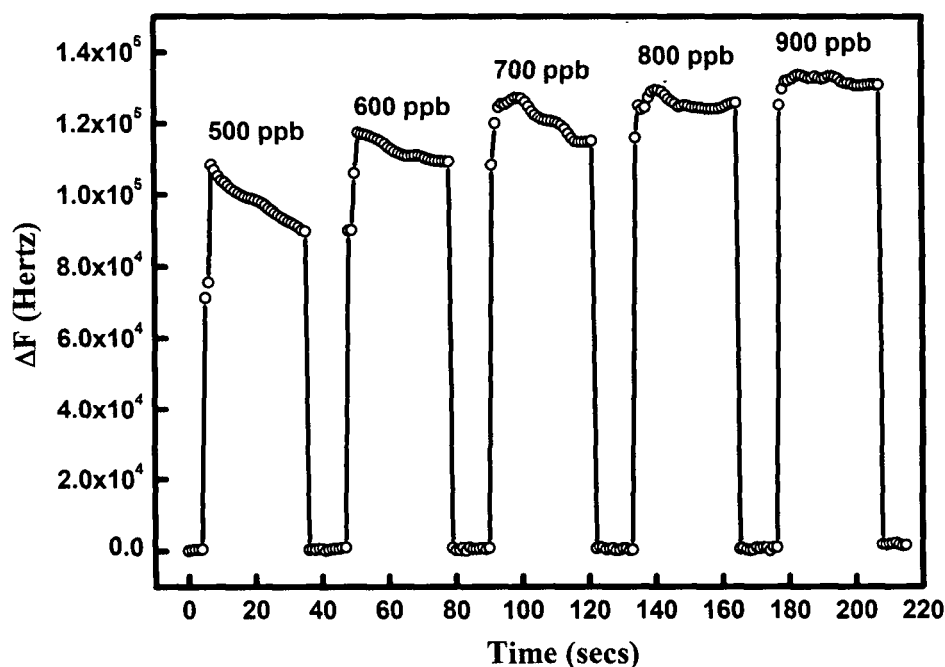


Figure 7.1: Response characteristics of the PANi nanofiber reinforced PVA nanocomposite modified QCM sensor after exposure to different concentration of free radicals in solutions

It is observed that the frequency of the crystal increases sharply with increase in the concentration of DPPH. The increase in the frequency indicates that the mass of the quartz crystal decreases after reacting with the free radicals in the solution, according to the Eq. (7.1). This response shows that the PANi nanofiber reinforced PVA nanocomposite coated quartz electrode is sensitive to very low concentrations of free radicals. Although, the sensor can be used for detection of higher free radical concentrations (>900 ppb), below 500 ppb no detectable signal has been obtained.

7.3.1.1. Linearity

It is highly desirable that the response obtained by a sensor should be linear against different concentration of the analytes. In order to investigate this, the PANi nanofiber reinforced PVA nanocomposite coated quartz crystal electrodes have been directly exposed to various concentrations of free radicals from 500 to 900 ppb. Fig. 7.2 shows a calibration curve that has been constructed by plotting the frequency shifts against the concentration of the free radical DPPH in solution. It is observed from Fig. 7.2 that the QCM sensor fabricated by coating a quartz crystal by PANi nanofiber reinforced PVA nanocomposite is linear in the concentration range investigated in the present work with a linear regression coefficient of $R^2 = 0.9685$.

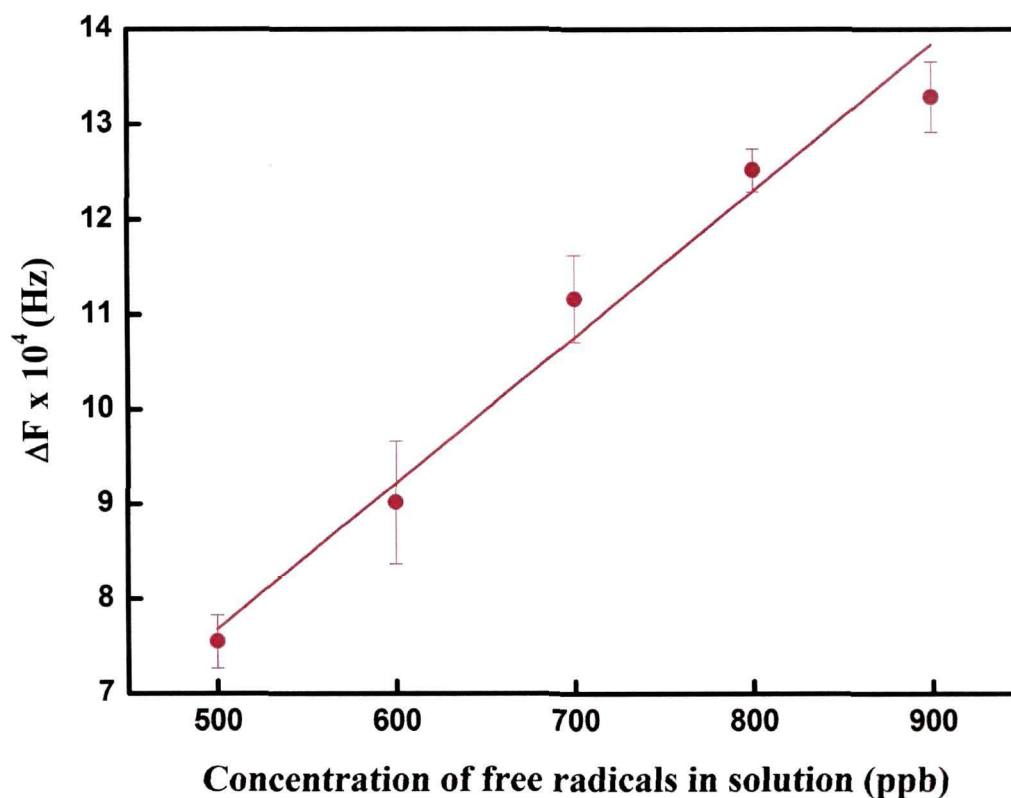


Figure 7.2: Calibration curve for determination of free radicals in solution. The frequency shifts of a PANi nanofiber reinforced PVA nanocomposite modified quartz crystal electrode in direct contact to the free radical solutions have been recorded after 2.5 min of exposure.

7.3.1.2. Sensitivity

The sensitivity is defined as the slope of the calibration graph shown in Fig. 7.2 [483]. Using the calibration curve, the sensitivity of the PANi nanofiber

reinforced PVA nanocomposites coated quartz crystal sensors with respect to the free radical DPPH has been calculated and the value of $149.87 \text{ Hz ppb}^{-1}$ has been obtained.

7.3.1.3. Response time

The response time can be defined as the time required for a sensor output to change from its previous state to a final settled value within a tolerance band of the correct new value. Fig. 7.3 shows the time required by the PANi nanofiber reinforced PVA nanocomposite coated QCM sensors to reach a stable final output value from the initial value after reacting with different concentrations of free radicals. It has been observed that the response time of the sensor decreases from 1.231 s to 0.779 s as the concentration of the free radical in solution increases from 500-900 ppb.

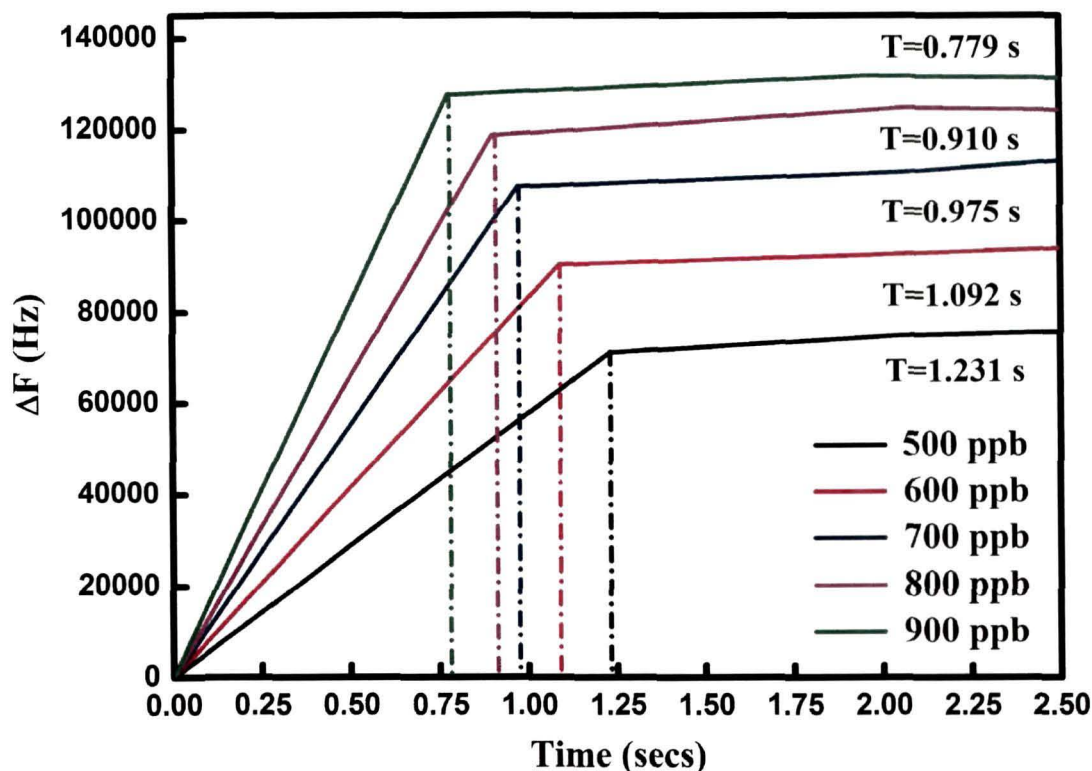


Figure 7.3: Plot for calculating the response time of the sensor for different concentration of free radicals in solution

7.3.2. Mechanism of sensing

It has been suggested in section 6.4 of Chapter 6 that after reacting with a free radical viz., DPPH, benzenoid rings in the PANi chains get oxidized to quinoid with the elimination of hydrogen atoms. The increase in frequency shift

indicates that the mass of the sensors decreases, which further supports the hypothesis. However, in order to prove the above hypothesis and the possible mechanism for which PANi nanofiber reinforced PVA nanocomposite acts as an active layer for the quartz crystal while sensing free radicals, some more experiments have been conducted.

The mechanism of free radical sensing by PANi nanofiber reinforced PVA nanocomposites have been investigated by studying the variations in the X-ray diffraction patterns, FTIR spectra, the impedance and ac conductivity spectra of the nanocomposites before and after reaction with different concentrations of free radicals viz., 500-900 ppb as used in the sensing experiments.

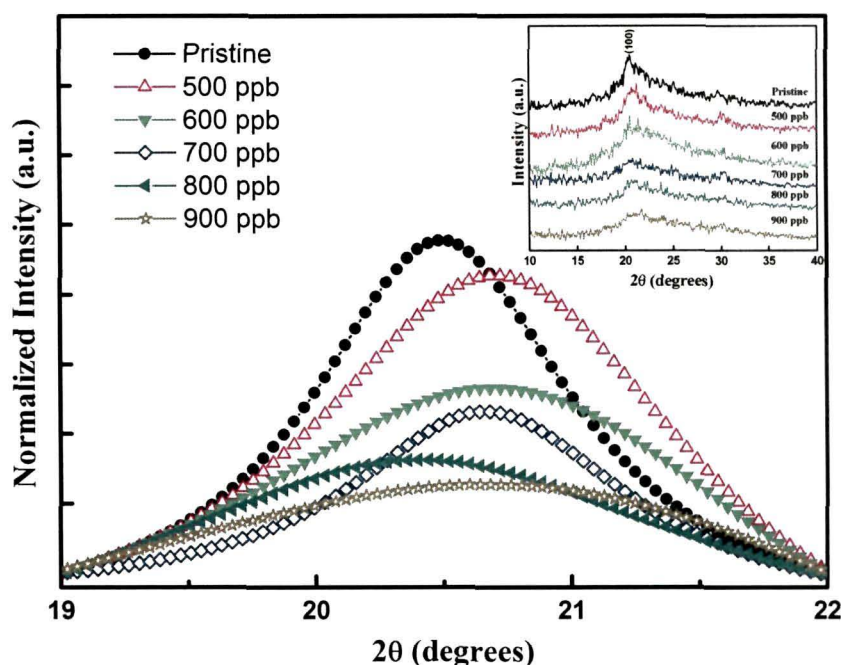


Figure 7.4: X-ray diffraction pattern of the PANi nanofiber reinforced PVA nanocomposite before and after exposure to different concentration of free radicals in solution showing the variation of the (100) reflection peak of PANi. Inset shows the X-ray diffraction pattern over the entire 2θ range.

Fig. 7.4 shows the variations in the (100) peak of PANi in the 2θ range from 19° - 22° . A single line approximation method [414] has been used for calculating the domain length and the strain in the PANi nanofiber reinforced PVA nanocomposite samples before and after reaction with different concentration of the analyte i.e. DPPH in this case. The variation in the domain length and strain in the PANi nanofiber reinforced PVA nanocomposites as a result of increasing the

concentration of the analyte has been presented in Table 7.1. It has been observed that the domain length (L) i.e., the local range of order within the PANi chains in the PANi nanofiber reinforced PVA nanocomposite samples decrease as the concentration of the free radical in solution increases, while the strain is found to increase. This is indicative of the fact that after reaction with the analyte the degree of crystallinity of the PANi nanofiber reinforced PVA nanocomposite decreases.

Table 7.1: Comparison of the domain length (L) and the strain (ϵ) in the PANi nanofiber reinforced PVA nanocomposites before and after exposure to different concentrations of free radicals

Concentration of free radical (DPPH) in ppb	Domain length (L)	Strain (ϵ)
0	22.66	1.16
500	20.18	1.45
600	18.21	1.91
700	17.13	2.43
800	13.45	2.61
900	10.11	3.01

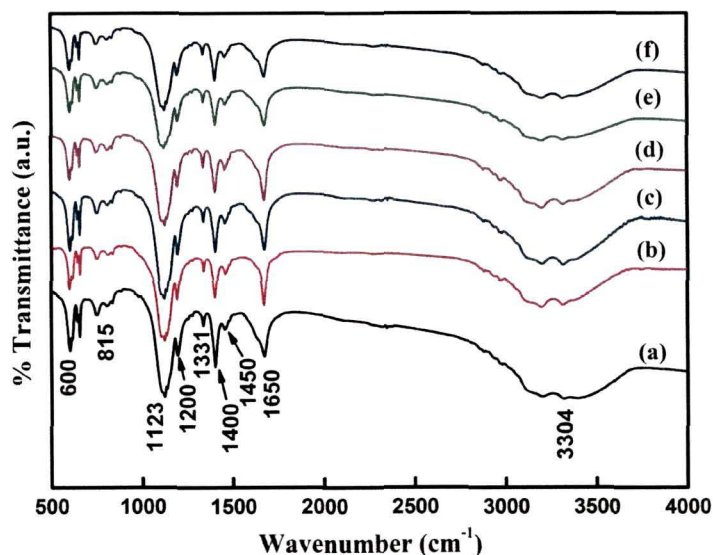


Fig 7.5: FTIR spectra of PANi nanofiber reinforced PVA nanocomposites (a) before and after exposure to (b) 500, (c) 600, (d) 700, (e) 800 and (f) 900 ppb

The FTIR spectrum of the polyaniline (PANi) nanofiber reinforced PVA nanocomposites before and after reaction with the analyte is shown in the Fig. 7.5. The band around 3300 cm⁻¹ is attributed to the N-H stretching vibrations while that at 1650 cm⁻¹ is a signature of the N-H bending vibration of PANi. The peak

observed at 815 cm^{-1} is ascribed to the N-H out of plane bending vibration. The strong band observed at 1140 cm^{-1} and the band at 1200 cm^{-1} are due to the C-C stretching and C-C twisting of the alkyl chain. The C-N stretching peak of the polymer is observed at 1336 cm^{-1} . The C-Cl stretching vibration observed around 600 cm^{-1} confirms the fact that the PANi nanofibers are in doped states. The vibrational bands around 1460 and 1400 cm^{-1} are assigned to C=C stretching vibration of the quinoid and benzenoid ring of PANi, respectively.

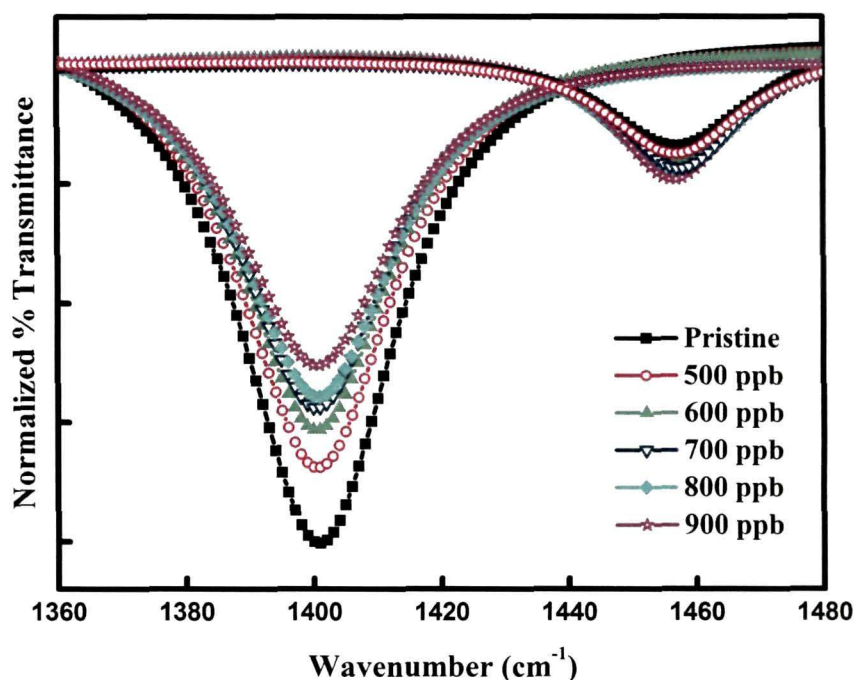


Figure 7.6: Comparison of the intensity of the C=C stretching vibration due to the benzenoid and quinoid structures of the PANi nanofiber reinforced PVA nanocomposites before and after exposure to free radicals in solution

The major variation in the FTIR spectra has been observed for the peaks corresponding to the C=C stretching vibrations of the para di-substituted benzene (benzenoid) and the quinone diimine (quinoid). It has been observed that the C=C stretching peak due to the benzenoid ring has decreased significantly whereas a corresponding increase in the C=C stretching peak due to the quinoid ring has increased but the increase is not that significant as can be observed from the Fig. 7.6. However, the decrease in the intensity of the C=C stretching vibration for the PANi nanofiber reinforced PVA nanocomposites after reaction with free radicals indicates that the conjugation length in the nanocomposites decrease with the increase in the concentration of the analyte. A decrease in the conjugation length

is an indication of the fact that the conductivity of the material decreases. In order to prove this fact the variations in the impedance spectra and the ac conductivity spectra of the PANi nanofiber reinforced PVA nanocomposites before and after exposure to the analyte DPPH have been studied.

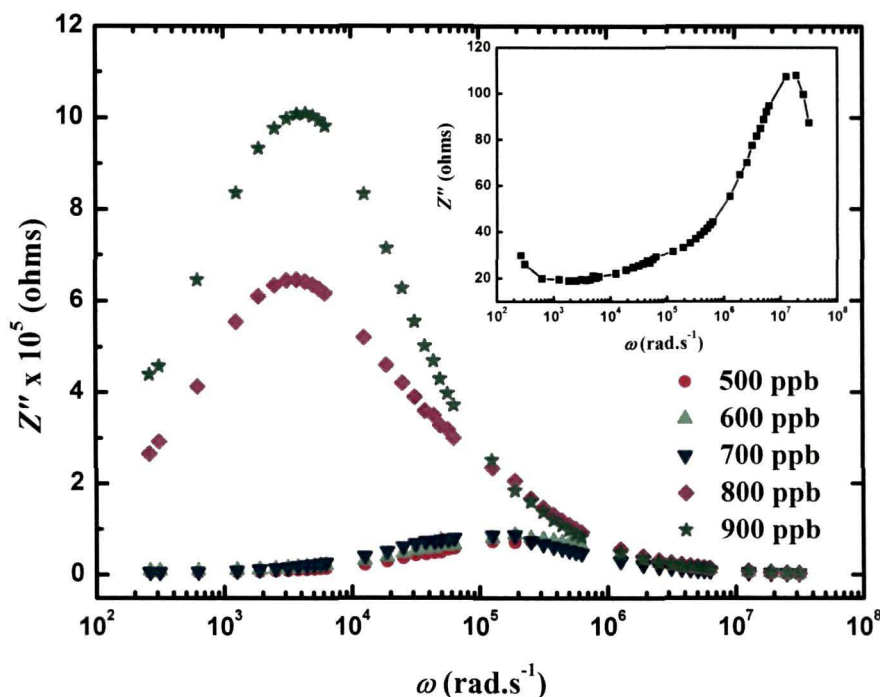


Figure 7.7: Z'' spectra of the PANi nanofiber reinforced PVA nanocomposites before and after exposure to different concentrations of free radicals in solution

Fig. 7.7 shows the variation of the imaginary part (Z'') of the complex impedance (Z^*) as a function of frequency for the PANi nanofiber reinforced PVA nanocomposites after exposure to different concentrations of free radicals in solution. The inset of Fig. 7.7 shows the variation of the imaginary part (Z'') of the complex impedance (Z^*) for the pristine sample. It is known that PANi exhibits two relaxation peaks in the Z'' spectra depending upon the amount of benzenoid and quinoid structures present in the PANi chain [451]. The lower frequency peak having higher impedance can be attributed to the phase of oxidized repeat units (quinoid units) and the higher frequency peak of a lower value of impedance to the phase of reduced repeat units (benzenoid units) of PANi. It is evident from the Fig. 7.7 that as the concentration of the analyte increases the relaxation peak observed in the Z'' spectra shifts from higher frequency to lower frequency region and the value of the imaginary part Z'' of complex impedance (Z^*) increases by

almost 10^4 times, which is an indication of the fact that there is indeed a transformation from the benzenoid to quinoid structure in the PANi chains upon exposure to the analyte and the transformation varies directly with concentration of the analyte.

The plot of ac conductivity of the PANi nanofiber reinforced PVA nanocomposites before and after exposure to the analyte is shown in Fig. 7.8. The experimental values of ac conductivity have been fitted to the Eq. 4.19 of Chapter 4 and it has been observed that the experimental data show a reasonably good fit to the Eq. 4.19 except for the sample exposed to 900 ppb of the analyte; which may be ascribed to electrode polarization effects.

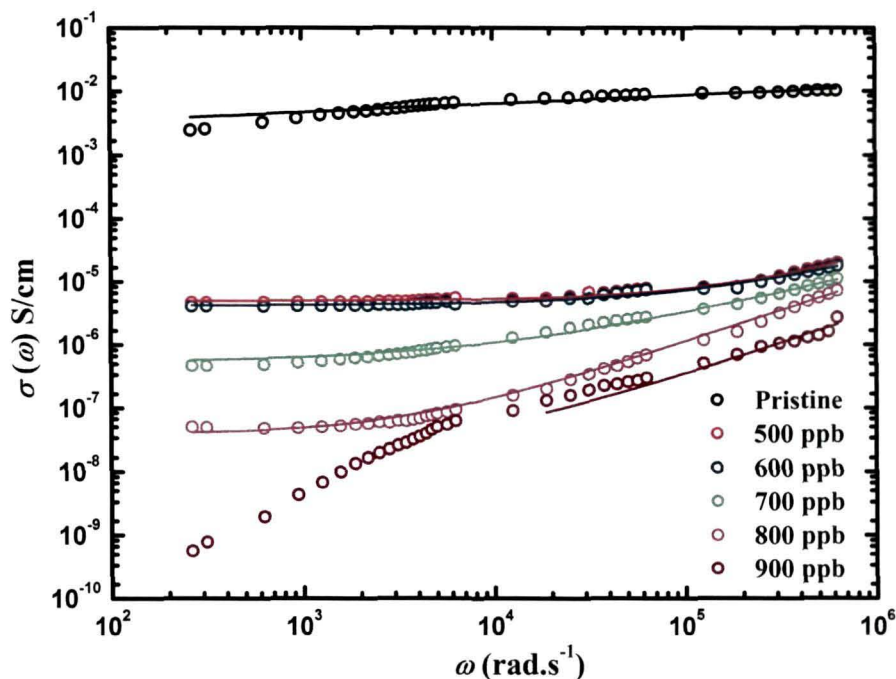


Figure 7.8: AC conductivity spectra of the PANi nanofiber reinforced PVA nanocomposite before and after exposure to different concentration of free radicals in solution

The origin of electrode polarization in this case is not clear but it may be assumed that upon exposure to 900 ppb of free radicals in solution there is some amount of morphological changes in the PANi nanofiber reinforced PVA nanocomposites. The values of the dc conductivity and the frequency exponent 's' are presented in Table 7.2. The ac conductivity in general obeys the universal power law with the exponent 's' varying from 0 to 1 as can be seen from the Table 7.2. A decrease in the value of dc conductivity obtained from the best fits of the experimental data with the Eq. (4.19) can be observed as the concentration of

analyte is increased, which may be ascribed to the decrease in conjugation length in the PANi nanofiber reinforced PVA nanocomposites upon exposure to different concentrations of free radicals due to the partial benzenoid to quinoid transformation.

Table 7.2: Values of dc conductivity and *s* parameter obtained from the best fits of the experimental data of ac conductivity (for the PANi nanofiber reinforced PVA nanocomposites before and after exposure to different concentrations of the free radical) with the Eq. (4.19)

Concentration (ppb)	σ_{dc} (S/cm)	's' parameter
0	5.13×10^{-3}	0.81
500	5.02×10^{-6}	0.92
600	4.19×10^{-6}	0.91
700	5.39×10^{-7}	0.88
800	4.24×10^{-8}	0.97
900	---	---

7.4. Polyaniline nanofiber reinforced PVA nanocomposite modified QCM sensors for sensing hydrochloric acid

Among the family of π -conjugated polymers, PANi deserves a special mention primarily because of its unique acid/base doping mechanism. As such it can be used as an acid sensor since doping of PANi also leads to the variation in its mass. So, PANi nanofiber reinforced PVA nanocomposites based QCM sensors can be an excellent candidate for the detection of acids in solution. In the present work we have fabricated a quartz crystal microbalance sensor coated with PANi nanofibers reinforced PVA nanocomposite for the detection of low concentration of hydrochloric acid in solution and investigated the device parameters of the sensor. The mechanism of HCl sensing by the PANi nanofiber reinforced PVA nanocomposites have also been investigated using some additional characterization techniques that includes X-ray diffraction and FTIR.

7.4.1. Characterization of the sensor

Quartz crystals coated with PANi nanofiber reinforced PVA nanocomposites have also been used to sense very small quantities of hydrochloric acid in an aqueous solution. The polymer-coated electrodes have been exposed to different concentrations (100-500 ppm) of a hydrochloric acid.

The response characteristic of the sensor for different concentration of hydrochloric acid in solution is shown in Fig. 7.9.

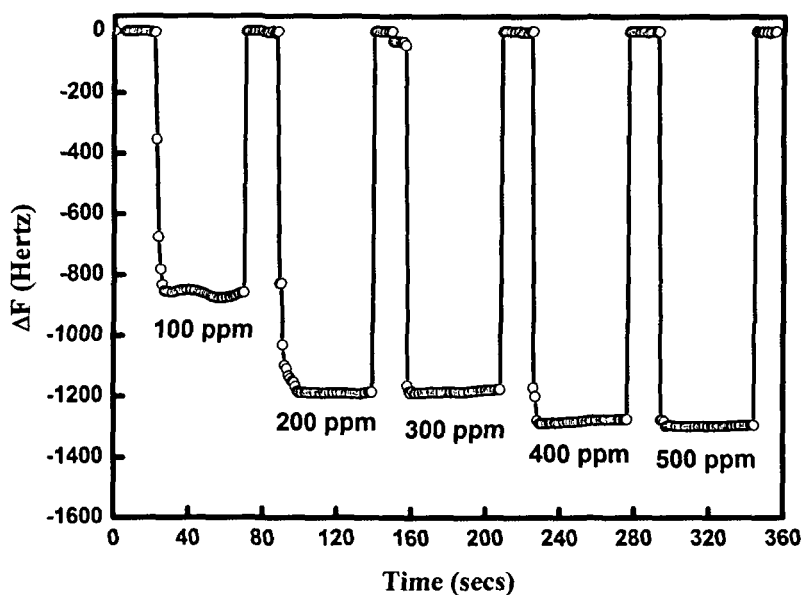


Figure 7.9: Response characteristics of the PANi nanofiber reinforced PVA nanocomposite modified QCM sensor after exposure to different concentration of hydrochloric acid in aqueous solutions

It has been observed that the frequency of the quartz crystal after sensing different concentrations of HCl decreases unlike that for the free radical sensor where an enhancement in the frequency of the quartz crystal has been observed. Thus, it immediately follows from the Sauerbrey's equation Eq. (7.1) that the mass of the quartz crystal increases after it has been exposed to HCl. The reaction of HCl with polyaniline is well known. The H^+ ions of HCl protonates polyaniline and the Cl^- ions are inserted in the polymer to neutralize the charge. Thus in both the cases the mass of the PANi nanofibers reinforced PVA nanocomposite coated quartz crystal should ideally increase. Likewise a negative frequency shift is expected as has been obtained for the sensor. The parameters associated with the sensor viz., linearity, sensitivity and the response time have been evaluated and are discussed in the subsequent sections.

7.4.1.1. Linearity

The linearity of the HCl sensor has been evaluated from a calibration curve in which the frequency shift has been plotted against the concentration of the analyte as shown in Fig. 7.10. PANi nanofiber reinforced PVA nanocomposite

coated quartz crystal electrodes have been directly exposed to various concentrations of hydrochloric acid (HCl) from 100 to 500 ppm. It is observed from Fig. 7.10 that the QCM sensor fabricated by coating a quartz crystal by PANi nanofiber reinforced PVA nanocomposite is linear in the concentration range of HCl investigated in the present work with a linear regression coefficient of $R^2=0.9321$.

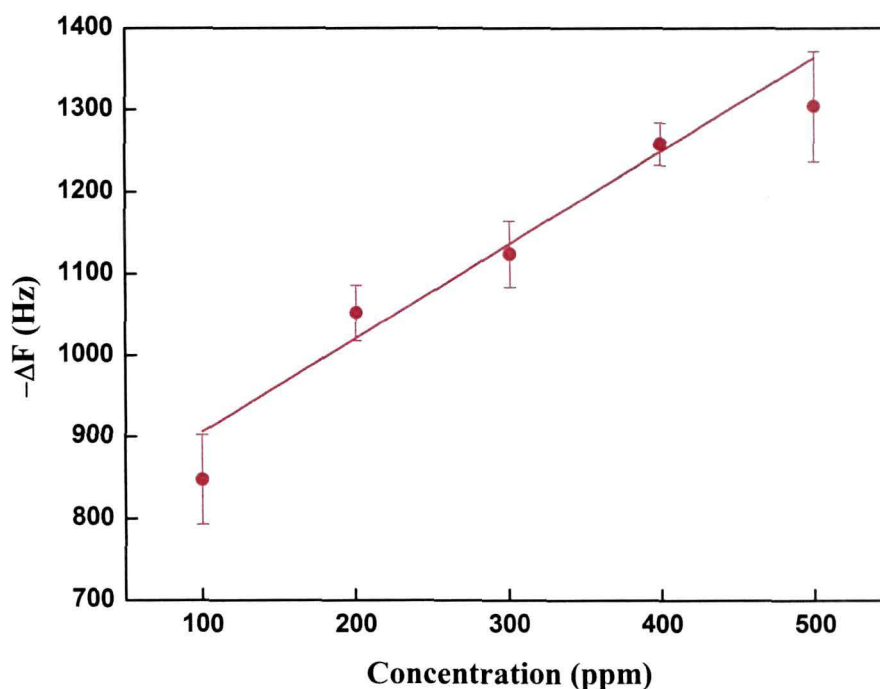


Figure 7.10: Calibration curve for determination of hydrochloric acid in solution. The frequency shifts of a PANi nanofiber reinforced PVA nanocomposite modified quartz crystal electrode in direct contact to the solutions have been recorded after 2.5 min of exposure

7.4.1.2. Sensitivity

The slope of the calibration curve as shown in Fig. 7.10 determines the sensitivity of the sensor. The sensitivity of the HCl sensor has been found to be 21.4 Hz.ppm^{-1} . Although the sensitivity of the HCl sensor is acceptable but it is much lower than that of the free radical sensor based on PANi nanofiber reinforced PVA nanocomposites.

7.4.1.3. Response time

Fig. 7.11 shows the time required by the PANi nanofiber reinforced PVA nanocomposite coated QCM sensors to reach a stable final output value from the

initial value after reacting with different concentrations of hydrochloric acid. It has been observed that the response time of the sensor decreases from 2.88 secs to 1.66 secs as the concentration of the hydrochloric acid in the solution increases from 100-500 ppm.

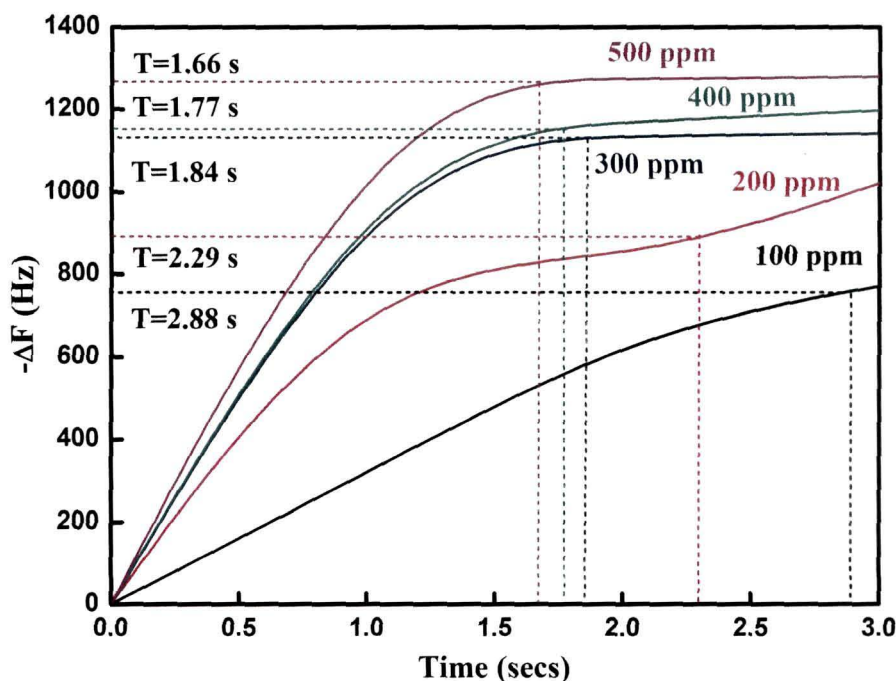


Figure 7.11: Plot for calculating the response time of the sensor for different concentration of hydrochloric acids in aqueous solution

7.4.2. Mechanism of sensing

As has been discussed earlier that two processes viz., protonation of polyaniline (PAni) and insertion of Cl^- counterions for maintaining charge neutrality of the polymer occurs when HCl is used to dope polyaniline. However, to validate the above statement and to have a better idea of the sensing mechanism for which PAni nanofiber reinforced PVA nanocomposites act as an active layer for the quartz crystal while sensing hydrochloric acids, some supplementary experiments have been conducted.

The mechanism of HCl sensing by PAni nanofiber reinforced PVA nanocomposites have been investigated by studying the variations in the X-ray diffraction patterns and FTIR spectra of the nanocomposites before and after reaction with different concentrations of hydrochloric acids viz., 100-500 ppm as used in the sensing experiments.

Fig. 7.12 shows the variations in X-ray diffraction patterns of the PANi nanofiber reinforced PVA nanocomposites before and after exposure to different concentrations of HCl. It is observed that the (110) reflections of PANi centered around $2\theta = 26^\circ$ attributed to the perpendicular periodicity of PANi is the most prominent peak. It is evident from the Fig. 7.12 that the intensity of the (110) peak increases as the concentration of the analyte is increased.

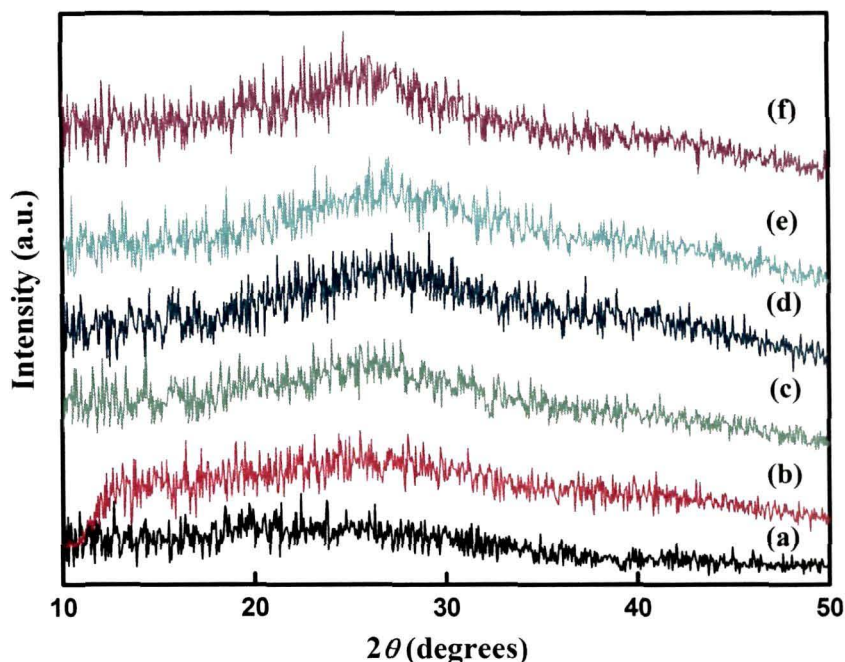


Figure 7.12: X-ray diffraction patterns of the PANi nanofiber reinforced PVA nanocomposites (a) before and after exposure to (b) 100 ppm, (c) 200 ppm, (d) 300 ppm, (e) 400 ppm and (f) 500 ppm of hydrochloric acid in solution.

Variations in the domain length and strain of the PANi nanofiber reinforced PVA nanocomposites before and after exposure to different concentrations of hydrochloric acid have been studied using a single line approximation method [414]. The variation in the domain length and strain in the PANi nanofiber reinforced PVA nanocomposites as a result of increasing the concentration of the analyte has been presented in Table 7.3.

It has been observed that the domain length (L) i.e., the local range of order within the PANi chains in the PANi nanofiber reinforced PVA nanocomposite samples increase as the concentration of the hydrochloric acid increases in the solution, while the strain is found to decrease. It has been reported that an increase in the Cl/N ratio improves the local range of order in polyaniline. Thus

upon exposure to different concentrations of hydrochloric acid the Cl/N ratio in the PANi nanofiber reinforced PVA nanocomposites increases and so does the domain length as is observed from the Table 7.3. The strain on the other hand decreases because of better ordering of the chains.

Table 7.3: Comparison of the domain length (L) and the strain (ϵ) in the PANi nanofiber reinforced PVA nanocomposites before and after exposure to different concentrations of hydrochloric acid in solution

Concentration of hydrochloric acid (HCl) in ppm	Domain length (L)	Strain (ϵ)
0	15.21	3.16
100	17.23	2.71
200	20.01	2.16
300	22.36	2.01
400	27.13	1.51
500	29.92	1.28

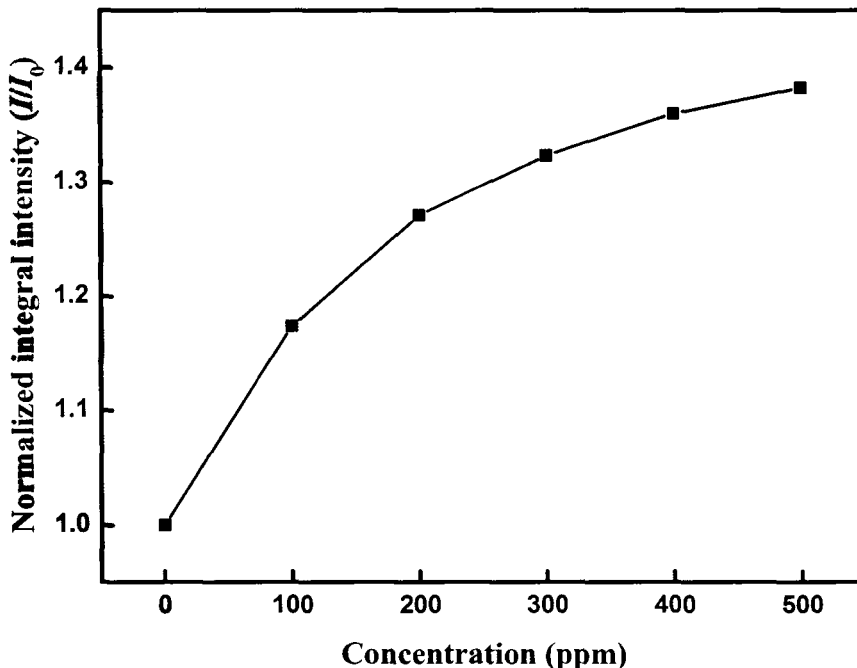


Fig 7.13: Variation of the normalized integral intensity (I/I_0) as a function of the concentration of analyte.

The variation in the overall degree of crystallinity has been studied from the variation in the normalized integral intensity (I/I_0) of the nanocomposites upon exposure to different concentrations of HCl. Fig. 7.13 shows the plot of the normalized integral intensity as a function of the concentration of the analyte. It has been observed that the integral intensity of the PANi nanofiber reinforced

PVA nanocomposites increases as the concentration of HCl is increased. This indicates that the degree of crystallinity of the PANi nanofiber reinforced PVA nanocomposites increases with the increase in the concentration of the analyte.

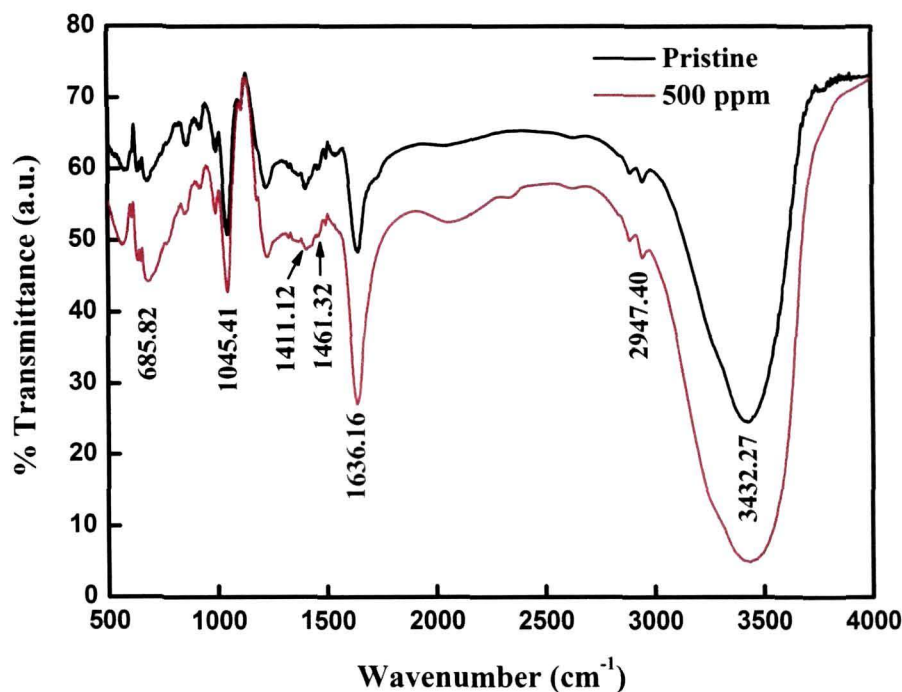


Figure 7.14: FTIR spectra of PANi nanofibers reinforced PVA nanocomposite before and after exposure to 500 ppm of hydrochloric acid.

In order to reveal the mechanism of HCl sensing by the PANi nanofiber reinforced PVA nanocomposites the variations in the molecular structure of the nanocomposite has been investigated using FTIR spectroscopy. The FTIR spectra of the PANi nanofiber reinforced PVA nanocomposites before and after reaction with 500 ppm of the analyte are shown in the Fig. 7.14. As has been described earlier in Chapter 5, the FTIR spectra of PANi nanofiber reinforced PVA nanocomposite consists of the band around 3300 cm^{-1} is attributed to the N-H stretching vibrations while that at 1650 cm^{-1} is a signature of the N-H bending vibration of polyaniline (PANi). The N-H out of plane bending vibration peak is observed at 815 cm^{-1} . The strong band observed at 1140 cm^{-1} and the band at 1200 cm^{-1} are due to the C-C stretching and C-C twisting of the alkyl chain. The C-N stretching peak of the polymer is observed at 1336 cm^{-1} . The C-Cl stretching vibration observed around 600 cm^{-1} confirms the fact that the PANi nanofibers are in doped states. The vibrational bands around 1460 and 1400 cm^{-1} are assigned to C=C stretching vibration of the quinoid and benzenoid ring of PANi, respectively.

It is evident from the figure that almost all the bands observed in the pristine PANi nanofiber reinforced PVA nanocomposites exhibit an increase in their intensity after reacting with 500 ppm of HCl. Especially, it is observed the N-H stretching and N-H bending vibrations of PANi nanofiber reinforced PVA nanocomposites are significantly enhanced after reaction with 500 ppm of HCl. This confirms the fact that HCl leads to the protonation of polyaniline in the PANi nanofiber reinforced PVA nanocomposites. Another important variation is the increase in the C-Cl stretching peak at 685.82 cm^{-1} . This proves the fact that it is not only protonation of polyaniline that increases the mass of the PANi nanofiber reinforced PVA nanocomposite coated quartz crystal but also the insertion of Cl⁻ counterions in the interstitial spaces of the PANi nanofiber reinforced PVA nanocomposites that leads to the mass increase and hence a negative frequency shift is observed in the response characteristic of the sensor.

Thus, from X-ray diffraction and FTIR studies it can be confirmed that when the PANi nanofiber reinforced PVA nanocomposite coated quartz crystal is exposed to different concentrations of HCl, its mass increases due to the protonation of PANi and the subsequent insertion of the Cl⁻ ions leading to the decrease in the frequency of the quartz crystal.

7.5. Summary

Polyaniline nanofiber reinforced PVA nanocomposites synthesized by *in-situ* rapid mixing polymerization have been used as the active layer for the fabrication of modified quartz crystal microbalance sensors for sensing free radicals and HCl in solution. It has been observed that these modified QCM sensors can be used to detect ppb level of free radicals in solution. The linearity of the sensor has been found to be excellent with a linear regression coefficient of 0.9685. The sensitivity of the free radical sensor has been found to be $149.87\text{ Hz ppb}^{-1}$. The response time of the sensor has been observed to decrease with the increase in the analyte concentration. It has also been observed that the local range of order in the PANi nanofiber reinforced PVA nanocomposite decreases upon exposure to different concentrations of the free radicals, which indicate that the material amorphizes after reacting with the analyte. FTIR spectra reveal a partial transformation from benzenoid to quinoid structures in the PANi chains that can

significantly decrease the conjugation length and affect charge transport through the material. The impedance plots also indicate that with the increase in the concentration of the analyte, the benzenoid structure gets oxidized to the quinoid structure giving rise to a shift in the relaxation peak towards lower frequency region is observed. The ac conductivity plots show good fit with the universal power law and it has been observed that the dc conductivity of the PANi nanofiber reinforced PVA nanocomposites obtained from the best fits of the experimental data decreases with the increase in the concentration of the analyte. QCM based sensors modified with PANi nanofiber reinforced PVA nanocomposites can be a very cost effective and sustainable method for the detection of harmful free radicals in food and polymer products and also for in-vitro sensing of free radicals from biological systems.

Using the same nanocomposite material as the active layer, sensors have also been fabricated to detect low concentrations of HCl in solution. The HCl sensor also is found to be linear in the concentration range studied in the present work with a linear regression coefficient of 0.9321. The sensitivity, however, is lower than the free radical sensor. These sensors have also been found to have very fast response for detecting different concentrations of HCl in solution and the response time decreases with the increase in the analyte concentration. Low level detection of HCl by the PANi nanofibers reinforced PVA nanocomposite coated QCM sensors have been ascribed to the protonation of polyaniline followed by the subsequent insertion of Cl⁻ counterions in the polymer resulting in increase in the mass and a corresponding decrease in the frequency of the quartz crystal. These results have been well corroborated by XRD and FTIR analyses.

Chapter 8

CONCLUSIONS AND FUTURE PROSPECTS

This chapter presents in detail the main conclusions drawn from the present work. The limitations and future prospects in the emerging area of research in conducting polymer based nanostructured materials have also been briefly discussed towards the end of this chapter.

8.1. Conclusions:

The present work deals with the synthesis of polyaniline (PAni) based nanostructured materials viz., PAni nanofibers and PAni nanofiber reinforced PVA nanocomposites using interfacial and *in-situ* rapid mixing polymerization techniques with a view to investigate the application potential of these materials in biomedical and sensor applications. PAni based nanostructured materials have been irradiated with 90 MeV O⁷⁺ ions and the physico-chemical modifications in the nanofibers have been thoroughly investigated employing different characterization techniques. The major conclusions drawn from the present work are enumerated below:

1. Transmission electron microscopy of the pristine and irradiated PAni nanofibers reveals fragmentation of the PAni nanofibers. It has been observed that upon SHI irradiation the average diameter of the PAni nanofibers decreases from 29.35 to 9.45 nm for the nanofibers doped with HCl and from 50 nm to 11.38 nm for the nanofibers doped with CSA. The fragmentation of PAni nanofibers upon SHI irradiation has been ascribed to deposition of tremendous amount of electronic energy in the material leading to the amorphization and fragmentation of PAni nanofibers within the core of the tracks. As the fluence is increased the tracks overlap and the fragmentation increases resulting in reduction of the size of PAni nanofibers. Transmission electron microscopy of the PAni nanofiber reinforced PVA

nanocomposites reveals that PANi nanofibers of average diameter around 30 nm are formed within the PVA matrix. Scanning electron microscopy shows that surface morphology of the nanocomposite roughens and the porosity decreases as the aniline content in the nanocomposites increases. The reduction in the porosity and the enhancement in the density of the nanocomposites upon SHI irradiation have been ascribed to the dislocation of the polymer chains from the hilly to the valley regions due to the deposition of huge amount of electronic energy under the impact of swift heavy ions.

2. It has been evaluated from XRD analysis that as the irradiation fluence increases the crystalline domain size decreases while the strain increases. The decrease in the integral intensity (area) for the (100) reflection peak with increasing fluence suggests that the PANi nanofibers are amorphized. Enhancement in strain in the material may be attributed to the creation of dislocations and defects in the material upon SHI irradiation. The increase in d -spacing indicates an increase in the $C_{\text{ring}}-N-C_{\text{ring}}$ tilt angle with respect to the (a, b) basal plane of PANi. This has been associated with the reduction in π -stacking among the PANi chains and de-doping of the doping states of PANi nanofibers upon SHI irradiation. XRD analysis shows that unlike pure PANi nanofibers, in case of the PANi nanofiber reinforced PVA nanocomposites there is an enhancement in the degree of crystallinity of the nanocomposite upon SHI irradiation. This has been ascribed to the cross-linking of PANi nanofibers within the PVA matrix.
3. Vibrational spectra of the pristine and SHI irradiated PANi nanofibers investigated using FTIR and μR spectroscopic techniques bring out a very significant result i.e., a benzenoid to quinoid transition in the PANi nanofibers upon SHI irradiation. Although it is generally accepted that FTIR and Raman active modes are mutually exclusive but for amorphous materials all the modes can be active in both IR and Raman since the selection rules valid for a crystalline structure no longer holds for an amorphous material. The benzenoid to quinoid transition leads to a decrease in the π -conjugation length. De-doping and amorphization of PANi

nanofibers have also been confirmed by micro-Raman (μR) spectroscopy. In case of the PANi nanofiber reinforced PVA nanocomposites, FTIR reveals that upon SHI irradiation the basic polymer structure is retained, however, the C-C stretching band intensifies while the C-C twisting vibration decreases indicating that the polymer undergoes cross-linking upon SHI irradiation. In the PANi nanofiber reinforced PVA nanocomposites unlike PANi nanofibers there is a partial deformation from the quinoid to the benzenoid induced by SHI irradiation that has been attributed to the availability of the hydrogen rich polyvinyl alcohol matrix in the nanocomposites unlike that in case of the polyaniline nanofibers. Thus swift heavy ion irradiation can lead to both types of transition depending upon the properties of the pristine PANi based nanostructured material. We conclude that the benzenoid to quinoid ratio is of great importance in case of PANi based nanostructured materials since it governs the physicochemical properties exhibited by PANi and vibrational spectroscopy can be very useful tool to investigate the benzenoid to quinoid transition in these materials.

4. UV-Visible spectroscopy studies indicate that there is an increase in the optical band gap of the PANi nanofibers upon SHI irradiation, which has been attributed to the fragmentation of the PANi nanofibers upon SHI irradiation and also a decrease in the extent of conjugation, which suggests that the adjacent phenyl rings of the polymer have larger torsion angles with respect to the plane of the nitrogen atoms. This fact is also corroborated by the μR and FTIR results, which reveal a benzenoid to quinoid transition causing reduction in π -conjugation. In the PANi nanofiber reinforced PVA nanocomposites, UV-Visible studies indicate that the density of states in the polaron band located deep inside the band-gap of the nanocomposites increases upon SHI irradiation.
5. The structural disorders in PANi nanofibers have been found to anneal out as a result of SHI irradiation as confirmed by the decreasing value of Urbach tail width with increasing ion fluence, which enhances the band gap. Quantum confinement effect is another probable reason that might be

responsible for the observed enhancement in the band gap since upon SHI irradiation the nanofibers are found to be fragmented.

6. Dielectric spectroscopy of the PANi based nanostructured materials reveals that relaxations in these materials are of non-Debye type with a distribution of relaxation times. Strong low frequency dispersion in the permittivity spectra indicates that hopping is the dominant charge transport mechanism. As the temperature increases the relaxation peak in the permittivity spectra is suppressed, which is ascribed to the fact that with increasing temperature larger number of charge carriers participate in the relaxation process and the dc conductivity term dominates. The disappearance of the peak due to benzenoid units of PANi nanofibers in the impedance spectra as a result of SHI irradiation also indicates a benzenoid to quinoid transition in the PANi nanofibers upon SHI irradiation. Existence of a master curve in the modulus spectra reveals that the dynamic processes occurring at different frequencies exhibit the same activation energy. These results suggest that there is an increased coupling among the localized short range dipolar motion in the PANi nanofibers.
7. The decrease of the frequency exponent 's' in the experimental ac conductivity curves with increasing temperature for the pristine and SHI irradiated PANi nanofibers suggests that correlated barrier hopping (CBH) is the dominant charge transport mechanism. Low values of polaron binding energy (0.30–0.80 eV) calculated using the experimental values of the frequency exponent 's' confirms the existence of single polarons as the major charge carriers in both the pristine and SHI irradiated PANi nanofibers. Although there is little variation in the charge transport mechanism and the nature of charge carriers in the PANi nanofibers upon SHI irradiation but there is a significant decrease in the conductivity of the PANi nanofibers upon SHI irradiation. The increase in the density of states in PANi nanofibers with increasing irradiation fluence reveals a decrease in delocalization, which is responsible for the observed decrease in the conductivity. In case of the PANi nanofiber reinforced PVA nanocomposites, the conductivity has been found to increase with the increase in irradiation fluence as observed

from the I-V characteristics of the pristine and irradiated samples and is also corroborated by dielectric spectroscopy, XRD and FTIR results. The conductivity results depict that although there is an increase in the conductivity but the charge transport mechanism follows the correlated barrier hopping (CBH) model.

8. Positron annihilation lifetime spectroscopy (PALS) has been employed to explain the observed enhancement in the conductivity of the PANi nanofiber reinforced PVA nanocomposites upon SHI irradiation. PALS result reveals that there is a sharp decrease in the shortest and the intermediate lifetime components after irradiation but with the increase in the ion fluence the lifetime components show almost similar values. The sharp decrease in the lifetime components has been attributed to the creation of local lattice distortions (polaron) and chain defects formed by the SHI irradiation induced perturbation in the intermolecular forces in the vicinity of the ion track, which leads to an enhancement in the conductivity of the nanocomposites.
9. It has been observed that the HCl- and CSA-doped polyaniline nanofibers, besides their better processibility, have better potency as antioxidant and haemolysis-preventing agents as compared to their bulk counterparts. In case of the PANi nanofiber reinforced PVA nanocomposites, it has been observed that the antioxidant activity and the biocompatibility increase with the increase in aniline content in the nanocomposites. The observed enhancement in the antioxidant and haemolysis prevention activity of the PANi nanofibers and the PANi nanofiber reinforced PVA nanocomposites as compared to bulk has been attributed to the reduction in particle size and changes in structural conformation, as evident from TEM, XRD, micro-Raman (μ R) and FTIR spectroscopy. The antioxidant activity of the PANi nanofibers increases as the irradiation fluence is increased. This result conflicts with the fact that after SHI irradiation there is a benzenoid to quinoid transformation in the PANi main chain and as such the antioxidant activity should decrease since the quinoid unit does not have any hydrogen to scavenge DPPH. However, the decrease in size of the PANi nanofibers

after SHI irradiation leads to an increase in the availability of surface reaction sites which offsets the lack of hydrogen due to the benzenoid to quinoid transition. The hemolysis prevention capability and the biocompatibility of the PANi nanofibers are also found to increase with the irradiation fluence. Reduction in particle size and changes in structural conformation, viz., the change in torsion angle of $C_{\text{ring}}-N-C_{\text{ring}}$, are found to be major factors determining the availability of surface states for reaction which greatly affects the antioxidant and haemolysis prevention activity of PANi nanofibers. Polyaniline based nanostructured materials thus provide tremendous potential in the field of biomedical science and technology and can be very important in applications such as synthetic antioxidants nerve cell regeneration, tissue engineering and reinforcements for rubber and polymer products to sustain their stability.

10. Polyaniline nanofibers reinforced PVA nanocomposites have been successfully used as the active layer for the fabrication of modified quartz crystal microbalance sensors for low level detection of free radicals and HCl in solution. The linearity of the free radical and HCl sensors has been found to be excellent with a linear regression coefficient of 0.9685 and 0.9321, respectively. The sensitivity of the free radical sensor has been found to be $149.87 \text{ Hz.ppb}^{-1}$ while for HCl sensor the sensitivity is much lower $\sim 21.4 \text{ Hz.ppm}^{-1}$. Both the sensors have also been found to have very fast response time that decreases with the increase in the analyte concentration. The sensing mechanism of free radical and HCl by the PANi nanofiber reinforced PVA nanocomposites have also been investigated by XRD, FTIR, dielectric spectroscopy and ac conductivity studies. It has been found that PANi nanofiber reinforced PVA nanocomposites lose hydrogen atoms to neutralize the free radical and hence the mass of the quartz crystal decreases with corresponding increase in the frequency shift that can be easily detected. On the other hand, low level detection of HCl by the PANi nanofiber reinforced PVA nanocomposite coated QCM sensors have been ascribed to the increase in the mass and a corresponding decrease in the frequency of the quartz crystal due to the protonation of polyaniline followed by the subsequent

insertion of Cl⁻ counterions in the polymer that has been well supported by XRD and FTIR results. Thus, QCM based sensors modified with PANi nanofiber reinforced PVA nanocomposites can be a very cost effective and sustainable method for the detection of harmful analytes.

8.2. Limitations and Future prospects:

The study carried out in the present thesis clearly shows that conducting polymer based nanostructured materials in general and Polyaniline based nanostructured materials in particular have great potential for multifunctional applications specifically in biomedical and sensor applications. However, a lot of scope still remains in this field to realize the true potential of these materials. Although PANi nanofibers have been found to have excellent antioxidant activity and biocompatibility, *in-vivo* studies of these materials are a must to use these materials in biomedical applications. PANi nanofiber reinforced PVA nanocomposites have been found to be excellent active layers for QCM based sensors. But field studies of these sensors can be done to investigate the interferences from other factors. Since the PANi nanofiber reinforced PVA nanocomposites are highly stable, one can also use them as active sensing material for other type of sensor configurations viz., chemiresistors, SAW sensors, electrochemical sensors etc. SHI irradiation effects on the sensing properties of the PANi nanofiber reinforced PVA nanocomposites have not been studied in the present thesis due to the fact that irradiation of the sensing device which consists of a coating of the nanocomposite over a quartz crystal with imprinted gold electrodes might damage the device. However, fabrication of PANi nanofiber reinforced PVA nanocomposite based sensors in other configurations may be suitable to study the effects of SHI irradiation upon the sensing properties of these materials. In order to enhance the selectivity, one can also investigate this material as a suitable matrix for enzyme immobilization so as to fabricate biosensors since these material have been found to be biocompatible from the studies conducted in the present thesis. Polyaniline based nanostructured materials also promise great potential for applications as actuators, coatings for window panes, packaging of electronic equipments, smart windows etc. that remain to be investigated.

REFERENCES

1. Shirakawa, H., *et al.* Synthesis of Electrically Conducting Organic Polymers: Halogen Derivatives of Polyacetylene, $(\text{CH})_x$, *J. Chem. Soc. Chem. Commun.*, 578-580, 1977.
2. Chiang, C. K., *et al.* Electrical conductivity in doped polyacetylene, *Phys. Rev. Lett.*, **39** (17), 1098-1101, 1977.
3. Chiang, C. K., *et al.* Conducting polymers: Halogen doped polyacetylene, *J. Chem. Phys.*, **69** (11), 5098-5104, 1978.
4. Chiang, C. K., *et al.* Synthesis of highly conducting films of derivatives of polyacetylene, $(\text{CH})_x$, *J Am. Chem. Soc.*, **100** (3), 1013-1015, 1978.
5. Heeger A. J., Nobel Lecture: Semiconducting and metallic polymers: The fourth generation of polymeric materials, *Rev. Mod. Phys.*, **73** (3), 681-700, 2001.
6. MacDiarmid A. G., Nobel Lecture: "Synthetic metals": A novel role for organic polymers, *Rev. Mod. Phys.*, **73** (3), 701-712, 2001.
7. Shirakawa, H., Nobel Lecture: The discovery of polyacetylene film—the dawning of an era of conducting polymers, *Rev. Mod. Phys.*, **73** (3), 713-718, 2001.
8. Wernet, W., *et al.*, A new series of conducting polymers with layered structure: Polypyrrole n-alkylsulfates and n-alkylsulfonates, *Die Makromolekulare Chemie, Rapid Commun.*, **5** (3), 157-164, 1984.
9. Manohar, S. K., *et al.* N-substituted derivatives of polyaniline, *Synth. Met.*, **29** (1), 349-356, 1989.
10. MacDiarmid, A. G., and Epstein, A. J. Polyanilines: a novel class of conducting polymers, *Faraday Discuss. Chem. Soc.*, **88**, 317-332, 1989.
11. Wei, Y., *et al.* Synthesis and electrochemistry of alkyl ring-substituted polyanilines, *J. Phys. Chem.*, **93** (1), 495-499, 1989.

References

12. Epstein, A. J. and MacDiarmid A. G., Novel concepts in electronic polymers: Polyaniline and its derivatives, *Makromolekulare Chemie. Macromolecular Symposia*, **51** (1), 217-234, 1991.
13. Yue, J., *et al.* Effect of sulfonic acid group on polyaniline backbone, *J. Am. Chem. Soc.*, **113** (7), 2665-2671, 1991.
14. Cui, C. X., and Kertesz, M. Two helical conformations of polythiophene, polypyrrole, and their derivatives, *Phys. Rev. B*, **40** (14), 9661-9670, 1989
15. Lee, C., *et al.* The preparation of polypyrrole and polythiophene in the presence of ferrocene derivatives, *Synth. Met.*, **55** (2-3), 1119-1122, 1993.
16. Mattoso, L. H. C., *et al.* Studies on the chemical syntheses and on the characteristics of polyaniline derivatives, *J. Polym. Sci. Part A: Polym. Chem.*, **33** (8), 1227-1234, 1995.
17. MacDiarmid, A. G., Polyaniline and polypyrrole: Where are we headed? *Synth. Met.*, **84** (1-3) 27-34, 1997.
18. Groenendaal, L., *et al.*, Poly(3,4-ethylenedioxythiophene) and Its Derivatives: Past, Present, and Future, *Adv. Mater.*, **12** (7), 481-494, 2000.
19. Kanazawa, K. K., *et al.*, Electrical properties of pyrrole and its copolymers, *Synth. Met.*, **4** (2), 119-130, 1981.
20. Tourillon, G., and Garnier, F., Effect of dopant on the physicochemical and electrical properties of organic conducting polymers, *J. Phys. Chem.*, **87** (13), 2289-2292, 1983.
21. Heeger, A. J., Charge storage and charge transport in conducting polymers: solitons, polarons and bipolarons, *Phil. Trans. R. Soc. Lond. A*, **314**, 17-35, 1985.
22. Satoh, M., *et al.*, Dependences of electrical and mechanical properties of conducting polypyrrole films on conditions of electrochemical polymerization in an aqueous medium, *Synth. Met.*, **14** (4), 289-296, 1986.
23. Waltman, R. J., and Bargon, J., Electrically conducting polymers: a review of the electropolymerization reaction, of the effects of chemical structure on polymer film properties, and of applications towards technology, *Canadian J. Chem.*, **64** (1), 76-95, 1986.

24. Roth, S., Charge transport in conducting polymers, *Adv. Solid State Phys.*, **24**, 119-132, 1984.
25. Patil, A. O., *et al.*, Optical properties of conducting polymers, *Chem. Rev.*, **88** (1), 183-200, 1988.
26. Yoshino, K., *et al.*, Electrical and optical properties of poly(3-alkylthiophene), *Synth. Met.*, **28** (1-2), 349-357, 1989.
27. Huang, W. S., and MacDiarmid, A. G., Optical properties of polyaniline, *Polymer*, **34** (9), 1833-1845, 1993.
28. Yoshino, K., *et al.*, Electrical and optical properties of molecularly doped conducting polymers, *Synth. Met.*, **78** (3), 301-312, 1996.
29. Hourouebie, P., *et al.*, Microwave and optical properties of soluble conducting polymers, *Synth. Met.*, **85** (1-3), 1437-1438, 1997.
30. Friend, R. H., *et al.*, Electroluminescence in conjugated polymers, *Nature*, **397**, 121-128, 1999.
31. Daoust, G., and Leclerc, M., Structure-property relationships in alkoxy-substituted polythiophenes, *Macromolecules*, **24** (2), 455-459, 1991.
32. Kiani, M. S., and Mitchell, G. R., Structure property relationships in electrically conducting copolymers formed from pyrrole and N-methyl pyrrole, *Synth. Met.*, **46** (3), 293-306, 1992.
33. McCullough, R. D., *et al.*, Self-orienting head-to-tail poly(3-alkylthiophenes): new insights on structure-property relationships in conducting polymers, *J. Am. Chem. Soc.*, **115** (11), 4910-4911, 1993.
34. Leclerc, M., *et al.*, Structure-property relationships in polyaniline derivatives, *Synth. Met.*, **55** (2-3), 1527-1532, 1993.
35. Leclerc, M., and Faid, K., Electrical and optical properties of Processable Polythiophene Derivatives: Structure-Property relationships, *Adv. Mater.*, **9** (14), 1087-1094, 1997.
36. Goyette, M. -A., and Leclerc, M., Structure-property relationships in poly(*o*-phenylenediamine) derivatives, *J. Electroanal. Chem.*, **382** (1-2), 17-23, 1995.
37. Winokur, M. J., and Chunwachirasiri, W., Nanoscale structure-property relationships in conjugated polymers: Implications for present and future

References

- device applications, *J. Polym. Sci. Part B: Polym. Phys.*, **41** (21), 2630–2648, 2003.
38. Saxena, V., and Malhotra, B. D., Prospects of conducting polymers in molecular electronics, *Curr. Appl. Phys.*, **3** (2–3), 293–305, 2003.
39. Ryu, K. S., *et al.*, Redox supercapacitor using polyaniline doped with Li salt as electrode, *Solid State Ionics*, **152–153**, 861–866, 2002.
40. Snook, G. A., *et al.*, Conducting-polymer-based supercapacitor devices and electrodes, *J. Power Sources*, **196** (1), 1–12, 2011.
41. Argun, A. A., *et al.*, Multicolored Electrochromism in Polymers: Structures and Devices, *Chem. Mater.*, **16** (23), 4401–4412, 2004.
42. Mortimer, R. J., *et al.*, Electrochromic organic and polymeric materials for display applications, *Displays*, **27** (1), 2–18, 2006.
43. McQuade, D. T., *et al.*, Conjugated Polymer-Based Chemical Sensors, *Chem. Rev.*, **100** (7), 2537–2574, 2000.
44. Baughman, R. H., Conducting polymer artificial muscles, *Synth. Met.*, **78** (3), 339–353, 1996.
45. Smela, E., Conjugated Polymer Actuators for Biomedical Applications, *Adv. Mater.*, **15** (6), 481–494, 2003.
46. Jager, E. W. H., *et al.*, Microfabricating Conjugated Polymer Actuators, *Science*, **290** (5496), 1540–1545, 2000.
47. Joo, J., and Lee, C. Y., High frequency electromagnetic interference shielding response of mixtures and multilayer films based on conducting polymers, *J. Appl. Phys.*, **88** (1), 513–518, 2000.
48. Wang, Y., and Jing, X., Intrinsically conducting polymers for electromagnetic interference shielding, *Polym. Adv. Technol.*, **16** (4), 344–351, 2005.
49. Joo, J., and Epstein, A. J., Electromagnetic radiation shielding by intrinsically conducting polymers, *Appl. Phys. Lett.*, **65** (18), 2278–2280, 1994.
50. Wu, C. -Q., and Sun, X., Nonlinear optical susceptibilities of conducting polymers, *Phys. Rev. B*, **41** (18), 12845–12849, 1990.
51. Mamunya, Ye. P., *et al.*, Electrical and thermal conductivity of polymers filled with metal powders, *Eur. Polym. J.*, **38**, 1887–1897, 2002.

52. Mülhaupt, R., Hermann Staudinger and the Origin of Macromolecular Chemistry, *Angew. Chem. Int. Ed.*, **43** (9), 1054-1063, 2004.
53. Viswanathan, A., Wallace Carothers: More than the inventor of Nylon and Neoprene, *World Patent Information*, **32** (4), 300-305, 2010.
54. James L. K. (ed.), *Nobel laureates in chemistry, 1901-1992*, The American Chemical Society and The Chemical Heritage Foundation, United States of America, 1995.
55. Inzelt, G., *Conducting polymers: A new era in electrochemistry*, Springer-Verlag Berlin Heidelberg, Germany, 2008.
56. R. E. Campbell and Rosahn, P. D., *Yale J. Biol. Med.*, 1950, 527-543.
<http://www.ncbi.nlm.nih.gov/pmc/articles/PMC2599196/pdf/yjbm00344-0062.pdf>
57. <http://business.highbeam.com/industry-reports/chemicals/medicinal-chemicals-botanical-products>.
58. Letheby, H., On the Physiological properties of Nitrobenzole and Aniline, *Proceedings of the Royal Society of London*, **12** (1862-1863), 550-559, 1863.
59. Anft, B., Friedlieb Ferinand Runge: A forgotten chemist of the nineteenth century, *J. Chem. Educ.*, **32** (11), 566-574, 1955.
60. Fritzsche, J., Ueber das Anilin, ein neues Zersetzungsproduct des Indigo, *J. Prakt. Chem.*, **20** (1), 453-459, 1840.
61. Goppelsroeder, F., Studien über die Anwendung der Elektrolyse Zur Darstellung, zur Veränderung und zur Zerstörung der Farbstoffe ohne oder in Gegenwart von vegetabilischen oder animilischen Fasern, *Elektrotechnische Rundschau*, **19**, 1047-1051, 1891.
62. Szarvasy, E., Electrolytic preparation of induline dyes, *J. Chem. Soc.*, **77**, 207-212, 1900.
63. Green, A. G., and Woodhead, A. E., Aniline-black and allied compounds, Part I, *J. Chem. Soc.*, **97**, 2388-2403, 1910.
64. Yasui, T., Electrolytic oxidation of aniline oil, *Bull. Chem. Soc. Japan*, **10** (8), 305-311, 1935.
65. Mohilner, D. M., *et al. J Electrochem Soc*, **84**, 3618, 1962.

References

66. Jozefowicz, M., *et al.*, Conductivité électronique et propriétés chimiques de polyanilines oligomères (Conductivity and chemical properties of oligomeric polyanilines), *J. Polym. Sci. C (Polym. Symp.)*, **16**, 2943-2954, 1967.
67. de Surville, R., *et al.*, Electrochemical chains using protolytic organic semiconductors, *Electrochim Acta*, **13** (6), 1451-1458, 1968.
68. Diaz, A. F. and Logan, J. A., Electroactive polyaniline films, *J. Electroanal. Chem.*, **111** (1), 111-114, 1980.
69. Chiang, J. C., and MacDiarmid, A. G., 'Polyaniline': Protonic acid doping of the emeraldine form to the metallic regime, *Synth. Met.*, **13** (1-3), 193-205, 1986.
70. Bolto, B. A., *et al.* Electronic Conduction in Polymers III: Electronic Properties of Polypyrrole. *Aust. J. Chem.*, **16**, 1090-1103, 1963.
71. Diaz, A. F. Electrochemical Preparation and Characterization of Conducting Polymers. *Chemica Scripta*, **17**, 145-148, 1981.
72. Diaz, A. F. and Hall, B. Mechanical-Properties of Electrochemically Prepared Polypyrrole Films, *IBM J. Res. Dev.*, **27**, 342-347, 1983.
73. Gommans, H. H. P. *Charge transport and interface phenomena in semiconducting polymers*, Universiteitsdrukkerij, Eindhoven University of Technology, Eindhoven, 2005.
74. MacDiarmid, A. G., The concept of 'doping' of conducting polymers: the role of reduction potentials, *Phil. Trans. R. Soc. Lond. A*, **314**, 3-15, 1985.
75. Kanatzidis, M. G., Polymeric Electrical Conductors, *Chem. Eng. News*, **68**, 36-54, 1990.
76. Nigrey, P. J., *et al.*, Electrochemistry of polyacetylene, (CH)_x: electrochemical doping of (CH)_x films to the metallic state, *J. Chem. Soc. Chem. Commun.* **1979**, 594-595, 1979.
77. MacInnes, D., *et al.*, Organic batteries: reversible n- and p- type electrochemical doping of polyacetylene, (CH)_x, *J. Chem. Soc. Chem. Commun.* **1981**, 317-319, 1981.
78. Ziemelis, K. E., *et al.*, Optical spectroscopy of field-induced charge in poly(3-hexyl thienylene) metal-insulator-semiconductor structures: Evidence for polarons, *Phys. Rev. Lett.* **66** (17), 2231-2234, 1991.

79. Genoud, F., *et al.*, ESR study of electrochemical doping in the conducting polymer polypyrrole, *Phys. Rev. Lett.* **55** (1), 118–121, 1985.
80. Cao, Y., *et al.*, Counter-ion induced processibility of conducting polyaniline and of conducting polyblends of polyaniline in bulk polymers, *Synth. Met.*, **48** (1), 91–97, 1992.
81. Ahonen, H. J., *et al.*, *n*- and *p*- Doped Poly(3,4-ethylenedioxythiophene): Two Electronically Conducting States of the Polymer, *Macromolecules*, **33** (18), 6787–6793, 2000.
82. de Leeuw, D. M., *et al.*, Stability of *n*-type doped conducting polymers and consequences for polymeric microelectronic devices, *Synth. Met.*, **87** (1), 53–59, 1997.
83. Heeger, A. J., *et al.*, Solitons in conducting polymers, *Rev. Mod. Phys.*, **60** (3), 781–850, 1988.
84. Burroughes J. H., *et al.*, New semiconductor device physics in polymer diodes and transistors, *Nature*, **335**, 137–141, 1988.
85. Burroughes J. H., *et al.*, Light-emitting diodes based on conjugated polymers, *Nature*, **347**, 539–541, 1990.
86. MacDiarmid, A. G., Synthetic metals: a novel role for organic polymers, *Synth. Met.*, **125** (1), 11–22, 2001.
87. Tong, J. S., *et al.*, Ion-beam-induced electrical conductivity in plasma-polymerized aniline film, *Synth. Met.*, **68** (2), 125–131, 1995.
88. Wang, C. S., *et al.*, *Mechanical and Electrical properties of Heat-Treated Ladder Polymer Fiber*, in *Mat. Res. Soc. Symp. Proc.*, **247: Electrical, Optical and Magnetic properties of Organic Solid State Materials**, Chiang, L. Y. *et al.*, eds., Materials Research Society, Pittsburg, Pennsylvania, USA, 1992, p-747.
89. Heeger, A. J., The Critical Regime of the Metal-Insulator Transition in Conducting Polymers: Experimental Studies, *Physica Scripta*, T102, 30–35, 2002.
90. Anderson, P. W., Absence of Diffusion in Certain Random Lattices, *Phys. Rev.* **109** (5), 1492–1505, 1958.
91. Anderson, P. W., Model for the Electronic Structure of Amorphous Semiconductors, *Phys. Rev. Lett.*, **34** (15), 953–955, 1975.

References

92. McMillan, W. L., Scaling theory of the metal-insulator transition in amorphous materials, *Phys. Rev. B*, **24** (5), 2739–2743, 1981.
93. Menon, R., *et al.*, *Metal-Insulator Transition in Doped Conducting Polymers*, in *Handbook of Conducting Polymers*, 2nd ed., Skotheim, T. A., *et al.*, eds., Marcel Dekker, Inc. New York, 1998, p. 27.
94. Kohlman, R. S., *et al.*, *Insulator-Metal Transition mid Inhomogeneous Metallic State in Conducting Polymers*, in *Handbook of Conducting Polymers*, 2nd ed., Skotheim, T. A., *et al.*, eds., Marcel Dekker, Inc. New York, 1998, p. 85.
95. Kohlman, R. S., *et al.*, Drude Metallic Response of Polypyrrole, *Phys. Rev. Lett.*, **74** (5), 773–776, 1995.
96. Kohlman, R. S., *et al.*, Crossover in Electrical Frequency Response through an Insulator-Metal Transition, *Phys. Rev. Lett.*, **77** (13), 2766–2769, 1996.
97. Epstein, A. J., *Conducting Polymers: Electrical Conductivity*, in *Physical Properties of Polymer Handbook*, 2nd ed., Mark, J. E., ed., Springer Science & Business Media, LLC, 233 Spring Street, New York, NY 10013, USA, 2007, pp-725-755.
98. Chen, J., *et al.*, *Molecular Electronic Devices*, in *Encyclopedia of Nanoscience and Nanotechnology*, Nalwa, H. S., *et al.*, , American Scientific Publishers, USA, 2004, Vol. 5, pp. 633-662.
99. Kertesz, M., *et al.*, Conjugated Polymers and Aromaticity, *Chem. Rev.*, **105** (10), 3448–3481, 2005.
100. Girlando, A., *et al.*, Electron-phonon coupling in conjugated polymers: Reference force field and transferable coupling constants for polyacetylene, *J. Chem. Phys.*, **98** (9), 7459-7465, 1993.
101. Bredas, J. L., *et al.*, The role of mobile organic radicals and ions (solitons, polarons and bipolarons) in the transport properties of doped conjugated polymers, *Synth. Met.*, **9** (2), 265–274, 1984.
102. Bredas, J. L., and Street, G. B., Polarons, bipolarons, and solitons in conducting polymers, *Acc. Chem. Res.*, **18** (10), 309–315, 1985.
103. Mizes, H. A., and Conwell, E. M., Stability of polarons in conducting polymers, *Phys. Rev. Lett.* **70** (10), 1505–1508, 1993.

104. Scott, J. C., *et al.*, Electron-spin-resonance studies of pyrrole polymers: Evidence for bipolarons, *Phys. Rev. B*, **28** (4), 2140–2145, 1983.
105. Bredas, J. L., Bipolarons in Doped Conjugated Polymers: A Critical Comparison Between Theoretical Results and Experimental Data, *Mol. Cryst. Liq. Cryst.*, **118** (1), 49-56, 1985.
106. Kaufman, J. H., *et al.*, Gravimetric Electrochemical Voltage Spectroscopy: In Situ Mass Measurements during Electrochemical Doping of the Conducting Polymer Polypyrrole, *Phys. Rev. Lett.*, **53** (26), 2461–2464, 1984.
107. Albery, W. J., *et al.*, Spectroscopic and electrochemical studies of charge transfer in modified electrodes, *Faraday Discuss. Chem. Soc.*, **88**, 247-259, 1989.
108. Kivelson, S., and Heeger, A. J., Intrinsic conductivity of conducting polymers, *Synth. Met.*, **22** (4), 371–384, 1988.
109. Huang, H., and Pickup, P. G., A Donor–Acceptor Conducting Copolymer with a Very Low Band Gap and High Intrinsic Conductivity, *Chem. Mater.*, **10** (8), 2212–2216, 1998.
110. Kivelson, S., Electron hopping in a soliton band: Conduction in lightly doped $(\text{CH})_x$, *Phys. Rev. B*, **25** (6), 3798–3821, 1982.
111. Chance, R. R., *et al.*, Bipolaron transport in doped conjugated polymers, *Phys. Rev. B*, **29** (8), 4491–4495, 1984.
112. Mott, N. F., and Davis, E. A., *Electronic processes in non-crystalline materials*, Clarendon, Oxford, UK, 1979.
113. Zuppiroli, L., *et al.*, Hopping in disordered conducting polymers, *Phys. Rev. B*, **50** (8), 5196–5203, 1994.
114. Sheng, P., *et al.*, Hopping Conductivity in Granular Metals, *Phys. Rev. Lett.* **31** (1), 44–47, 1973.
115. Huang, J., *et al.*, Mechanochemical Route to the Conducting Polymer Polyaniline, *Macromolecules*, **38** (2), 317-321, 2005.
116. Masters, J. G., Polyaniline: Allowed oxidation states, *Synth. Met.*, **41** (1–2), 715–718, 1991.

References

117. Huang, W. S., *et al.*, Polyaniline, a novel conducting polymer. Morphology and chemistry of its oxidation and reduction in aqueous electrolytes, *J. Chem. Soc., Faraday Trans. 1*, **82**, 2385-2400, 1986.
118. Hagiwara, T., *et al.*, Structural analysis of deprotonated polyaniline by solid-state ^{13}C N.M.R, *Synth. Met.*, **26** (2), 195-201, 1988.
119. MacDiarmid *et al.*, Polyaniline: Synthesis and properties of pernigraniline base, *Synth. Met.*, **41** (1-2), 621-626, 1991.
120. Bredas, J. L., *et al.*, Highly conducting polyparaphenylene, polypyrrole, and polythiophene chains: an ab initio study of the geometry and electronic-structure modifications upon doping, *Phys. Rev. B*, **29** (12), 6761-6773, 1984.
121. Stafstrom, S., *et al.*, Polaron lattice in highly conducting polyaniline: theoretical and optical studies, *Phys. Rev. Lett.*, **59** (13), 1464-1467, 1987.
122. MacDiarmid, A. G., *et al.*, Polyaniline: a new concept in conducting polymers, *Synth. Met.*, **18** (1-3), 285-290, 1987.
123. MacDiarmid, A. G., and Heeger, A. J., Organic metals and semiconductors: The chemistry of polyacetylene, $(\text{CH})_x$, and its derivatives, *Synth. Met.*, **1** (2), 101-118, 1980.
124. Ginder, J. M., *et al.*, Insulator-to-metal transition in polyaniline, *Solid State Commun.*, **63** (2), 97-101, 1987.
125. Epstein A. J., *et al.*, Insulator-to-metal transition in polyaniline, *Synth. Met.*, **18** (1-3), 303-309, 1987.
126. Wallace, G. G., *et al.*, Conductive Electroactive Polymers-Intelligent Materials System 2nd ed. Ch. 5, Boca Raton London New York Washington, D.C., 2003
127. Wan, M., and Yang, J., Mechanism of proton doping in polyaniline, *J. Appl. Polym. Sci.*, **55** (3), 399-405, 1995.
128. Wan, M., Absorption spectra of thin film of polyaniline, *J. Polym. Sci. Part A: Polymer Chemistry*, **30** (4), 543-549, 1992.
129. Wan, M., The influence of polymerization method and temperature on the absorption spectra and morphology of polyaniline, *Synth. Met.*, **31** (1), 51-59, 1989.

130. Pouget, J. P., *et al.*, X-ray structure of polyaniline, *Macromolecules*, , **24** (3), 779-789, 1991.
131. Yue, J., and Epstein A. J., Synthesis of self-doped conducting polyaniline, *J. Am. Chem. Soc.*, **112** (7), 2800-2801, 1990.
132. Yue, J., *et al.*, Effect of sulfonic acid group on polyaniline backbone, *J. Am. Chem. Soc.*, **113** (7), 2665-2671, 1991.
133. Yue, J., *et al.*, Comparison of different synthetic routes for sulphonation of polyaniline, *Polymer*, **33** (20), 4410-4418, 1992.
134. Chan, H. S. O., *et al.*, Characterization of chemically and electrochemically prepared polyanilines in inverse microemulsions, *J. Mater. Chem.*, **3** (11), 1109-1115, 1993.
135. Cameron, R. E., and Clement, S. K., Preparation of conductive polyaniline having controlled molecular weight, *US Patent No. 5008041*, Apr 16, 1991.
136. Osaheni, J. A., *et al.*, Nonlinear optical properties of polyanilines and derivatives, *J. Phys. Chem.*, **96** (7), 2830-2836, 1992.
137. Weinberger, B. R., *et al.*, Magnetic susceptibility of doped polyacetylene, *Phys. Rev. B*, **20** (1), 223-230, 1979.
138. Wan, M., *Conducting Polymers with Micro or Nanometer Structure*, Tsinghua University Press, Ch. 2, Beijing and Springer-Verlag GmbH Berlin Heidelberg, 2008.
139. Fehse, K., *et al.*, Combination of a polyaniline anode and doped charge transport layers for high-efficiency organic light emitting diodes, *J. Appl. Phys.* **101**, 124509 (4 pp), 2007.
140. Irimia-Vladu, M., *et al.*, Vacuum-Processed Polyaniline-C₆₀ Organic Field Effect Transistors, *Adv. Mater.*, **20** (20), 3887-3892, 2008.
141. Wang, X. -F., *et al.*, Hybrid electrochemical supercapacitors based on polyaniline and activated carbon electrodes, *Acta, Phys. -Chim. Sin.*, **21** (3), 261-266, 2005.
142. Dhawan, S. K., *et al.*, Electromagnetic shielding behaviour of conducting polyaniline composites, *Sci. Tech. Adv. Mater.*, **4** (2), 105-113, 2003.
143. Geim A. K., and Novoselov K. S., The rise of grapheme, *Nat. Mater.*, **6**, 183-191, 2007.

References

144. Deepshikha and Basu, T., A Review on Synthesis and Characterization of Nanostructured Conducting Polymers (NSCP) and Application in Biosensors, *Anal. Lett.*, **44**, 1126–1171, 2011.
145. Wallace, G. G., and Innis, P. C., Inherently Conducting Polymer Nanostructures, *J. Nanosci. Nanotech.*, **2** (5), 441–451, 2002.
146. Wan, M., A Template-Free Method Towards Conducting Polymer Nanostructures, *Adv. Mater.*, **20** (15), 2926–2932, 2008.
147. Jang, J., and Yoon, H., Formation Mechanism of Conducting Polypyrrole Nanotubes in Reverse Micelle Systems, *Langmuir*, **21** (24), 11484–11489, 2005.
148. Tran, H. D., *et al.*, One-Dimensional Conducting Polymer Nanostructures: Bulk Synthesis and Applications, *Adv. Mater.*, **21** (14–15), 1487–1499, 2009.
149. Zhang, X., and Manohar, S. K., Bulk Synthesis of Polypyrrole Nanofibers by a Seeding Approach, *J. Am. Chem. Soc.*, **126** (40), 12714–12715, 2004.
150. Jang, J., *et al.*, Fabrication of polyaniline nanoparticles using microemulsion polymerization, *Macromol. Res.*, **15** (2), 154–159, 2007.
151. Jang, J., and Yoon, H., Facile fabrication of polypyrrole nanotubes using reverse microemulsion polymerization, *Chem. Commun.*, 720–721, 2003.
152. Zussman, E., *et al.*, Formation of nanofiber crossbars in electrospinning, *Appl. Phys. Lett.* **82** (6), 973–975, 2003.
153. Jackowska, K., *et al.*, Hard template synthesis of conducting polymers: a route to achieve nanostructures, *J. Solid State Electrochem.*, **12** (4), 437–443, 2008.
154. Zhang, X., *et al.*, Controllable Synthesis of Conducting Polypyrrole Nanostructures, *J. Phys. Chem. B*, **110** (3), 1158–1165, 2006.
155. Huang, J., *et al.*, Polyaniline Nanofibers: Facile Synthesis and Chemical Sensors, *J. Am. Chem. Soc.*, **125** (2), 314–315, 2003.
156. Jang, J., *et al.*, Chemical Sensors Based on Highly Conductive Poly(3,4-ethylenedioxythiophene) Nanorods, *Adv. Mater.*, **17** (13), 1616–1620, 2005.
157. Xia, L., *et al.*, Conducting polymer nanostructures and their application in biosensors, *J. Colloid and Interface Sci.*, **341** (1), 1–11, 2010.

158. Tseng, R. J., *et al.*, Polyaniline Nanofiber/Gold Nanoparticle Nonvolatile Memory, *Nano Lett.*, **5** (6), 1077–1080, 2005.
159. Huang, J., and Kaner, R. B., Flash welding of conducting polymer nanofibers, *Nature Mater.*, **3**, 783 – 786, 2004.
160. Concrete, From Wikipedia- The free encyclopedia <http://en.wikipedia.org/wiki/Concrete>.
161. Sarmah, S., *Development of conducting polymer based nanocomposites for multifunctional applications and swift heavy ion irradiation studies*, Ph.D. Thesis, Tezpur University, Assam, India, 2011.
162. Richardson, T., *Composites: A design guide*, Industrial Press Inc. 200, New York, 1987.
163. Sharma, S. C., *Composite Materials*, Narosa Publishing House, New Delhi, India, 2000.
164. Murugan, A. V., *Synthesis and characterization of Organo-inorganic conducting Polymer based nanocomposites for Electrochemical power sources*, Ph.D. Thesis, National Chemical Laboratory, Pune, India, 2004.
165. Gangopadhyay, R., and De, A., Conducting Polymer Nanocomposites: A Brief Overview, *Chem. Mater.*, **12** (3), 608–622, 2000.
166. Malinauskas, A., *et al.*, Conducting polymer-based nanostructured materials: electrochemical aspects, *Nanotechnology*, **16** (10), R51-R62, 2005.
167. Baibarac, M., and Gómez-Romero, P., Nanocomposites Based on Conducting Polymers and Carbon Nanotubes: From Fancy Materials to Functional Applications, *J. Nanosci. Nanotech.*, **6** (2), 289-302, 2006.
168. Godovsky, D. Y., *et al.*, Preparation of nanocomposites of polyaniline and inorganic semiconductors, *J. Mater. Chem.*, **11** (10), 2465-2469, 2001.
169. Jurczyk, M. U., *et al.*, Polyaniline-based nanocomposite materials for hydrogen storage, *Int. J. Hydrogen Energy*, **32** (8), 1010–1015, 2007.
170. Bidan, G., *et al.*, New nanocomposites based on “tailor dressed” magnetic particles in a polypyrrole matrix, *Adv. Mater.*, **6** (2), 152-155, 1994.
171. Han, M. G., and Armes, S. P., Synthesis of Poly (3,4- ethylenedioxy thiophene)/Silica Colloidal Nanocomposites, *Langmuir*, **19** (11), 4523–4526, 2003.

References

172. Lu, X., *et al.*, Preparation and characterization of inorganic/organic hybrid nanocomposites based on Au nanoparticles and polypyrrole, *Mater. Lett.*, **60** (23), 2851–2854, 2006.
173. Wei, Y., *et al.*, One-Step UV-Induced Synthesis of Polypyrrole/Ag Nanocomposites at the Water/Ionic Liquid Interface, *Nanoscale Res. Lett.*, **5** (2), 433–437, 2010.
174. Armes, S. P., *et al.*, Conducting polymer-colloidal silica composites, *Polymer*, **32** (13), 2325–2330, 1991.
175. Maeda, S., *et al.*, Surface Characterization of Conducting Polymer-Silica Nanocomposites by X-ray Photoelectron Spectroscopy, *Langmuir*, **11** (6), 1899–1904, 1995.
176. Maeda, S., and Armes, S. P., Preparation and Characterization of Polypyrrole-Tin(IV) Oxide Nanocomposite Colloids, *Chem. Mater.*, **7** (1), 171–178, 1995.
177. Partch, R., *et al.*, Conducting polymer composites: I. Surface-induced polymerization of pyrrole on iron(III) and cerium(IV) oxide particles, *J. Colloid Interface Sci.*, **144** (1), 27–35, 1991.
178. Huang, C. -L., *et al.*, Coating of Uniform Inorganic Particles with Polymers: II. Polyaniline on Copper Oxide, *J. Colloid Interface Sci.*, **170** (1), 275–283, 1995.
179. Suri, K., *et al.*, Nanocomposite of polypyrrole-iron oxide by simultaneous gelation and polymerization, *Synth. Met.*, **126** (2–3), 137–142, 2002.
180. Suri, K., *et al.*, Phase change induced by polypyrrole in iron-oxide polypyrrole nanocomposite, *Bull. Mater. Sci.*, **24** (6), 563–567, 2001.
181. Suri, K., *et al.*, Thermal transition behaviour of iron oxide-polypyrrole nanocomposites, *Curr. Appl. Phys.*, **3** (2–3), 209–213, 2003.
182. Sharma, R., *et al.*, Magnetic properties of polypyrrole-coated iron oxide nanoparticles, *J. Phys. D: Appl. Phys.*, **38**, 3354–3359, 2005.
183. Biswas, M., *et al.*, Water dispersible conducting nanocomposites of poly(N-vinylcarbazole), polypyrrole and polyaniline with nanodimensional manganese (IV) oxide, *Synth. Met.*, **105** (2), 99–105, 1999.

184. Gan, L. M., *et al.*, Preparation of conducting polyaniline-coated barium sulfate nanoparticles in inverse microemulsions, *Mater. Chem. Phys.*, **40** (2), 94-98, 1995.
185. Maity, A., and Biswas, M., Water-dispersible conducting nanocomposites of binary polymer systems. I. Poly(N-vinylcarbazole)-polyaniline- Al_2O_3 nanocomposite system, *J. Appl. Polym. Sci.*, **94** (2), 803-811, 2004.
186. Bhattacharya, A., *et al.*, A new conducting nanocomposite – PPy-zirconium (IV) oxide, *Mater. Res. Bull.*, **31** (5), 527-530, 1996.
187. Baraton, M. -I., *et al.*, Investigation of the TiO_2 /PPV nanocomposite for gas sensing applications, *Nanotechnology* **9**, 356-359, 1998.
188. Murugan, A. V. *et al.*, Synthesis and characterization of a new organo-inorganic poly(3,4-ethylene dioxythiophene) PEDOT/ V_2O_5 nanocomposite by intercalation, *J. Mater. Chem.*, **11** (10), 2470-2475, 2001.
189. Kaushik, A., *et al.*, Hybrid Cross-Linked Polyaniline- WO_3 Nanocomposite Thin Film for NO_x Gas Sensing, *J. Nanosci. Nanotech.*, **9** (3), 1792-1796, 2009.
190. Parvatikar, N., *et al.*, Electrical and humidity sensing properties of polyaniline/ WO_3 composites, *Sens. Actuators B: Chem.*, **114** (2), 599-603, 2006.
191. Miomandre, F., *et al.*, Silica-Polypyrrole Core-Shell Nanocomposites as Active Materials for Dielectrophoretic Displays, *J. Nanosci. Nanotech.*, **8** (9), 4353-4359, 2008.
192. Liu, X., *et al.*, Controllable fabrication of SiO_2 /polypyrrole core-shell particles and polypyrrole hollow spheres, *Mater. Chem. Phys.*, **109** (1), 5-9, 2008.
193. Stejskal, J., *et al.*, Polyaniline Dispersions. 6. Stabilization by Colloidal Silica Particles, *Macromolecules*, **29** (21), 6814-6819, 1996.
194. Marinakos, S. M., *et al.*, Template Synthesis of One-Dimensional Au, Au-Poly(pyrrole), and Poly(pyrrole) Nanoparticle Arrays, *Chem. Mater.*, **10** (5), 1214-1219, 1998.
195. Deng, J., *et al.*, Magnetic and conducting Fe_3O_4 -cross-linked polyaniline nanoparticles with core-shell structure, *Polymer*, **43** (8), 2179-2184, 2002.

References

196. Hao, L. -Y., *et al.*, Sandwich Fe₂O₃@SiO₂@PPy ellipsoidal spheres and four types of hollow capsules by hematite olivary particles, *J. Mater. Chem.*, **14**, 2929–2934, 2004.
197. Xu, J., *et al.*, Solution Route to Inorganic Nanobelt-Conducting Organic Polymer Core-Shell Nanocomposites, *J. Polym. Sci.: Part A: Polym. Chem.*, **43** (13), 2892–2900, 2005.
198. Fujii, S., *et al.*, One-step synthesis of polypyrrole-coated silver nanocomposite particles and their application as a coloured particulate emulsifier, *J. Mater. Chem.*, **17**, 3777–3779, 2007.
199. Li, X., *et al.*, Electromagnetic Functionalized and Core-Shell Micro/Nanostructured Polypyrrole Composites, *J. Phys. Chem. B*, **110** (30), 14623–14626, 2006.
200. Yang, X., *et al.*, Synthesis of novel sunflower-like silica/polypyrrole nanocomposites via self-assembly polymerization, *Polymer*, **47** (1), 441–447, 2006.
201. Feng, X., *et al.*, Ag/Polypyrrole Core-Shell Nanostructures: Interface Polymerization, Characterization, and Modification by Gold Nanoparticles, *J. Phys. Chem. C*, **111** (24), 8463–8468, 2007.
202. Zhu, C. -L., *et al.*, Synthesis of core/shell metal oxide/polyaniline nanocomposites and hollow polyaniline capsules, *Nanotechnology*, **18** (27), 275604 (6pp), 2007.
203. Chuang, F. -Yi., and Yang, S. -M., Cerium dioxide/polyaniline core-shell nanocomposites, *J. Colloid Interface Sci.*, **320** (1), 194–201, 2008.
204. Kobayashi, Y., *et al.*, Synthesis of metallic copper nanoparticles coated with polypyrrole, *Colloid Polym. Sci.*, **287** (7), 877–880, 2009.
205. Ruiz-Hitzky, E., Conducting Polymers Intercalated in Layered Solids, *Adv. Mater.*, **5** (5), 334–340, 1993.
206. Jeevanandam, P., and Vasudevan, S., Conductivity of a Confined Polymer Electrolyte: Lithium–Polypropylene Glycol Intercalated in Layered CdPS₃, *J. Phys. Chem. B*, **102** (24), 4753–4758, 1998.

207. Arun, N., *et al.*, Orientation and Motion of Interlamellar Water: An Infrared and NMR Investigation of Water in the Galleries of Layered $\text{Cd}_{0.75}\text{PS}_3\text{K}_{0.5}(\text{H}_2\text{O})_y$, *J. Am. Chem. Soc.*, **122** (25), 6028–6038, 2000.
208. Kojima, Y., *et al.*, Mechanical properties of nylon 6-clay hybrid, *J. Mater. Res.*, **8**, 1185–1189, 1993.
209. Wang, M., *et al.*, Poly(vinylidene fluoride-hexafluoropropylene)/organo-montmorillonite clays nanocomposite lithium polymer electrolytes, *Electrochim. Acta*, **49** (21), 3595–3602, 2004.
210. Nanocomposite Electrolytes with Fumed Silica and Hectorite Clay Networks: Passive versus Active Fillers, *Adv. Func. Mater.*, **13** (9), 710–717, 2003.
211. Wu, C. -G., *et al.*, Redox Intercalative Polymerization of Aniline in V_2O_5 Xerogel. The Postintercalative Intralamellar Polymer Growth in Polyaniline/Metal Oxide Nanocomposites is Facilitated by Molecular Oxygen, *Chem. Mater.*, **8** (8), 1992–2004, 1996.
212. Kerr, T. A., *et al.*, Concurrent Polymerization and Insertion of Aniline in Molybdenum Trioxide: Formation and Properties of a $[\text{Poly}(\text{aniline})]_{0.24}\text{MoO}_3$ Nanocomposite, *Chem. Mater.*, **8** (8), 2005–2015, 1996.
213. Shouji, E., and Buttry, D. A., New Organic–Inorganic Nanocomposite Materials for Energy Storage Applications, *Langmuir*, **15** (3), 669–673, 1999.
214. Lira-Cantú, M., and Gómez-Romero, P., The Organic-Inorganic Polyaniline/ V_2O_5 System. Application as a High-Capacity Hybrid Cathode for Rechargeable Lithium Batteries, *J. Electrochem. Soc.*, **146** (6), 2029–2033, 1999.
215. Murugan, A. V., Electrochemical properties of microwave irradiated synthesis of poly(3,4-ethylenedioxythiophene)/ V_2O_5 nanocomposites as cathode materials for rechargeable lithium batteries, *Electrochim. Acta*, **50** (24), 4627–4636, 2005.
216. Murugan, A. V., *et al.*, Electrochemical studies of poly (3,4-ethylenedioxythiophene) PEDOT/ VS_2 nanocomposite as a cathode

References

- material for rechargeable lithium batteries, *Electrochem. Commun.*, **7** (2), 213-218, 2005.
217. Murugan A.V., Synthesis and Characterization of organo-inorganic Poly (3, 4-Ethylenedioxy thiophene) PEDOT/ MoS₂ Nanocomposite via *in situ* oxidative polymerization, *J. Mater. Res.*, **21**(1), 112 - 118, 2006.
218. Jang, J., and Oh, J. H., Fabrication of a highly transparent conductive thin film from Polypyrrole/Poly(methyl methacrylate) Core/Shell Nanospheres, *Adv. Func. Mater.*, **15** (3), 494-502, 2005.
219. Bhadra, J., and Sarkar, D., Field effect transistor fabricated from polyaniline-polyvinyl alcohol nanocomposite, *Indian J. Phys.*, **84** (6), 693-697, 2010.
220. Deka, M., *et al.*, Effect of dedoped (insulating) polyaniline nanofibers on the ionic transport and interfacial stability of poly(vinylidene fluoride-hexafluoropropylene) based composite polymer electrolyte membranes, *J. Memb. Sci.*, **327** (1-2), 188-194, 2009.
221. Cortés, P., *et al.*, Effects of nanofiber treatments on the properties of vapor-grown carbon fiber reinforced polymer composites, *J. Appl. Polym. Sci.*, **89** (9), 2527-2534, 2003.
222. Andrews, R., and Weisenberger, M.C., Carbon nanotube polymer composites, *Curr. Opinion in Solid State and Mater. Sci.*, **8** (1), 31-37, 2004.
223. Zeng, J., *et al.*, Processing and properties of poly(methyl methacrylate)/carbon nano fiber composites, *Composites Part B: Engg.*, **35** (2), 173-178, 2004.
224. Lee, H., *et al.*, Characterization of carbon nanotube/nanofiber-reinforced polymer composites using an instrumented indentation technique, *Composites Part B: Engineering*, **38** (1), 58-65, 2007
225. Khanna, V., and Bakshi, B. R., Carbon Nanofiber Polymer Composites: Evaluation of Life Cycle Energy Use, *Environ. Sci. Technol.*, **43** (6), 2078-2084, 2009.
226. Williams, J. S., Materials modification with ion beams, *Rep. Prog. Phys.*, **49** (1986) 491-587.

227. Szymonski, M., et al., Ion-beam-induced surface modification and nanostructuring of A_{III}B_V semiconductors, *Progress in Surface Science*, **74** (1-8), 331-341, 2003.
228. Hussain, A. M. P., et al., Effects of 160 MeV Ni¹²⁺ ion irradiation on HCl doped polyaniline electrode, *J. Phys. D: Appl. Phys.*, **39** (4), 750-755, 2006.
229. Srivastava, A., et al., Study of Swift Heavy Ion Modified Conducting Polymer Composites for Application as Gas Sensor, *Sensors*, **6** (4), 262-269, 2006.
230. Davenas, J., et al., Role of the modifications induced by ion beam irradiation in the optical and conducting properties of polyimide, *Nucl. Instrum. Meth. B*, **32** (1-4), 136-141, 1988.
231. Bouffard, S., et al., Basic phenomena induced by swift heavy ions in polymers, *Nucl. Instrum. Meth. B*, **105** (1-4), 1-4, 1995.
232. Lee, E. H., Ion-beam modification of polymeric materials - fundamental principles and applications, *Nucl. Instrum. Meth. B*, **151** (1-4), 29-41, 1999.
233. Toulemonde, M., et al., Track formation and fabrication of nanostructures with MeV-ion beams, *Nucl. Instrum. Meth. B*, **216**, 1-8, 2004.
234. Foulds, N. C., and Lowe, C. R., Enzyme entrapment in electrically conducting polymers. Immobilisation of glucose oxidase in polypyrrole and its application in amperometric glucose sensors, *J. Chem. Soc. Faraday Trans. 1*, **82** (4), 1259-1264, 1986.
235. Umana, M., and Waller, J., Protein-modified electrodes. The glucose oxidase/polypyrrole system, *Anal. Chem.*, **58** (14), 2979-2983, 1986.
236. Wong, J.Y., et al., Electrically conducting polymers can noninvasively control the shape and growth of mammalian cells, *Proc. Natl. Acad. Sci. USA*, **91**, 3201-3204, 1994.
237. Shi, G., et al., A novel electrically conductive and biodegradable composite made of polypyrrole nanoparticles and polylactide, *Biomaterials*, **25** (13), 2477-2488, 2004.
238. Baughman, R. H., Conducting polymer artificial muscles, *Synth. Met.*, **78** (3), 339-353, 1996.

239. Pernaut, J. -M., and Reynolds, J. R., Use of Conducting Electroactive Polymers for Drug Delivery and Sensing of Bioactive Molecules. A Redox Chemistry Approach, *J. Phys. Chem. B*, **104** (17), 4080–4090, 2000.
240. Kane-Maguire, L. A. P., and Wallace, G. G., Communicating with the building blocks of life using organic electronic conductors, *Synth. Met.*, **119** (1-3), 39-42, 2001.
241. Kamalesh, S., *et al.*, Biocompatibility of electroactive polymers in tissues, *J. Biomed. Mater. Res.*, **52** (3), 467-478, 2000.
242. Han, G., and Shi, G., Conducting polymer electrochemical actuator made of high-strength three-layered composite films of polythiophene and polypyrrole, *Sens. Actuators B: Chem.*, **99** (2-3), 525–531, 2004.
243. Roemer, M., *et al.*, Microactuators based on conducting polymers, *Anal. Bioanal. Chem.*, **373** (8), 754-757, 2002.
244. Hutchison, A. S., *et al.*, Development of polypyrrole-based electromechanical actuators, *Synth. Met.*, **113** (1-2), 121–127, 2000.
245. Kulinsky, L., *et al.*, System-based approach for an advanced drug delivery platform. *Proc SPIE Int Soc Opt Eng*, (Smart Structures and Integrated Systems; 61730M/1-61730M/6), **6173**, 2006, doi:10.1117/12.658890.
246. Mazzoldi, A., and De Rossi, D., Conductive-polymer-based structures for a steerable catheter. *Proc SPIE Int Soc Opt Eng*, (Smart Structures and Materials 2000: Electroactive Polymer Actuators and Devices (EAPAD)), **3987**, 273–80, 2000, doi:10.1117/12.387786.
247. Smela, E., and Gadegaard, N., Surprising volume change in PPy(DBS): an atomic force microscopy study, *Adv. Mater.*, **11** (11), 953–957, 1999.
248. Low, L.M., *et al.*, Microactuators toward microvalves for responsive controlled drug delivery, *Sens. Actuators B: Chem.*, **67** (1-2), 149–60, 2000.
249. Guimard, N. K., *et al.*, Conducting polymers in biomedical engineering, *Prog. Polym. Sci.*, **32** (8-9), 876–921, 2007.
250. Wadhwa, R., *et al.*, Electrochemically controlled release of dexamethasone from conducting polymer polypyrrole coated electrode, *J. Cont. Rel.*, **110** (3), 531–541, 2006.

251. Abidian, M. R., *et al.*, Conducting polymer nanotubes for controlled drug release, *Adv. Mater.*, **18** (4), 405–409, 2006.
252. Li, Y., *et al.*, Controlled release of heparin from polypyrrole–poly(vinyl alcohol) assembly by electrical stimulation, *J. Biomed. Mater. Res. A*, **73A** (2), 171–81, 2005.
253. Li, M., *et al.*, Electrospinning polyaniline-contained gelatin nanofibers for tissue engineering applications, *Biomaterials*, **27** (13), 2705–2715, 2006
254. Green, R. A., *et al.*, Conducting polymers for neural interfaces: Challenges in developing an effective long-term implant, *Biomaterials*, **29** (24–25), 3393–3399, 2008.
255. Cui, X., *et al.*, In vivo studies of polypyrrole/peptide coated neural probes, *Biomaterials*, **24** (5), 777–787, 2003.
256. Gizdavic-Nikolaidis, M., *et al.*, Conducting polymers as free radical scavengers. *Synth. Met.*, **140** (2-3), 225–232, 2004.
257. Hsu, C. F., *et al.*, Scavenging of DPPH free radicals by polypyrrole powders of varying levels of overoxidation and/or reduction, *Synth. Met.*, **158** (21–24), 946–952, 2008.
258. Meixner, H., and Lampe, U., Metal oxide sensors, *Sens. Actuators B: Chem.*, **33** (1-3), 198–202, 1996.
259. Bai, H., and Shi, G., Gas Sensors Based on Conducting Polymers, *Sensors* **7** (3), 267–307, 2007.
260. Nylander, C.; *et al.*, An ammonia detector based on a conducting polymer. *Proc. of the Int. Meet. on Chem. Sensors*, Fukuoka, Japan, 203–207, 1983.
261. Koul, S., and Chandra, R., Mixed dopant conducting polyaniline reusable blend for the detection of aqueous ammonia, *Sens. Actuators B: Chem.*, **104** (1), 57–67, 2005.
262. Dixit, V., *et al.*, Carbon monoxide sensitivity of vacuum deposited polyaniline semiconducting thin film, *Sens. Actuators B: Chem.*, **104** (1), 90–93, 2005.
263. McGovern, S. T., *et al.*, Micro-humidity sensors based on a processable polyaniline blend, *Sens. Actuators B: Chem.*, **107** (2), 657–665, 2005.

References

264. Jurevičiūtė, I., *et al.*, Polyaniline-modified electrode as an amperometric ascorbate sensor, *Sens. Actuators B: Chem.*, **107** (2), 716–721, 2005.
265. Zucolotto, V., *et al.*, Nanoscale processing of polyaniline and phthalocyanines for sensing applications, *Sens. Actuators B: Chem.*, **113** (2), 809–815, 2006.
266. Itoh, T., *et al.*, Preparation of layered organic–inorganic nanohybrid thin films of molybdenum trioxide with polyaniline derivatives for aldehyde gases sensors of several tens ppb level, *Sens. Actuators B: Chem.*, **128** (2), 512–520, 2008.
267. Bendikov, T. A., *et al.*, Development and environmental application of a nitrate selective microsensor based on doped polypyrrole films, *Sens. Actuators B: Chem.*, **106** (2), 512–517, 2005.
268. Ameer, Q., and Adeloju, S. B., Polypyrrole-based electronic noses for environmental and industrial analysis, *Sens. Actuators B: Chem.*, **106** (2), 541–552, 2005.
269. Nicolas-Debarnot, D., and Poncin-Epaillard, F., Polyaniline as a new sensitive layer for gas sensors, *Anal. Chim. Acta*, **475** (1-2), 1–15, 2003.
270. Sabah, S., *et al.*, Solid-State valproate ion selective sensor based on conducting polypyrrole films for determination of valproate in pharmaceutical preparations, *Sens. Actuators B: Chem.*, **114** (1), 489–496, 2006.
271. Clark, L.C., and Lyons, C., Electrode systems for continuous monitoring in cardiovascular surgery. *Ann. NY Acad. Sci.*, **102**, 29–45, 1962.
272. Gerard, M., *et al.*, Application of conducting polymers to biosensors, *Biosensors and Bioelectronics*, **17** (5), 345–359, 2002.
273. Sadik, O. and Wallace, G. G., Pulsed amperometric detection of proteins using antibody containing conducting polymers. *Anal. Chim. Acta*, **279** (2), 209–212, 1993.
274. Karyakin, A. A., *et al.*, Processable polyaniline as an advanced potentiometric pH transducers. *Anal. Chem.*, **71** (13), 2534–2540. 1999.

275. Schuhmann, W., *et al.*, Comparison of native and chemically stabilized enzymes in amperometric enzyme electrodes, *Sens. and Actuators. B: Chem.*, **7** (1-3), 393–398, 1992.
276. Evtugyn, G. A., *et al.*, Sensitivity and selectivity of electrochemical enzyme sensors for inhibitor determination, *Talanta*, **46** (4), 465–484, 1998.
277. Trojanowicz, M., *et al.*, Enzyme entrapped polypyrrole modified electrode for flow-injection determination of glucose. *Biosensors and Bioelectronics*, **5** (2), 149–156, 1990.
278. Fortier, G., *et al.*, Optimization of a polypyrrole glucose oxidase sensor. *Biosensors and Bioelectronics*, **5** (6), 473–490, 1990.
279. Zhu, M., *et al.*, Fabrication of polypyrrole–glucose oxidase biosensor based on multilayered interdigitated ultramicroelectrode array with contained trenches, *Sens. Actuators B: Chem.*, **B110** (2), 382–389, 2005.
280. Liu, C., *et al.*, Covalent immobilization of glucose oxidase on film prepared by electrochemical copolymerization of thiophene-3-acetic acid and 3-methylthiophene for glucose sensing. *Eur. Polym. J.*, **43** (8), 3264–3276, 2007.
281. Ramanathan, K., *et al.*, Covalent immobilization of glucose oxidase to poly(o-amino benzoic acid) for application to glucose biosensor. *J. Appl. Polym. Sci.*, **78** (3), 662–667, 2000.
282. Singh, S., *et al.*, Cholesterol biosensor based on cholesterol esterase, cholesterol oxidase and peroxidase immobilized onto conducting polyaniline films, *Sens. Actuators B: Chem.*, **115** (1), 534–541, 2006.
283. Kumar, A., *et al.*, Immobilization of cholesterol oxidase and potassium ferricyanide on dodecylbenzene sulfonate ion doped polypyrrole film, *J. Appl. Polym. Sci.*, **82** (14), 3486–3491, 2001.
284. Pandey, P. C., and Mishra, A. P., Conducting polymer-coated enzyme microsensor for urea. *Analyst*, **113** (2), 329–331, 1988.
285. Unwin, P.R., and Bard, A. J., Ultramicroelectrode voltammetry in a drop of solution: a new approach to the measurement of adsorption isotherms at solid–liquid interface, *Anal. Chem.*, **64** (2), 113–119, 1992.
286. Lu, W., *et al.*, Pulsed electrochemical detection of proteins using conducting polymer sensors. *Anal. Chim. Acta*, **315** (1-2), 27–32, 1995.

References

287. Bartlett, P. N., Whitaker, R. G., Strategies for the development of amperometric enzyme electrodes. *Biosensors*, **3** (6), 359-379, 1988.
288. Lavrik, N.V. *et al.*, Composite polyaniline/calixarene Langmuir- Blodgett films for gas sensing, *Nanotechnology*, **7** (4), 315-319, 1996.
289. Virji, S. *et al.*, Polyaniline nanofiber gas sensors: Examination of response mechanisms. *Nano Lett.*, **4** (3), 491-496, 2004.
290. Santhanam, K. S. V., *et al.*, A chemical sensor for chloromethanes using a nanocomposite of multiwalled carbon nanotubes with poly(3-methylthiophene), *Sens. Actuators B: Chem.*, **106** (2), 766-771. 2005.
291. Agbor, N. E., *et al.*, Polyaniline Thin-Films for Gas-Sensing. *Sens. Actuators B: Chem.*, **28** (3), 173-179, 1995.
292. Liu, D. M.; *et al.*, A new carbon monoxide sensor using a polypyrrole film grown on an interdigital-capacitor substrate. *Sens. Actuators B: Chem.*, **41** (1-3), 203-206, 1997.
293. Mabeck, J.T., and Malliaras, G. G., Chemical and biological sensors based on organic thin-film transistors. *Anal. Bioanal. Chem.*, **384** (2), 343-353, 2006.
294. Chen, H., *et al.*, Chemical effects in organic electronics. *Chem. Mater.*, **16** (23), 4728-4735, 2004.
295. Van, C. N., and Potje-Kamloth, K., The influence of thickness and preparation temperature of doped polypyrrole films on the electrical and chemical sensing properties of polypyrrole/gold Schottky barrier diodes. *J. Phys. D: Appl. Phys.* 2000, **33** (18), 2230-2238.
296. Brédas, J. L., *et al.*, Polarons and bipolarons in polypyrrole: Evolution of the band structure and optical spectrum upon doping, *Phys. Rev. B*, **30** (2), 1023-1025, 1984.
297. Nicho, M.E.; *et al.*, Polyaniline composite coatings interrogated by a nulling optical-transmittance bridge for sensing low concentrations of ammonia gas. *Sens. Actuators B: Chem.*, **76** (1-3), 18-24, 2001.
298. Hu, H.; *et al.*, Adsorption kinetics of optochemical NH₃ gas sensing with semiconductor polyaniline films. *Sens. Actuators B: Chem.*, **82** (1), 14-23, 2002.

299. Elizalde-Torres, J.; *et al.*, NO₂-induced optical absorbance changes in semiconductor polyaniline thin films. *Sens. Actuators B: Chem.*, **98** (2-3), 218-226, 2004.
300. Yuan, J. M., and El-Sherif, M. A., Fiber-optic chemical sensor using polyaniline as modified cladding material, *IEEE Sens. J.*, **3** (1), 5-12, 2003.
301. Cao, W. Q., and Duan, Y. X., Optical fiber-based evanescent ammonia sensor, *Sens. Actuators B: Chem.*, **110** (2), 252-259, 2005.
302. Bansal, L., and El-Sherif, M., Intrinsic optical-fiber sensor for nerve agent sensing, *IEEE Sens. J.*, **5** (4), 648-655, 2005.
303. Agbor, N. E., *et al.*, An optical gas sensor based on polyaniline Langmuir-Blodgett films, *Sens. Actuators B: Chem.*, **41** (1-3), 137-141, 1997.
304. Sih, B.C., *et al.*, Surface-plasmon resonance sensing of alcohol with electrodeposited polythiophene and gold nanoparticle-oligothiophene films, *J. Appl. Phys.*, **98** (11), 114314 (1-4), 2005.
305. Do, J. S., and Chang, W. B., Amperometric nitrogen dioxide gas sensor: preparation of PAN/Au/SPE and sensing behaviour, *Sens. Actuators B: Chem.*, **72** (1-2), 101-107, 2001.
306. Diab, N. and Schuhmann, W. Electropolymerized manganese porphyrin/polypyrrole films as catalytic surfaces for the oxidation of nitric oxide, *Electrochim. Acta*, **47** (1-2), 265-273, 2001.
307. Liu, Y. C., *et al.*, Characteristics of Pd/Nafion oxygen sensor modified with polypyrrole by chemical vapor deposition, *J. Solid State Electrochem.*, **6** (5), 351-356, 2002.
308. Chang, S. M., *et al.*, The principle and applications of piezoelectric crystal sensors, *Mater. Sci. Eng. C-Biomimetic Supramol. Syst.*, **12** (1-2), 111-123, 2000.
309. Penza, M.; *et al.*, Gas sensing properties of Langmuir-Blodgett polypyrrole film investigated by surface acoustic waves, *IEEE Trans. Ultrason. Ferroelectr. Freq. Control*, **45** (5), 1125-1132, 1998.
310. Penza, M., *et al.*, Monitoring of NH₃ gas by LB polypyrrole-based SAW sensor, *Sens. Actuators B: Chem.*, **47** (1-3), 218-224, 1998.
311. Milella, E., and Penza, M., SAW gas detection using Langmuir-Blodgett polypyrrole films, *Thin Solid Films*, **329**, 694-697, 1998.

References

312. O'Sullivan, C. K., and Guilbault, G. G., Commercial quartz crystal microbalances – theory and applications, *Biosensors & Bioelectronics*, **14** (8-9), 663-670, 1999.
313. Wang, X., *et al.*, Nanofibrous polyethyleneimine membranes as sensitive coatings for quartz crystal microbalance-based formaldehyde sensors, *Sens. Actuators B: Chem.*, **144** (1), 11-17, 2010.
314. Matsuguchi, M., and Kadowaki, Y., Poly(acrylamide) derivatives for QCM-based HCl gas sensor applications, *Sens. Actuators B: Chem.*, **130** (2), 842-847, 2008.
315. Su, P. -G., and Chang, Y. -P., Low-humidity sensor based on a quartz-crystal microbalance coated with polypyrrole/Ag/TiO₂ nanoparticles composite thin films, *Sens. Actuators B: Chem.*, **129** (2), 915-920, 2008.
316. Si, P., *et al.*, Polymer coated quartz crystal microbalance sensors for detection of volatile organic compounds in gas mixtures, *Anal. Chim. Acta* **597** (2), 223-230, 2007.
317. Wang, X., *et al.*, A highly sensitive humidity sensor based on a nanofibrous membrane coated quartz crystal microbalance, *Nanotechnology*, **21** (5), 055502 (6pp), 2010.
318. Sai, V. V. R., *et al.*, Immobilization of Antibodies on Polyaniline Films and Its Application in a Piezoelectric Immunosensor, *Anal. Chem.* **78** (24), 8368-8373, 2006.
319. Zheng, J., *et al.*, Polyaniline-TiO₂ nano-composite-based trimethylamine QCM sensor and its thermal behavior studies, *Sens. Actuators B: Chem.*, **133** (2), 374-380, 2008.
320. Jaruwongrungrsee, K., *et al.*, Quartz Crystal Microbalance humidity sensor using electrospun PANI micro/nano dots, *Proc. of the 7th IEEE International Conference on Nanotechnology, IEEE-NANO 2007*, 316-319, 2007. (doi: 10.1109/NANO.2007.4601198).
321. Yan, Y., *et al.*, Polyaniline-Modified Quartz Crystal Microbalance Sensor for Detection of Formic Acid Gas, *Water, Air, & Soil Pollution*, 2011, doi: 10.1007/s11270-011-0943-1.

322. Syritski, V., *et al.*, Environmental QCM sensors coated with polypyrrole, *Synth. Met.*, **102** (1-3), 1326-1327, 1999.
323. Cao, Y., *et al.*, Influence of chemical polymerization conditions on the properties of polyaniline, *Polymer*, **30** (12), 2305-2311, 1989.
324. Huang, J., and Kaner, R. B., A General Chemical Route to Polyaniline Nanofibers, *J. Am. Chem. Soc.*, **126** (3), 851-855, 2004.
325. Zhang, X., *et al.*, Synthesis of Polyaniline Nanofibers by "Nanofiber Seeding", *J. Am. Chem. Soc.*, **126** (14), 4502-4503, 2004.
326. Li, W., and Wang, H. -L., Oligomer-Assisted Synthesis of Chiral Polyaniline Nanofibers, *J. Am. Chem. Soc.*, **126** (8), 2278-2279, 2004.
327. Chiou, N. -R., and Epstein, A. J., Polyaniline Nanofibers Prepared by Dilute Polymerization, *Adv. Mater.*, **17** (13), 1679-1683, 2005.
328. Tran, H. D., *et al.*, Toward an Understanding of the Formation of Conducting Polymer Nanofibers, *ACS Nano*, **2** (9), 1841-1848, 2008.
329. Huang, J., Synthesis and applications of conducting polymer polyaniline nanofibers, *Pure Appl. Chem.*, **78** (1), 15-27, 2006.
330. Huang, J., and Kaner, R. B., Nanofiber Formation in the Chemical Polymerization of Aniline: A Mechanistic Study, *Angew. Chem. Int. Ed.*, **43** (43), 5817-5821, 2004.
331. Chiou, N, -R., *et al.*, Growth and alignment of polyaniline nanofibres with superhydrophobic, superhydrophilic and other properties, *Nature Nanotechnology*, **2**, 354 - 357, 2007.
332. Surwade, S. P., *et al.*, Origin of Bulk Nanoscale Morphology in Conducting Polymers, *Macromolecules* **42**, 1792-1795, 2009.
333. Su, W. P., *et al.*, Solitons in polyacetylene, *Phys. Rev. Lett.*, **42** (25), 1698-1701, 1979.
334. Park, Y. -W., *et al.*, Electrical transport in doped polyacetylene, *J. Chem. Phys.*, **73** (2), 946-957, 1980.
335. Epstein, A. J., *et al.*, Role of Solitons in Nearly Metallic Polyacetylene, *Phys. Rev. Lett.*, **50** (23), 1866-1869, 1983.
336. Frankevich, E. L., *et al.*, On the Conductivity Mechanism of Weakly Doped Polyacetylene, *Physica Status Solidi (b)*, **132** (1), 283-294, 1985.

References

337. Townsend, P. D., and Friend, R. H, Photoexcitation in Durham-route polyacetylene: Self-localization and charge transport, *Phys. Rev. B*, **40** (5), 3112-3120, 1989.
338. Etemad, S., *et al.*, Electronic Excitations in Polyacetylene, *Mol. Cryst. Liq. Cryst.*, **77** (1-4), 43-63, 1981.
339. Kivelson, S., Electron hopping conduction in the soliton model of polyacetylene, *Phys. Rev. Lett.*, **46** (20), 1344-1348, 1981.
340. Efros, A. L., and Shklovskii, B. I., Coulomb gap and low temperature conductivity of disordered systems, *J. Phys. C: Solid State Phys.*, **8**, L49-L51, 1975.
341. Baughman, R. H., and Shacklette, L. W., Conjugation length dependent transport in conducting polymers from a resistor network model, *J. Chem. Phys.*, **90** (12), 7492-7504, 1989.
342. Epstein, A. J., *et al.*, Inhomogeneous disorder and the modified Drude metallic state of conducting polymers, *Synth. Met.*, **65** (2-3), 149-157, 1994.
343. Kaiser, A. B., Electronic transport properties of conducting polymers and carbon nanotubes, *Rep. Prog. Phys.*, **64** (1), 1-49, 2001.
344. Li, Q., *et al.*, Granular-rod model for electronic conduction in polyaniline, *Phys. Rev. B*, **47** (4), 1840-1845, 1993.
345. Deutscher, G., *et al.*, $T^{3/7}$ Hopping conductivity in a class of disordered systems, *Europhys. Lett.*, **4** (5), 577-582, 1987.
346. Philipp, A., *et al.*, Non-ohmic behaviour of iodine-doped polyacetylene, *Solid State Commun.*, **43** (11), 857-861, 1982.
347. Pocharsi, J., and Roth, S., Conductivity of doped polyacetylene with mechanically-modified morphology, *Synth. Met.*, **30** (1), 109-114, 1989.
348. Sheng, P., and Klafter, J., Hopping conductivity in granular disordered systems, *Phys. Rev. B.*, **27** (4), 2583-2586, 1983.
349. Ehinger, K., and Roth, S., Non-solitonic conductivity in polyacetylene, *Philos. Mag. B*, **53** (4), 301-320, 1986.
350. Yoon, C. O., *et al.*, Hopping transport in doped conducting polymers in the insulating regime near the metal-insulator boundary: polypyrrole, polyaniline and polyalkylthiophenes, *Synth. Met.*, **75** (3), 229-239, 1995.

351. Holland, E. R., Conductivity studies of polyaniline doped with CSA, *J. Phys.: Condens. Matter*, **8** (17), 2991-3002, 1996.
352. Pouget, J. P., *et al.*, Recent structural investigations of metallic polymers, *Synth. Met.*, **65** (2-3), 131-140, 1994.
353. Joo, J., *et al.*, Microwave dielectric response of mesoscopic metallic regions and the intrinsic metallic state of polyaniline, *Phys. Rev. B*, **49** (4), 2977-2980, 1994.
354. Yau, S. -T., *et al.*, Tunneling spectroscopy and spectroscopic imaging of granular metallicity of polyaniline, *Appl. Phys. Lett.*, **74** (5), 667-669, 1999.
355. Wang, Z. H., *et al.*, Transport and EPR studies of polyaniline: A quasi-one-dimensional conductor with three-dimensional "metallic" states, *Phys. Rev. B*, **45** (8), 4190-4202, 1992.
356. Raghunathan, A., *et al.*, ¹³C CP/MAS NMR, XRD, d.c. and a.c. electrical conductivity of aromatic acids doped polyaniline, *Synth. Met.*, **81** (1), 39-47, 1996.
357. Sixou, B., *et al.*, Effect of aging induced disorder on transport properties of PANI-CSA, *Synth. Met.*, **84** (1-3), 703-704, 1997.
358. Subramaniam, C. K., *et al.*, Conductivity and thermopower of blends of polyaniline with insulating polymers (PETG and PMMA), *Solid State Commun.*, **97** (3), 235-238, 1996.
359. Cai, Z., and Martin C. R., Electronically conductive polymer fibers with mesoscopic diameters show enhanced electronic conductivities, *J. Am. Chem. Soc.*, **111** (11), 4138-4139, 1989.
360. Parthasarathy, R. V., and Martin, C. R., Template-Synthesized Polyaniline Microtubules, *Chem. Mater.*, **6** (10), 1627-1632, 1994.
361. Duchet, J., *et al.*, Chemical synthesis of polypyrrole: structure-properties relationship, *Synth. Met.*, **98** (2), 113-122, 1998.
362. Yoon, C. O., *et al.*, Electrical transport in conductive blends of polyaniline in poly(methyl methacrylate), *Synth. Met.*, **63** (1), 47-52, 1994.
363. Long, Y., *et al.*, Electrical conductivity of a single conducting polyaniline nanotube, *Appl. Phys. Lett.*, **83** (9), 1863-1865, 2003.

References

364. Long, Y., *et al.*, Electronic transport in single polyaniline and polypyrrole microtubes, *Phys. Rev. B*, 71 (16), 165412 (7pp), 2005.
365. Jonscher, A. K., *Dielectric Relaxation in Solids*, Dielectric Press, London, 1983.
366. Elliott, S. R., AC conduction in amorphous chalcogenide and pnictide semiconductors, *Adv. Phys.* 36 (2), 135-218, 1987.
367. Pollak, M., and Geballe, T. H., Low-Frequency Conductivity Due to Hopping Processes in Silicon, *Phys. Rev.*, 122 (6), 1742-1753, 1961.
368. Miller, A., and Abrahams, E., Impurity Conduction at Low Concentrations, *Phys. Rev.*, 120 (3), 745-755, 1960.
369. Austin, I. G., and Mott, N. F., Polarons in crystalline and non-crystalline materials, *Adv. Phys.*, 18 (71), 41-102, 1969.
370. Emin, D., and Holstein, T., Studies of small polaron motion IV. Adiabatic theory of the Hall effect, *Ann. Phys.*, 53 (3), 439-520, 1969.
371. Long, A. R., Frequency dependent loss in amorphous semiconductors. *Adv. Phys.*, 31 (5), 553-637, 1982.
372. Fritzsche, H., *Electronic and structural properties of amorphous semiconductors*, Le Comber, P. G. *et al.*, eds, Academic Press, New York, 1973.
373. Anderson, P. W., *et al.*, Anomalous low temperature thermal properties of glasses and spin glasses, *Philos. Mag.*, 25 (1), 1-9, 1972.
374. Phillips, W. A., Tunneling states in amorphous solids, *J. Low. Temp. Phys.*, 7 (3-4), 351-360, 1972.
375. Pollak, M., and Pike, G. E., AC conductivity of glasses, *Phys. Rev. Lett.*, 28 (22), 1449-1451, 1972.
376. Migahed, M. D., *et al.*, Electric modulus and AC conductivity studies in conducting PPy composite films at low temperature, *J. Phys. Chem. Solids*, 65 (6), 1121-1125, 2004.
377. Gangopadhyay, R., *et al.*, Transport properties of polypyrrole-ferric oxide conducting nanocomposites, *J. Appl. Phys.*, 87 (5), 2363-2371, 2000.
378. Barrau, S., *et al.*, DC and AC Conductivity of Carbon Nanotubes-Polyepoxy Composites, *Macromolecules*, 36 (14), 5187-5194, 2003.

379. Gilroy, K. S., and Phillips, W. A., An asymmetric double-well potential model for structural relaxation processes in amorphous materials, *Philos. Mag. B*, **43** (5), 735-746, 1981.
380. Palmer, R. G., *et al.*, Models of Hierarchically Constrained Dynamics for Glassy Relaxation, *Phys. Rev. Lett.*, **53** (10), 958-961, 1984.
381. Anderson, P. W., Model for the Electronic Structure of Amorphous Semiconductors, *Phys. Rev. Lett.*, **34** (15), 953-955, 1975.
382. Pollak, M., On the frequency dependence of conductivity in amorphous solids, *Philos. Mag.*, **23**, 519-543, 1971.
383. Efros, A. L., On the theory of a.c. conduction in amorphous semiconductors and chalcogenide glasses, *Philos. Mag. B*, **43** (5), 829-838, 1981.
384. Scher, H., and Lax, M., Stochastic Transport in a Disordered Solid. II. Impurity Conduction, *Phys. Rev. B*, **7** (10), 4502-4519, 1973.
385. Movaghar, B., *et al.*, The Hall mobility in hopping conduction, *J. Phys. C: Solid State Phys.*, **14**, 5127-5137, 1981.
386. Time domain dielectric spectroscopy: An advanced measuring system, *Rev. Sci. Instrum.*, **67** (9), 3208-3216, 1996.
387. Jonscher, A. K., The 'universal' dielectric response, *Nature*, **267**, 673 - 679, 1977.
388. Jonscher, A. K., Dielectric relaxation in solids, *J. Phys. D: Appl. Phys.*, **32** (14), R57-R70, 1999.
389. Hill, R. M., and Dissado, L. A., Debye and non-Debye relaxation, *J. Phys. C: Solid State Phys.*, **18**, 3829-3836, 1985.
390. Cole K. S., and Cole R. S., Dispersion and absorption in dielectrics: I. alternating current characteristics, *J. Chem. Phys.*, **9** (4), 1484-1490, 1941.
391. Davidson, D. W., and Cole, R. H., Dielectric relaxation in glycerol, propylene glycol and N-propanol, *J. Chem. Phys.*, **19** (12), 341-351, 1941.
392. Havriliak, S., and Negami, S., A Complex plane representation of dielectric and mechanical relaxation processes in some polymers, *Polymer*, **8**, 161-210, 1967.
393. Fink, D., and Chadderton, L. T., Ion-Solid Interaction: Status and Perspectives, *Braz. J. Phys.*, **35** (3B), 735-740, 2005.

394. Norman, A., Thermal Spike Effects in Heavy-Ion Tracks, *Rad. Res. Supp.*, **7**, 33-37 (1967).
395. Lea, D. E., *Actions of Radiations on Living Cells*, 2nd ed., Cambridge Univ. Press, London, 1955.
396. Seitz, F., On the disordering of solids by action of fast massive particles, *Discuss. Faraday Soc.*, **5**, 271-282, 1949.
397. Dienes, G. J., and Vineyard, G. H., *Radiation Effects in Solids*, Interscience, New York, 1957.
398. Ingalls, R. B., *et al.*, Thermal - Spike Model of Low LET Radiolysis: Temperature Dependence of Reactions Induced by Radiolysis in Liquid Toluene, *J. Chem. Phys.*, **41** (3), 837-840, (1964).
399. Seitz, F., On the Theory of the Bubble Chamber, *Phys. Fluids*, **1** (1), 2-13, 1958.
400. Fleischer, R. L., *et al.*, Tracks of Charged Particles in Solids, *Science*, **149** (3682), 383-393, 1965.
401. Fleischer, R. L., *et al.*, Ion Explosion Spike Mechanism for Formation of Charged - Particle Tracks in Solids, *J. Appl. Phys.*, **36** (11), 3645-3652, 1965.
402. Bringa, E. M., and Johnson, R. E., Coulomb Explosion and Thermal Spikes, *Phys. Rev. Lett.*, **88** (16), 165501 (4 pp), 2002.
403. Anilkumar, P., and Jayakannan, M., Divergent Nanostructures from Identical Ingredients: Unique Amphiphilic Micelle Template for Polyaniline Nanofibers, Tubes, Rods, and Spheres, *Macromolecules*, **41** (20), 7706-7715, 2008.
404. Kim, B. -J., *et al.*, Preparation of Polyaniline Nanoparticles in Micellar Solutions as Polymerization Medium, *Langmuir*, **16** (14), 5841-5845, 2000.
405. Kumar, S., *et al.*, Synthesis of 1-dimensional polyaniline nanofibers by reverse microemulsion, *Colloid & Polym. Sci.*, **287** (9), 1107-1110, 2009.
406. Singh, J. P., *et al.*, Swift heavy ion-based materials science research at NSC, *Nucl. Instrum. Meth. B*, **156** (1-4), 206-211, 1999.
407. Biersack, J. P., and Haggmark, L., A Monte Carlo computer program for the transport of energetic ions in amorphous targets, *Nucl. Instrum. and Meth.*, **174** (1-2), 257-269, 1980.

408. Ruska, E., The development of the electron microscopy and of electron microscopy, Nobel Lecture, December 8, 1986, http://nobelprize.org/nobel_prizes/physics/laureates/1986/ruska-lecture.pdf.
409. Kruger, D. H., *et al.*, Helmut Ruska and the visualisation of viruses, *The Lancet*, **355** (9216), 1713–1717, 2000.
410. Kaufmann, E. N., *Characterization of Materials*, John Wiley & Sons, Inc., Hoboken, New Jersey, 2003.
411. Hussain, A. M. P., *Swift heavy ion irradiation effects on electrodeposited conducting polymer based electrodes for redox supercapacitors*, Ph.D. Thesis, Tezpur University, Assam, India, 2006.
412. Warren, B. E., and Averbach, B. L., The effect of Cold-Work distortion on X-ray patterns, *J. Appl. Phys.*, **21** (3), 595-599, 1950.
413. Warren, B. E., and Averbach, B. L., The separation of Cold-Work distortion and Particle size broadening in X-ray patterns, *J. Appl. Phys.*, **23** (4), 497, 1952.
414. de Keijer, Th. H., *et al.*, Use of the Voigt Function in a Single-Line Method for the Analysis of X-ray Diffraction Line Broadening, *J. Appl. Cryst.*, **15** (3), 308-314, 1982.
415. Delhez, R., *et al.*, *Accuracy in Powder Diffraction*, Natl Bur. Stand. Spec. Publ. 567, Block, S., *et al.*, eds, pp. 213-253, 1980.
416. Cook, A., Hendrik Christoffel van de Hulst Ridder in de Orde van Nederlandse Leeuw, *Biograp. Mem. Fellows of the Royal Society*, **47**, 466-479, 2001.
417. Langford, J. I., A rapid method for analysing the breadths of diffraction and spectral lines using the Voigt function, *J. Appl. Cryst.*, **11** (1), 10-14, 1978.
418. Nandi, R. K., and Sen Gupta, S. P., The analysis of X-ray diffraction profiles from imperfect solids by an application of convolution relations, *J. Appl. Cryst.*, **11** (1), 6-9, 1978.

419. Yoshino, K., *et al.*, Absorption cross section measurements of carbon dioxide in the wavelength region 118.7 - 175.5 nm and the temperature dependence, *J. Quant. Spectrosc. Radiat. Transfer*, **55**, 53-60, 1996.
420. Graebner, J. E., Simple correlation between optical absorption and thermal conductivity of CVD diamond, *Diamond and Related Materials*, **4** (10), 1196-1199, 1995.
421. Bhattacharyya, D., *et al.*, Bandgap and optical transitions in thin films from reflectance measurements, *Vacuum*, **43** (4), 313-316, 1992.
422. Capaccioli, S., *et al.*, Dielectric response analysis of a conducting polymer dominated by the hopping charge transport, *J. Phys.: Condens. Matter*, **10** (25), 5595-5617, 1998.
423. Papathanassiou, A. N., *et al.*, Hopping charge transport mechanisms in conducting polypyrrole: Studying the thermal degradation of the dielectric relaxation, *Appl. Phys. Lett.*, **87** (15), 154107 (1-3), 2005.
424. Tsangaris, G. M., *et al.*, Electric modulus and interfacial polarization in composite polymeric systems, *J. Mater. Sci.*, **33** (8), 2027-2037, 1998.
425. Hong, X., *et al.*, Free-Volume Hole Properties of Gas-Exposed Polycarbonate Studied by Positron Annihilation Lifetime Spectroscopy, *Macromol.*, **29** (24), 7859-7864, 1996.
426. Positron annihilation spectroscopy for chemical analysis: A novel probe for microstructural analysis of polymers, *Microchem. J.*, **42** (1), 72-102, 72-102.
427. Serpen, A., *et al.*, A New Procedure To Measure the Antioxidant Activity of Insoluble Food Components, *J. Agric. Food Chem.*, **55** (19), 7676-7681, 2007.
428. Miki, M., *et al.*, Free-radical chains oxidation of rat red blood cells by molecular oxygen and its inhibition by α -tocopherol, *Arch. Biochem. Biophys.*, **258** (2), 373-380, 1987.
429. Adla, A., *et al.*, Investigation of heavy ion tracks in polymers by transmission electron microscopy, *Nucl. Instrum. Meth. B*, **185** (1-4), 210-215, 2001.
430. Wang, Z. C., *et al.*, The S_e sensitivity of metals under swift-heavy-ion irradiation: a transient thermal process, *J. Phys.: Condens. Matter*, **6** (34), 6733-6750, 1994.

431. Toulemonde, M., *et al.*, Track formation in SiO₂ quartz and the thermal-spike mechanism, *Phys. Rev. B*, **49** (18), 12457–12463, 1994.
432. G. Szenes, Analysis of the evolution of latent tracks in polyvinylidene fluoride, *Nucl. Instr. and Meth. B*, **155** (3), 301-307, 1999.
433. Sun, Y., *et al.*, The damage process induced by swift heavy ion in polycarbonate, *Nucl. Instrum. Meth. B*, **212**, 211-215, 2003.
434. Tagowska, M., *et al.*, Polyaniline nanotubes—anion effect on conformation and oxidation state of polyaniline studied by Raman spectroscopy, *Synth. Met.*, **142** (1-3), 223-229, 2004.
435. Colombari, Ph., *et al.*, Vibrational Study of Short-Range Order and Structure of Polyaniline Bases and Salts, *Macromolecules*, **32** (9), 3080-3092, 1999.
436. Cochet, M., *et al.*, Theoretical and experimental vibrational study of polyaniline in base forms: non-planar analysis. Part I, *J. Raman Spectrosc.*, **31** (11), 1029-1039, 2000.
437. Cochet, M., *et al.*, Theoretical and experimental vibrational study of emeraldine in salt form. Part II, *J. Raman Spectrosc.*, **31** (12), 1041-1049, 2000.
438. Bazzouzi, E. A., SERS Spectra of Polythiophene in Doped and Undoped States, *J. Phys. Chem.*, **99** (17), 6628–6634, 1995.
439. Ehrenfreund, E., *et al.*, Amplitude and phase modes in trans-polyacetylene: Resonant Raman scattering and induced infrared activity, *Phys. Rev. B*, **36** (3), 1535–1553, 1987.
440. Del Zoppo, M., *et al.*, A relationship between Raman and infrared spectra: the case of push–pull molecules, *Chem. Phys. Lett.*, **287** (1-2), 100-110, 1998.
441. Fahrenbruch, A. L., and Bude, R. H., *Fundamentals of Solar Cells*, Academic, New York, p. 49, 1983.
442. Urbach, F., The Long-Wavelength Edge of Photographic Sensitivity and of the Electronic Absorption of Solids, *Phys. Rev.*, **92** (5), 1324-1324, 1953.
443. Migahed, M. D., and Zidan, H. M., Influence of UV-irradiation on the structure and optical properties of polycarbonate films, *Curr. Appl. Phys.*, **6** (1), 91–96, 2006.

References

444. Sreekumar, R., *et al.*, Enhancement of band gap and photoconductivity in gamma indium selenide due to swift heavy ion irradiation, *J. Appl. Phys.*, **103** (2), 023709 (9pp), 2008.
445. Kim, T. -Y., *et al.*, Quantum confinement effect of silicon nanocrystals *in situ* grown in silicon nitride films, *Appl. Phys. Lett.*, **85** (22), 5355-5357, 2004.
446. Chen, S. A., and Liao, C. S., Conductivity relaxation and chain motions in conjugated conducting polymers: neutral poly(3-alkylthiophenes), *Macromolecules*, **26** (11), 2810-2816, 1993.
447. Javadi, H. H. S., *et al.*, Charge transport in the "emeraldine" form of polyaniline, *Synth. Met.* **29** (1), 409-416, 1989.
448. Zuo, F., *et al.*, ac conductivity of emeraldine polymer, *Phys. Rev. B*, **39** (6), 3570-3578, 1989.
449. Papathanassiou, A. N., *et al.*, Localized and long-distance charge hopping in fresh and thermally aged conductive copolymers of polypyrrole and polyaniline studied by combined TSDC and dc conductivity, *J. Phys. Chem. Solids*, **63** (9), 1771-1778, 2002.
450. Bengoechea, M. R., *et al.*, Effects of confinement on the phase separation in emeraldine base polyaniline cast from 1-methyl-2-pyrrolidinone studied via dielectric spectroscopy, *J. Phys.: Condens. Matter*, **14** (45), 11769-11778, 2002.
451. Afzal, A. B., *et al.*, Investigation of Structural and Electrical Properties of Polyaniline/Gold Nanocomposites, *J. Phys. Chem. C*, **113** (40), 17560-17565, 2009.
452. Lee, H. T., *et al.*, Conductivity Relaxation of 1-Methyl-2-pyrrolidone-Plasticized Polyaniline Film, *Macromolecules*, **28** (23), 7645-7652, 1995.
453. C. T. Moynihan, Analysis of electrical relaxation in glasses and melts with large concentrations of mobile ions, *J. Non-Cryst. Solids*, **172-174** (2), 1395-1407, 1994.
454. Elliot, S. R., Use of the modulus formalism in the analysis of ac conductivity data for ionic glasses, *J. Non-Cryst. Solids*, **170** (1), 97-100, 1994.

455. Kyritsis, A., *et al.*, Dielectric relaxation spectroscopy in poly(hydroxyethyl acrylates)/water hydrogels, *J. Polym. Sci. B: Polym. Phys.*, **33** (12), 1737–1750, 1995.
456. Patel, H. K., and Martin, S. W., Fast ionic conduction in $\text{Na}_2\text{S}+\text{B}_2\text{S}_3$ glasses: Compositional contributions to nonexponentiality in conductivity relaxation in the extreme low-alkali-metal limit, *Phys. Rev. B*, **45** (18), 10292–10300, 1992.
457. Lu, H., *et al.*, Influence of the relaxation of Maxwell-Wagner-Sillars polarization and dc conductivity on the dielectric behaviors of nylon 1010, *J. Appl. Phys.*, **100** (5), 054104 (7pp), 2006.
458. Samui, A. B., *et al.*, Synthesis and characterization of polyaniline–maleic acid salt, *Synth. Met.*, **125** (3), 423–427, 2001.
459. Albuquerque, J. E., *et al.*, A simple method to estimate the oxidation state of polyanilines, *Synth. Met.*, **113** (1–2), 19–22, 2000.
460. Kaiser, A. B., *et al.*, Polypyrrole micro-line: current–voltage characteristics and comparison with other conducting polymers, *Curr. Appl. Phys.*, **4**, 497–500, 2004.
461. Long, Y. Z., *et al.*, *A Review on Electronic Transport Properties of Individual Conducting Polymer Nanotubes and Nanowires* in Nanowires Science and Technology, Lupu, N., ed., INTECH, Croatia, pp. 402, 2010.
462. Kim, K. M., *et al.*, The Effect of Silica Addition on the Properties of Poly((vinylidene fluoride)-co-hexafluoropropylene)-Based Polymer Electrolytes, *Macromol. Chem. Phys.*, **202** (6), 866–872, 2001.
463. Laermans, C., *et al.*, Positron annihilation lifetimes in irradiated crystalline quartz versus the 'glassy' thermal conductivity, *J. Phys. C: Solid State Phys.*, **17**, 763–768, 1984.
464. Sanyal, D., *et al.*, Study of transition metal ion doped mullite by positron annihilation techniques, *J Mater Sci*, **31** (13), 3447–3451, 1996.
465. Das, B., *et al.*, Study of Polyaniline Polyacrylamide Composites by Positron Annihilation Technique, *J. Appl. Polym. Sci.*, **89**, 930–933, 2003.
466. Peng, Z. L., *et al.*, Study of polyaniline by positron annihilation technique, *Synth. Met.*, **64**, 33–37, 1994.

References

467. Riley, P. A., Free Radicals in Biology: Oxidative Stress and the Effects of Ionizing Radiation, *Int. J. Radiat. Biol.*, **65** (1), 27-33, 1994.
468. Asada, K., and Yoshikawa, T., *Frontiers of Reactive Oxygen Species in Biology and Medicine*, Elsevier, Amsterdam, 1994.
469. Halliwell, B., Antioxidants in Human Health and Disease, *Annu. Rev. Nutr.*, **16**, 33-50, 1996.
470. Scott, G., *Atmospheric Oxidation and Antioxidants vol I-III*, Elsevier , Amsterdam, 1993.
471. Helaly, F. M., *et al.*, Effect of some polyaromatic amines on the properties of NR and SBR vulcanizates, *Polym. Degrad. Stab.*, **64** (2), 251-257, 1999.
472. Wang, J., *et al.*, Antioxidant activity of polyaniline nanofibers, *Chin. Chem. Lett.*, **18** (8), 1005-1008, 2007.
473. Naik, G. H., *et al.*, Comparative antioxidant activity of individual herbal components used in Ayurvedic medicine, *Phytochem.*, **63** (1), 97-104, 2003.
474. Singh, S., *et al.*, Kinetics of hydrogen abstraction from proton donord by DPPH, *Canad. J. Chem.*, **44** (22), 2657-2662, 1966.
475. Hazell, J. E., and Russell, K. E., The Reaction of 2, 2-Diphenyl-1-Picrylhydrazyl with Secondary Amines, *Canad. J. Chem.*, **36** (12), 1729-1734, 1958.
476. Gutteridge, J. M. C., Thiobarbituric acid-reactivity following iron-dependent free-radical damage to amino acids and carbohydrates, *FEBS Lett.*, **128** (2), 343-346, 1981.
477. Halliwell, B., and Gutteridge, J. M. C., Formation of a thiobarbituric-acid-reactive substance from deoxyribose in the presence of iron salts: The role of superoxide and hydroxyl radicals, *FEBS Lett.*, **128** (2), 347-352, 1981.
478. Gutteridge, J. M. C., Iron promoters of the Fenton reaction and lipid peroxidation can be released from haemoglobin by peroxides, *FEBS Lett.*, **201** (2), 291-295, 1986.
479. Sauerbrey, G., The use of quartz oscillators for weighing thin layers and for microweighing, *Z. Phys.* **155**, 206-222, 1959.
480. Zweier, J. L., and Kuppusamy, P., Electron paramagnetic resonance measurements of free radicals in the intact beating heart: A technique for

- detection and characterization of free radicals in whole biological tissues, *Proc. Natl. Acad. Sci. USA (Medical Sciences)*, **85**, 5703-5707, 1988.
481. Khramtsov, V., et al., NMR spin trapping: detection of free radical reactions using a phosphorus-containing nitron spin trap, *Magn Reson Med.*, **42**, 228-234, 1999.
482. Molyneux, P., The use of the stable free radical diphenylpicrylhydrazyl (DPPH) for estimating antioxidant activity, *Songklanakarinn J. Sci. Technol.*, **26**, 211-219, 2004.
483. Miller, J. C., and Miller, J. N., *Statistics for Analytical Chemistry*, 2nd ed., Ellis Horwood, UK, pp. 117, 1988.

LIST OF PUBLICATIONS

A. In refereed International/National journals

1. Somik Banerjee and A. Kumar, "Polyaniline nanofiber reinforced PVA nanocomposite coated quartz crystal microbalance based free radical sensor" Communicated to *Sens. Actuators B*.
2. Somik Banerjee and A. Kumar, "Swift heavy ion irradiation induced structural, optical and conformational modifications in conducting polymer nanostructures" Communicated to *Advanced Materials Letters*.
3. Sujata Pramanik, N. Karak, Somik Banerjee and A. Kumar, "Effects of solvent interactions on the conformation and local chain ordering of PANi nanofibers prepared by interfacial polymerization", *J. Appl. Polym. Sci.* (accepted).
4. Somik Banerjee and A. Kumar, "Optical band-gap and Urbach's tail in polyaniline nanofibers and irradiation induced effects", *Nucl. Instr. and Meth. B*, 269 (2011) 2798.
5. Somik Banerjee and A. Kumar, "Dielectric spectroscopy for probing the relaxation and charge transport in polypyrrole nanofibers", *J. Appl. Phys.* 109 (2011), 114313.
6. Somik Banerjee and A. Kumar, "Swift heavy ion irradiation induced structural and conformational changes in polypyrrole nanofibers", *Rad. Eff. Def. Solids*, iFirst, 2011, 1-8, doi: 10.1080/10420150.2010.542560.
7. Jyoti P Saikia, Somik Banerjee, B. K. Konwar and A. Kumar, "Biocompatible novel starch/polyaniline composites: Characterization, anticytotoxicity and antioxidant activity", *Colloids and Surfaces B: Biointerfaces*, 81 (2010) 158.
8. Somik Banerjee and A. Kumar, "Micro-raman investigation of the structural and conformational changes in polyaniline nanofibers", *Nucl. Instr. and Meth. B*, 268 (2010) 2683.
9. A. Kumar and Somik Banerjee, "Swift heavy ion irradiation: A novel technique for tailoring the size of polyaniline nanofibers" *Int. J. Nanosci.*, 10 (1-2), (2011), 161.

10. A. Kumar, Somik Banerjee, J.P. Saikia and B. K. Konwar, "Swift heavy ion irradiation induced enhancement in the antioxidant activity and biocompatibility of polyaniline nanofibers" *Nanotechnology*, **21** (2010) 175102.
11. A. Kumar, M. Deka and Somik Banerjee, "Enhanced ionic conductivity in oxygen ion irradiated poly(vinylidene fluoride-hexafluoropropylene) based nanocomposite gel polymer electrolytes" *Solid State Ionics*, **181** (2010) 609.
12. Somik Banerjee and A. Kumar, "Dielectric properties and charge transport in polyaniline nanofiber reinforced PMMA composites" *J. Phys. Chem. Solids*, **71** (2010) 381.
13. Somik Banerjee, Jyoti P Saikia, A. Kumar and B. K. Konwar; "Antioxidant activity and haemolysis prevention efficiency of polyaniline nanofibers" *Nanotechnology*, **21** (2010) 045101.
14. Somik Banerjee, Smritimala Sarmah and Ashok Kumar; "Photoluminescence in HCl doped polyaniline nanofibers" *Journal of Optics.*, **38**(2) (2009), 124-130.
15. Smritimala Sarmah, Somik Banerjee, Ashok Kumar; "Ion Transport in Dedoped Polyaniline Nanofiber-P(VDF-HFP)-LiCF₃SO₃ Composite Electrolyte" *J.Polym. Mater.*, **25**(3), (2008) 427.

B. In International/ National Conference proceedings:

1. A. Kumar and Somik Banerjee, "Size Dependent Antioxidant Activity of Polypyrrole Nanofibers", *Proceedings of the 55th DAE Solid State Symposium-2011, AIP Conference Proceedings*, **1349**, 399-400, 2011
2. Smritimala Sarmah, Somik Banerjee and A. Kumar, *Proceedings of the XXXII Optical Society of India Symposium*, Eds. P. P. Sahu and P. Deb, pp. 63.

C. Book chapters:

1. A. Kumar, Somik Banerjee and Smritimala Sarmah, "Ionic transport in dedoped (insulating) Polyaniline nanofiber dispersed composite polymer electrolytes" *Developments in Nanocomposites*, Kamal K Kar, A. Hodzic (Eds.) (in press)
2. A. Kumar and S. Banerjee, "Swift heavy ion irradiation induced strain generation and fragmentation in polyaniline nanofibers" *Photonics and Quantum structures*, D. Mohanta, Gazi. A. Ahmed (Eds.) Ch-10, pp 93-101, 2012, ISBN: 978-81-8487-098-5.

3. A. Kumar and S. Banerjee, "Conducting polymers: Intelligent functional systems" *Photonics and Quantum structures*, D. Mohanta, Gazi. A. Ahmed (Eds.) Ch-5, pp 47-57, 2012, ISBN: 978-81-8487-098-5
4. A. Kumar, Somik Banerjee and M. Deka, "Electron microscopy for understanding swift heavy ion irradiation effects on Electroactive polymers", *Microscopy Book Series. IV, Vol 3*, A. Méndez-Vilas and L. Labajos-Broncano (Eds.) pp-1755-1768, 2010, ISBN (13): 978-84-614-6191-2.

D. Patents:

1. A. Kumar and Somik Banerjee "A single step process for making polyaniline nanofibers reinforced polymer nanocomposite based transparent, antistatic and UV-protective coatings by in-situ rapid mixing polymerization". (Indian patent pending, Indian Patent No: 675/KOL/2010).

E. International/ National Conference and symposia attended:

1. Somik Banerjee and A. Kumar, *International Congress on Renewable Energy (ICORE-2011)*, Tezpur University, Tezpur, Assam, India, 2-4 November, 2011.
2. Somik Banerjee and A. Kumar, *Nuclear and Atomic Techniques in Pure and Applied Sciences (NATPAS-2011)*, Tezpur University, Tezpur, Assam, India, 1-3 February, 2011
3. Somik Banerjee and A. Kumar, *National Conference on Smart Nanostructures (NCSN-2011)*, Tezpur University, Tezpur, India, 18-20 January, 2011.
4. Somik Banerjee and A. Kumar, *International Conference on Fundamentals and Applications of Nanoscience and Technology (ICFANT-2010)*, Jadavpur University, Kolkata, India, 9-11 Dec, 2010.
5. Somik Banerjee and A. Kumar, *Swift Heavy Ions for Materials Engineering and Characterization (SHIMEC-2010)*, Inter University Accelerator Centre (IUAC), New Delhi, India, October 6-9, 2010
6. Somik Banerjee and A. Kumar, *National Conference on Renewable Energy at Tezpur University, Assam, India, March 23-25, 2010.*
7. Somik Banerjee, Meghraj Adhikary and A. Kumar, *National Conference on Condensed Matter Physics at NEHU, Shillong, Meghalaya, India, March 22-23, 2010.*

8. Somik Banerjee and A. Kumar, *International Conference on Advanced Nanomaterials and Nanotechnology (ICANN) at IIT Guwahati, Assam, India, Dec 9-11, 2009.*
9. Somik Banerjee and A. Kumar, *National Seminar on Photonics and Quantum Structures at Tezpur University, Assam, India, November 4-6, 2009.*
10. Somik Banerjee, A. Kumar and D. K. Avasthi, *Condensed matter Days (CM Days) at Jadavpur University, Kolkata, India, 26-28 August, 2009.*
11. Smritimala Sarmah, Somik Banerjee and A. Kumar, *XXXIII Symposium of the Optical society of India at Tezpur University, Assam, India*